



THE UNIVERSITY  
*of* ADELAIDE

**The Impact of Undulating Leading-Edge Modifications  
on the Flow Characteristics of NACA 0021 Foils**

**Nikan Rostamzadeh Torghabeh**

A thesis submitted in fulfilment of the requirements  
for the degree of Ph.D. in Mechanical Engineering  
November 2015

School of Mechanical Engineering  
The University of Adelaide  
South Australia, 5005  
Australia

# Abstract

In contrast to active flow control schemes that require an external energy source, passive flow control methods have been of great interest to engineers and scientists, due to their potential in augmenting the performance characteristics of various engineering systems, in addition to reducing fabrication, operation and maintenance costs. In aerodynamics, while the two primary passive flow control approaches, known as leading-edge and trailing-edge modifications, have proven successful in improving performance efficiency, complexities may arise in determining the design guidelines that ensure minimal penalties such as an increase in the drag force while improving lift-generation capabilities.

Operating at high attack angles, wings with undulating leading-edge modifications, in the form of protrusions similar to those on the humpback whale's pectoral flippers (tubercles) and wavy leading-edge configurations, have been shown to render aero-hydrodynamic loading benefits with negligible penalties in the transitional flow regime. These advantages include higher post-stall lift, reduced drag and lower tonal noise, in comparison with unmodified wings of the same cross-sectional profile. Hence, the undulating leading-edge modification has been proposed as a viable passive flow control method.

To account for the superior behaviour of the modified wings, a number of studies have attributed the observed advantages to the generation of streamwise vortices. Accordingly, analogies of tubercles to vortex generators, wing fences and delta wings have been proposed. Consensus, however, on the underlying flow mechanism triggered by the presence of a tubercled leading edge in different flow regimes has not been reached. In addition, the formation mechanism of streamwise vortices over tubercled foils is in question.

The present project aims to contribute to this research area by exploring the mechanism associated with the flow over full-span wings with undulating leading edges in the laminar, transitional and near-

turbulent regimes. The project also aims to investigate the underlying flow dynamics responsible for the development of streamwise vortices. To this end, theoretical, experimental and numerical approaches were adopted.

In the theoretical approach, *Prandtl's non-linear lifting-line theory* was employed to examine the effect of an undulating leading edge on the spanwise circulation distribution of the bound vortex. Experimental work in the form of wind tunnel force and pressure measurement tests were performed on a wavy wing to study the similarities and differences in the loading behaviour of a tubercled and a wavy wing in the transitional flow regime. On the numerical front, Computational Fluid Dynamics was utilized to perform comprehensive investigations into the flow structure around modified wings in three flow regimes. This allowed investigation of higher Reynolds number flows.

The results of the study demonstrate that wings with undulating leading edges (tubercled and wavy leading edges) alter the flow field in a fundamentally similar manner across the laminar, transitional and near-turbulent regimes. The presence of an undulating leading edge induces a spanwise pressure gradient that gives rise to flow skewness, which in turn leads to the development of streamwise vortices in line with a mechanism known as *Prandtl's secondary flow of the first kind*. In addition, spanwise circulation of the bound vortex associated with pairs of counter-rotating streamwise vortices behaves in a cyclic manner along the span of a modified wing. The spanwise vortex sheets, accordingly, appear to be rippled in the immediate vicinity of a wing with an undulating leading edge.

The loading behaviour of the wings with tubercles is shown to be dependent on the flow regime in which they operate. In the laminar and transitional flow regimes, the counter-rotating streamwise vortices induce a momentum-transfer enhancement effect whereby the flow from the separated flow region is transported to the neighbouring areas where the boundary layer remains attached to the surface of the wing. Whereas the unmodified wing loses lift abruptly in the lower limit of the transitional flow regime, possibly due to the burst of a laminar separation bubble, the tubercled foil maintains more attached flow which leads to a more gradual loss of lift at high attack angles.

In the near-turbulent flow regime, numerical results show that, contrary to the trend in the lower limit of the transitional flow regime, post-stall lift generated by a full-span tubercled wing is lower than that of an unmodified wing. It is observed that the unmodified wing's loss of lift is less abrupt in the near-turbulent regime than in the transitional regime due to the presence of higher momentum fluid within the boundary layer. On the other hand, the momentum transfer effect associated with the tubercled foil is still at play, however the lift coefficient of the tubercled foil is lower than that of the unmodified foil at post-stall attack angles. The inferior performance of the tubercled wing, compared with that of the unmodified, highlights the significance of the role played by Reynolds number effects and the influence of the cross-sectional profile on the performance of the modified wing in question.

The present project provides a better understanding of the impact of full-span wings modified with undulating leading edges on the underlying flow mechanism across a wide spectrum of the Reynolds number.

# Contents

<b>Abstract</b>	i
<b>Declaration</b>	vii
<b>Acknowledgements</b>	viii
<b>Nomenclature</b>	ix
<b>Chapter 1. Introduction</b>	1
<b>Chapter 2. Background Literature</b>	6
2.1 Historical Background of Flow Control.....	6
2.2 Boundary Layer Control in External Flow .....	7
2.3 Lift Augmentation Methods.....	8
2.3.1 Trailing-edge Modifications (Trailing-edge High Lift Devices) .....	8
2.3.2 Leading-edge Modifications (Leading-edge High Lift Devices) .....	10
2.3.3 Turbulators .....	11
2.3.4 Blowing.....	12
2.3.5 Suction .....	12
2.3.6 Zero-Net Mass-Flux Jets.....	13
2.3.7 Wall Heat and Cooling.....	13
2.3.8 Vortex Generators .....	14
2.3.9 Wing Fences.....	16
2.3.10 Acoustic Excitation .....	16
2.3.11 Moving Surface Boundary Layer Control.....	17
2.3.12 Plasma Actuation .....	17
2.3.13 Lift Enhancement by Tubercles .....	18
2.4 Drag Reduction Methods .....	19
2.4.1 Friction Drag Reduction.....	19
2.4.2 Induced Drag Reduction .....	23
2.4.3 Wave Drag Reduction.....	24
2.4.4 More Modern Drag Reduction Methods .....	24
2.5 Summary of Flow Control Methods .....	25

2.6 Humpback Whale Tubercles: A Nature-inspired Approach to Flow Control.....	27
2.6.1 Aero-Hydrodynamic Loading Behavior .....	28
2.6.1.1 <i>Bluff Bodies Modified with Tubercle-like Features</i> .....	28
2.6.1.2 <i>Initial Numerical Studies on Wings with Tubercles</i> .....	29
2.6.1.3 Performance of Humpback Flipper Models.....	30
2.6.1.4 Performance of Full-span Wings with Tubercles.....	32
2.6.1.5 Performance of Flipper Models vs. Full-span Airfoils with Tubercles.....	35
2.6.1.6 Performance of Finite-span Wings without Taper or Sweep .....	35
2.6.2 Flow Structure Investigations .....	36
2.6.2.1 <i>Flow Visualization on Full-span Wings</i> .....	36
2.6.2.2 Numerical Studies on Flipper Models.....	38
2.6.2.3 Numerical Studies on Full-span Airfoils.....	39
2.6.2.4 Numerical Studies on Finite-span Wings.....	42
2.6.3 A Theoretical Study on Flipper Models.....	42
2.6.4 Experimental Work on an Alternative to the Tubercle Configuration.....	43
2.6.5 Experimental Studies on Delta Wings with Tubercles .....	44
2.7 Summary of the Literature and the Knowledge Gaps.....	45
2.8 Aims and Objectives of the Project.....	47
<b>Chapter 3. Flow over a Wavy Foil in the Transitional Regime</b>	<b>56</b>
Paper 1: The effect of undulating leading-edge modifications on NACA 0021 airfoil characteristics	
58	
<b>Chapter 4. Flow over Tubercled Foils in the Transitional Regime</b>	<b>78</b>
Paper 2: The formation mechanism and impact of streamwise vortices on NACA 0021airfoil's	
performance with undulating leading edge modification.....	80
<b>Chapter 5. Flow over a Tubercled Foil in the Laminar Regime</b>	<b>103</b>
Paper 3: Evolution of the streamwise vortices generated between leading edge tubercles.....	105
<b>Chapter 6. Flow over a Tubercled Foil in the Transitional and Near-Turbulent Flow</b>	
<b>Regimes</b>	<b>148</b>
Paper 4: Exploring Reynolds Number Effects on the Flow Mechanism over a Tubercled Airfoil based	
on the NACA 0021 baseline profile.....	150

<b>Chapter 7. Summary, Conclusions and Recommendations for Future Work</b>	198
7.1 Summary .....	198
7.1.1 Similarities in the Characteristics Associated with the Flow over Wavy and Tubercled Wings	198
7.1.2 Flow Mechanism for Tubercled wings in the Transitional Regime .....	199
7.1.3 Flow Mechanism for a Tubercled Wing in the Laminar Regime .....	201
7.1.4 Flow Mechanism for a Tubercled Wing in the Near-Turbulent Regime .....	203
7.2 Conclusions .....	205
7.2.1 Similarities .....	205
7.2.2 Differences .....	206
7.2.3 Influence of Geometric Parameters on the Performance of Wavy Foils.....	207
7.3 Recommendations for Future Work.....	208
<b>Appendix A</b>	210
Conference paper 1: The Effect of Wavy Leading Edge Modifications on NACA 0021 Airfoil Characteristics .....	210
<b>Appendix B</b>	214
Conference paper 2: An Experimental and Computational Study of Flow over a NACA 0021 Airfoil with Wavy Leading Edge Modification.....	214

# Declaration

I certify that this work contains no material which has been accepted for the award of any other degree or diploma in my name, in any university or other tertiary institution and, to the best of my knowledge and belief, contains no material previously published or written by another person, except where due reference has been made in the text. In addition, I certify that no part of this work will, in the future, be used in a submission in my name, for any other degree or diploma in any university or other tertiary institution without the prior approval of the University of Adelaide and where applicable, any partner institution responsible for the joint-award of this degree.

I give consent to this copy of my thesis when deposited in the University Library, being made available for loan and photocopying, subject to the provisions of the Copyright Act 1968.

The author acknowledges that copyright of published works contained within this thesis resides with the copyright holder(s) of those works.

I also give permission for the digital version of my thesis to be made available on the web, via the University's digital research repository, the Library Search and also through web search engines, unless permission has been granted by the University to restrict access for a period of time.

Nikan Rostamzadeh Torghabeh



# Acknowledgements

My deepest gratitude is expressed to Professor Bassam Dally, Associate Professor Richard Kelso and Dr. Zhao Feng Tian whose encouragement, wisdom, patience and knowledge have tremendously helped me progress towards my academic goals. I could not have asked for better supervisors.

I would like to dedicate this thesis, first and foremost, to my wonderful mother to whom I owe most of my progress in life, my loving father who has made numerous sacrifices for me, and my kind brother with whom I have many fond childhood memories. I wish to thank my best friends Saleh Mahmoud and Iman Mafi whose sense of humor and enthusiasm made the journey a delightful experience. My appreciation also extends to Shiva Jade Motlagh for her emotional support.

I wish to thank my incredible friends Houman Alipoor, Dr. Mohsen Bazghaleh, Amin Miremadi, Dr. Arash Mehdizadeh, Sonia Pakniyat, Farzin Ghannadi, Pourya Aryan, Vahid Bakhti, Dr. Pawel Kuklik, Adam Klimkevich, Ladan Sahafi, Erwin Hamminga, Eyad Hassan, and Dr. Kristy Hansen from whom I've learned a great deal.

# Nomenclature

AOA / $\alpha$	angle of attack (deg)
A	foil planform area (m <sup>2</sup> )
C	foil mean chord (m)
C <sub>D</sub>	drag coefficient
C <sub>f</sub>	skin friction coefficient
C <sub>L</sub>	lift coefficient
C <sub>p</sub>	pressure coefficient
D	drag force (N)
L	lift force (N)
p	static pressure (Pa)
p <sub>∞</sub>	freestream static pressure (Pa)
Re	Reynolds number
S	foil span (m)
T <sub>u</sub>	turbulence intensity
U <sub>∞</sub>	freestream speed (m.s <sup>-1</sup> )
$\vec{u}$	velocity (m.s <sup>-1</sup> )
y <sup>+</sup>	wall – normal, non-dimensionalized distance
δ	boundary layer thickness
Γ	circulation (m <sup>2</sup> .s <sup>-1</sup> )
$\vec{\omega}$	vorticity (s <sup>-1</sup> )
ρ	density (kg.m <sup>-3</sup> )
ν	kinematic viscosity (m <sup>2</sup> .s <sup>-1</sup> )
τ	wall shear stress (Pa)

# Chapter 1

## Introduction

Flow control is defined as the ability to alter the character or disposition of a natural flow field actively or passively in order to effect a desired change [4]. As such, this branch of fluid mechanics has immense technological importance. Through the successful manipulation of the boundary layer, a wide variety of industrial applications can be enhanced [5]. An example of this achievement in modern aviation, is the vortex generator which is employed successfully to improve the aerodynamic performance of commercial aircraft such as the B737 and B767 [15]. Consequently, efficient flow control, whether passive or active, can offer tangible economical benefits through saving fuel costs for air, sea and land vehicles per year [4]. It is estimated that a 5% increase in the maximum lift coefficient in aircraft landing would allow a 25% payload increase [1]. Drag reduction for a tractor-trailer vehicle, can save in excess of 50 million barrels of oil [13]. Equally important, efficient flow control devices aim to have minimal adverse environmental impact, for instance low noise profiles and negligible air pollution.

Flow control in aerodynamics is primarily targeted towards flow separation control within the boundary layer. In most cases, it is desirable to delay separation in order to reduce form drag, increase lift and improve pressure recovery over a lifting body [4]. While numerous methods to postpone separation have shown significant improvements, typical disadvantages such as an increase in parasitic drag, energy consumption, system weight and reliability often arise [17]. Furthermore, in three-dimensional boundary layers, that are ubiquitous in practical flow scenarios, the prediction of separation becomes difficult [18]. Addressing such challenges requires further research into novel boundary layer flow control techniques that are less complex to implement, more economically viable and incur lower overall penalty.

Leading-edge tubercles, which are the protrusions observed on the pectoral flippers of the humpback whale, have been demonstrated to augment aero- or hydro-dynamic efficiency, when incorporated

into the design of lifting bodies [7, 10-12]. To date, several studies have suggested that leading-edge tubercles manipulate the surrounding flow field by generating streamwise vortices to yield such benefits [2, 6, 16]. Hence, tubercles can be regarded and utilized as a viable, nature-inspired form of passive flow control device.

One application of tubercles, currently in use, is industrial ceiling fans for large buildings. It is reported that a five-blade tubercle-modified fan system is 25% more efficient and consumes 20% less electricity than a 10-blade unmodified configuration [3]. Furthermore, tubercles suppress the generation of tonal noise, for a range of frequencies adjacent to the tonal peak, compared to their unmodified counterparts [8]. Leading-edge tubercles can also increase the energy generation by wind turbine blades [14]. WhalePower Corporation [9] has shown an increase in electrical generation at moderate wind speeds using tubercles on a 35kW variable-pitch wind turbine. It is conceivable that a tubercle-like leading-edge modification could be incorporated into the design of aircraft wings. Therefore, with the elimination of flaps and slats (in particular for Micro Air Vehicles), the weight of the aircraft as well as fuel consumption would decrease [3].

While the loading characteristics of full-span and finite-wings with tubercles and tubercle-like features have been previously studied in the transitional flow regime, the flow mechanism that renders the aero- or hydro-dynamic benefits is still not fully understood. In addition, the role of streamwise vortices in the loading behaviour of modified wings can be further explored. Finally, the flow mechanism and loading behaviour of tubercled wings in the laminar and turbulent flow regimes are in question. Accordingly, the present project aims to investigate these research knowledge gaps. It is believed that gaining insight into the underlying flow mechanism activated by the presence of tubercles, can further elucidate the advantages as well as the limitations of this novel form of passive flow control method for industrial applications.

The presented document is intended for Thesis by Publication and organised into seven chapters that chronologically follow the progress of the project. These chapters are succinctly introduced in this section.

To gain perspective on where tubercles stand amongst other flow control devices, Chapter 2 contains an overview of conventional, as well as more recently-developed flow control methods. It has been attempted to provide the conceptual principles behind the flow control techniques to highlight the flow mechanism under which they operate. The advantages and drawbacks of the reviewed flow control methods, as reported in the literature, are also discussed with qualitative and quantitative details, where available. The second part of the chapter focuses on a comprehensive review of the studies contributing to our knowledge about the aero- and hydro-dynamic loading characteristics of tubercled lifting bodies, in addition to their impact on the flow structure. This leads to the final section of the chapter, which reveals the research avenues pursued by the present work. Accordingly, the aims and objectives of the project are defined, and the methodology adopted is elaborated on.

Chapter 3 contains a published article in the Physics of Fluids journal titled, "[The effect of undulating leading-edge modifications on NACA-0021 airfoil characteristics](#)". This work focuses on examining the effects of wavy and tubercled leading edges, on the spanwise circulation distribution of a NACA-0021 airfoil, using a theoretical approach. Measurements of flow-induced forces and pressure in a wind tunnel were performed in the transitional flow regime to evaluate the loading behaviour of several wavy foils against a tubercled and an unmodified foil. In addition, a numerical study was carried out to explore the characteristics of the flow structure around a wavy foil.

Chapter 4 contains a published article in the Physics of Fluids journal titled, "The formation mechanism and impact of streamwise vortices on NACA 0021 airfoil's performance with undulating leading edge modification". This work examines the underlying mechanism responsible for the development of streamwise vortices over tubercled foils in the transitional regime. Computational Fluid Dynamics was utilized to probe into the flow structure around several tubercled foils to gain further insight into the mechanism accounting for the superior loading characteristics of the modified foils in comparison with the unmodified NACA-0021 foil in the transitional flow regime.

Chapter 5 contains an article accepted for publication in the Journal of Fluid Mechanics titled, "Evolution of streamwise vortices generated between tubercles." This study examines the underlying

flow mechanism activated by the presence of leading edge tubercles in the laminar flow regime. A Computational Fluid Dynamics investigation was conducted to compliment the PIV experimental work by Hansen [6].

Chapter 6, contains an article submitted to the Journal of Theoretical and Computational Fluid Dynamics titled, "Exploring Reynolds number effects on the flow mechanism over a tubercled airfoil". In this numerical study, the flow over a tubercled foil in the transitional flow regime was compared and contrasted to that of the near-turbulent regime. In addition, the loading characteristics of the modified foil were compared to those of the unmodified foil in the near-turbulent flow regime.

Finally, chapter 7 provides a comprehensive summary of the work conducted, and the findings of the project, followed by the key conclusions. In addition, suggestions for future research endeavours are presented as the closing section of Chapter 7.

## References

- [1] D. J. Butter, "Recent Progress on Development and Understanding of High Lift Systems," presented at the AGARD Conference on Improvement of Aerodynamic Performance Through Boundary Layer Control and High Lift Systems AGARD CP-365, 1984.
- [2] D. Custodio, "The Effect of Humpback Whale-Like Leading Edge Protuberances on Hydrofoil Performance," Master of Science Thesis submitted to Worcester Polytechnic Institute, December 2007.
- [3] E. F. Fish, P. Weber, M. Murray, and L. Howle, "The Tubercles on Humpback Whales' Flippers: Application of Bio-Inspired Technology," *Integrative and Comparative Biology*, vol. 51, pp. 203-213, 2011.
- [4] M. Gad-el-Hak, *Flow Control: Passive, Active, and Reactive Flow Management*: Cambridge University Press, 2007.
- [5] C. Hale, M. Amir, K. Kontis, and N. Shah, "Active and Passive Flow Control Studies at Subsonic Speeds at The University of Manchester " presented at the AIAA Aerospace Sciences Meeting and Exhibit, Reno, Nevada 2008.
- [6] K. L. Hansen, "Effect of Leading Edge Tubercles on Airfoil Performance," Doctor of Philosophy Thesis, Mechanical Engineering, University of Adelaide, Adelaide, SA, Australia, 2012.
- [7] K. L. Hansen, R. M. Kelso, and B. B. Dally, "Performance variations of leading-edge tubercles for distinct airfoil profiles," *AIAA Journal of Aircraft*, vol. 49:185-94, 2011.
- [8] K. L. Hansen, R. M. Kelso, and C. I. Doolan, "Reduction of flow induced tonal noise using leading edge sinusoidal modifications," *Acoustics Australia*, vol. 40, 2012.
- [9] L. E. Howle, "WhalePower Wenvor blade. A report on the efficiency of a WhalePower Corp., 5 meter prototype wind turbine blade ", BelleQuant Engineering, PLLC2009.
- [10] H. Johari, C. Henoeh, D. Custodio, and A. Levshin, "Effects of Leading Edge Protuberances on Airfoil Performance," *AIAA Journal*, vol. 45:11, November 2007.

- [11] D. S. Miklosovic, M. M. Murray, and L. Howle, "Experimental Evaluation of Sinusoidal Leading Edges," *Journal of Aircraft*, vol. 44:1404–1407, 2007.
- [12] D. S. Miklosovic, M. M. Murray, L. E. Howle, and F. E. Fish, "Leading Edge Tubercles Delay Stall on Humpback Whale Flippers," *Physics of Fluids*, vol. 16(5) pp. L39-L42, 2004.
- [13] V. U. Muirhead and E. G. Saltzman, "Reduction of Aerodynamic Drag and Fuel Consumption for Tractor-Trailer Vehicles," *Journal of Energy*, vol. 3, pp. 279-284, 1979.
- [14] T. Muller, "Biomimetics: Design by nature," *Nat. Geo.*, vol. 213: 68-91, 2008.
- [15] H. A. Mwenegoha and M. Jabbal, "Investigation of Passive Flow Control Techniques to Enhance the Stall Characteristics of a Microlight Aircraft," *International Journal of Flow Control*, vol. 5, 2013.
- [16] H. T. C. Pedro and M. H. Kobayashi, "Numerical Study of Stall Delay on Humpback Whale Flippers," *AIAA Paper 2008-0584*, 7-10 January 2008.
- [17] P. Poisson-Quiton, "On the Mechanism and Application of the Control of the Boundary Layer over Airplanes," presented at the Int. Colloquium on Mechanics, 1950.
- [18] M. Tobak and D. J. Peake, "Topology of Three-Dimensional Separated Flows," *Ann. Rev. Fluid Mech.*, vol. 14, pp. 61-85, 1982.

# Chapter 2

## Background Literature

### 2.1 Historical Background of Flow Control

Gad-el-Hak [38] provides a comprehensive review of the historical background of flow control, which is reviewed in this sub-section. The evolution of flow control can be viewed within five distinct eras: the empirical era (prior to 1900); the scientific era (1900-1940); the World War II era (1940-1970); the energy crisis era (1970-1990); and the new era (1990s and beyond). Even in prehistoric times, streamlined spears and boomerangs were shaped specifically to fly smoothly in air. Evidence of the successful efforts to control the flow of water in Egypt and Mesopotamia exists in the form of irrigation canals [8, 19]. In that period, however, understanding of the basics of fluid motion was very limited and methods were devised on the basis of empirical attempts that relied heavily on trial and error.

The scientific era began with Prandtl's comprehensive manuscript [90], detailing the boundary layer theory and the mechanisms of flow separation. Subsequently, the emergence of flow control devices, designed based on the fundamental flow behaviour principles accelerated. The advancement was further motivated by the Second World War and the Cold War [38], 1940-1970. Armies in both the east and west investigated flow control methods and adopted the findings in the design of missiles, torpedos and submarines. Two outstanding examples of this era are laminar flow control techniques and polymer drag reduction methods [64].

The development of flow control for civilian applications was the centre of attention due to the energy crisis in 1973. During the years 1970-1990, many private corporations and government agencies invested considerably in drag-reduction-oriented projects to maximize energy utilization of air, sea and land vehicles [38]. This was a remarkable turn of attention from the military sector, seen prior to 1973. In the following decades, the availability of robust, relatively inexpensive computer programs enabled engineers and scientists to perform complex numerical simulations to predict the behavior of



fluids using Computational Fluid Dynamics (CFD). This trend is still in progress and has provided tremendous benefits where analytical and experimental approaches to address flow control problems are onerous. Two primary flow control examples from this era are the numerical studies on transition-delaying compliant coatings and large eddy breakup devices to reduce skin-friction drag [37]. In addition to more traditional methods, reactive flow control has also been introduced to manipulate the coherent structures in transitional and turbulent shear flows [20]. Areas such as chaos control, neural networks and micro-electro-mechanical systems (MEMS), have contributed to the development of reactive flow control. In the following sections, due to its relevance to the present project, focus is specifically placed on boundary layer control in external flow.

## **2.2 Boundary Layer Control in External Flow**

Ludwig Prandtl's seminal work on boundary layer development revolutionized fluid dynamics in the early 20th century. The description of how fluids behave in close proximity to a wall boundary, as proposed by Prandtl, has had a profound impact on various branches of fluid mechanics. Ever since Prandtl's ground-breaking paper [90], scientists and engineers have attempted different methods to control and manipulate the behaviour of the boundary layer to improve the efficiency of a given flow application [44].

Aerodynamics of lifting bodies, in particular, regards the lift-to-drag ratio as a measure of efficiency [2], and therefore it is desirable to achieve higher values of this ratio. The primary mechanisms through which aerodynamic efficiency is improved involves procedures to prevent or delay boundary layer flow separation. This is especially significant in situations where the flow encounters an adverse pressure gradient. Under such circumstances the boundary layer is susceptible to flow separation, a phenomenon which often results in the reduction of the lift force and a subsequent rise in drag, known as stall [2]. It is expected that the three primary forms of stall: leading-edge, trailing-edge and thin-airfoil stall, may occur for one airfoil at different Reynolds numbers. This can also be true for different airfoils at the same Reynolds number [114]. Evidently, stall is an undesirable phenomenon, both in terms of power requirements and stability.

Both passive and active flow control methods have been developed to, either increase the lift, reduce the drag or introduce a combination of the two by various means to manipulate the behaviour of the boundary layer. Most active flow control techniques aim to modify the flow field by utilizing actuation and sensing components [44]. In contrast to active flow control, passive flow control methods to augment the aerodynamic performance of lifting bodies are of considerable interest due to their ease of manufacture, maintenance and economic viability, as they primarily rely on stationary components that enable different forms of wing geometry shaping to enhance mixing or control the pressure gradient. The following pages provide a non-exhaustive review of a number of flow control devices, currently in use and under ongoing research. These methods have been categorized according to the aero-hydrodynamic forces they enhance. A few references have been included in each case.

## 2.3 Lift Augmentation Methods

### 2.3.1 Trailing-edge Modifications (Trailing-edge High Lift Devices)

A rippled (wavy) trailing edge can be incorporated into the design of an airfoil to act as a passive flow control device [78]. One impact of the wavy trailing edge on the flow structure is the development of lateral pressure gradients that drive the fluid with low momentum towards a bifurcation line located between the rippled trailing edge's trough and peak. Consequently, a form of boundary layer relief occurs whereby the adverse effects of a strong pressure gradient are alleviated in the streamwise direction, and more attached flow is maintained near the trailing edge. Morin and Barber [78] demonstrated that, for a wing with a wavy trailing edge, the maximum lift coefficient and the stall angle were increased. The convoluted surfaces such as those seen in Figure 2.1, enhance mixing and have also been used in turbofans.

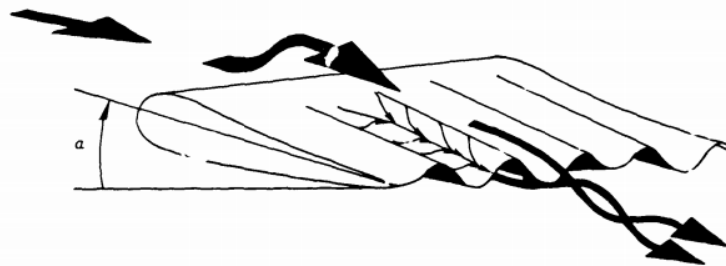


FIG 2.1 Flow over an airfoil with a rippled trailing edge [78]

The use of self-activated movable flaps (artificial bird feathers) near the trailing edge is another method for flow separation control. These components that lift from the surface on the suction side, as a response to reversed flow due to flow separation, provide a physical barrier to prevent the flow from moving upstream towards the leading edge [6]. Since drag can be a concern due to the presence of such arrangements, as well as the early onset of boundary layer transition, the flaps are mostly installed very close to the trailing edge.

Plain and split flaps (Figure 2.2) with the fulcrum in front of the trailing edge have been popular since 1930 [97]. Today, Fowler flaps are incorporated into the design of airliners which offer retractable slats and slotted flaps. The basic mechanism involved in augmenting the generated amount of lift by flaps is to impart more momentum to the fluid by deflecting the flow stream in a certain direction. In other words, the deflection of these devices varies the camber and chord of the wing. A superior design to split flaps incorporates strongly deflected small flaps wherein the fulcrum lies at the trailing edge of the wing. These flow control components, that can be as small as 1% of the chord, are capable of achieving a distinct increase in the lift coefficient [43].

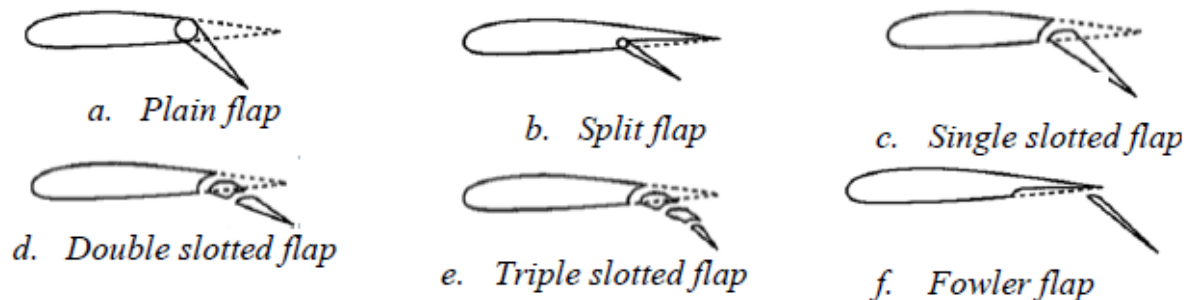


FIG 2.2 A number of trailing-edge high-lift devices [97]

The Gurney flap, is another device to increase lift. The Gurney flap, which is a small flap often mounted at right angles to the chordline at the trailing edge, can offer advantages by increasing the aerodynamic loading on the pressure side of the wing, while reducing the pressure on the suction side [82]. This arrangement is also useful if the same overall lift is to be generated, in which case, the loading of the upper side is relieved. The Gurney flap, in effect, alters the Kutta condition and

introduces counter-rotating vortices that markedly change the flow field and lead to an increase in the amount of circulation generated around the airfoil [65].

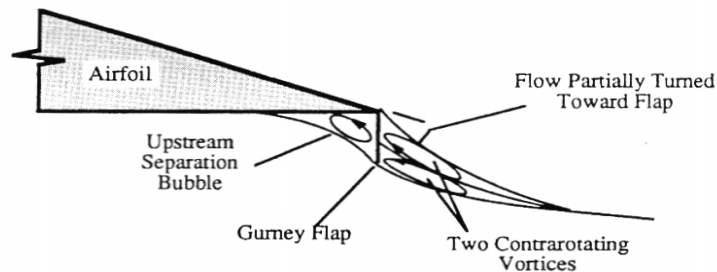


FIG 2.3 Schematic of an airfoil equipped with a Gurney flap at the trailing edge [56] (from description in [65])

### 2.3.2 Leading-edge Modifications (Leading-edge High Lift Devices)

Modifications to the leading edge have been researched and implemented as long ago as 1917 [49]. A lift increase of 25% was achieved by a spanwise slot, cut parallel to the leading edge of the aircraft H.P.17, as tested by Handley Page [5]. Lift increases of up to 50% were achieved when the shape of the slot was modified on various airfoils. The effect of the number of slots on the lift coefficient was studied by Smith [106] and van Dam [117] who attempted to explain the mechanism by which a multiple number of leading-edge slots enhance the lift coefficient of an airfoil. They proposed that each slot produced a fresh boundary layer and the overall pressure recovery of a multi-element system was divided among all the elements. This way the boundary layer does not grow continuously and the thin turbulent boundary layers would withstand stronger adverse pressure gradients.

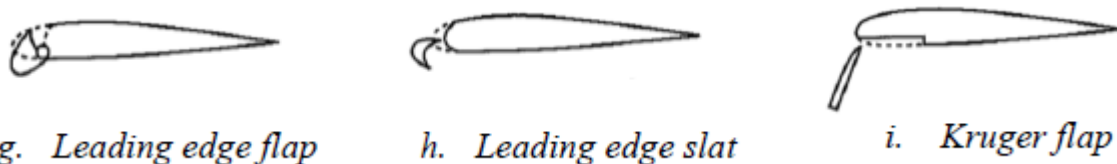


FIG 2.3 A number of leading-edge high-lift devices [97]

An 11% increase in the maximum lift coefficient was reported when a droop nose was applied to the leading edge of transonic wing sections at low speeds [58]. The droop nose, reduces the curvatures from the stagnation region (alters the camber) which leads to high suction peaks at high attack angles.

However the design of the droop nose proves challenging, as the suction peak that forms under the "chin" of the droop, on the lower side, may become supercritical at low cruise lift coefficients. Thus a discrepancy of up to 2%, between the design target lift coefficient and the measured value can arise [49].

Streamwise vortices, to be generated within the boundary layer, can be created by a serrated leading edge. These small serrations can be installed near the stagnation region, on the pressure side of an airfoil. Soderman [107] carried out wind tunnel experiments on a NACA 661-021 airfoil with a serrated leading edge (based on an owl wing) at a Reynolds number equal to 2,320,000 and found that the maximum lift coefficient, as well as the stall angle were improved. Also, the drag on the foil was not increased at low angles of attack and was decreased at high attack angles. It was reported that geometric parameters such as the size of the serrations, their locations and spacing, influenced the aerodynamic behaviour of the airfoil.

### 2.3.3 Turbulators

Another passive flow control device, referred to as the turbulator (Figure 2.4), is designed based on the notion that a turbulent boundary can withstand stronger adverse pressure gradients, as opposed to a laminar boundary layer [101]. Accordingly, turbulators which resemble thin strips, are placed on the suction surface of an airfoil to render enhanced momentum exchange through mixing as the laminar boundary layer encounters these devices. This is known as *tripping* the laminar boundary layer. The main disadvantage associated with the presence of turbulators is the rise in the drag force due to the skin friction from the turbulent boundary layer. The placement position, length and height of turbulators can determine the performance of the lifting body and therefore, are important design parameters [101].

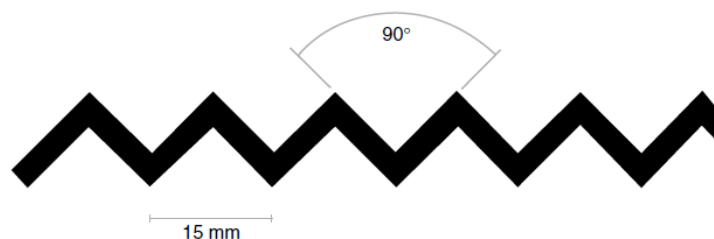


FIG 2.4 Zigzag shaped turbulator for microlight aircraft [81]

### 2.3.4 Blowing

Energy can be added to the boundary layer by means of blowing air through a slot over the wing's surface. Consequently, the re-energized boundary layer could overcome strong adverse pressure gradients to delay separation [5]. This method is observed in nature in the thumb pinion of a pheasant, the split-tail of a falcon and the layered wing feathers of a number of birds [37]. Blown flaps operate under this mechanism by directing a jet of air bled from the aircraft's engine to the rear section of the wing at different angles. Flow attachment can be achieved for blown flap angles of up to 60 degrees [51]. The amount of air added to the flow stream alters the amount of circulation generated around the lifting surface. If this amount exceeds the limit necessary to prevent boundary layer separation, the generated circulation rises above the value predicted by potential theory [69].

Control flexibility can also be improved by applying oscillations in addition to the steady blowing of air. This way the developed coherent structures can be regulated by the periodic motion of the membrane. These two main disadvantages of blowing methods are the complexity of their deployment, and the costs associated with the increase in weight and the drag force due to the presence of extra components [86]. Also, transpiration through active methods is rarely considered due to the power requirements and the complexity of the mechanism, especially in event of an engine failure, wherein power requirements become crucial [49].

### 2.3.5 Suction

If the decelerating particles near the wall in a boundary layer are removed, the gradient of the velocity in the wall-normal direction is increased, and separation is averted [37]. This was shown by Prandtl's flow visualization work [90] on a cylinder with a spanwise slit on one side. The boundary layer in his experiments, remained attached over a considerable area over the cylinder's surface. A suction coefficient, given in equation 2.1, is defined to determine the speed of the suction fluid, necessary to prevent flow separation.

$$C_q = \frac{v_w}{U_\infty} \quad (2.1)$$

where  $v_w$  and  $U_\infty$  represent the suction fluid and free-stream flow speed, respectively. For a laminar boundary layer, Trukendrodt [116] computed the suction coefficient for a Zhukovski airfoil to be a function of the Reynolds number and equal to  $1.12 \text{Re}^{-0.5}$ . The suction coefficient, in a turbulent boundary layer is estimated using empirical approaches. Schlichting and Pechau [98] reported that a suction coefficient between 0.002 to 0.004, is needed to prevent boundary layer separation.

### **2.3.6 Zero-Net Mass-Flux Jets**

Another form of active flow control method employs the zero-net mass-flux jet (ZNMFJ) concept. ZNMFJs introduce linear momentum to the flow field without net-mass injection across the system boundaries [21]. The main advantage of this scheme is that it takes the required fluid from the local field without the introduction of external “fluid control” [30]. The use of an oscillating membrane, as the actuator, allows the fluid to enter and exit the field through an orifice. In this mechanism, the existing fluid, forms a shear layer which helps to develop coherent structures that entrain higher momentum fluid from the irrotational flow field into the boundary layer, resulting in a delay in separation or re-attachment. Recently, Esmaeili Monir, Tadjfar, and Bakhtian [30] showed that by placing the oscillating membrane at the 12%-chord location of a NACA 23012 (at a Reynolds number equal to 2,190,000), stall characteristics were significantly improved. An optimal blowing ratio equal to three was reported in this study. In general, the performance of ZNMFJs depends on multiple structural, geometrical and flow parameters that pose challenges in the efficient application of ZNMFJS. Glezer and Amitay [40] provide a comprehensive review of synthetic jets (ZNMFJs) that operate based on the described fundamental concept.

### **2.3.7 Wall Heating and Cooling**

Cooling a surface over which compressible flow in the form of a gas is passing, increases the density and decreases viscosity of the fluid in the wall region [37]. These effects change the velocity profile of the boundary layer, leading to a delay in flow separation. The use of this method is, however, limited to compressible flows at high speeds. Gadd [39] provides a comprehensive summary of the research conducted to study the effect of heat transfer on boundary layer separation.

With liquids, heating the wall decreases the viscosity, but does not change the density appreciably. Aroesty and Berger [4] reported that the boundary layer separation can still be delayed to a small extent by heating the wall over which water is flowing. Nonetheless, experimental data are still needed to confirm this effect [37]. Other methods to induce a viscosity gradient in the wall-normal direction are film boiling, cavitation, chemical reactions among others.

### **2.3.8 Vortex Generators**

Vortex generators resemble airfoils with small aspect ratios that are typically mounted normal to the wing's surface. These components introduce helical streams of air that carry high-momentum fluid into the boundary layer, where there is retarded flow near the surface [12]. The main penalty associated with vortex generators is their drag. Also, the configuration and arrangement of vortex generators, which include their height (with respect to the boundary layer thickness), their orientation, and the planform shape, are critical. This is because the poorly-arranged vortex generators may cause the aerodynamic efficiency to decrease. Vortex generators that are placed too close to one another, for instance, may produce co-rotating vortices that undergo an annihilation process [5].

Bruyes [16] pioneered the use of vortex generators to increase mixing in the boundary layer. Subsequently, Schubauer and Spangenberg [99] conducted experiments to determine the effects of forced mixing in the boundary layer. Several vortex generators and their mixing capabilities were tested on the boundary layer formed on a flat surface. It was found that the effect of forced mixing was similar to the effects of a reduction of the adverse pressure gradient, where the shear layer becomes less susceptible to separation.

Rao and Mehrota [92] looked into the effect of two types of vortex generators, namely blunt obstacles and vanes, on the drag force exerted on a flat plate. It was reported that in all test cases the vane type vortex generators increased drag, while obstacle-type generators placed upstream of the plate produced a very small change in drag. Furthermore, a reduction in drag was achieved when the vanes were placed a short distance above the plate.



The significance of the position and location of vortex generators on the drag and lift forces on an airfoil were examined by Brown [15]. In an experimental study, a number of forward-facing wedges were placed on the upper surface of an airfoil that was positioned at high angles of attack. It was found that the position of the wedges played a critical role in the results obtained. Placement of the vortex generators at the leading edge yielded the highest increase in lift (17%) and a slight drag penalty. The mid-chord placement led to a 100% rise in drag and 10% decline in the lift force.

Skin friction measurements on a surface downstream of vortex generators were undertaken by Spangler and Wells [109]. The heights of the vortex generators selected were 2%, 10% and 20% of the local boundary layer thickness. The generated counter-rotating vortices maximized the energy transfer to the boundary layer, but they caused an increase in total drag that mainly came from skin friction.

Pearcy [88] suggested a set of design rules to optimize the performance of vortex generators to prevent boundary layer separation. He examined previous studies and based his design rules on the measurements of stream-wise velocity, from which he determined the location of vortices and the effects of vortices on the boundary layer, for different vortex array arrangements. It was concluded that, for a pair of co-rotating vortices, the spacing between the generators is the most important parameter. While the generators must be close to the surface, they should not be too far apart, otherwise the effect of one generator in sweeping low-momentum fluid away from the surface would be cancelled by the other generator, sweeping the same fluid back to the surface. The use of a spacing-to-generator height ratio from 5 to 6 was recommended, and it was noted that satisfactory results are obtained when a generator with a height of 1% of the chord length is placed far upstream on the foil.

For vortex generators that produce counter-rotating vortex pairs, Pearcy [88] recommended a spacing-to-height ratio of 10, which is a compromise between effectiveness and stream-wise persistence. This is due to the fact that counter-rotating pairs tend to move towards each other, convecting out of the boundary layer under the influence of their fictitious image vortices next to the wall. However if

effectiveness over a short range is the only requirement, then a spacing-to-height ratio of 4 or 5 is more suitable. This implies that counter-rotating vortices are more effective when the distance between adjacent vortices is larger than the spacing between vortices and their flow images.

### **2.3.9 Wing Fences**

Wing fences are flat plates mounted at right angles to the suction surface of finite-span wings [46]. Since spanwise flow on swept wings can lead to wingtip stall [93], wing fences are placed parallel to the free-stream flow direction to inhibit the development of spanwise flow. On the stalled wingtip of a swept wing, a nose-up pitching moment could be developed as the centre of pressure moves upstream at high attack angles [14]. As a result, deep stall may occur. Deep stall is a situation which is undesirable with regard to stability and often hard to recover from. To prevent this event, wing fences are adopted as spanwise-flow obstruction devices. The main disadvantage of wing fences, is their contribution to an increase in the drag coefficient despite their small surface area [84].

### **2.3.10 Acoustic Excitation**

Sound fields can affect vortex shedding. It was shown by Blevins [9] that a sound field affects the velocity field rather than the pressure field around a lifting body, a phenomenon which influences vortex shedding. Improvements in the lift coefficient can be achieved by sound excitation and are strongly dependent on the flow incidence angle as demonstrated by Hsiao, Lui and Shyr [52]. They reported an increase of about 40% in the lift coefficient at an 18-22-degree attack angle range, whereby the excitation frequency was maintained at 100Hz. In contrast, under conditions of pre-stall, the effect of excitation on lift characteristics was negligible. These researchers found that the optimal location for excitation was near the flow separation point. Under these conditions, flow mixing (momentum transport) is enhanced and a lower suction peak on the upper side of the leading edge is produced in the post-stall zone. Also the wake emanating from an excited flow field was narrower compared to that of an unperturbed field. The challenges associated with this form of flow control are associated with the determination of acoustic parameters such as the forcing location and excitation frequency [49].

### 2.3.11 Moving Surface Boundary Layer Control

Swanson [113] reviewed the Magnus effect as a potential means for flow control within a moving boundary layer. Favre [32] used two rollers to rotate a belt around an airfoil, a mechanism that delayed separation up to a 55-degree incidence angle. Despite improvements in aerodynamic efficiency, complexities in design often arise due to the geometric requirements of the rotating belt or cylinders installed. For instance, since the wing chords on most aircraft varies along the span, the cylinders or belts need to have diameters or lengths that vary accordingly.

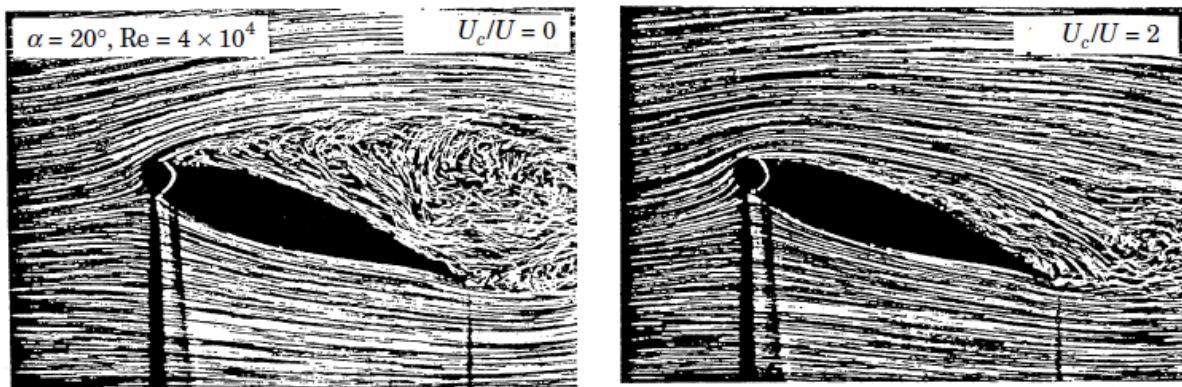


FIG 2.5 Airfoil without a rotating cylinder (left), airfoil with the leading edge rotating cylinder [75]

Vibration problems were also reported in wind tunnel tests carried out on a Joukowski airfoil fitted with a series of fast-rotating cylinders, placed at different locations [75]. Further investigations showed that a critical speed ratio exists between the cylinder surface speed and that of the free stream. Also, the gap size between the cylinder and the foil's surface plays an important role in the development of the flow. A large unsealed gap has an adverse effect on the flow [77]. Incorporating two rotating cylinders, one at the leading edge and the other at the trailing edge, can bring about a 19.5% increase in the maximum lift coefficient. Nevertheless, a drag penalty is associated with the rotating cylinders. In addition, roughness effects can alter the aerodynamic efficiency profile [76].

### 2.3.12 Plasma Actuation

In recent years, a number of studies have adopted plasma actuation techniques to introduce aerodynamic loading advantages. The aim has been to understand the underlying physical mechanisms of the actuator interaction with the flow field, and to develop a practical flow control

device (PFC) [91]. The mechanism of lift enhancement by plasma actuation is still not fully understood, however Particle Image Velocimetry (PIV) and Direct Numerical Simulation (DNS) data have clarified how the drag force is increased. Corke, He and Patel [24] performed experiments on NACA 0009, using weakly-ionized plasma actuators, in order to study the aerodynamic forces. While lift was increased, the drag force also rose, diminishing the overall aerodynamic efficiency. However, when the actuators were placed in series, the drag increase was eliminated. Enloe, McLaughlin and VanDyken [29] concluded that the plasma induces an electrostatic body force on the surrounding fluid that is proportional to the net charge density as well as the strength of the electric field. Guillermo and D'Adamo [42] studied electro-hydrodynamic actuators operating by DC pulsed plasma, and predicted the addition of momentum in the boundary layer with changes in the fluid properties. Hence, the presence of the electrostatic body force and momentum addition to the boundary layer may explain the observed increase in the lift force [91].

Plasma actuation flow control has also shown promising results with regard to flow separation control on thin airfoils intended for use on micro air vehicles at low Reynolds numbers [119]. It is possible to alter the flow velocity at a particular location on the airfoil's surface by the momentum-addition effect of the plasma actuators. In this manner, the magnitude of the lift force is altered. In other words, by adding momentum to the flow field, circulation is modified and consequently the aerodynamic forces vary. This approach was demonstrated, by Hall, Jumper, Corke and McLaughlin [45], to work successfully even within an inviscid flow field. It was shown that the placement of the actuator farther aft on the airfoil surface, enhanced lift generation further, as the actuator had a stronger impact on the Kutta condition [119].

### **2.3.13 Lift Enhancement by Tubercles**

In contrast to many conventional flow control devices, passive leading-edge modifications inspired by the humpback whale tubercles have been shown to yield aero-hydrodynamic benefits with negligible penalties at high attack angles [74]. These forms of modifications have the potential to be utilized as flow control devices with a host of industrial applications. Due to the relevance of the present project

to leading-edge modifications using tubercles, Section 2.6 is dedicated to a comprehensive review of these lift-enhancing flow control devices.

## **2.4 Drag Reduction Methods**

### **2.4.1 Friction Drag Reduction**

Airfoil shaping techniques have been adopted to mitigate the effects of friction (viscous) drag through the control of the laminar portion of the boundary layer. To this end, in the early 1980s, NASA developed a series of modified airfoils, known as the Natural Laminar Flow (NLF) series, using computer optimization schemes [70]. The optimised profiles were capable of extending the laminar portion of the boundary layer, and maintaining laminar flow up to the mid-chord location by improving the extent of the favourable pressure gradient. Consequently, the surface pressure distribution on NLF airfoils remained nearly constant over a larger area along the chord.

Airfoil shaping is also a suitable option for swept wings where the sweep angle is less than 20 degrees. For higher Reynolds number flows and wings with higher sweep angles, the flow suction method is, however, more appropriate [94]. For three-dimensional swept wings, the integration of a natural laminar flow airfoil is a complex task. It requires a comprehensive study of the optimum pressure distribution as a function of sweep angle, as well as Mach and Reynolds number effects [10].

In the hybrid laminar flow concept, suction is applied near the leading-edge region to regulate the development of cross-flow as well as the Tollmien Schlichting instabilities [55]. In more modern techniques, such as those using Flexible Composite Surface Deturbulators, the availability of new materials and fabrication techniques is exploited to alter the fundamental drag production mechanism [55]. Flexible Composite Surface Deturbulators (FCSD) modify the boundary layer by attenuating turbulent mixing in a thin layer of separated flow [102]. In the presence of a chord-wise pressure gradient, a laminar-separation bubble, occupying a large area over the airfoil, is sustained by FCSD's. The bubble behaves in a similar manner to a slip-layer which increases the speed of the fluid particles in the shear-free external flow, thus significantly reducing skin friction drag.

The principal challenge with regard to Laminar Flow Control (see Figure 2.6 as an example) is associated with the type of instabilities that occur within a particular application. In other words, the difficulties lie in determining whether linear or non-linear transition mechanisms are at play. Early transition caused by roughness, waviness and spanwise contamination on swept wings, are examples of bypass transition that are not dominated by a single linear instability mechanism [55]. In order for Laminar Flow Control techniques to be successful, parameters influencing bypass transition must be identified and controlled [18].

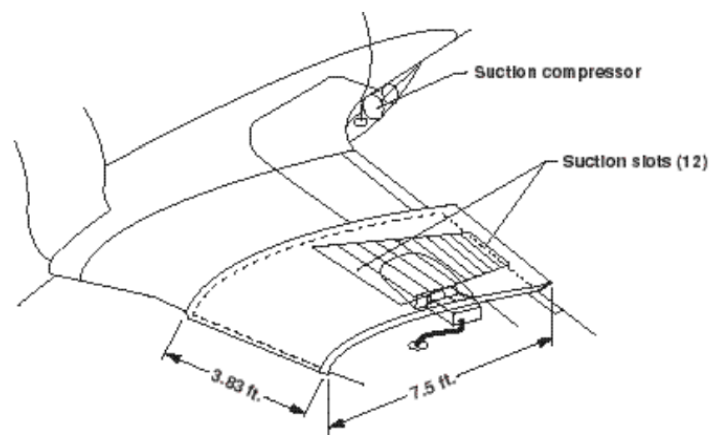


FIG 2.6 Schematic of a Laminar Flow Control mechanism on an F90 aircraft wing [13]

In the turbulent boundary layer, drag reduction can be achieved by the use of longitudinal grooved surfaces that resemble shark skin. These devices, known as riblets, are the most extensively studied form of passive flow control elements to reduce drag [120]. Figure 2.7 shows a sketch of one type of riblets with the defining geometric parameters. Merkle and Deustch [72] provide a comprehensive report on the effects of riblets' geometric variations on drag reduction. Drag reduction can also be achieved by Large Eddy Breakup Devices (LEBDs) which are streamwise-oriented thin plates mounted in the turbulent boundary layer parallel to the surface [62]. The concept behind the design of riblets and LEBDs is framed around the origins of friction drag in a turbulent boundary layer. Since large eddies contribute the most to friction drag, riblets and LEBDs aim to preclude the formation of these vortices in order to minimise skin friction drag in aeronautical applications [55]. Riblets constrain the large eddies, while LEBDs periodically straighten the boundary layer flow so as to reduce the adverse effects of streamwise vortices on the wing. It has been shown that the drag force

can be reduced by up to 5% using either riblets or LEBDs. Despite their effectiveness in reducing drag, the main disadvantage of using riblets and LEBD's are the manufacturing and maintenance costs [55].

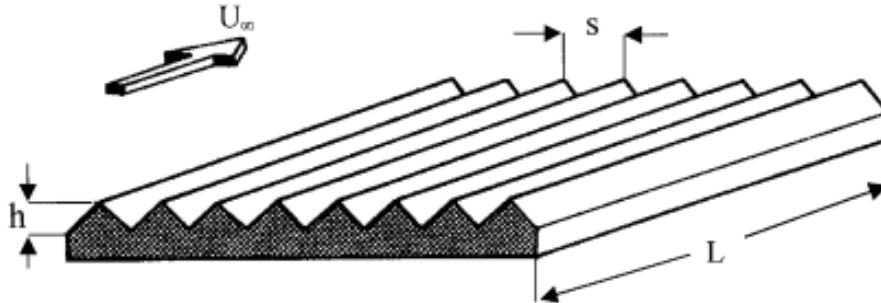


FIG 2.7 Sketch of a riblet with associated geometric parameters as illustrated in [95]

Sirovich and Karlsson [103] incorporated a series of randomised, V-shaped protuberances into a fully-developed turbulent boundary layer and achieved a drag reduction of 12%. When the same patterns were incorporated using a regular pattern, as opposed to a randomized one, the drag rose up to 20%. The notion behind the design of the drag-reducing features in their study was based on a fundamental understanding of the origins of drag in a turbulent boundary layer. Embedded within the boundary layer are a series of weak oblique plane waves that interact with the primary streamwise vortices. Artificially randomizing the phases of the waves and the vortices has been shown through numerical simulations to lead to less bursting and a lower friction drag profile as a result [37]. Another, recently-proposed, method to reduce drag is through wall oscillation. Akhavan, Jung, and Mangiavacchi [1] reported a 40% decrease in drag based on the results from Direct Numerical Simulations of a turbulent channel flow, whereby one of the walls underwent spanwise oscillations. It was stated that spanwise wall oscillations suppressed the Reynolds stresses, and the viscous sub-layer was thickened due to wall oscillations. Similar effects were reported in wind tunnel tests by Choi and Clayton [23]. The main disadvantage associated with this method, however, is the energy expenditure incurred to activate the wall oscillations.

Koeltzsch, Dinkelacker, and Grundmann [61] introduced a novel class of riblets whose shape assumed a converging-diverging pattern. These riblets were constructed using angled surface grooves that generated surface roughness. Placed in a fully-developed turbulent pipe flow, the riblets dramatically

affected the flow field and the characteristics of the boundary layer. The azimuthal mean velocity and turbulence intensity fields, in particular, saw large-scale spanwise variations, caused by the presence of the riblets.

Further investigation into the effects of the newly-designed riblet on the developed turbulent boundary layer, in the absence of a pressure gradient, was recently conducted by Nugroho [83] (Figure 2.8). The results of detailed flow measurements showed that a series of counter-rotating streamwise vortices is produced that forms an up-flow above the converging region and a down-flow above the diverging region of the grooved surface. In the up-flow zone, the local mean velocity is low, while the local turbulence intensity is high. Thus, the boundary layer is thicker in this zone as the fluid momentum is low. The converse is the case over the diverging section, as the downwash (down-flow) results in the presence of higher momentum fluid and lower turbulence intensity in comparison. Hence, the boundary layer is thinner.

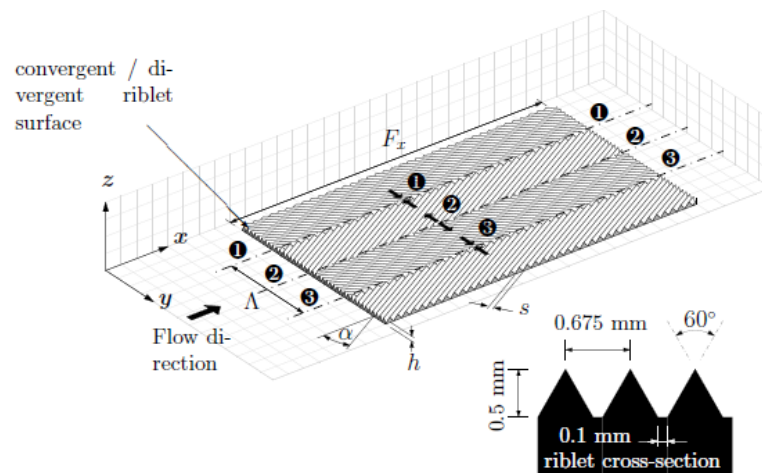


FIG 2.8 Schematic of the converging and diverging riblet as shown in the PhD thesis by Nugroho [83]

The variation in boundary layer thickness in the spanwise direction is remarkable, as the thickness approximately doubles over the diverging section, while the riblet height is merely around 1% of the boundary layer thickness. Large-scale flow features reported in this study bear resemblance to the *superstructures* discovered by Hutchins and Masuric [53, 54]. It is conceivable that these highly-ordered surface structures can be adopted as a flow control method to manipulate boundary layer characteristics, including the drag force.



## 2.4.2 Induced Drag Reduction

Another form of drag on finite-span wings is caused by the formation of wingtip vortices and is known as lift-induced drag or induced drag. One effect of the trailing (tip) vortices is to induce a small downward velocity component in the neighbourhood of the wing that changes the local incidence angle [2]. This phenomenon leads to the generation of additional drag on the aircraft wings. To minimize induced drag, boundary conditions at wing tips can be altered by either adding mechanical components to the tip region or eliminating the tips completely. Also, blowing through active or passive means can dramatically reduce induced drag (up to 40%). This can be achieved by the installation of wing tip engines such as the engine nacelle. An alternative is to use ring wings or joined wings and tails to replace wing tips altogether [55].

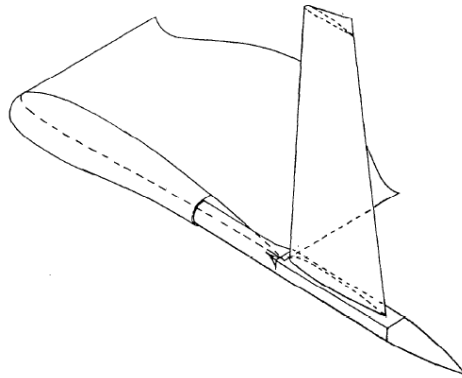


FIG 2.9 Lockheed vortex diffuser vane. Free-stream flow direction is from left to right. [79]

Winglets, tip sails, vortex diffuser vanes (see Figure 2.9) and tip turbines are another class of devices that aim to minimize the effects of tip vortices and recover momentum from the tip flow. As the effective aspect ratio of the wing is increased by these devices, so is the percentage of the wing area affected by the tip vortices. The process of tip vortex formation is also impacted by the presence of these flow control devices. For instance, the vortex diffuser vane, whereby a spar is positioned behind the wing tip, allows the tip vortex to concentrate before it is intercepted. A 5%-15% decrease in induced drag during Conventional take-off and landing can be achieved using these devices. Manufacturing, design and maintenance costs are a major concern with these flow control devices as well [55].

### **2.4.3 Wave Drag Reduction**

One class of wave reduction methods is based on the notion that weakening the generated shock over a wing reduces drag. Altering wing sweep, applying area ruling and reduced thickness as well as the inclusion of wing twist/camber/warp in the design of lifting bodies are classical approaches to reducing wave drag [17]. There are also wave reduction techniques based on non-linear approaches developed using Computational Fluid Dynamics techniques. Nose spikes to increase the effective body length and base blunting that reduces the strength of the recompression shock are examples of such methods [55]. Aero-spike devices cause the bow shock to interact with the spike's boundary layer, resulting in a separated shear layer that engulfs the spike, an effect which transforms the strong bow shock into a weaker one. The disadvantage associated with the spike is the imposition of local thermal loading, brought about by the re-attachment of the disturbed turbulent flow at the dome [100]. The peaks in the thermal field may even damage the dome of the blunt body. In addition, the drag-reducing effect of the spike is diminished at moderate to high attack angles.

Another group of wave drag reduction methods is aimed at using the shock wave via reflection/interaction to make favourable interference for the generation of thrust or lift [17]. Ring wings and parasol wings are examples of favourable interference-based lifting bodies. An efficient lifting surface, as well as the partial cancellation of the body/nacelle wave drag are obtained in the case of the parasol wing [63].

### **2.4.4 More Modern Drag Reduction Methods**

In recent years, microfabrication has developed considerably. Materials that incorporate arrays of Micro-Electro-Mechanical Systems (MEMS) are now manufactured to contain sensors, actuators and electronic circuitry with sizes of a few microns to a few millimetres [115]. Potentially, these components can be utilized to impact the formation and behaviour of coherent flow structures, for instance in wall-bounded turbulent flows. By active enhancement of mixing in the near-wall regions of a turbulent boundary layer, flow separation can be modulated through interactive distributed control [94]. Actuators can act upon the information received by the sensors located in the boundary

layer to destroy the burgeoning coherent turbulent structures whose bursts account for the generation of skin friction drag [121]. The performance of the wing, therefore, could potentially be optimized by reducing cruise drag and even maximizing lift. AEROMEMS 2 [121] is a European project aimed at flow separation control by pre-conditioning of the boundary layer. An important phase of their task is to identify the occurrence of instabilities, whether in the form of counter-rotating vortices or streaks. Although a promising field of research, substantial research and development are still required for the realization of drag reduction technologies by MEMS on a practical scale such as medium-sized aircraft. Systems integration, robustness, maintenance and certification are but a number of 'roadblocks' to overcome before successful application of MEMS in aeronautical engineering is realized [121].

## **2.5 Summary of Flow Control Methods**

Introducing a desired change in a flow field is of significant interest to aerodynamicists. In the previous sections, it was shown how active (requiring energy expenditure) and passive (requiring no auxiliary power) flow techniques impact the boundary layer to bring about advantageous outcomes, including lift augmentation and drag reduction. These approaches have proven effective in manipulating the aerodynamic forces. Achieving improved aerodynamic efficiency is, however, often accompanied by penalties. Therefore, the suitability of the flow control methods, in many cases, depends on the correct identification of the transition or flow separation zone, a region where instabilities are likely to grow in magnitude. By delaying laminar-to-turbulent transition and preventing or suppressing separation, critical flow regions are controlled and as a consequence aerodynamic efficiency is enhanced [37].

While the widely-used conventional high-lift, drag-reducing devices that modify the boundary layer introduce aerodynamic advantages, there exist several challenges to overcome or minimize the drawbacks attributed to their deployment (see Tables 2.1-2). These issues pertain to cost, maintenance and reliability. Further progress in this field may target schemes to combine the existing devices or

methods, such as combining suction with the use of riblets to exploit the benefits of both techniques [38].

Table 2.1 Lift enhancement devices and their disadvantages

<b>Lift Augmentation Method</b>	<b>Challenges</b>
Leading-edge modifications : Slats, slots, droop nose configuration	-Aircraft to be designed for flight at high attack angles -Drag penalty -Visibility issues -Slats tend to increase the lift curve slope
Trailing-edge modifications: Flaps (plain, split, Fowler etc.) Ripples	-Drag penalty -Issues with the gap between the flap and main wing body -May increase the pitching moment -Fowler flaps tend to increase the lift curve slope
Vortex generators	-Drag penalty -Design complexities
Blowing, suction	-Power requirements -Costs associated with weight
ZNMFJs	-Influence of configuration parameters associated with the actuator and the generated oscillations on the flow field still not fully explored
Acoustic excitations	-Sensitivity of the flow field to excitation frequency and location
Surface boundary layer control	-Design complexity -Power requirements

Table 2.2 Drag reduction devices and their disadvantages

<b>Drag Reduction Method</b>	<b>Challenges</b>
Hybrid laminar flow control devices	-Complexity in transition prediction -Increase in Specific Fuel Consumption
Wing tip devices to reduce induced drag	-Manufacturing, design and maintenance costs
Skin friction reduction using riblets in turbulent flows	-Manufacturing and maintenance costs
Angled groove roughness	-Influence of configuration parameters on the flow structure still not fully understood -Quantified data on drag reduction required
Shock control and trailing edge devices	-Imposition of thermal loading in some cases -Increase in weight
MEMS components to modify the boundary layer	-Designs for practical aircraft scale requiring decades of research

As pointed out in section 2.3.13, leading-edge modifications using tubercles have shown promising flow control benefits with negligible penalties, in particular at high attack angles. What follows is a

comprehensive review of the previous studies that have examined the effects of leading-edge modifications by tubercle or tubercle-like features.

## **2.6 Humpback Whale Tubercles: A Nature-inspired Approach to Flow Control**

Nature, with its elegance and mystique, has always served as a generous source of inspiration and creativity [7]. Even in the 21<sup>st</sup> century, fluid mechanists tremendously benefit from their observations in nature and strive to mimic and incorporate the efficient mechanisms employed in the locomotion of various species. In aeronautics, the conceptual design ideas behind several flow control devices such as trailing-edge flaps, riblets and leading-edge slats, were all inspired by nature. Turbomachinery is another area that could exploit the inspirations derived from nature. Nevertheless, one reservation about the industrial application of nature-mimicked designs in turbo machinery, is the spectrum of flow Reynolds numbers (associated with locomotion among different species) that falls below the range in which most turbomachinery components operate [25].

One of the few baleen animals that swims under high Reynolds numbers flow conditions has intrigued engineers and marine biologists for a long time. Although the humpback whale (*Megaptera Novaeangliae*) has mammoth physical attributes (up to 14m in length and over 30 tonnes in mass), its dynamic agility for executing tight turns when catching prey is remarkable [59]. Unlike other baleopterids that swim towards the prey, the humpback whale initially swims away from the schools of fish, then makes a sharp rolling U-turn known as the "inside loop" to attack the prey [34]. When rolling in this banking turn, hydrodynamic lift forces are developed on the pectoral flippers whose horizontal components act as the force towards the centre of the turn (the centripetal force) [124]. The humpback flippers (Figure 2.10) are the largest among cetaceans and resemble high aspect-ratio wings with a cross-sectional profile similar to NACA-643-021 [35].

Fish and Battle [35], for the first time, postulated that the protuberances on the leading-edge of the humpback whale's pectoral flippers, known as tubercles, may account for the animal's extraordinary manoeuvrability. They proposed that tubercles act similar to strakes on planes that produce vortices

which ameliorate stall characteristics at high attack angles. To date, several studies have broadened our understanding of how tubercles influence the loading characteristics including the lift and drag profiles, as well as the flow structure around tubercled lifting bodies. The following sections provide a comprehensive review of the experimental, numerical and analytical investigations on tubercle-modified bodies, revealing research areas that have not been fully explored.

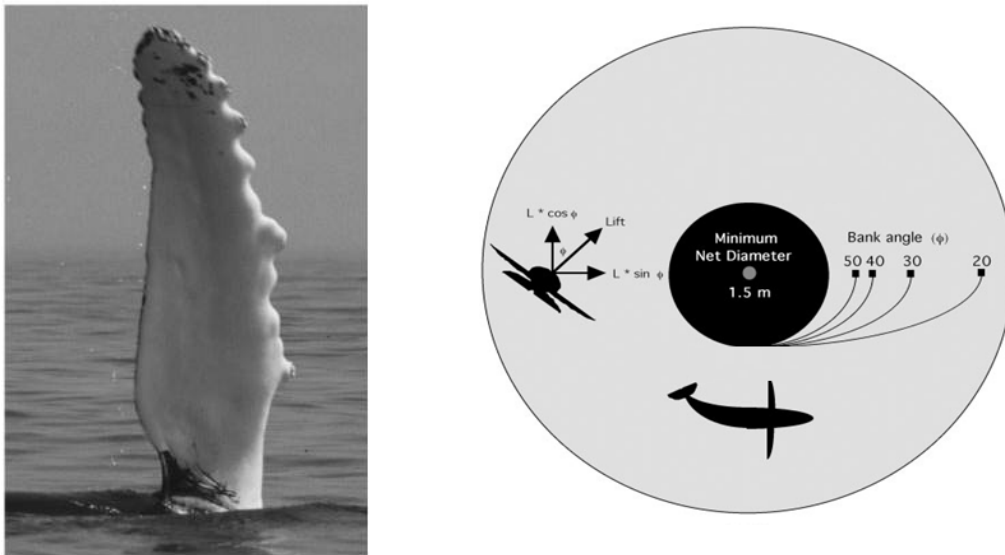


FIG 2.10 (a) Humpback flipper showing tubercles on the leading edge. (b) A humpback whale executing sharp banking turn. A bubble net is produced from the humpback's blowhole that traps the prey [33].

## 2.6.1 Aero-Hydrodynamic Loading Behavior

### 2.6.1.1 Bluff Bodies Modified with Tubercle-like Features

The idea of modifying a bluff body with a sinusoidal configuration was adopted by Owen, Szewczyk, and Bearman [85]. They conducted wind tunnel force measurements on circular cylinders with sinusoidal profiles at a diameter-based Reynolds number of 33,000. The results showed a 47% reduction in the drag force, compared to an unmodified cylinder. In addition, visualisation in laminar flow, at a Reynolds number equal to 100, revealed that the wakes behind the troughs were wider than those behind the peaks. More importantly, it was observed that for the modified cylinders the Kármán vortex shedding was suppressed, which could explain the desired drag reduction phenomenon. The study by Owen *et al.* [85] showed a potential benefit of spanwise undulations with regard to drag reduction associated with bluff bodies. It must be noted that the observed reduction in drag was accounted for by a vortex-suppression mechanism.

### **2.6.1.2 Initial Numerical Studies on Wings with Tubercles**

Watts and Fish [122] pioneered the research into the effect of tubercles on wing performance in a numerical study. In their investigation, an inviscid panel method solver was developed to model high Reynolds-number flows. Accordingly, the model was utilized to compare the performance of a tubercled finite-span wing based on a NACA 63-021 profile, against its unmodified equivalent at a 10-degree angle of attack. The results demonstrated the overall superior performance of the tubercled wing with a 4.8% increase in lift, a 10.9% reduction in induced drag and a 17.6% increase in the lift-to-drag ratio. The observed increase in lift was attributed to higher pressure acting on the lower side of the tubercled wing as opposed to a significant change in pressure contours on the suction side. Although the CFD simulation showed that the scalloped (tubercled) wing yielded higher lift and lower induced drag values, when shear forces were estimated it was reported that tubercles may raise the form drag by 11% at a 10-degree angle of attack. It was predicted that tubercles may alter stall behaviour in a similar manner to vortex generators. It must be noted that the inviscid-based solver, used in this study was incapable of probing into the complex near- and post-stall flow behaviour of the tubercled wing due to its inherent limitations in resolving viscous forces.

A second numerical study, as reported by Fish and Lauder [36], was carried out by Paterson, Wilson, and Stern [87] in which an unsteady Reynolds Averaged Navier Stokes (URANS) scheme was adopted to model the flow over a tubercled and an unmodified NACA 63-021 baseline airfoil. The Reynolds number, based on the chord, was 1,000,000 and the modelling was performed at a 10-degree angle of attack. The results demonstrated a dramatic change in the static pressure contours on the tubercled airfoil, with less severe adverse pressure gradients on the suction side. In addition, regions containing vorticity of larger magnitude, posterior to the troughs, were realized. The presence of strong vorticity was accompanied by a delay in flow separation in the immediate vicinity of the trailing-edge, behind the tubercle peaks. This was the first study to suggest a possible connection between a delay in flow separation and the presence of vorticity concentration in flows over tubercled bodies.

### **2.6.1.3 Performance of Humpback Flipper Models**

Miklosovic, Murray, Howle and Fish [74] carried out wind tunnel force measurement tests on scaled finite-span models of an idealized humpback whale flipper (scale:1/4) with and without tubercles. The NACA 0020 profile was selected as the baseline airfoil for the humpback flipper models. The shape of the leading-edge of the tubercled wing was a decaying sinusoidal curve that approximated the tubercle spacing observed on the humpback flipper. The Reynolds numbers for the tests were between 505,000 and 520,000, which fall in the operating range of the humpback whale's movement in its environment. The experiments showed a 40% delay in the stall angle for the wing with tubercles, accompanied by a 6% increase in the maximum lift coefficient and lower drag coefficient in the post-stall regime. In addition, the lift-to-drag ratio of the modified wing was greater with the exception of angles between 10 and 12 degrees (see Figure 2.11). Further tests (at  $Re=135,000-550,000$ ) were done to investigate the effect of Reynolds numbers on aerodynamic forces and it was found that the lift coefficient at moderate attack angles was relatively insensitive to Reynolds numbers above 400,000, while a consistent trend for the drag coefficient could not be definitively established. The researchers proposed that a vortex-generating mechanism, similar to that employed by vortex generators attached to an aircraft wing, may explain the higher lift characteristics. It was hypothesized that through energizing the scalloped flipper's boundary layer, tubercles inhibit chord-wise separation that accounts for earlier stall on an otherwise unperturbed wing.

To assess the effect of wing sweep on the aerodynamic performance of finite-span wings with tubercles, Murray, Miklosovic, Fish and Howle [80] undertook a series of force measurements at a Reynolds number equal to 550,000. The performance of three swept tubercled models, based on the NACA 0020 cross-section, at sweep degrees of 0, 15 and 30 degrees, were compared with swept unmodified wings. The results indicated that the tubercled wings delayed stall by 40%, 48% and 21% for the sweep angles of 0, 15 and 30 degrees, respectively. Furthermore, the wings with the sinusoidal protrusions yielded higher maximum lift coefficients by 6%, 9% and 4% compared to the values reported for the wings with smooth leading-edges at the aforementioned sweep angles. It was observed that the augmented lift coefficients were accompanied by limited drag penalties for the



tubercled wings. The authors came to the conclusion that incorporating tubercles enhanced the aerodynamic characteristics of a finite span flipper model, however they acknowledged that the flow dynamics underpinning the mechanism were not properly understood. It was commented that it remained a question whether tubercles act in a manner similar to vortex generators [96] or wing fences [50] or a combination of the two. Stanway [110] focused on water tunnel force measurements on humpback flipper prototypes with NACA 0020 cross sections at Reynolds numbers between 44,000 and 120,000. The results showed that in all test cases the tubercled wing delayed stall compared to the unmodified wing. However, with the exception of the highest Reynolds number case, the maximum lift coefficient was reduced for the flipper model. This observation was important, since it pointed out the significant effects of the Reynolds number (flow regime) as well as the type of stall (leading- or trailing-edge) on the performance of wings with tubercles. Furthermore, planar Particle Image Velocimetry (PIV) measurements conducted on a plane placed parallel to the suction surface of the models, confirmed the presence of vortical structures (containing surface-normal vorticity) of opposite sign. The strength of the measured vorticity increased between angles of attack 10 and 18 degrees.

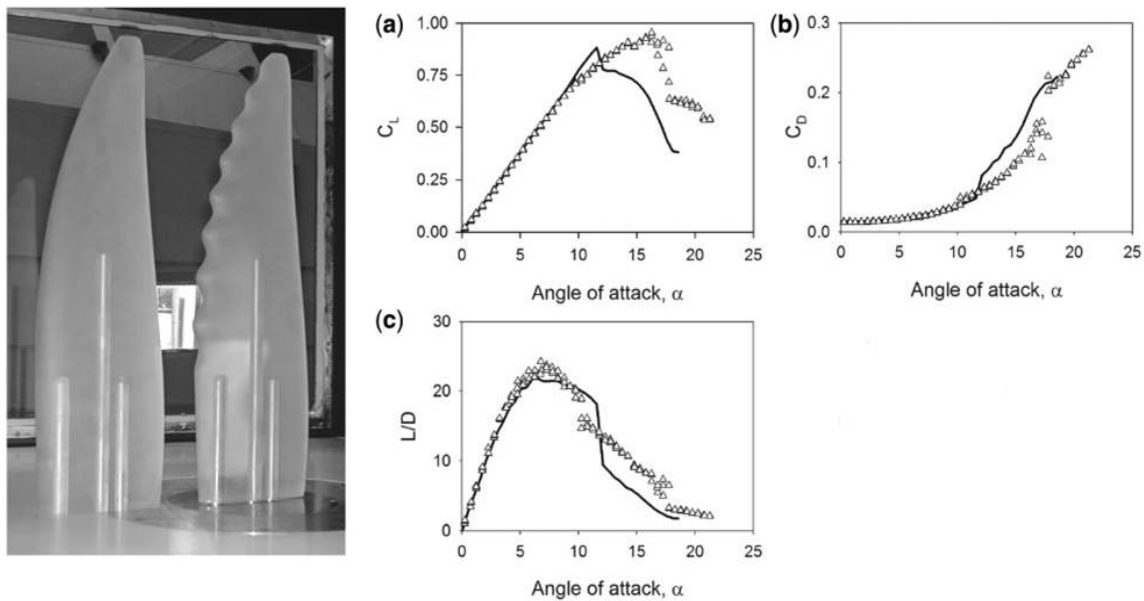


FIG 2.11 Idealized flipper models used by Miklosovic *et al.* [74] (left). Measured (a) Lift, (b) drag and (c) Lift-to-drag ratio versus angle of attack plots for the flipper models obtained by the same researchers. Solid line and triangles pertain to the values for the unmodified and tubercled models, respectively (right).

Bolzon, Kelso, and Arjomandi [11] carried out wind tunnel force measurement tests at  $Re=220,000$  on swept tubercled wings with taper based on the NACA-0021 baseline profile. Results showed that,

compared to an unmodified swept wing, the tubercled wing saw a reduction in lift for all angles of attack considered ( $0^{\circ} - 10^{\circ}$ ). The drag force was also reduced at low attack angles for the modified wing. For the angles of attack between  $1^{\circ} - 8^{\circ}$ , the reduction in lift was within 4-6%, whereas the drag was decreased 7-9.5%. Also, the lift-to-drag ratio, saw an increase of 2-6% in the aforementioned attack angle range. Moreover, it was found that the addition of tubercles weakened the strength of the wingtip vortex, resulting in a reduction of induced-drag.

#### 2.6.1.4 Performance of Full-span Wings with Tubercles

While previous work focussed on flipper wing models, Stein and Murray [112] carried out wind tunnel experiments on full-span airfoils (Figure 2.12). The designs were based on a NACA 0020 profile, and wind tunnel force measurements were undertaken on foils with and without tubercles, as well as an unmodified model with vortex generators at  $Re=250,000$ . The experiments showed that, in contrast to the previous findings, the tubercled foil incurred a 31% decrease in the maximum lift coefficient compared to the unmodified one and its drag coefficient was considerably greater for attack angles beyond 7 degrees. Also, the previously-proposed function of tubercles as vortex generators was questioned based on the evidence that the lift and drag curves for the foils with tubercles and vortex generators did not exhibit similar trends. The authors concluded that the role of tubercles cannot simply be to inhibit the chordwise progression of stall.



FIG 2.12 The full-span foils with tubercles (left), unmodified (middle) and the model with vortex generators (right) used by Stein *et al.* [112]

Johari, Henoch, Custodio, and Levshin [57] performed water tunnel experiments to study the effects of varying the tubercle amplitude and wavelength on the performance of full-span NACA 634-021 foils. The amplitudes ranged from 2.5% to 12% of the mean chord, while spanwise wavelengths were configured at 25% and 50% of the mean chord. These parameters were selected such that they would correspond to those measured for a humpback whale. The observations indicated that the role played by amplitude is more pronounced on the resulting force and moment coefficients, while the wavelength's influence was minimal. With regard to drag, it was found that the protrusions increased the drag coefficient in the pre-stall stage; however they did not impact this coefficient in the post-stall phase. Hence, the loading characteristics study showed that the foils with tubercles in the pre-stall regime exhibit inferior performance compared to the unmodified one. In contrast, the tubercle-modified foils outperformed the foil with the smooth leading-edge in the post-stall regime, by approximately 50%, extending the stall angle by almost 9 degrees.

Hansen, Kelso, and Dally [48] investigated the effects of various tubercle wavelength and amplitude combinations on the performance of full-span wings based on the NACA 65-021 and NACA 0021 profiles. Wind tunnel force measurements conducted at a low Reynolds number of 120,000 demonstrated that all scalloped foils (with the exception of one foil) displayed superior post-stall lift and drag coefficients compared to the equivalent unmodified foils. Nonetheless, in the pre-stall phase, tubercled foils exhibited degraded loading behaviour. With regard to geometric variations, it was found that reducing the tubercle amplitude yielded higher values of lift coefficient and larger stall angles for both full-span airfoils. Past the stall point, however, tubercles with larger amplitudes performed best. Furthermore, in contrast to the previous reports by Johari *et al.* [57] where the wavelength's effect was reported to be minimal, the results revealed the influence of the wavelength and showed that its reduction provided better aerodynamic characteristics in all respects. Despite this finding, it was noted that decreasing the wavelength past a certain point introduced undesirable traits. Moreover, Hansen [46] postulated that the amplitude-to-wavelength ratio was a key parameter, influencing the strength of the generated counter-rotating vortices. Also, the optimum tubercle

amplitude and wavelength bore strong resemblance to the spacing and height of optimum vortex generators.

Through the use of boundary layer trips, Hansen [46, 48] demonstrated that surface roughness appeared to delay separation of the boundary layer on the suction side. When the boundary layer was tripped to turbulence, the effectiveness of tubercles did not deteriorate. Thus, this study suggested that the fundamental flow control mechanism triggered by the presence of tubercles was not significantly influenced by altering the state of the boundary layer.

Pressure measurement tests were also undertaken by Hansen [46] on the unmodified NACA 0021 airfoil as well as a tubercled foil with an amplitude equal to 30mm and a wavelength of 8mm at  $Re=120,000$ . For the first time, it was experimentally shown that, for the tubercled airfoil, the peak pressure value was most negative in the trough section. Moreover, the chordwise pressure gradient behind the trough was observed to be more adverse, compared to that of the peak. Whereas the unmodified foil stalled at an attack angle equal to 13 degrees, the integration of static pressure around the tubercled foil's cross-sections showed higher amounts of lift being generated beyond 13 degrees for the airfoil with tubercles.

In order to examine the effect of tubercle wavelength on lift curve characteristics of a NACA 0018 profile, Arai, Doi, Nakashima, and Mutsuda [3] undertook force measurements in a circular water channel where the Reynolds number was maintained at 138,000. Additionally, a Large Eddy Simulation (LES) study was carried out, by incorporating the experimental flow parameters. It must be noted that Arai *et al.* [3] introduced a difference into the arrangement of protuberances on the foils' leading-edge compared to the previous studies. Unlike the foregoing designs, only half of the sinusoidal curve, which included the peaks, was modelled and the troughs did not appear on the leading-edge. The results demonstrated that the flow behind the tubercles remained attached at post-stall incidence angles, which accounted for higher lift coefficients. Contrary to the findings by Johari *et al.* [57], it was found that, among the wings that had the same amplitude, the ones with shorter wavelength performed better. This finding is in accordance with the observations made by Hansen *et*

*al.* [46, 48]. Also, the CFD results elucidated the role played by longitudinal vortices in inhibiting separation at the leading-edge and energizing the boundary layer. Furthermore, it was found that protuberances near the wingtips did not produce any beneficial effect in delaying stall, while altering the position of tubercles along the span produced different effects depending on the shape of the wing.

### **2.6.1.5 Performance of Flipper Models vs. Full-span Airfoils with Tubercles**

Miklosovic, Murray, and Howle [73] presented a second study in which wind tunnel experiments were carried out on a pair of finite-span wings at Reynolds numbers 534,000-631,000, as well as a pair of full-span airfoils at Reynolds numbers equal to 274,000-277,000. All the models had the NACA 0020 as their baseline section. The results confirmed the findings by Johari *et al.* [57] that suggested tubercles are beneficial for full-span wings (with no taper or sweep) in the post-stall regime. By comparison, the pre-stall advantages only manifest themselves for finite-span flipper models. Based on these observations, it was inferred that tubercles inhibited the spanwise progression of stall, due to their inherent three- dimensional effects. A potential application of airfoils with tubercles was suggested in turbine blades past their stall point where the flat lift curve could offer desirable traits.

### **2.6.1.6 Performance of Finite-span Wings without Taper or Sweep**

Through a series of wind tunnel force measurement tests on finite-span airfoils with tubercled and unmodified NACA 0021, Hansen *et al.* [47] showed that the effect of tubercles on the formation of the tip vortex, in relation to stall characteristics, is not significant at  $Re=120,000$ . This conclusion was reached based on the observation that, similar to full-span airfoils, finite-span modified models, in comparison with the unmodified foil, produced lower and higher lift force in the pre-stall and post-stall phases respectively. Additionally, finite-span airfoils with smaller wavelengths and amplitudes proved most aerodynamically efficient. This study, again, pointed to the possible Reynolds number effects on the aerodynamic performance of tubercle-modified airfoils.

A recent experimental study by Custodio, Henoch, and Johari [27] was conducted using the high-speed water tunnel facility at the US Naval Undersea Warfare Center to assess the performance of finite-span tubercled wings at Reynolds numbers up to 450,000. All the tubercled wings had the NACA 63<sub>4</sub>-021 cross-sectional profile with protuberance amplitudes of 2.5% to 12% of the mean chord length. These researchers found that, with the exception of one modified wing that resembled the flipper model, all the other tubercled wings (with rectangular planforms) produced lift-to-drag ratios which were comparable to or lower than those of the baseline wing. It was also reported that the lift and drag coefficients for the tubercled models showed little dependence on the Reynolds numbers above 360,000, whereas the hydrodynamic forces were greatly influenced by the Reynolds number at 90,000. With regard to the influence of geometric parameters on hydrodynamic characteristics, the amplitude-to-wavelength ratio appeared to be an indicator of the stall type, namely abrupt or soft (gradual loss of lift). Nonetheless, the maximum lift coefficient and stall angle strongly depended on the leading-edge curve amplitude.

## **2.6.2 Flow Structure Investigations**

### **2.6.2.1 Flow Visualization on Full-span Wings**

Custodio [26] performed dye visualization over a tubercled hydrofoil at  $Re=1,500$ . His results revealed the presence of counter-rotating streamwise vortices behind the troughs. The sense of rotation was such that the vortices behind every other trough rotated in the same direction. Moreover, the organization of the counter-rotating vortices displayed a bi-periodic pattern as shown in Figure 2.13.

It was argued that, since tubercles induce a sweep angle at the leading-edge, they trigger a distinct spanwise flow which gives rise to the formation of streamwise vortices. Due to the curved surface of the foils, these counter-rotating vortices migrate to the troughs (chord minima) and form low-pressure regions. It was conjectured that the role of tubercles is similar to that of delta wings which, owing to their low pressure cores, create additional lift force at high angles of attack. The author remarked that in the pre-stall regime, this lift generating mechanism does not prove advantageous for the scalloped

model since the lift loss due to flow separation behind the troughs is severe and cannot be compensated for by the lift produced by means of the vortices.

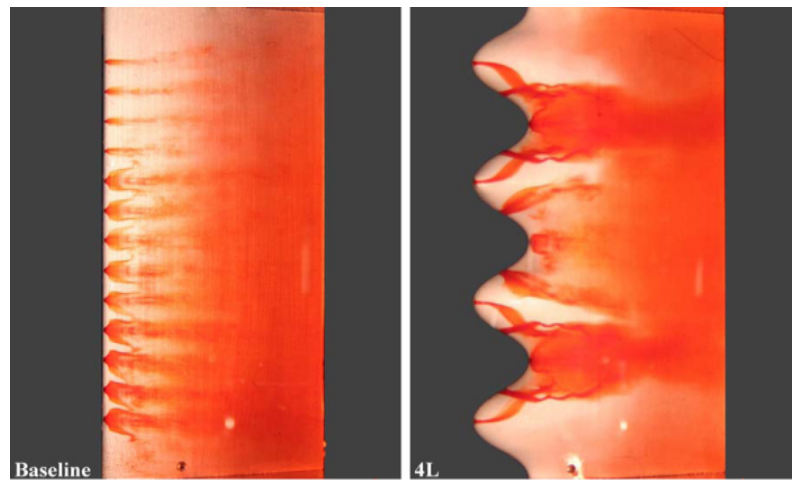


FIG 2.13 Dye flow visualisation for the unmodified and airfoil with tubercles at a 24-degree attack angle by Custodio [26]

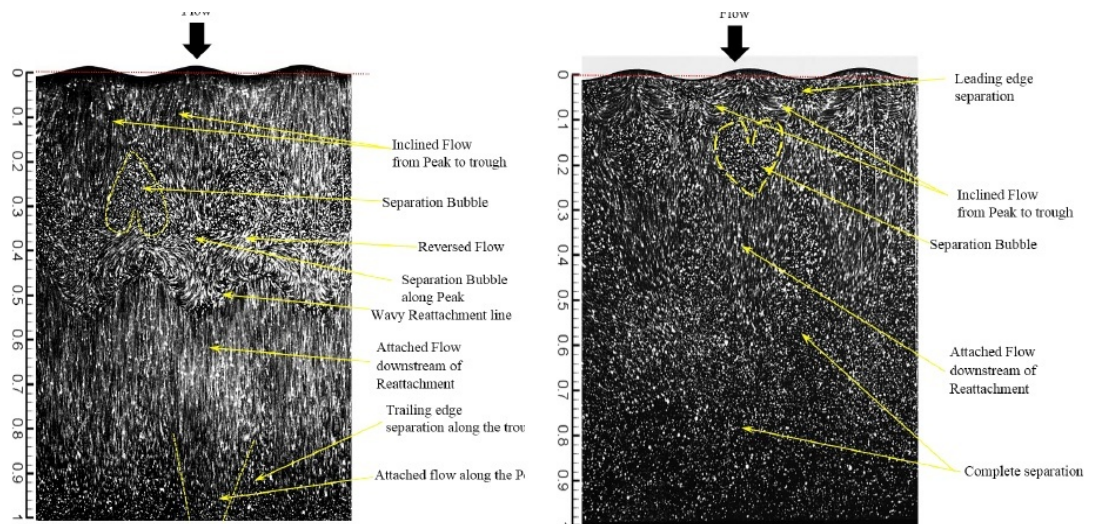


FIG 2.14 Laminar separation bubble as observed on a tubercled airfoil at  $Re=120,000$  pre-stall (left) and post-stall (right) [60]

Karthikeyan, Sudhakar and Suriyanarayana [60] examined the surface flow over a tubercled airfoil, based on the NACA 4415 profile, against its unmodified counterpart at  $Re=120,000$ . Using oil, they identified the presence of laminar separation bubbles (LSB) in both cases. Whereas on the unmodified foil there existed one bubble that extended along the entire span of the foil, on the tubercle-modified foil, a series of isolated LSBs appeared along the span (see Figure 2.14). At a post-stall angle of 18 degrees, flow separation was delayed to regions located approximately 50% downstream of the

modified leading-edge, while flow separation was observed to occur over the entire suction surface of the unmodified airfoil.

Hansen [46], in a series of water tunnel experiments, adopted PIV to visualize the vorticity field around a NACA0021-based airfoil with tubercles at  $Re=2230$ . The planes to realize the velocity and vorticity fields, were oriented normal to the free-stream flow direction and located at five chordwise positions on the suction side of the airfoil. Contours of streamwise vorticity illustrated the presence of pairs of counter-rotating vortices. For a given measurement plane, the circulation associated with streamwise vorticity was shown to increase with the angle of attack. Also the circulation of the streamwise vortices saw an increase in value in the downstream direction.

Zhang, Wang, and Xu [126] investigated the flow field around a tubercled full-span airfoil with the NACA 63<sub>4</sub>-021 cross-sectional profile using Particle Image Velocimetry methods. The study of the boundary layer and the vorticity fields demonstrated that flow attachment is maintained at high attack angles over the tubercle bumps. In addition, the leading-edge protuberances modified the flow patterns of the airfoil boundary layer through the chordwise and spanwise evolution of the interacting streamwise vortices. The Reynolds number associated with the flow for this study was 200,000.

### **2.6.2.2 Numerical Studies on Flipper Models**

In order to evaluate the role of tubercles in flow separation and the vorticity field, a numerical simulation was carried out by Pedro and Kobayashi [89] on the tubercled and unmodified flipper models tested by Miklosovic *et al.* [74]. In their CFD study, a Detached Eddy Simulation scheme was employed to analyse the flow at  $Re=500,000$ . The simulation was conducted at angles of attack between 12 and 18 degrees. The contours of vorticity showed a chaotic outboard region towards the tip for both wings due to flow separation, however in the midsection of the flippers the differences became evident. The modified wing displayed higher values of the magnitude of vorticity compared to the unmodified model, suggesting the presence of streamwise vortices that were aligned with the tubercles. The investigation led to the conclusion that the streamwise vortices may account for the



superior performance of the tubercled flipper wing as they draw higher momentum fluid into the boundary layer, thus inhibiting separation towards the trailing edge.

In order to visualize the flow field using two commercial CFD packages, namely STAR-CCM+ [111] and SolidWorks Flow Simulation [108], Weber, Howle, Murray, and Miklosovic [123] conducted a RANS-based numerical study on the same flipper wings as those used by Miklosovic *et al.* [74] in the original wind tunnel experiments. Other flow parameters were accordingly matched. The flow visualisation analysis demonstrated that the smooth leading-edge flipper stalled mainly towards the trailing-edge, while the tubercled flipper stalled in the troughs. On the other hand, at high attack angles, behind the tubercle troughs the flipper model with tubercles displayed more attached flow along the span, which accounted for the higher lift coefficient. The authors remarked that a more accurate model such as Detached Eddy Simulation (used by Pedro and Kobayashi [89]) may be needed to capture more of the flow structure details.

### **2.6.2.3 Numerical Studies on Full-span Airfoils**

Malipeddi, Mahmoudnejad, and Huffmann [68] conducted numerical modelling on full-span airfoils with the NACA 2412 as the cross-section profile to investigate the effect of leading-edge protuberances at  $Re=570,000$ . Five wings were modelled including an unmodified wing and four with different tubercle wavelengths (25% to 50% of the chord) and amplitudes (2.5% to 5% of the chord). The simulation results, using the DES turbulent model, were in agreement with previous finding with regard to loading characteristics. The modified wings produced more lift post-stall, while their performance was degraded in the pre-stall zone, compared to the airfoil with the smooth leading-edge. The results also showed that flow momentum transfer to the boundary layer, due to the presence of streamwise vortices, could explain higher post-stall lift.

Lin *et al.* [66] carried out a Large Eddy Simulation study on two types of full-span modified airfoils, as well as the NACA 0021, at  $Re=160,000$ . According to this study, the baseline foil stalled at 12 degrees while the foil, whose tubercles appeared both on the leading and trailing edges, achieved lower lift coefficients at angles below 12 degrees. Consistent with the previous studies, it was reported

that, in the post-stall zone, the maximum lift coefficient increased by up to 20% for the modified airfoil in comparison with that of the baseline foil.

Lohry, Clifton, and Matinelli [67] adopted a Reynolds Averaged Navier-Stokes numerical scheme to model the flow over full-span tubercled airfoils in the Reynolds number range 62,500 to 500,000. They found that the Shear Stress Transport (SST) model proposed by Menter [71] was capable of reproducing more closely the experimental data obtained by Miklosovic *et al.* [73] than the Spalart-Almaras turbulence model. The patterns of skin friction lines in the separated flow regions suggested that tubercles act similar to vortex generators for full-span airfoils. The other observation was a sharp increase in the values of turbulent kinetic energy (TKE) for the tubercled foil along the separation line (see Figure 2.15).

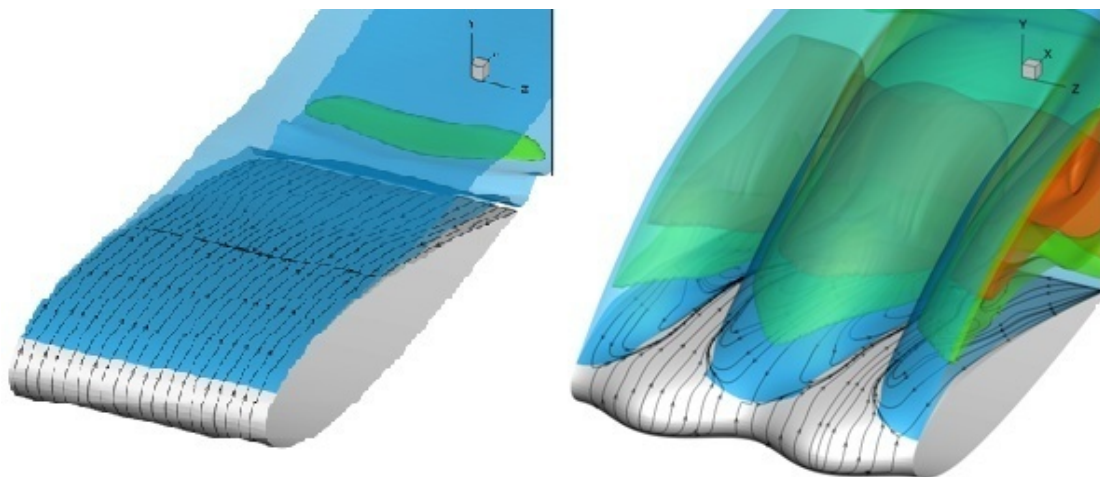


FIG 2.15 Iso-surfaces of turbulent kinetic energy for an unmodified foil at  $AOA=14^\circ$  (left) and a tubercled foil (right) [67]

Dropkin, Custodio, Henoch and Johari [28] simulated the flow over a tubercled and an unmodified airfoil, based on the NACA 63<sub>4</sub>-021 profile, at a wide range of Reynolds numbers. The sinusoidal amplitude and wavelength of the leading edge for the modified foil were maintained at 12% and 50% of the mean chord. Similar to previous studies, this work reported the presence of low-pressure pockets within the troughs of the modified foil. It was shown that, at a Reynolds number equal to 180,000, the tubercled foil produced lower lift and higher drag before stall, however, in the post-stall zone, the lift coefficient of the modified foil was higher for a large range of attack angles, while the

drag coefficients of the two foils were comparable. This study also pointed out the significance of Reynolds number effects in the loading characteristics of tubercled foils. Notably, the lift coefficient of the modified foil was reported to be lower than that of the unmodified at  $Re= 3,000,000$  for a large range of attack angles. Numerical simulations suggested that increasing the Reynolds number had a more dramatic effect on the lift-generating characteristics of the unmodified foil, compared to those of the airfoil with leading-edge tubercles.

A numerical investigation implemented by Large Eddy Simulation was undertaken by Skillen, Revell, Pinelli, Piomelli and Favier [104, 105]. They studied the flow structure around three full-span airfoils with the NACA 0021 baseline profile set at a 20-degree (post-stall) incidence angle at a Reynolds number of 120,000. They proposed the existence of a secondary flow mechanism whereby near-surface low-momentum fluid from behind the tubercle peak (chord maximum) is carried to the region behind the trough (chord minimum). Subsequently, the low-momentum fluid behind the tubercle peak is replaced by high-momentum fluid from outside the boundary layer that eventually leads to a delay in flow separation downstream of the peak, reduction in the size of the separated flow region and augmented lift. This mechanism was contrasted with the one suggested by Favier, Pinelli, and Piomelli [31] who attributed the formation of vortices to the development of Kelvin-Helmholtz instabilities at a significantly lower Reynolds number equal to 800 in their Direct Numerical Simulation study at a 20-degree angle of attack. It was also shown that tubercle wavelength and amplitude of the leading-edge curve of a lifting body can influence the wake topology, the size of the recirculation zone and the strength of the wake vortex shedding. For amplitude-to-chord ratios ( $A/C$ ) of less than 0.07 the intensity of the vortices was too weak to stabilise the separation region. In contrast, for amplitude-to-chord ratios greater than or equal to 0.07, the frequency spectrum was observed to plateau, resulting in the weakening of the wake vortex shedding phenomenon. The separation characteristics, on the other hand, were influenced by the tubercle wavelength. Whereas the flow was fully separated for  $A/C = 0.07$ , and a wavelength-to-chord of 0.5, the flow was attached behind the tubercle peaks for  $A/C= 0.07$ , and a wavelength-to-chord ratio of unity.

### **2.6.2.4 Numerical Studies on Finite-span Wings**

Yoon, Hung, Jung, and Kim [125] performed a parametric analysis on five finite tubercled wings (based on the NACA 0020 profile) at a Reynolds number equal to 1,000,000, using CFD. For comparison purposes, a new parameter,  $R_w$ , was defined which denoted the ratio of the span length covered by the tubercles to the span of the wing. For  $R_w < 1$ , tubercles were placed towards the wingtip. The results of the simulation showed that the unmodified and tubercled wings with an  $R_w$  equal to 0.2 stalled at a 20 degree attack angle while the stall angle for wings with larger ratios ( $R_w = 0.4, R_w = 0.6, R_w = 0.8$  and  $R_w = 1.0$ ) occurred at lower angles (12 and 16 degrees). In the post-stall region, the finite wings with  $R_w$  ratios equal to 0.4, 0.6, 0.8 and 1.0 experienced higher values of lift and surpassed the amount of lift produced by the unmodified wing. The contour plots of the limiting near-surface streamlines suggested the presence of stream-wise vortices which was consistent with previous findings [26].

### **2.6.3 A Theoretical Study on Flipper Models**

Disputing the previously-proposed notion that tubercles act similar to vortex generators, van Nierop, Alben, and Brenner [118] argued that the amplitude and wavelength of protuberances were considerably larger than the boundary layer thickness, therefore the analogy of tubercles to vortex generators was not plausible. They presented an analytical aerodynamic model which predicted low-pressure zones in the tubercle troughs and the onset of separation behind them. This observation was later confirmed by Hansen [46] through a series of wind tunnel pressure measurement tests on full-span tubercled foils. It was argued that since the airfoil sections for both peaks and troughs have nearly the same thicknesses but different chord lengths, separation must occur behind troughs since their corresponding chords are of shorter lengths and thus impose a higher adverse pressure gradient. Also, the analysis demonstrated that the downwash behind a tubercle peak is larger than behind a tubercle trough, therefore the local (effective) incidence angle is larger behind a trough, which may be a reason why the trough stalls prior to the peak at high attack angles. van Nierop *et al.* [118] acknowledged that their model did not capture a number of the aerodynamic characteristics originally

observed by Miklosovic *et al.* [74] including the higher maximum lift coefficient and the sudden drop in lift.

#### 2.6.4 Experimental Work on an Alternative to the Tubercle Configuration

Wind tunnel force measurement tests were undertaken by Hansen [46] on full-span airfoils with a novel form of leading-edge modification (see Figure 2.16) proposed by Kelso (via private communication). This modification was based on the recognition that tubercles cause a cyclic variation in the bound vortex circulation. It was hypothesized that a spanwise variation in the geometric attack angle would induce similar effects to those of tubercles. Also noteworthy is that Zverkov, Zanin and Kozlov [127] had previously postulated that the boundary layer generated by the flow over a wing with a rippled leading edge would sustain a more adverse pressure gradient compared to that of an unmodified wing and exhibit better loading characteristics.

The tests by Hansen [46] were conducted at  $Re=120,000$  on wavy wings with the NACA 0021 baseline profile. The waviness of the leading-edge that effectively altered the geometric angle of attack, impacted the aerodynamic performance of the airfoils in an analogous manner to tubercles. Compared to the unmodified wing, the *wavy wings* exhibited lower lift in the pre-stall and higher lift in the post-stall phase, with lower magnitudes of the drag force. Furthermore, it was found that amongst the wings of the same angular amplitude, the one with the smallest wavelength had the most superior aerodynamic performance. On the other hand, increasing the angular amplitude improved the aerodynamic performance among the wings with the same wavelength.

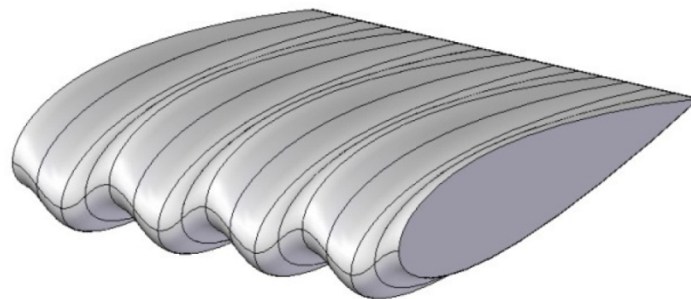


FIG 2.16 Section of a wavy model in the perspective view as shown in Hansen's doctoral thesis [46]. Note that in this configuration the geometric attack angle varies sinusoidally along the span.

### **6.6.5 Experimental Studies on Delta Wings with Tubercles**

To study the near-surface flow topology and structure of a delta wing with leading-edge sinusoidal protuberances, Goruney and Rockwell [41] utilized a stereoscopic technique of high image density particle velocimetry at a Reynolds number equal to 15,000. Maintaining the angle of attack at 15 degrees and the wing sweep angle at 50 degrees, the researchers tested wings with varying tubercle wavelengths and amplitudes in a water tunnel facility. The findings demonstrated that for the wing with the straight leading-edge, a large separation zone occurred, while with the wings with tubercles, the near-surface topology was completely altered when certain combinations of wavelengths and amplitudes were applied. It was found that for small ratios of wavelength to amplitude, with the increase in amplitude, a separation focus point translated towards the leading-edge. However this focus point was removed and substituted by a focus of attachment once the amplitude to chord ratio was reduced to a value of 0.02. The surface-normal vorticity contours indicated a varied distribution of vorticity with high gradients towards the leading-edge, followed by single and dual concentration of vorticity at larger ratios of amplitude to chord. Surface-normal velocity patterns on the other hand, showed reattachment zones near the symmetry plane of the wing.

Another experimental study focusing on delta wings with sinusoidal leading-edges (see Figure 2.17) was carried out by Chen, Pan, and Wang [22] using wind and water tunnel facilities. They compared the aerodynamic characteristics of several flat-plate-shaped delta wings with leading-edge tubercles of varying wavelengths and amplitudes against a baseline delta wing at a Reynolds number equal to 270,000. Enhanced aerodynamic behaviour in the form of delayed stall was achieved without a reduction in the maximum lift coefficient for wings whose amplitudes were smaller or equal to five percent of the root mean chord. In addition, analysing surface oil-flow on the tubercled delta wing at high attack angles suggested the contribution of the vortex breakdown, originating from the peaks, to the turbulent kinetic energy of the flow, thus increasing the size of the attached flow region.

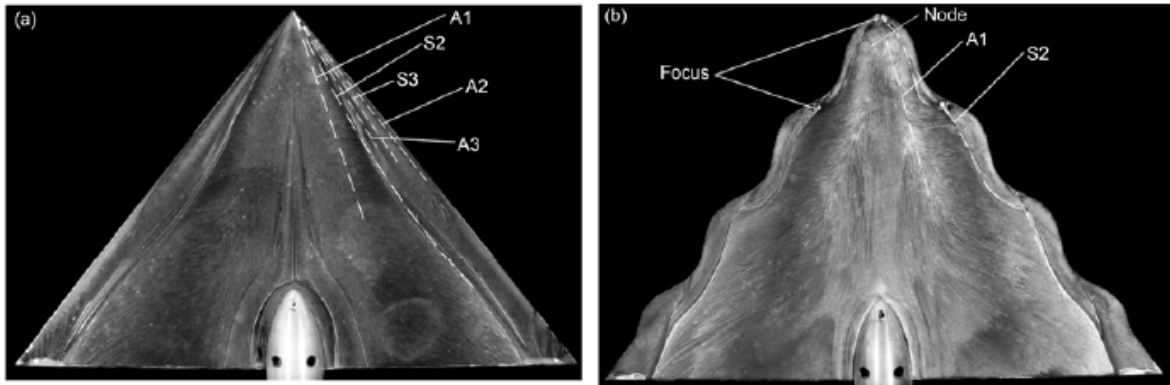


FIG 2.17 Tubercles used on an unmodified and a modified delta wing by Chen *et al.* [22]

## 2.7 Summary of the Literature and the Knowledge Gaps

Tubercles that resemble sinusoidally-shaped protuberances, as observed on the leading-edges of the humpback whale's pectoral flippers, render hydro-aerodynamic advantages. Augmented lift achieved by tubercled wings at high attack angles is one of such desired traits. This is especially important since, an abrupt loss of lift on various components used in turbomachinery and aeronautics, can be ameliorated by means of tubercled leading-edge designs. Hence, the incorporation of these protuberances can be utilized as cost-effective passive flow control devices.

As introduced in the foregoing section, previous works had demonstrated that such benefits are primarily realized near the stall or at post-stall angles, depending on the planform geometric configuration and the flow regime in which the tubercled lifting body operates. The presented literature review reveals that there is general consensus regarding the loading behaviour and the flow structure around a tubercled-modified lifting body in the following reported observations:

1. Humpback flipper models with tubercles on their leading edges exhibit delayed stall and higher maximum lift coefficients at Reynolds numbers in the proximity of 500,000 [74];
2. Tubercles incorporated into full-span wings, which are untapered and nominally two dimensional, display inferior lift coefficients in the pre-stall region at Reynolds numbers in the proximity of 120,000-300,000, but generally superior performance in the post-stall zone, in comparison with lift coefficients achieved by unmodified full-span airfoils [48, 57];
3. Stream-wise vorticity is present in the flow field behind tubercles [46, 89, 105];

4. Flow separation initially occurs behind the tubercle troughs [46, 118, 123];
5. The tubercle amplitude-to-wavelength ratio may determine the strength of the generated streamwise vortices. Also, the optimum values of these parameters, correspond to the optimum values of vortex generators spacing and height [48].

In spite of the key findings highlighted above, the question remains regarding what fundamental flow mechanisms are triggered by the presence of tubercles, prior to and post stall. Analogies of tubercles to vortex generators [112], wing fences [80], delta wings [26] as flow control devices have been proposed in competing theories. Meanwhile, there is compelling evidence to suggest that streamwise vorticity plays a crucial role in the performance of tubercled wings. The understanding of the fundamentals of the formation mechanism of streamwise vorticity and its impact on wing performance is of keen importance and has not been extensively explored.

The wind tunnel force measurement tests on the full-span *wavy wings* by Hansen [46] proved that these wings produced similar aerodynamic loading behaviour to airfoils with tubercles. In light of this finding, the question remains whether these two modified wings operate under the same flow mechanism. Also, the effect of geometric parameters of the wavy configuration, including the wavelength and the angular amplitude, on the aerodynamic performance of the wavy wings can be further explored.

As pointed out previously, wind and water tunnel force measurement tests on full-span tubercled wings were done primarily near the lower limit of the transitional flow regime spectrum ( $Re \leq 300,000$ ) [48, 57, 73, 126]. The recent experimental work by Custodio *et al.* [27] extended the Reynolds number range to investigate its effects on the performance of finite-wings. It was found that the hydrodynamic forces generated by the tubercled foils did not vary significantly for the cases where  $Re \geq 360,000$ , while at  $Re=90,000$  the behavior of the hydrodynamic forces was noticeably different. Even though this study assessed the performance of finite-span wings, it is reasonable to assume that flow-regime dependence is also relevant in cases where the loading characteristics of full span tubercled wings are in question. Hence, a significant research gap exists regarding the behavior



of full-span wings with tubercles operating at higher Reynolds numbers, in particular where  $Re \geq 10^6$ . To the best of the author's knowledge, the numerical work by Dropkin *et al.* [28] (conducted at  $Re = 3 \times 10^6$ ) and the experimental work by Hansen [46], wherein surface roughness was used to trip the boundary layer to turbulence, have been the only two studies that attempted to examine the effects of turbulence on the loading behavior of tubercled wings. Therefore, it is worthwhile to determine Reynolds number effects on the flow structure and loading characteristics of foils with tubercled leading edges operating within the upper limit of the transitional flow regime, where the influence of turbulence is more prominent.

Finally, the flow structure and loading behaviour of a tubercled foil at very low Reynolds numbers, where the boundary layer is entirely laminar, has not been examined extensively. One notable study is the numerical work by Favier, Pinelli, and Piomelli [31] who attributed the formation of vortices to the development of Kelvin-Helmholtz instabilities at a Reynolds number equal to 800. Hansen's [46] investigation into the evolution of streamwise vorticity over a full-span tubercled foil operating at  $Re=2,230$  is another attempt at understanding Reynolds number effects in the laminar regime. Despite the invaluable findings of these researchers, the underlying flow mechanism associated with the flow over tubercled foils in the laminar regime has still not been determined. An investigation into the surface flow topology and loading characteristics can enrich our understanding of the flow mechanism at low-Reynolds number flows.

## **2.8 Aims and Objectives of the Project**

The present project aims to deepen our understand of the underlying flow mechanism triggered by the presence of an undulating leading-edge on full-span wings, across a broad spectrum of Reynolds numbers pertaining to the fully-laminar, transitional and near-turbulent flow regimes. Throughout this work, the term "undulating leading-edges" refers to foils modified with either tubercles (incorporating cyclic spanwise variations in chord length) or wavy configurations (incorporating cyclic spanwise variations in the geometric attack angle).

The associated objectives for the primary aim is to examine the flow structure around a series of modified wings with undulating leading edges. The surface pressure and flow topology, on one hand, and the velocity and vorticity fields on the other, are of interest and leave clues to the underlying flow mechanism. Another objective is to analyse the development of the spanwise circulation distribution which is closely linked to the generation of lift. This is a viable approach, as the analysis would lead to further insight into the effect of an undulating leading edge on the flow structure and consequently the flow mechanism involved.

The second aim of the project is to determine the formation mechanism of vortices and the impact of the vorticity field on the lift-generating capabilities of tubercle-modified wings. As pointed out in the literature, it has been proposed that streamwise vortices exchange momentum with the flow in the boundary layer and possibly render aerodynamic benefits. The associated objective is to understand the flow structure in the vicinity of the modified foil and determine the formation, strength and evolution of such vortical features.

Finally, the project aims to establish the influence of the wavy airfoil's geometric parameters (amplitude and wavelength) on the aerodynamic loading performance of modified wings. The associated objective is to directly measure the aerodynamic forces (lift and drag) on a number of wavy wings in the transitional flow regime. The loading behaviour of full-span wings with the same amplitude and the same wavelength, respectively, will be compared and contrasted against the unmodified baseline airfoil.

To summarize the aims:

1. To understand the underlying flow mechanism triggered by the presence of an undulating leading edge on full-span wings in a broad spectrum of flow regimes;
2. To determine the formation mechanism and impact of streamwise vortices in the flow associated with full-span wings with undulating leading-edges;

3. To determine the role of wing geometric parameters including the angular amplitude and wavelength, first defined by Hansen [46], on the aerodynamic performance of full-span wavy wings;

The objectives are summarised as follows:

1. To examine the flow structure around wings with an undulating leading-edge in the fully-laminar, transitional and near-turbulent flow regimes. Analyses of the surface flow topology, pressure and vorticity fields will aid to accomplish this objective;
2. To compare and contrast the loading characteristics of an unmodified airfoil against full-span wings with tubercles in the fully-laminar and turbulent flow regimes;
3. To compare and contrast the loading characteristics of several wavy full-span wings with varying amplitudes and wavelength in the transitional flow regime;
4. To determine surface pressure distributions at various spanwise locations on a full-span wavy wing in the transitional flow regime;
5. To utilize an aerodynamic model to obtain the spanwise distribution of circulation at various attack angles for both wavy and tubercled wings

It must be noted that while the design criteria for tubercled foils vary in the literature (for instance, a design criterion based on a constant maximum foil thickness-to-chord ratio), in the present work, emphasis was placed on the choice of the cross-sectional profile. Accordingly, for all the modified foils, NACA 0021 was selected as the baseline profile as it closely matches the cross-sectional profile of the humpback whale flipper [74]. It was expected that the global effects of tubercles on the flow field are nearly uniform as far as small variations in design criteria are concerned. Nonetheless, a research gap exists in assessing the effects of such design variations which is beyond the scope of the present project.

## References

- [1] R. Akhavan, W. J. Jung, and N. Mangiavacchi, "Turbulence Control of Wall Bounded Flows by Spanwise Oscillations," *Appl. Scientific Res.*, vol. 51, pp. 299-303, 1992.
- [2] J. Anderson, *Fundamentals of Aerodynamics*, Fourth ed.: McGraw-Hill International Higher Education, 2005.
- [3] H. Arai, Y. Doi, T. Nakashima, and H. Mutsuda, "A Study on Stall Delay by Various Wavy Leading Edges," *Journal of Aero Aqua Bio-mechanisms*, vol. 1, pp. 18-23, 2010.
- [4] J. Aroesty and S. A. Berger, "Controlling the Separation of Laminar Boundary Layers in Water: Heating and Suction," Santa Monica, California. USA 1975.
- [5] C. H. Barnes, "Handley Page Aircraft since 1907," ed: Putman, 1988, p. 210.
- [6] D. Bechert, Bruce, W. Hage, and R. Meyer, "Biological surfaces and their technological application – laboratory and flight experiments and separation control," *AIAA Paper*, 1997.
- [7] J. Benyus, *Biomimicry: Innovation Inspired by Nature*. New York, NY: William Morrow and Company Inc., 1997.
- [8] A. K. Biswas, *History of Hydrology*. Amsterdam, Netherlands, 1970.
- [9] R. D. Blevins, "The Effect of Sound on Vortex Shedding from Cylinders," *Journal of Fluid Mechanics*, vol. 161, pp. 217-237, 1985.
- [10] Boeing Commercial Airplane Company Preliminary Design Department, "Natural Laminar Flow Analysis and Trade Studies " NASA Contractor Report 459029, Seattle, USA 1979.
- [11] M. D. Bolzon, R. M. Kelso, and M. Arjomandi, "19th Australasian Fluid Mechanics Conference Melbourne, Australia 8-11 December 2014 The Effects of Tubercles on Swept Wing Performance at Low Angles of Attack," presented at the AFMC, Melbourne, Australia, 2014.
- [12] M. B. Bragg and G. M. Gregorek, "Experimental Study of Aifoil Performance with Vortex Generators," *Journal of Aircraft*, vol. 24, pp. 305-309, 1987.
- [13] A. Braslow, *A History of Suction-Type Laminar-Flow Control with Emphasis on Flight Research*. Washington, DC 20546, : NASA History Division Office of Policy and Plans (NASA Headquarters), 1999.
- [14] G. V. Bristow, *Ace the technical pilot manual* New York: McGraw-Hill, 2002.
- [15] A. P. Brown, "An experimental investigation of the aerodynamic effects of forward facing wedges on the upper surface and leading edge of an aerofoil, with emphasis at high angles of attack," Aeronautical Research Laboratories, Australia 1983.
- [16] H. Bruyes, "Fluid Mixing Device ", 1951.
- [17] D. M. Bushnell, "Turbulent Drag Reduction for External Flows," *Aircraft Drag Prediction and Reduction: AGARD report 723*, 1985.
- [18] D. M. Bushnell, "Aircraft drag reduction-a review," *Proceedings of the Institution of Mechanical Engineers, Part G: Journal of Aerospace Engineering*, 2003 2003.
- [19] K. W. Butzer, *Early Hydraulic Civilization in Egypt*. Chicago: University of Chicago Press, 1976.
- [20] B. J. Cantwell, "Organized motion in Turbulent Flow," *Ann. Rev. Fluid Mechanics*, vol. 13, pp. 457-515, 1981.
- [21] J. E. Cater, Soria, J., "The evolution of round zero-net-mass-flux jets " *Journal of Fluid Mechanics*, vol. 472, 2002.
- [22] H. Chen, C. Pan, and J. J. Wang, "Effects of sinusoidal leading edge on delta wings performance and mechanism," *Science China Technological Sciences* vol. 56, pp. 772-779, 2013.
- [23] K. S. Choi and B. R. Clayton, "The Mechanism of Drag Reduction with Wall Oscillation," in *Proc. Int. Symp. on Sea Water Drag Reduction* ed. Naval Undersea Warfare Center, New Port, Rhode Island 1998, pp. 229-235.

- [24] T. C. Corke, C. He, and M. P. Patel, "Plasma Flaps and Slats: An Application of Weakly Ionized Plasma Actuators," *AIAA 2nd Flow Control Meeting 2004-2127*.
- [25] A. Corsini, G. Delibera, and A. Sheard, "On the Role of Leading-Edge Bumps in the Control of Stall Onset in Axial Fan Blades " *Journal of Fluids Engineering*, vol. 135, 2013.
- [26] D. Custodio, "The Effect of Humpback Whale-Like Leading Edge Protuberances on Hydrofoil Performance," Master of Science Thesis submitted to Worcester Polytechnic Institute, December 2007.
- [27] D. Custodio, C. W. Henocho, and H. Johari, "Aerodynamic Characteristics of Finite Span Wings with Leading-Edge Protuberances," *AIAA Journal*, vol. 53, 2015.
- [28] A. Dropkin, D. Custodio, C. W. Henocho, and H. Johari, "Computation of Flowfield Around an Airfoil with Leading Edge Protuberances " *Journal of Aircraft*, vol. 49, September-October 2012
- [29] C. L. Enloe, T. E. McLaughlin, and K. D. VanDyken, "Mechanisms and Responses of a Single Dielectric Barrier Discharge Plasma Actuator: Plasma Morphology.," *AIAA Journal*, vol. 42, pp. 589-594, 2004.
- [30] H. Esmaeili Monir, M. Tadjfar, and A. Bakhtian, "Tangential synthetic jets for separation control," *Journal of Fluids and Structures*, vol. 45, pp. 50-65, 2014.
- [31] J. Favier, A. Pinelli, and U. Piomelli, "Control of the separated flow around an airfoil using a wavy leading edge inspired by humpback whale flippers," *Comptes Rendus Mecanique*, vol. 3401(1):107-114, 2011.
- [32] A. Favre, "Contribution a L'etude Experimentale des Mouvement Hydrodynamiques a Deux Dimensions," Thesis, The University of Paris, 1938.
- [33] E. F. Fish, L. Howle, and M. Murray, "Hydrodynamic flow control in marine mammals," *Integrative and Comparative Biology*, vol. 48, pp. 788-800, 2008.
- [34] E. F. Fish, P. Weber, M. Murray, and L. Howle, "The Tubercles on Humpback Whales' Flippers: Application of Bio-Inspired Technology," *Integrative and Comparative Biology*, vol. 51, pp. 203-213, 2011.
- [35] F. E. Fish and J. M. Battle, "Hydrodynamic Design of the Humpback Whale Flipper," *Journal of Morphology*, vol. 225, pp. 51-60, 1995.
- [36] F. E. Fish and G. V. Lauder, "Passive and active flow control by swimming fishes and mammals," *Annu. Rev. Fluid Mech*, vol. 38, pp. 193-224, 2006.
- [37] M. Gad-el-Hak, *Flow Control: Passive, Active, and Reactive Flow Management*: Cambridge University Press, 2007.
- [38] M. Gad-el-Hak, "Modern Developments in Flow Control," *Applied Mechanics Reviews*, vol. 49, 7, pp. 365-379, 1996.
- [39] G. E. Gadd, "Boundary Layer Separation in the Presence of Heat Transfer," *AGARD report. No 280, NATO, Rhode-Saint-Genese. Belgium*, 1960.
- [40] A. Glezer and M. Amitay, "Synthetic Jets," *Annual Review of Fluid Mechanics* vol. 34, pp. 503-529, 2002.
- [41] T. Goruney and D. Rockwell, "Flow Past a Delta Wing with a Sinusoidal Leading Edge: Near-Surface Topology and Flow Structure," *Exp. Fluids*, vol. 47, pp. pp. 321-331., 2009.
- [42] A. Guillermo and J. D'Adamo, "Flow Control with Electrohydrodynamic Actuators," *AIAA Journal*, vol. 40, 2002.
- [43] W. Hage, R. Meyer, and Schatz, "Comparison of experimental and numerical work on three dimensional trailing edge modifications on airfoils " *Integrating CFD and Experiments in Aerodynamics* 2005.
- [44] C. Hale, M. Amir, K. Kontis, and N. Shah, "Active and Passive Flow Control Studies at Subsonic Speeds at The University of Manchester " presented at the AIAA Aerospace Sciences Meeting and Exhibit, Reno, Nevada 2008.
- [45] K. Hall, E. Jumper, T. C. Corke, and T. E. McLaughlin, "Potential Flow Model of a Plasma Actuator as a Lift Enhancement Device," *AIAA* 2005-786.

- [46] K. L. Hansen, "Effect of Leading Edge Tubercles on Airfoil Performance," Doctor of Philosophy Thesis, Mechanical Engineering, University of Adelaide, Adelaide, SA, Australia, 2012.
- [47] K. L. Hansen, R. M. Kelso, and B. Dally, "An Investigation of Three Dimensional Effects on the Performance of Tubercles at Low Reynolds Numbers," presented at the 17th Australian Fluid Mechanics Conference, Auckland, New Zealand, 2010.
- [48] K. L. Hansen, R. M. Kelso, and B. B. Dally, "Performance variations of leading-edge tubercles for distinct airfoil profiles," *AIAA Journal of Aircraft*, vol. 49:185-94, 2011.
- [49] H. Heap and W. Crowther, "A review of current leading edge device technology and of options for innovation based on flow control," presented at the RAeS, London, 2003.
- [50] S. F. Hoerner, *Fluid dynamic drag: Practical Information on Aerodynamic and Hydrodynamic Lift*, Second ed.: Hoerner Fluid Dynamics, 1985.
- [51] E. Houghton and P. Carpenter, "Aerodynamics for Engineering Students," ed MA: Butterworth-Heinemann, 2003, pp. 485-503.
- [52] F. B. Hsiao, C. F. Lui, and J. Y. Shyr, "Control of Wall Separated Flow by Internal Acoustic Excitation," vol. 28, pp. 1440-1446, 1990.
- [53] N. Hutchins, Marusic, I., "Evidence of very long meandering streamwise structures in the logarithmic region of turbulent boundary layers," *Journal of Fluid Mechanics*, vol. 579, pp. 1-28, 2007a.
- [54] N. Hutchins, Marusic, I., "Large-scale influences in near-wall turbulence," *Phil. Trans. R. Soc. London*, vol. 365, pp. 647-664, 2007b.
- [55] M. Jahanmiri, "Aircraft Drag Reduction: An Overview," Chalmers University of Technology Goteborg, Sweden 2011.
- [56] C. S. Jang, J. C. Ross, and R. M. Cummings, "Computational Evaluation of an Airfoil with a Gurney Flap " presented at the AIAA 10th Applied Aerodynamics Conference, 1992.
- [57] H. Johari, C. Heno, D. Custodio, and A. Levshin, "Effects of Leading Edge Protuberances on Airfoil Performance," *AIAA Journal*, vol. 45:11, November 2007.
- [58] J. Jupp, "Wing aerodynamics and the science of compromise," *RAeS Lanchester Lecture*, 2001.
- [59] C. M. Jurasz and V. P. Jurasz, "Feeding Modes of the Humpback Whale, *Megaptera novaeangliae*, in Southeast Alaska," *Scientific Reports of the Whales Research Institute*, vol. 31, pp. 69-83, 1979.
- [60] N. Karthikeyan, S. Sudhakar, and P. Suriyanarayanan, "Experimental Studies On The Effect Of Leading Edge Tubercles On Laminar Separation Bubble," in *52nd Aerospace Sciences Meeting*, ed: American Institute of Aeronautics and Astronautics, doi:10.2514/6.2014-1279, 2014.
- [61] K. Koeltzsch, Dinkelacker, A., Grundmann, R., "Flow over convergent and divergent wall riblets," *Exp. Fluids.*, vol. 33, 2002.
- [62] V. L. Kornilov, "Effect of vertical large eddy breakup devices on the drag of a flat plate," *Thermophysics and Aeromechanics*, vol. 17, 2009.
- [63] R. M. Kulfan, "Application of favorable aerodynamic interference to supersonic airplane design," *SAE paper 90-1988*, 1990.
- [64] G. V. Lachmann, *Boundary Layer Control and Flow Control* vol. 1-2. Oxford: Pergamon Press, 1961.
- [65] R. H. Liebeck, "Design of subsonic airfoils for high lift," *Journal of Aircraft*, vol. 15, 1978.
- [66] Y. Lin, T. Robinson, J. Early, D. Riordan, J. Tweedie, and L. Magee, "Implementation of Menter's transition model on an isolated natural laminar flow nacelle," *AIAA Journal*, vol. 49:824-835., 2011.
- [67] M. Lohry, D. Clifton, and L. Martinelli, "Characterization and Design of Tubercle Leading-Edge Wings," presented at the Computational Fluid Dynamics (ICCFD7), Big Island, Hawaii, 2012.

- [68] A. K. Malipeddi, N. Mahmoudnejad, and K. A. Huffmann, "Numerical Analysis of Effects of Leading-Edge Protuberances on Aircraft Wing Performance " *Journal of Aircraft* vol. 49, 2012
- [69] B. W. McCormick, "Aerodynamics of V/STOL flight," ed New York: Dover Publications, 1999, p. 8.
- [70] R. J. McGhee, J. K. Viken, W. Pfenninger, and W. D. Beasley, "Experimental Results for a Flapped NLF Airfoil with high L/D Ratio," *NASA TM-85788*, 1984.
- [71] F. R. Menter, "Two-Equation Eddy-Viscosity Turbulence Models for Engineering Applications," *AIAA Journal* vol. 32, pp. 1598-1605, 1994.
- [72] C. Merkle and S. Deustch, "Microbubble drag reduction in liquid turbulent boundary layers " *Applied Mechanics Reviews*, vol. 45(3), pp. 103-127, 1992.
- [73] D. S. Miklosovic, M. M. Murray, and L. Howle, "Experimental Evaluation of Sinusoidal Leading Edges," *Journal of Aircraft*, vol. 44:1404–1407, 2007.
- [74] D. S. Miklosovic, M. M. Murray, L. E. Howle, and F. E. Fish, "Leading Edge Tubercles Delay Stall on Humpback Whale Flippers," *Physics of Fluids*, vol. 16(5) pp. L39-L42, 2004.
- [75] V. J. Modi, "Moving Surface Boundary Layer Control: A Review " *Journal of Fluids and Structures*, vol. 11, pp. 627-663, 1997.
- [76] V. J. Modi, M. S. U. K. Fernando, and T. Yokomizo, "Moving Surface Boundary Layer Control: Studies with Bluff Bodies and Application," *AIAA Journal*, vol. 29, pp. 1400-1406, 1991.
- [77] V. J. Modi and F. Mokhtarian, "Fluid Dynamics of Airfoils with Moving Surface Boundary Layer Control " *Journal of Aircraft*, vol. 25, pp. 163-169, 1988.
- [78] B. Morin and T. Barber, "Experimental and Analytical Study of Rippled Trailing Edge Airfoils For Compressor Application " Naval Postgraduate School, Monterey, CA 1991.
- [79] W. Mulcay and J. Chu, "Rotary Balance Data for a Single-Engine Agricultural Airplane Configuration for an Angle of Attack Range of 8 to 90 degrees," NASA Contractor Report 3311, 1980.
- [80] M. M. Murray, D. S. Miklosovic, F. E. Fish, and L. E. Howle, "Effects of Leading Edge Tubercles on a Representative Whale Flipper Model at Various Sweep Angles," in *Proceedings of the 14th Unmanned Untethered Submersible Technology (UUST)*, Durham, New Hampshire, August 2005.
- [81] H. A. Mwenegoha and M. Jabbal, "Investigation of Passive Flow Control Techniques to Enhance the Stall Characteristics of a Microlight Aircraft," *International Journal of Flow Control*, vol. 5, 2013.
- [82] R. Mycose, M. Papadakis, and I. Heron, "Gurney flaps experiments on airfoils, wings and reflection plane model," *Aircraft* vol. 35, 1998.
- [83] B. Nugroho, "Highly ordered surface roughness effects on turbulent boundary layers," Doctor of Philosophy, Mechanical Engineering, The University of Melbourne, Australia, 2015.
- [84] E. Obert, *Aerodynamic Design of Transport Aircraft*: IOS Press, 2009.
- [85] J. C. Owen, A. A. Szewczyk, and P. W. Bearman, "Suppressing Karman Vortex Shedding by Use of Sinuous Circular Cylinders," *American Physical Society*, vol. 12:S9, November 21-23, 1999
- [86] B. Pamadi, *Performance, Stability, Dynamics, and Control of Airplanes*: AIAA Education Series, 2004.
- [87] E. G. Paterson, R. V. Wilson, and F. Stern, "General-purpose parallel unsteady RANS CFD code for ship hydrodynamics," *IIHR Hydrosci. Eng. Rep.*, vol. 531, 2003.
- [88] H. H. Pearcy, *Shock-induced Separation and its Prevention by Design and Boundary Layer Control* GV Lachmann Ed., 1961.
- [89] H. T. C. Pedro and M. H. Kobayashi, "Numerical Study of Stall Delay on Humpback Whale Flippers," *AIAA Paper 2008-0584*, 7-10 January 2008.
- [90] L. Prandtl, "Über Flussigkeitsbewegung Bei Sehr Kleiner Reibung (Fluid Flow in very little Friction)," presented at the Third Intern. Math. Congress, Heidelberg, 1904.

- [91] K. Ramakumar and J. Jacob, "Flow Control And Lift Enhancement Using Plasma Actuators," presented at the 35th AIAA Fluid Dynamics Conference and Exhibit, Ontario, Canada, 2005.
- [92] D. M. Rao and S. C. Mehrota, "Flat-Plate Drag Measurements with Vortex Generators in Turbulent Boundary Layer," NACA CR-172125, 1983.
- [93] L. Reithmaier, *Mach 1 and beyond: The illustrated guide to high-speed flight*. New York: McGraw-Hill, 1995.
- [94] J. Reneaux, "Overview on drag reduction technologies for civil transport aircraft," presented at the European Congress on Computational Methods in Applied Sciences and Engineering (ECCOMAS), 2004.
- [95] J. P. Robert, "Drag reduction: an industrial challenge. Special Course on Skin Friction Drag Reduction," *AGARD report. No 786, Paper No 2.*, 1992.
- [96] J. Roskam and C. E. Lam, *Airplane Aerodynamics and Performance Design Analysis & Research*, 1997.
- [97] M. Sadraey, *Aircraft Design: A systems Engineering Approach*: Wiley, 2012.
- [98] H. Schlichting and W. Pechau, "Auftriebserhöhung von Tragflügeln durch kontinuierlich verteilte Absaugung," *ZFW*, vol. 7, pp. 113-119, 1959.
- [99] G. B. Schubauer and W. G. Spangenberg, "Forced Mixing in Boundary Layers " *Journal of Fluid Mechanics*, vol. 8, pp. 10-31, 1960.
- [100] E. Schulein, "Wave drag reduction concept for blunt bodies at high angles of attack," German Aerospace Center DLR, Institute of Aerodynamics and Flow Technology, Bunsenstr. 10, 37073 Gottingen (Germany)2009.
- [101] M. Simons, *Model Aircraft Aerodynamics*. Dorset, UK, 1999.
- [102] S. K. Sinha and S. Ravande, "Drag Reduction of Natural Laminar Flow Airfoils with a Flexible Surface Deturbulator," presented at the 3rd AIAA Flow Control Conference San Fransisco, California, 2006.
- [103] L. Sirovich and S. Karlsson, "Turbulent Drag Reduction by Passive Mechanisms," *Nature*, vol. 388, pp. 753-755, 1997.
- [104] A. Skillen, A. Revell, J. Favier, A. Pinelli, and U. Piomelli, "LES Study into the Flow Physics of an Undulating Leading-Edged Wing," presented at the ERCOFTAC international symposium Unsteady separation in fluid-structure interaction, Mykonos, Greece, 2013.
- [105] A. Skillen, A. Revell, A. Pinelli, U. Piomelli, and J. Favier, "Flow over a Wing with Leading-Edge Undulations," *AIAA Journal*, pp. 1-9, 2014.
- [106] A. M. O. Smith, "High-Lift Aerodynamics," *Journal of Aircraft*, vol. 12, pp. 501-530, 1975.
- [107] P. Soderman, "Aerodynamic Effects of Leading-Edge Serrations on a Two-dimensional Airfoil " National Aeronautics and Space Administration, Wahington DC 1972.
- [108] SolidWorksFS, 2009 ed. Concord MA: Dassault Systemes SolidWorks Corp, 2009.
- [109] J. G. Spangler and C. S. Wells, "Effects of spiral longitudinal vortices on turbulent boundary layer skin friction," NACA CR-145, 1964.
- [110] M. J. Stanway, "Hydrodynamic effects of leading-edge tubercles on control surfaces and in flapping foil propulsion," Master of Science in Ocean Engineering Mechanical Engineering, Massachusetts Institute of Technology, February 2008.
- [111] STAR-CCM+, 4.02 ed. New York: CD-Adapco, 2009.
- [112] B. Stein and M. M. Murray, "Stall Mechanism Analysis of Humpback Whale Flipper Models," in *Proc. of Unmanned Untethered Submersible Technology (UUST)*, Durham, NH, August 2005.
- [113] W. M. Swanson, "The Magnus Effect: A Summary of Investigations to Date," *Journal of Basic Engineering*, vol. 83, pp. 461-470, 1961.
- [114] I. Tani, "Low-Speed Flows Involving Bubble Separations," *Prog. Aeronautical Sci.*, vol. 5, pp. 70-103, 1964.
- [115] P. Thiede, "Drag reduction technologies " presented at the Proceedings of the CEAS/Dragnet European Drag Reduction Conference, Potsdam, Germany, 2000.



- [116] H. Trukendrodt, "Ein einfaches Naherungsverfahren zum Berechnen der laminaren Reibungsschicht mit Absaugung," *Forschg.Ing.*, vol. 22, pp. 147-157, 1956.
- [117] C. P. van Dam, "The aerodynamic design of multi-element high-lift systems for transport airplanes," *Progress in Aeorospace Science*, vol. 38, pp. 101-144, 2002.
- [118] E. van Nierop, S. Alben, and M. P. Brenner, "How Bumps on Whale Flippers Delay Stall: an Aerodynamic Model," *Physical review letters*, vol. 100(5): 054502, 7 February 2008.
- [119] A. Vorobiev, R. M. Rennie, and E. Jumper, "Lift Enhancement by Plasma Actuators at Low Reynolds Numbers," *Journal of Aircraft*, vol. 50, 2013.
- [120] M. J. Walsh, "Riblets as a viscous drag reduction technique," *AIAA Journal*, vol. 21, 1983.
- [121] C. Warsop, "MEMS and Microsystems Technologies-Their Potential and Status for Drag Reduction and Separation Control," in *European Congress on Computational Methods in Applied Sciences and Engineering (ECCOMAS)*, ed. Jyväskylä 2004.
- [122] P. Watts and P. E. Fish, "The Influence of Passive Leading Edge Tubercles on Wing Performance," in *Proc. of 12th Internat Symp Unmanned Untethered Submersible Technology (UUST)*, Durham NH: Autonomous Undersea Systems Institute, 2001.
- [123] P. Weber, L. Howle, M. Murray, and D. Miklosovic, "Computational Evaluation of the Performance of Lifting Surfaces with Leading-Edge Protuberances," *Journal of Aircraft* vol. 48, March-April 2011.
- [124] D. Weihs, "Effects of Swimming Path Curvature on the Energetics of Fish Swimming," *Fish Bull*, vol. 79, pp. 171-176, 1981.
- [125] H. S. Yoon, P. A. Hung, J. H. Jung, and M. C. Kim, "Effect of the wavy leading edge on hydrodynamic characteristics for flow around low aspect ratio wing," *Computers & Fluids (Elsevier)*, vol. 49 (2011) 276–289, June 2011.
- [126] M. M. Zhang, G. F. Wang, and J. Z. Xu, "Experimental study of flow separation control on a low-Re airfoil using leading-edge protuberance method," *Experimental Fluids*, vol. 55:1710, 2014.
- [127] I. Zverkov, B. Zanin, and V. Kozlov, "Disturbuences Growth in Boundary Layers on Classical and Wavy Surface Wings," *AIAA*, vol. 46, 2008.

## Chapter 3

# Flow over a Wavy Foil in the Transitional Regime

As stated in Chapter 2, full-span wavy wings, whereby the geometric attack angle varies sinusoidally along the span, were demonstrated by Hansen [1] to produce similar aerodynamic traits to those with tubercles. This observation provided a degree of evidence to reinforce the notion that the fundamental flow mechanisms triggered by the presence of wavy and tubercled leading-edges are identical. To verify this conjecture, analytical, experimental and numerical studies were conducted, and the results are reported in the presented paper titled, “[The effect of undulating leading-edge modifications on NACA-0021 airfoil characteristics](#)”, published in *Physics of Fluids*.

On the analytical front, Prandtl’s non-linear lifting-line theory was employed to assess the behaviour of spanwise circulation on the presence of an undulating leading edge. If, indeed, the underlying flow mechanism associated with the flow over a tubercled and a wavy wing are the same, the distribution of spanwise circulation would exhibit similar trends.

To assess the influence of the geometric parameters associated with the wavy leading edge (angular amplitude and wavelength) on its aerodynamic performance, the three wavy airfoils, previously tested by Hansen [1], along with a newly-designed and fabricated wavy wing, and the baseline NACA-0021 airfoil, underwent wind tunnel force measurement tests in the transitional flow regime at  $Re=120,000$ . Furthermore, surface pressure measurement tests were conducted under the same flow conditions on the newly-fabricated wavy wing. The analysis of the surface pressure distribution, for the three main spanwise locations, namely the peak, the trough and the middle section, provided another platform for comparison of the flow structure with that of a tubercled wing.

Finally, further knowledge of the flow structure around a wavy airfoil was obtained by the computational fluid dynamics study investigating the transitional flow regime at several attack angles. Validation of the model was based on the surface pressure distribution data obtained in this work. Analysing the surface flow topology, by means of plotting the limiting shear stress lines, as well as

examining the boundary layer profile, revealed a number of features that were previously reported with reference to the flow over tubercled wings. In addition, investigating the vorticity field in the wake reinforced the validity of the hypothesis about the fundamental flow mechanism.

- [1] K. L. Hansen, "Effect of Leading Edge Tubercles on Airfoil Performance," Doctor of Philosophy Thesis, Mechanical Engineering, University of Adelaide, Adelaide, SA, Australia, 2012.

## Statement of Authorship

Title of Paper	The effect of undulating leading-edge modifications on NACA 0021 airfoil characteristics
Publication Status	<input checked="" type="checkbox"/> Published <input type="checkbox"/> Accepted for Publication <input type="checkbox"/> Submitted for Publication <input type="checkbox"/> Publication Style
Publication Details	Citation: Physics of Fluids (1994-present) <b>25</b> , 117101 (2013); doi: 10.1063/1.4828703

Name of Principal Author (Candidate)	Nikan Rostanzadeh	
Contribution to the Paper	Performed the literature review. Responsible for the preparation of the Computer Aided Design model of one of the wavy foils. Independently conducted theoretical analyses, experimental work (in the form of pressure and force measurement tests), and numerical simulations. Interpreted the findings and discussed the results. Planned and drafted the manuscript. Took primary responsibility for responding to reviewers.	
Signature		
	Date	22/11/2015

## Co-Author Contributions

By signing the Statement of Authorship, each author certifies that:

- i. the candidate's stated contribution to the publication is accurate (as detailed above);
  - ii. permission is granted for the candidate to include the publication in the thesis; and
- the sum of all co-author contributions is equal to 100% less the candidate's stated contribution

Name of Co-Author	Associate Professor Richard M. Kelso	
Contribution to the Paper	Supervised the work. Conceived of the design idea of the wavy wing based on Prandtl's lifting-line theory. Suggested the adopted theoretical approach. Helped interpret the results. Assisted with the editing of the manuscript.	
Signature	Date	23/11/2015

Name of Co-Author	Professor Bassam B. Dally	
Contribution to the Paper	Supervised the work. Provided assistance with the measurement techniques. Assisted with editing the manuscript.	
Signature	Date	23/11/2015

Name of Co-Author	Dr. Kristy Lee Hansen	
Contribution to the Paper	Designed three of the wavy wings with assistance from Associate Professor Richard M. Kelso. Provided guidance in the design of the wing with pressure taps, experimental methodology and coding for data analysis. Assisted with editing the manuscript. Developed the load cell apparatus.	
Signature	Date	20/11/2015



## The effect of undulating leading-edge modifications on NACA 0021 airfoil characteristics

N. Rostamzadeh, R. M. Kelso, B. B. Dally, and K. L. Hansen

Citation: [Physics of Fluids \(1994-present\)](#) **25**, 117101 (2013); doi: 10.1063/1.4828703

View online: <http://dx.doi.org/10.1063/1.4828703>

View Table of Contents: <http://scitation.aip.org/content/aip/journal/pof2/25/11?ver=pdfcov>

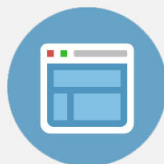
Published by the [AIP Publishing](#)

---



## Re-register for Table of Content Alerts

Create a profile.



Sign up today!



## The effect of undulating leading-edge modifications on NACA 0021 airfoil characteristics

N. Rostamzadeh, R. M. Kelso, B. B. Dally, and K. L. Hansen

*School of Mechanical Engineering, The University of Adelaide, Adelaide, SA 5005, Australia*

(Received 19 February 2013; accepted 16 October 2013; published online 5 November 2013)

In spite of its mammoth physical size, the humpback whale's manoeuvrability in hunting has captured the attention of biologists as well as fluid mechanists. It has now been established that the protrusions on the leading-edges of the humpback's pectoral flippers, known as tubercles, account for this species' agility and manoeuvrability. In the present work, Prandtl's nonlinear lifting-line theory was employed to propose a hypothesis that the favourable traits observed in the performance of tubercled lifting bodies are not exclusive to this form of leading-edge configuration. Accordingly, a novel alternative to tubercles was introduced and incorporated into the design of four airfoils that underwent wind tunnel force and pressure measurement tests in the transitional flow regime. In addition, a Computation Fluid Dynamics study was performed using the Shear Stress Transport transitional model in the context of unsteady Reynolds-Averaged Navier-Stokes at several attack angles. The results from the numerical investigation are in reasonable agreement with those of the experiments, and suggest the presence of features that are also observed in flows over tubercled foils, most notably a distinct pair of streamwise vortices for each wavelength of the tubercle-like feature. © 2013 AIP Publishing LLC. [<http://dx.doi.org/10.1063/1.4828703>]

### I. INTRODUCTION

Nature, with its elegance and mystique, has always served as a generous source of inspiration and creativity.<sup>4</sup> One peculiar instance that has intrigued fluid mechanists and zoologists for the past decade is the humpback whale's ability to turn around tight angles in its bubble-net feeding strategy.<sup>13</sup> When rolling in a banking turn, hydrodynamic lift forces are developed on the humpback's flippers whose horizontal components act as the centripetal force.<sup>22</sup> Fish and Battle<sup>9</sup> were the first to postulate that the sinusoidal-shaped protuberances on the leading-edges of the whale's pectoral flippers, known as tubercles, may account for the humpback's extraordinary manoeuvrability through maintaining lift at high attack angles.

To assess the aerodynamic performance of an idealised model of a humpback whale flipper, Miklosovic *et al.*<sup>17</sup> conducted a series of wind tunnel experiments that unveiled the desirable characteristics of tubercles at Reynolds numbers between 505 000 and 520 000, which fall in the operating range of the humpback. It was found that, compared to the finite-span wing without tubercles, the modified model increased the stall angle by nearly 40%, achieved a 6% increase in the maximum lift coefficient and incurred lower drag at high incidence angles.

Inspired by the initial promising results, Miklosovic *et al.*,<sup>16</sup> Johari *et al.*,<sup>12</sup> and Hansen *et al.*<sup>11</sup> carried out low Reynolds number force measurement tests on nominally two-dimensional foils, as opposed to finite wings, and at lower Reynolds numbers. Compared to the unmodified model, tubercled airfoils were found to display a degraded performance in the pre-stall regime; however, superior performance with regard to lift generation was observed post-stall. It was also demonstrated that tubercles soften the stall phase, while wings without modifications undergo an abrupt loss of lift.

In order to determine the fluid dynamics that account for the behavior of wings with tubercles, van Nierop *et al.*<sup>21</sup> and Pedro and Kobayashi,<sup>18</sup> carried out analytical and numerical studies on

flipper models, respectively. An important outcome of these investigations was the identification of counter-rotating streamwise vortices in the vicinity of lifting surfaces with tubercles. Hence, it was proposed that the beneficial aspects of lifting surfaces with tubercles may be associated with streamwise vorticity present in the flow field. Moreover, van Nierop *et al.*<sup>21</sup> showed that flow behind the peaks of the tubercles remains attached at high angles of attack, which could explain the superior performance of tubercled models compared to the unmodified wing at high attack angles wherein flow separation dominates a large area on the suction side of the wing. The tuft flow visualization work by Johari *et al.*<sup>12</sup> confirms that the flow behind the tubercle peak is less susceptible to flow separation than the flow behind the trough.

Even though previous work has illuminated a number of flow features associated with tubercled lifting bodies, the underlying flow mechanism remains to be fully explored. van Nierop's<sup>21</sup> prediction, later confirmed by Hansen,<sup>10</sup> that the pressure distribution behind a tubercle peak is different from that behind a trough implies that there is a variation in spanwise distribution of pressure over tubercled wings. On the other hand, according to Prandtl's lifting-line theory, change in spanwise loading is indicative of variation in the generated circulation around a wing's cross-section along the span. Thus, investigating the development of circulation can reveal the fundamental flow mechanics activated by the presence of tubercles.

In an attempt to gain further insight into the underlying flow mechanism, the present work employs Prandtl's nonlinear lifting-line theory to examine how circulation is developed around wings with two forms of leading-edge modification, namely the tubercled configuration and a novel alternative design referred to as the *wavy wing*. The hypothesis adopted was that the alternative modification would exhibit similar aerodynamic traits to the tubercle-modified wings, as both configurations are shown to operate under the same flow mechanism.

To assess the hypothesis, four modified NACA 0021-based airfoils were fabricated to undergo wind tunnel force and pressure measurement tests in the transitional flow regime. Furthermore, the flow structure around the wavy wing was examined using Computational Fluid Dynamics that aided the study of the vorticity field and the separation pattern in the vicinity of a full-span wavy wing.

## II. ANALYTICAL WORK

The nonlinear lifting line theory, developed by Ludwig Prandtl, is an extension of the classical lifting-line theory with an advantage over a linear approach. By incorporating experimental data corresponding to a full-span airfoil, this approach aims to capture the near- and post-stall behaviour of a finite wing. Despite being an approximate method, in the context of wings with modified leading-edges, this iterative scheme, as described in detail by Anderson,<sup>2</sup> elucidates how circulation, which is a key flow parameter, changes in the spanwise direction.

Herein, two forms of wings with undulating leading-edges were considered: the novel wavy model where the geometric angle of attack changes sinusoidally in the spanwise direction (Figure 1(a)) and the model with tubercles, where the chord varies in a sinusoidal manner along the span and (Figure 1(b)). Both airfoils are designed with the NACA 0021 baseline profile.

Each wavelength of the wing undulation was allocated a number of stations to represent various locations along the span (Figure 2). As an initial estimate, an elliptic lift distribution was assigned to the stations according to

$$\Gamma(y_n)_{\text{initial}} = \Gamma_0 \sqrt{1 - \left(\frac{2y_n}{b}\right)^2}. \quad (1)$$

$\Gamma_0$ , an arbitrary initial guess, was set to 0.4. The induced angle of attack was found by

$$\alpha_i(y_n) = \frac{1}{4\pi U_\infty} \int_{-b/2}^{b/2} \frac{d\Gamma/dy}{y_n - y} dy, \quad (2)$$

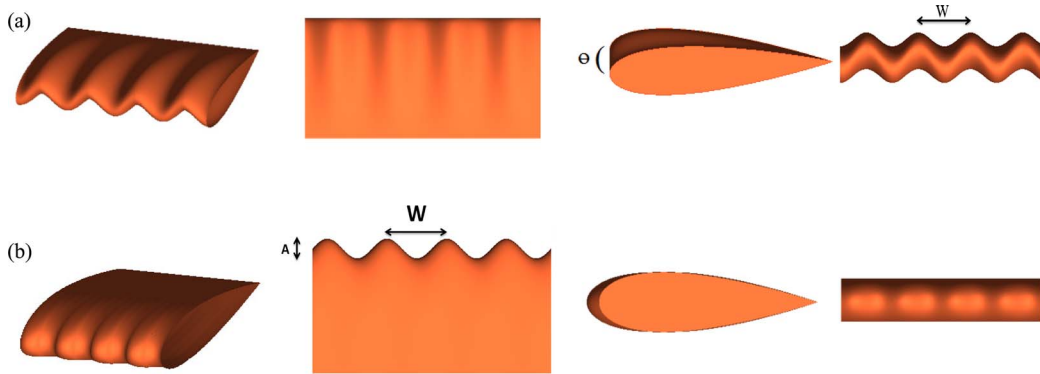


FIG. 1. Wavy wing section showing peak-to-peak angular amplitude ( $\theta$ ) expressed in degrees and wavelength ( $w$ ) in millimetres (a) and tubercled wing section showing the amplitude ( $A$ ) and wavelength ( $W$ ) expressed in millimetres (b).

where  $U_\infty = 25(\text{ms}^{-1})$  is the free-stream speed and  $b = 0.495$  (m) is the span. The values for geometric and flow parameters were selected to match those in the present work's experimental setup (refer to Sec. III).

Next, Simpson's rule was applied to compute the integral in (2):

$$\frac{\alpha_i(y_n)}{\zeta} = \sum_{j=2,4,6,8,\dots}^k \frac{(d\Gamma/dy)_{j-1}}{(y_n - y_{j-1})} + 4 \frac{(d\Gamma/dy)_j}{(y_n - y_j)} + \frac{(d\Gamma/dy)_{j+1}}{(y_n - y_{j+1})}, \quad (3)$$

$$\zeta = \frac{\Delta y}{12\pi U_\infty}. \quad (4)$$

Singularities occur at ( $y_n = y_{j-1}$ ,  $y_n = y_j$ ,  $y_n = y_{j+1}$ ). Therefore, these terms had to be estimated using the average of the neighbouring terms.<sup>2</sup> For instance, at ( $y_n = y_{j-1}$ ):

$$2 \frac{(d\Gamma/dy)_{j-1}}{(y_n - y_{j-1})} = \frac{(d\Gamma/dy)_{j-2}}{(y_n - y_{j-2})} + \frac{(d\Gamma/dy)_j}{(y_n - y_j)}. \quad (5)$$

For a wing with waves, the geometric angle of attack can be modelled by

$$\alpha_n = \frac{\theta}{2} \sin\left(\frac{2\pi}{w} y_n\right). \quad (6)$$

By contrast, for tubercles, the chord varies according to

$$c_n = \frac{A}{2} \sin\left(\frac{2\pi}{W} y_n\right) + c, \quad (7)$$

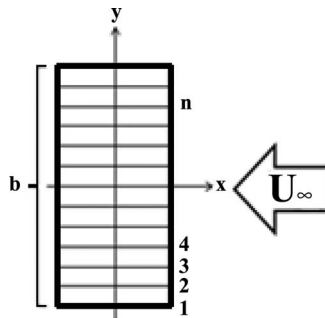


FIG. 2. The coordinate system with a number of stations marking various locations along the span (top view).



where  $c = 0.07(\text{m})$  is the mean chord. Given the geometric attack angle and the calculated induced angle in Eq. (2) at each station, the effective angle of attack was obtained by Prandtl's *Fundamental equation of lifting-line theory*:

$$\alpha_E = \alpha - \alpha_i. \quad (8)$$

At each station, the value of the effective attack angle was used to extract the baseline NACA 0021 lift coefficient, obtained from experimental data by Hansen *et al.*<sup>11</sup>

Using the Kutta-Joukowski's theorem, a new circulation distribution was found from the lift coefficient distribution:

$$\Gamma_n = \frac{1}{2} U_\infty c_n (C_L)_n. \quad (9)$$

The circulation distribution was then compared to the initial guess and updated in (10), where a typical value of 0.04 was selected for the damping coefficient,  $\varepsilon$ :

$$\Gamma_{\text{new}} = \Gamma_{\text{initial}} + \varepsilon(\Gamma_{\text{initial}} - \Gamma_n). \quad (10)$$

Subsequently, a loop was established by replacing  $\Gamma_{\text{initial}}$  with  $\Gamma_{\text{new}}$  in Eq. (1). Convergence was determined once the difference between two consecutive estimates of circulation at each station diminished to 0.001. Figure 3 illustrates how circulation varies along half of the span for a tubercled and a wavy wing pre- and post-stall at a Reynolds number of 120 000.

Prandtl's nonlinear lifting-line theory indicates that, in contrast to the unmodified wing, for the wavy and the tubercled wings, the distribution of circulation along the span assumes a fluctuating pattern similar to that of tubercles. The periodic variation of circulation points to a vortex generation phenomenon in the streamwise direction for both wings. It is noticed that with the increase in attack angle, the amplitude of fluctuations grows for the tubercled wing. Since the strength of the streamwise vortices is proportional to the slope of the circulation curve and the spacing between two neighbouring stations ( $\frac{\partial \Gamma}{\partial y} dy$ ), it is predicted that stronger vortices are generated at higher attack angles. In contrast, for the wavy wing, the amplitude of fluctuations is noticeably larger even at low angles, signifying the presence of stronger vortices. Also, noteworthy is the observation that for the wavy wing, the increase in the attack angle from  $11^\circ$  to  $15^\circ$  is not accompanied by a dramatic drop in the values of circulation along the span. This is contrary to the wing with the straight leading edge that experiences a rapid decrease in the values of circulation from  $13^\circ$  to  $15^\circ$ .

To predict the effect of the peak-to-peak angular amplitude and wavelength on the overall performance of wavy wings, circulation was integrated along the span ( $S$ ) for three finite wings to compare against the NACA0021 wing:

$$C_L = \frac{2}{U_\infty S} \int_{-b/2}^{b/2} \Gamma(y) dy. \quad (11)$$

As illustrated in Figure 4, up to  $8^\circ$ , all wings yield nearly the same values of lift coefficient. Past this angle, the slope of the lift curve for the unmodified wing increases and the wing produces the most amount of lift between  $8^\circ$  and  $14^\circ$ . The increase in the angle of attack by  $1^\circ$  from ( $14^\circ$  to  $15^\circ$ ) is characterized by a sudden drop in the lift coefficient, whereas the modified wings experience a less abrupt loss of lift. Nonetheless, the wavy models' maximum lift coefficients are lower, and their onset of stall occurs at lower angles of attack. Among the three wavy wings, the model with  $\theta = 2^\circ$ , undergoes a more rapid loss of lift compared to the ones with  $4^\circ$ . Hence, the stall behaviour of the wavy model  $\theta 4w15$  is expected to be most desirable as the decrease in the lift force on this wing between  $11^\circ$  and  $15^\circ$  angles of attack is the smallest. Post-stall, between  $15^\circ$  and  $20^\circ$ , all three wavy wings yield higher values of lift coefficient compared to the unmodified wing.

Given the observations above, it can be deduced that wavy wings with shorter wavelengths and larger peak-to-peak amplitudes are likely to display more favourable attributes such as attenuated stall effects by extending the stall margin. It can also be concluded that wavy wings' superior performance is expected to be achieved post-stall. Although the results presented here are derived

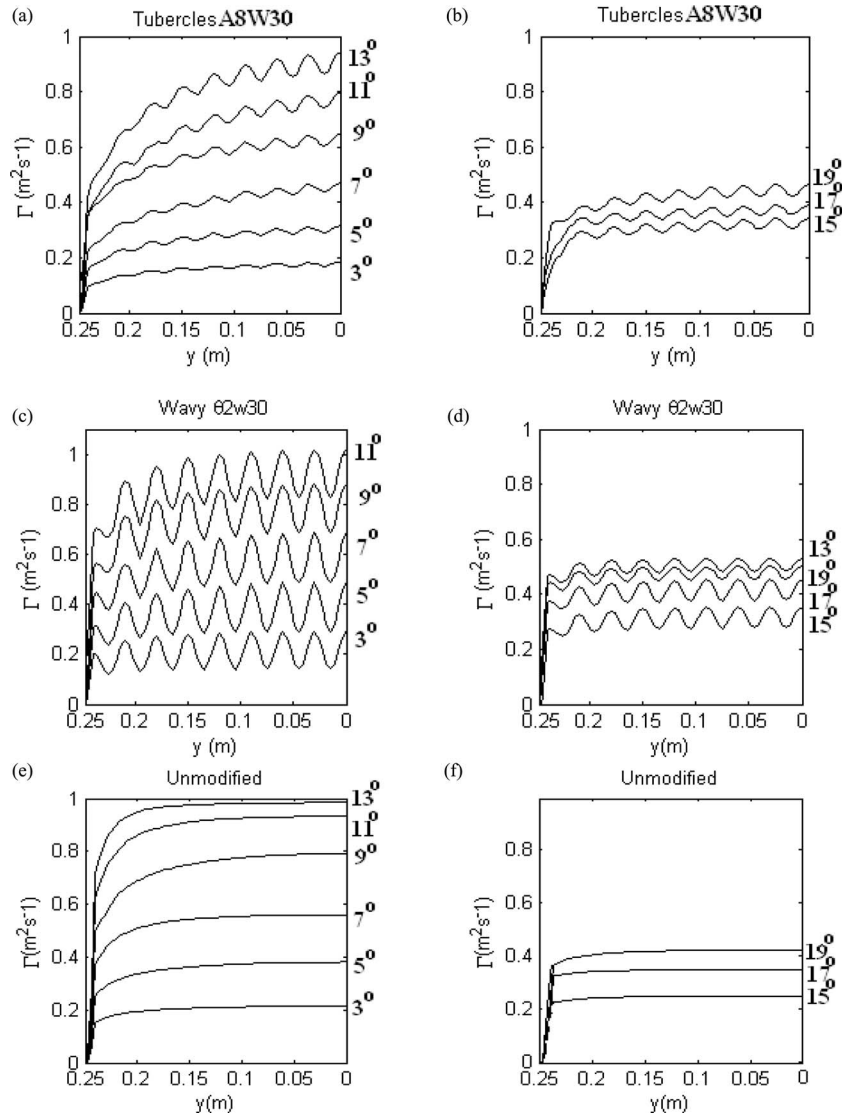


FIG. 3. Spanwise circulation for a tubercled, wavy and unmodified foil NACA 0021 at various incidence angles along half of the span.

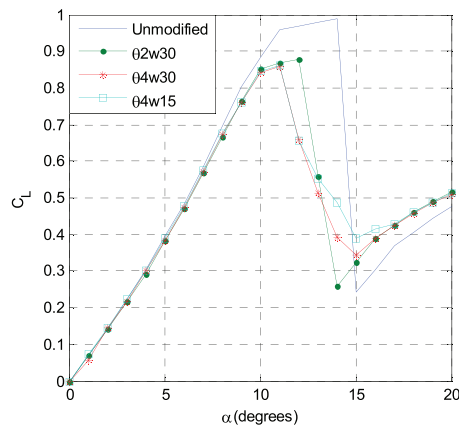


FIG. 4. Lift coefficient for three finite wavy wings obtained by Prandtl’s nonlinear lifting-line theory ( $Re = 120000$ ).

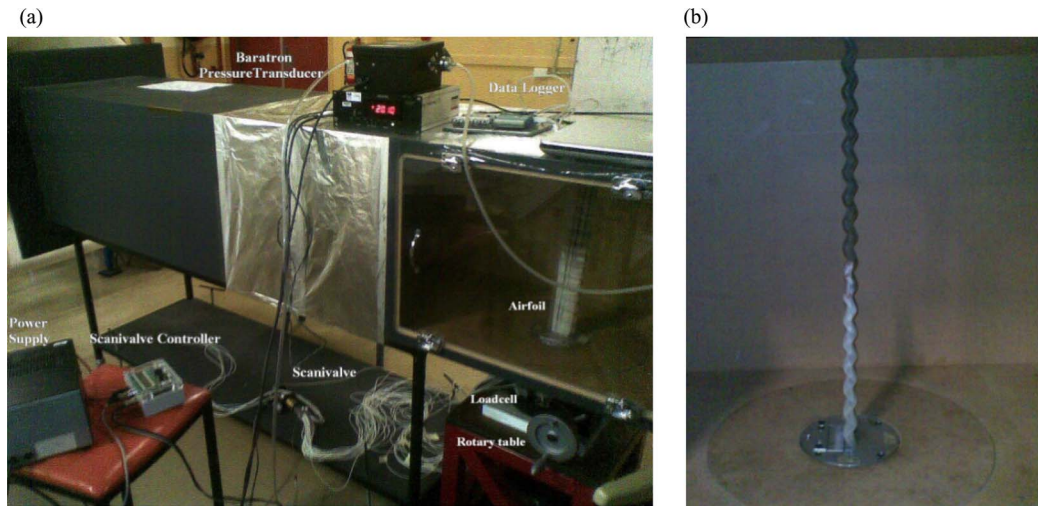


FIG. 5. Experimental setup for pressure and force measurement tests (a) and wavy foil as mounted in the test section (b).

for finite-span wings, it is conceivable that the global behaviour of spanwise circulation for full-span lifting surfaces is similar.

### III. FORCE AND PRESSURE MEASUREMENT TESTS

To assess the aerodynamic loading characteristics of full-span wavy foils against an unmodified model, a series of force measurement tests was performed at  $Re = 120\,000$  in the closed-loop KC wind tunnel at the University of Adelaide. The test section of the tunnel has a  $500(\text{mm}) \times 500(\text{mm})$  cross-section with a maximum blockage ratio of 6% at a  $25^\circ$  attack angle. To ensure 2D flow near the free-end wing tip, a wall clearance of 3 (mm) was maintained.<sup>3</sup> The turbulent intensity of the tunnel is approximately 0.8% ahead of the test subject. The experimental setup for both force and pressure measurement tests can be seen in Figure 5.

Force measurements were undertaken by a six-component load cell from (JR3, Inc., Woodland, CA, USA), with an uncertainty estimate of  $\pm 1, \%$ , to obtain normal and chordwise forces which were then converted into lift and drag. A Vertex rotary table was attached to the base of the load cell to allow accurate and repeatable changes in the attack angle.

Of the four NACA 0021-based wavy foils with varying wavelength and peak-to-peak angular amplitude, three were machined from aluminium and one was cast from epoxy resin (Figure 6). All the airfoils have mean chord and span lengths equal to 70 (mm) and 495 (mm), respectively.

With the sampling period of the analogue-to-digital converter set to 16 ms, 3000 data points, corresponding to normal and axial force components, were collected at each angle of attack. The tests were repeated four times for every foil and average values of the lift and drag coefficients were calculated accordingly. The average standard errors in estimating the population means for

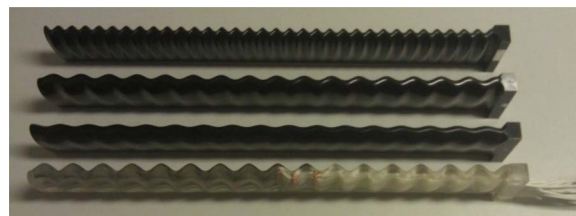


FIG. 6. Wavy foils : $\theta 4w15$ ,  $\theta 4w30$ ,  $\theta 2w30$ ,  $\theta 6.5w30$  (top to bottom).

TABLE I. Total error in calculating the lift and drag coefficients for the six wings tested.

Wing label	Total error in calculating $C_L$ due to solid blockage, wake blockage, and streamline curvature	Total error in calculating $C_D$ due to solid blockage, wake blockage, and streamline curvature
Unmodified NACA 0021	0.026	0.009
$\theta 2w30$	0.029	0.010
$\theta 4w30$	0.026	0.009
$\theta 6.5w30$	0.021	0.008
$\theta 4w15$	0.027	0.010
A8W30	0.022	0.009

lift and drag coefficients were 0.003 and 0.009, respectively. Wind tunnel corrections for solid blockage, wake blockage and streamline curvature were also applied to the results in accordance with recommendations by Barlow *et al.*<sup>3</sup> and are listed in Table I as averaged values over the entire range of attack angles.

Pressure measurement tests were performed on the wavy foil  $\theta 6.5w30$  at the same Reynolds number as that of the force measurement tests, i.e.,  $Re = 120\,000$ . Pressure taps were drilled onto the top surface of the foil in three rows along the 70-mm-chord lines corresponding to a trough, a peak and a middle cross-section as shown in Figure 7. Of the 30 bored taps, two were blocked including one at the stagnation point on a peak and therefore not used in the experiments. A series of PVC tubes, embedded in the foil, connected the surface pressure taps to the head-ports of a controller-modulated ScaniValve. To achieve high-precision pressure measurements, a 10-Torr (1333.2 Pa) MKS Baratron (model 220BD) with a resolution of 0.01% of the full scale range was utilized. The free-stream speed and static pressure were measured at 25 (m/s) and 14212.1 (Pa) below the ambient pressure. For each incidence angle, 2000 data points (per pressure port) were collected at a sampling rate of 200 Hz. It was observed that 200 Hz was sufficient to establish a typical small standard error of  $3.3 \times 10^{-3}$  (Pa) in estimating the population mean. As the taps were placed on one side (upper surface) of the wing, the data from the negative attack angles were used to determine the pressure values for the lower surface. Care was taken to ensure that the peak and trough pressure distributions were correctly matched.

### A. Performance effect of variation in wavy foil wavelength

Figure 8 shows that the unmodified and wavy foils produce nearly the same lift-curve slope up to  $4^\circ$ . At this point, the curves deviate from their linear trend which hints at extra lift produced

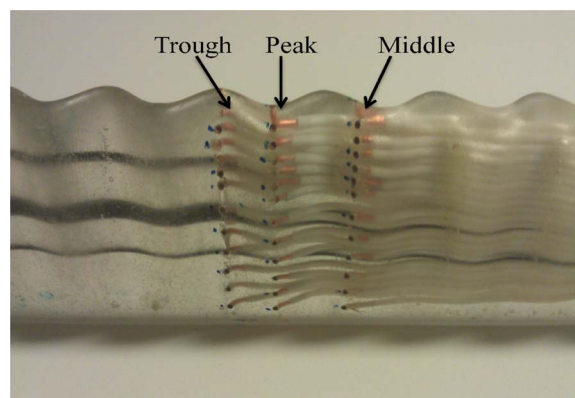


FIG. 7. Wavy wing section with three pressure tapping rows.

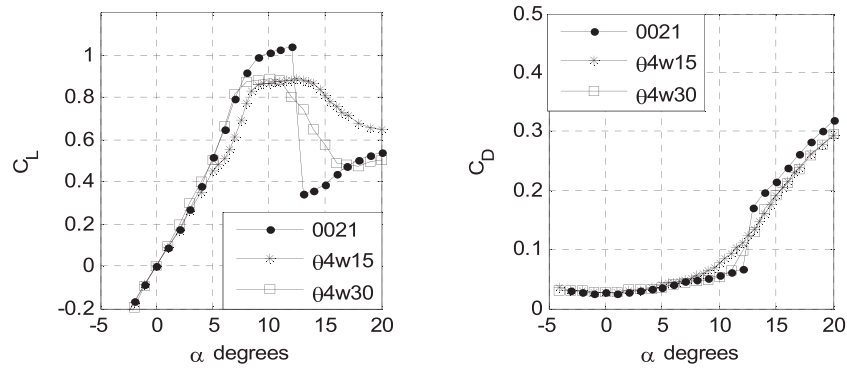


FIG. 8. Lift and drag coefficient versus attack angle for two wavy foils of varying wavelength, and the unmodified NACA 0021 ( $Re = 120000$ ).

by the presence of laminar separation bubbles (LSBs). With regard to the maximum lift coefficient, the unmodified foil achieves the highest value, followed by a dramatic loss of lift past  $12^\circ$ , and a consequent rise in drag.

The drag coefficient for the unmodified and wavy foil  $\theta 4w30$  assumes nearly the same values up to  $11^\circ$  of angle of attack, however post-stall (past  $13^\circ$ ) the unmodified foil's drag coefficients are higher than those of the other two foils'. Due to the fact that flow separation is mainly responsible for the increase in drag at higher angles (as opposed to shear), it can be deduced that flow separation must dominate over a larger surface area on the unmodified foil compared to the wavy wings. In addition, the increase in the drag force on the  $\theta 4w15$  wing is steadier, a phenomenon consistent with the behaviour of the lift force, as the loss of lift occurs less suddenly with respect to the increase in attack angle. Hence, between the wavy foils with the same wavelength,  $\theta 4w15$  outperforms  $\theta 4w30$  post-stall as it undergoes a more gradual stall with a higher amount of lift, indicating that smaller wavelengths may be more beneficial for design purposes.

## B. Performance effect of variation in wavy foil peak-to-peak angular amplitude

Comparison of the lift coefficient for the wavy foils of the same wavelength against the unmodified NACA 0021 foil (Figure 9) reveals that both wavy foils produce lower lift pre-stall. The unmodified and  $\theta 2w30$  foils exhibit a sudden loss of lift and nearly identical post-stall behaviour, however  $\theta 6.5w30$  shows superior performance past  $12^\circ$  with lower drag coefficients. Similar to the tests cases discussed in Sec. III A, it is speculated that flow separation at higher angles of attack occurs on a smaller surface area on the wavy wings. It is plausible that more flow remains attached on

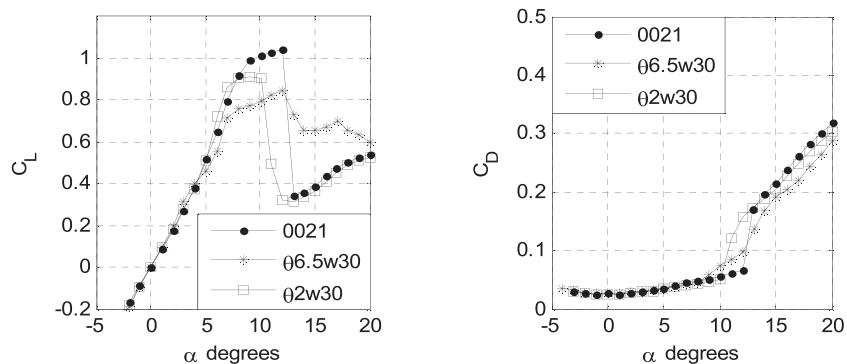


FIG. 9. Lift and drag coefficient versus the attack angle for two wavy foils of varying peak-to-peak angular amplitude and the unmodified NACA 0021 ( $Re = 120000$ ).

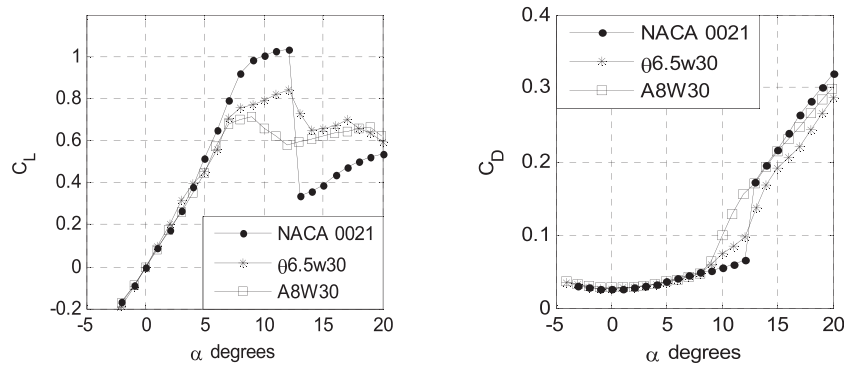


FIG. 10. Lift and drag coefficient curves for a tubercled, a wavy and an unmodified foil.

a particular cross-section (refer to Sec. IV B). The observations indicate that wavy foils with higher peak-to-peak amplitudes may render more aerodynamic benefits in the post-stall region. ( $\theta 4w30$  is shown in Fig. 8.)

### C. Aerodynamic behavior of modified wings compared to the unmodified foil

The wavy wing  $\theta 6.5w30$  was designed using the same leading-edge sinusoidal curve as that of one tubercled wing tested by Hansen *et al.*<sup>11</sup> In the current study, the same tubercled airfoil was re-tested against the unmodified and wavy foils (Figure 10).

Pre-stall, the standard NACA 0021 foil's aerodynamic performance is superior to the modified foils as more lift is generated with the smooth leading-edge wing, while the drag force on all foils (up to a  $9^\circ$  angle of attack) is almost identical. Whereas the NACA 0021 and wavy airfoils stall at  $12^\circ$ , the one with tubercles stalls at  $9^\circ$ . The post-stall region for the tubercled foil is characterised by a steady lift recovery phase, followed by a local maximum at  $19^\circ$ . For the wavy wing, the local post-stall peak occurs at  $17^\circ$ , and the lift coefficients assume higher values prior to this attack angle. A comparison between the drag curves reveals that the wavy foil performs better as the drag force is lower for angles above  $10^\circ$ . Hence, the overall performance of the wavy foil is more favorable to its geometrically matched counterpart. In contrast to the wings with undulating leading-edges, the NACA 0021 undergoes abrupt stall yielding lower values of the lift coefficient than the modified wings, rendering the modified models more advantageous.

### D. Aerodynamic efficiency of the tested wings

The lift-to-drag ratio is a true measure of aerodynamic efficiency.<sup>2</sup> Figure 11 shows how this ratio varies with respect to angle of attack for the tested unmodified NACA0021, four wavy wings and the tubercled wing at  $Re = 120\,000$ .

Of all the configurations tested, the highest L/D ratio is achieved by  $\theta 2w30$  at a  $7^\circ$  incidence angle pre-stall, while post-stall the same wing has the most inferior performance as its aerodynamic efficiency is the lowest and remains nearly constant at around 1.79. The most desirable envelope of operation for this wing occurs between  $4^\circ$  and  $9^\circ$  wherein the L/D ratio stands higher than for the other full-span wings. Aerodynamic efficiency for the unmodified foil, similar to that of  $\theta 2w30$ , diminishes rapidly which is explained by the decrease in lift and rise in drag between  $12^\circ$  and  $13^\circ$  for the unmodified and  $10^\circ$  and  $11^\circ$  of attack angle for the  $\theta 2w30$  wavy foil, respectively. The tubercled foil, and the three wavy foils ( $\theta 4w30$ ,  $\theta 6.5w30$ , and  $\theta 4w15$ ) undergo a more gradual loss of lift and rise in drag as evidenced by the less steep slopes of their corresponding L/D values. Post-stall the best performing wing is  $\theta 4w15$  with the highest values of lift-to-drag ratio between  $13^\circ$  and  $20^\circ$ , offering a large envelope of operation. The tubercled wing's efficiency is comparable to the wavy foils' past  $15^\circ$ , whereas pre-stall it only outperforms  $\theta 4w15$  (below  $8^\circ$ ).

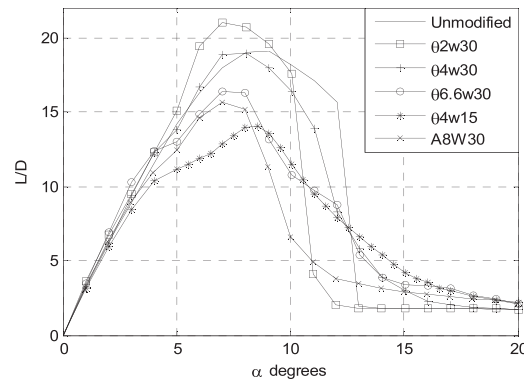


FIG. 11. Aerodynamic efficiency ( $L/D$ ) versus the attack angle for four wavy wings, one tubercled wing and the unmodified NACA 0021 foil at  $Re = 120\,000$ .

The analysis of the force measurement tests results reveals that even though the unmodified baseline foil achieves the highest lift coefficient pre-stall operation at transition to higher angles of attack is accompanied by a dramatic drop in aerodynamic efficiency. This unfavourable phenomenon can be overcome by means of a wavy leading-edge configuration as well as a tubercled arrangement. The performance of the  $\theta 6w15$  wavy wing, in particular, suggests its applicability potential in aero/hydrodynamic machinery where the angle of attack varies from low to high values such as in wind turbine and blades.

### E. Pressure measurement results

Figure 12 illustrates how pressure varies along a peak, trough and middle cross section of the wavy wing  $\theta 6.5w30$ . At a zero angle of attack, interestingly, the suction side of the peak is under higher pressure compared to the pressure side (lower surface). The plateau on the pressure curve between  $x/c = 0.4$  and  $x/c = 0.5$ , followed by a recovery zone suggests the presence of a LSB. This flow feature is often observed at low Reynolds numbers where separation due to strong adverse pressure gradients gives rise to Helmholtz-instabilities whose breakdown results in separation-induced transition and the formation of LSBs.<sup>8</sup> At  $\alpha = 2^\circ$  the wavy foil's trough experiences lower pressure on the suction side when compared to the peak. Two LSBs are found, one on the suction side of the trough and the other on the pressure side of the peak cross section (refer to Sec. IV B for further evidence). Increasing the angle of attack, forces the LSB to move towards the trough's leading-edge, as a drop in pressure occurs on the suction surface. Meanwhile, the pressure on the lower surface of the peak rises, and the LSB on this side moves towards the trailing edge, indicating that the separation point has translated further downstream. This trend continues up to a  $12^\circ$  attack angle. At  $\alpha = 12^\circ$  the overall shape of pressure distribution begins to alter, particularly for the suction surface of the middle cross-section. The flatness of the pressure curve past  $x/c = 0.3$  on the middle cross-section signifies that flow separation begins to affect a larger area on the airfoil as stall is initiated gradually. At higher angles, flow separation seems to have dominated the suction side; however, the leading-edge of the trough cross-section maintains low values of pressure that account for lift being generated in the post-stall zone. The low pressure zone in the vicinity of the trough region may account for the delay and extended stall features. It is of interest to note that previously research on tubercled wings have also identified the low pressure region in the trough,<sup>6,21</sup> providing further evidence that the flow mechanisms in wings with wavy and tubercled leading-edges are similar.

The amount of lift generated at each cross section was estimated by the trapezoidal rule for integration. Since there were no data available for the stagnation point on the trough, a shape-preserving interpolant curve-fit was applied to account for the error incurred. Also, the contribution of shear forces to lift, which in most cases is negligible, is not included.

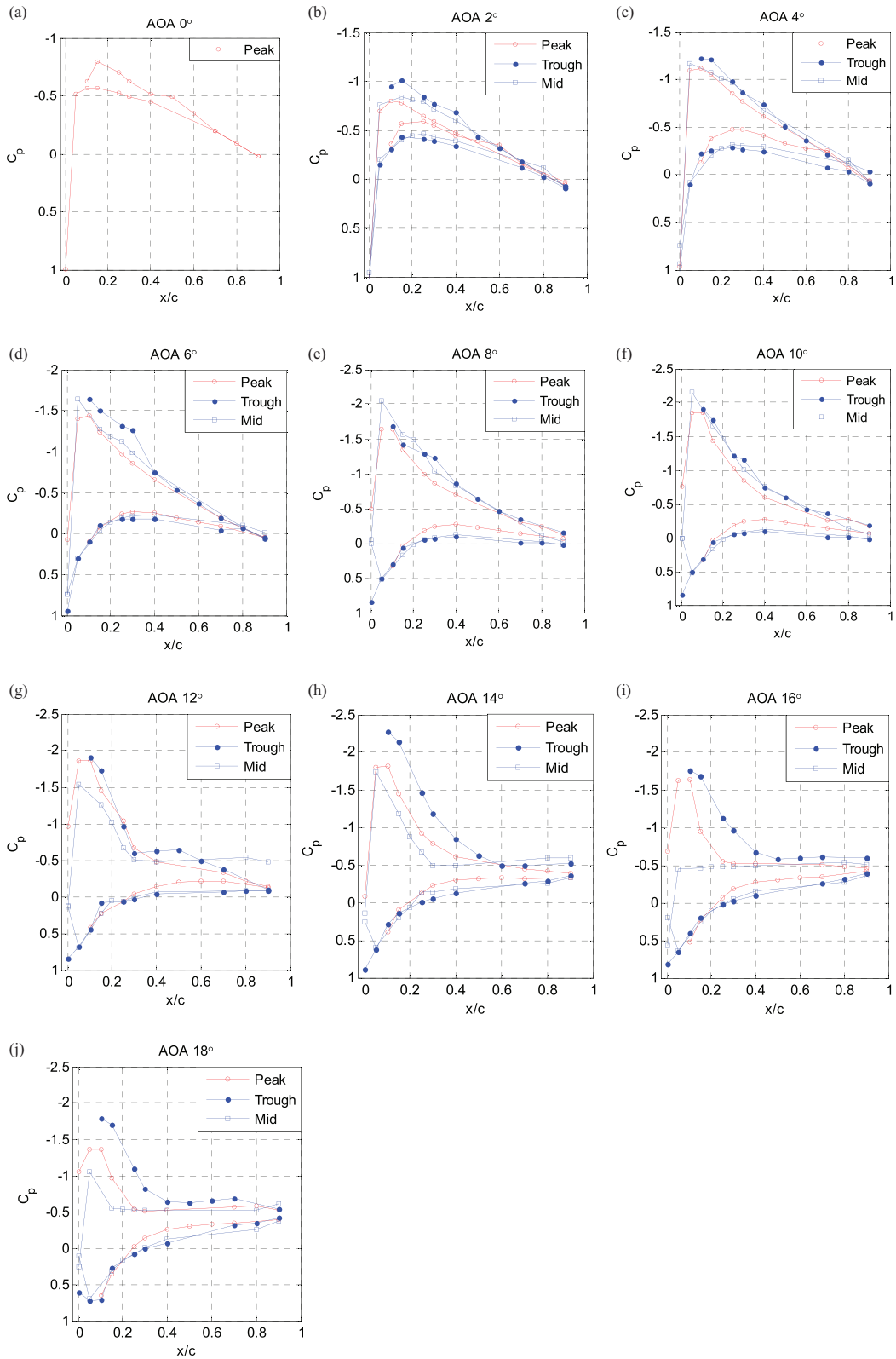


FIG. 12. Mean chordwise pressure distribution on a peak, trough, and mid cross-section at different attack angles ( $Re = 120\,000$ ).



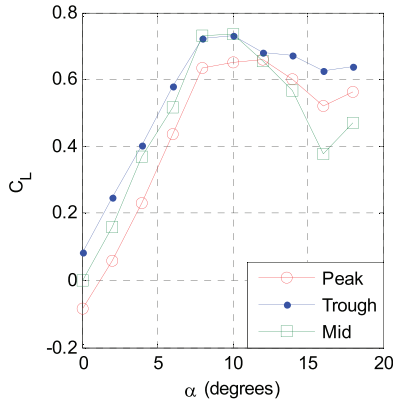


FIG. 13. Calculated sectional lift coefficient as a function of attack angle.

Figure 13 shows that both prior to and post stall, the trough produces more lift than the two other sections. Pre-stall the middle cross-section contributes to lift generation more than the peak; however, loss of lift is more prominent in this cross-section post-stall. Also noteworthy is that the total amount of lift on the wing section cannot be regarded as the average lift of the three sections as the flow structure is complex, and direct force measurement tests as reported in Secs. III A and III B are most reliable.

#### IV. COMPUTATIONAL FLUID DYNAMICS STUDY

Numerical simulation with the NACA 0021 profile has not been implemented extensively. Wolfe and Ochs<sup>23</sup> used CFD-ACE that solves the *Favre-Averaged-Navier-Stokes* equations using the Finite Volume method on a structured grid. The turbulence model used was  $k - \varepsilon$  and the Reynolds number reported in their study was 1 500 000. The other CFD study on the NACA 0021 airfoil that the authors are aware of, was carried out by Dhanasekaran and Govardhan<sup>7</sup> who simulated the flow over the blades of the Wells turbine with reasonable success.

In the present work, a complementary CFD investigation was performed using the commercial package ANSYS-CFX 12.1 suite<sup>1</sup> to model the unsteady flow over one wavelength of the wavy foil  $\theta 6.5w30$  with the NACA 0021 baseline profile at pre-stall incidence angles ( $0^\circ$ – $12^\circ$ ) at  $Re = 120\,000$ . The wavy foil  $\theta 6.5w30$  was chosen for the study as experimental data, in the form of surface pressure, were available for validation purposes. To capture the transitional nature of the flow, the newly formulated Shear Stress Transport  $\gamma - Re_\theta$ <sup>14</sup> model that has been successful in external aerodynamics<sup>5,14,15,19</sup> was employed. The continuity, momentum, intermittency (used to activate the onset of transition) and momentum-thickness Reynolds transport equations, along with the formulation of the Shear Stress Transport model can be found in are as follows:

$$\frac{\partial \rho}{\partial t} + \frac{\partial}{\partial x_j}(\rho U_j) = 0, \quad \frac{\partial}{\partial t}(\rho U_i) = -\frac{\partial}{\partial x_j}(\rho U_j U_i) - \frac{\partial \rho}{\partial x_i} + \frac{\partial}{\partial x_j}[\mu_{\text{eff}}(\frac{\partial U_i}{\partial x_j} + \frac{\partial U_j}{\partial x_i})], \quad i, j = 1, 2, 3, \quad (12)$$

$$\frac{\partial(\rho \gamma)}{\partial t} + \frac{\partial(\rho U_j \gamma)}{\partial x_j} = \tilde{P}_\gamma - E_\gamma + \frac{\partial}{\partial x_j}[(\mu + \frac{\mu_t}{\sigma_\gamma}) \frac{\partial \gamma}{\partial x_j}], \quad (13)$$

$$\frac{\partial(\rho \tilde{Re}_{\theta t})}{\partial t} + \frac{\partial(\rho U_j \tilde{Re}_{\theta t})}{\partial x_j} = P_{\theta t} + \frac{\partial}{\partial x_j}[\sigma_{\theta t}(\mu + \mu_t) \frac{\partial \tilde{Re}_{\theta t}}{\partial x_j}]. \quad (14)$$

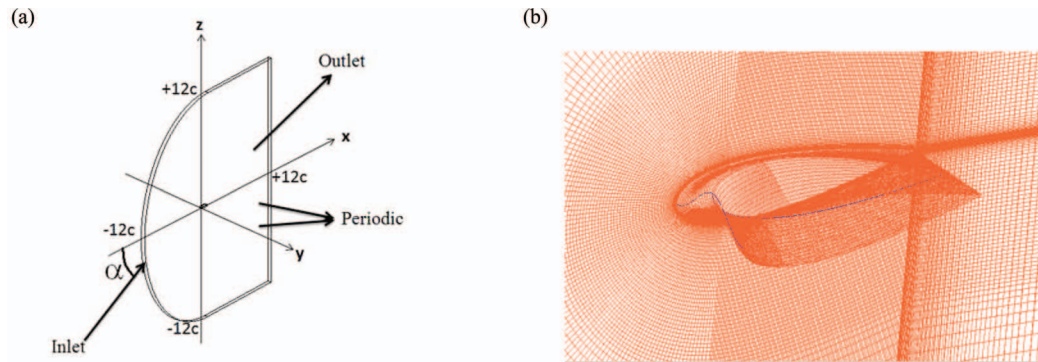


FIG. 14. The computational domain (a) and grid system near the foil (b).

The strain rate Reynolds numbers is defined as follows:

$$Re_v = \frac{\rho y^2 S}{\mu}. \quad (15)$$

Based on the maximum value of this number, the momentum-thickness Reynolds number is specified:

$$Re_\theta = \frac{\text{Max}(Re_\theta)}{2,193}. \quad (16)$$

The above equations are discretized and solved along with the equations for the Shear Stress Transport model whose formulation can be found in Ref. 14. ANSYS 12.1 implements a finite control volume-oriented finite element method to discretize the partial differential transport equations. A second-order backward Euler scheme was selected for temporal discretisation, while an alternating first and second-order accurate scheme was implemented for spatial discretisation.

A C-Grid topology (Figure 14) with hexahedral structured elements was constructed to designate the computational domain. The angle of attack was changed at the *Inlet* via the velocity components and *Periodic boundaries* were assigned to the side planes since one wavelength of the wing was modelled.

A grid resolution study was performed to establish a mesh-independent solution. Of the three generated grids, the one with a total number of nodes equal to  $3.5 \times 10^6$ , whose  $y^+$  values near the foil were maintained below 1, proved to be sufficient for grid independence. The effect of inlet turbulence levels on the onset of transition and aerodynamic loading behaviour has been noted in a previous study.<sup>5</sup> In the Shear Stress Transport turbulence model, the decay in turbulence intensity is dependent on the coarseness of the grid near the inlet region and the inverse of eddy viscosity.<sup>20</sup> Accordingly, to validate the appropriateness of the turbulence level, three cases were tested and compared with experimental findings at a  $0^\circ$  attack angle. The pressure coefficient was plotted for each case against the normalised chord location along a peak, while the friction coefficient plots were used to determine the location of the flow separation and re-attachment points (Figures 15 and 16).

The sensitivity of the solution to turbulence levels revealed that the case with the low turbulence level (1%) yielded results that are in better agreement with experimental findings (Table II). Therefore, the inlet turbulence level of (1%) was maintained for the rest of this work. It must be noted that experimental data for the friction coefficient were not available for comparison. Solution convergence of the eight transport equations was determined by achieving a maximum residual target of  $10^{-5}$  per time step. In addition, the lift and drag coefficients were used as monitor points during the solution process. The solution strategy comprised two different stages, a steady-state solution followed by a transient one. Initially, a steady-state run was performed and the behaviour of the residuals was monitored. It was observed that the residuals diminished steadily down to  $10^{-4}$  in the proximity of the seventieth iteration at which point a fluctuating pattern emerged. Subsequently, the steady-state solution was used as the initial condition for the transient solver. A time-step equal to

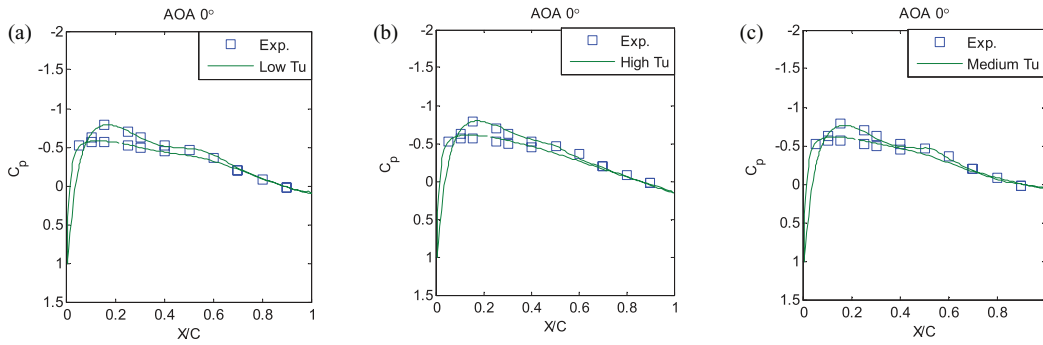


FIG. 15. Plots of pressure coefficient against normalised chordwise location for three levels of inlet turbulence compared with experimental data (peak cross-section).

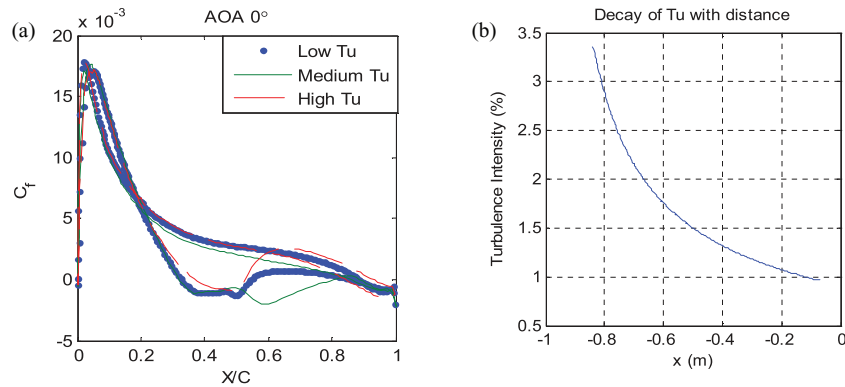


FIG. 16. Friction coefficient on the peak cross-section against normalised chordwise location for three levels of turbulence intensity (a) and the decay of turbulence intensity from inlet to the airfoil's leading-edge plotted for the low-turbulence intensity case (b).

TABLE II. Report of turbulence intensity sensitivity study.

Turbulence intensity (Tu) near the leading-edge of the wavy foil	x separation/c (peak)	x reattachment/c (peak)
Low (1%)	0.33	0.55
Medium (5%)	0.35	0.8
High (10%)	0.37	0.53

$5 \times 10^{-5}(s)$  with three inner loops was selected for the transient run. The results are presented for  $t = 0.01 (s)$  where the lift and drag forces stabilised.

## A. Validation results

Figure 17 shows that correspondence between the numerical solutions, from CFD modelling, with the data obtained from experiments is satisfactory. Discrepancies seem to appear at higher attack angles, suggesting that a higher-order turbulence model may prove more appropriate to capture flow behaviour post-stall. Nonetheless, the model has been successful in capturing transitional flow features including the laminar separation bubble as discussed in Sec. III E. In addition, the strong correspondence offers assurance that the flow physics are modelled correctly.

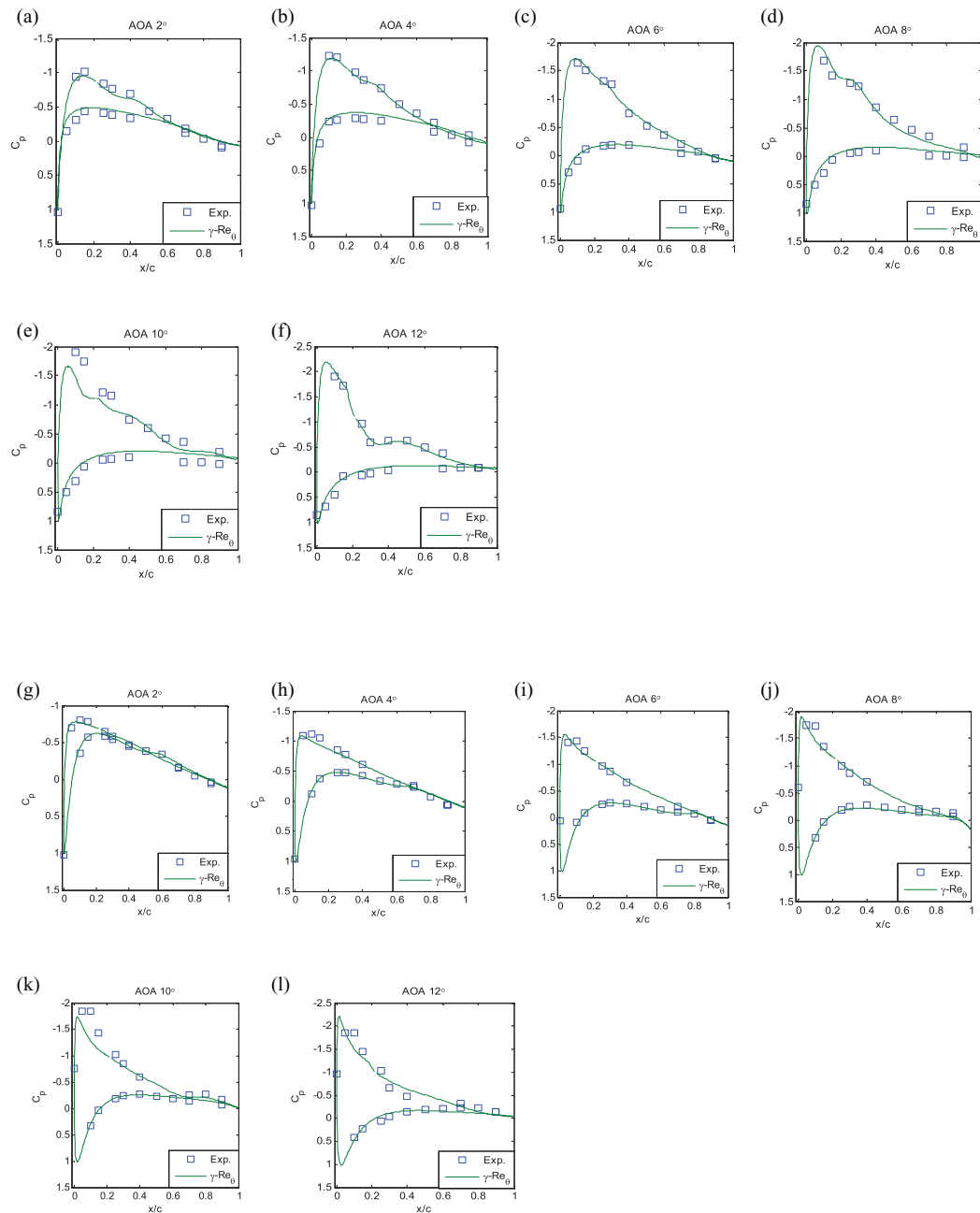


FIG. 17. Comparison of the experimental and numerical pressure coefficient on a trough cross-section (a)–(f) and comparison of the experimental and numerical pressure coefficient on a peak cross-section (g)–(l) ( $\theta 6.5w30$ ,  $Re = 120\,000$ ).

## B. Flow structure

Contours of streamwise vorticity have been plotted on planes oriented normal to the free-stream flow direction at four selected pre-stall attack angles (Figure 18). It is observed that a distinct pair of counter-rotating vortices is realised in the wake. Each vortex consists of smaller vortices, one originating from the upper and the other from the lower wing surface, imparting a slanted appearance to the pair. The magnitude of vorticity at the cores of the vortices decreases with distance from the trailing edge, suggesting a diffusion process as vorticity spreads outward from the cores. The pair appears to rotate towards each other, evolving to a near-parallel orientation as it convects

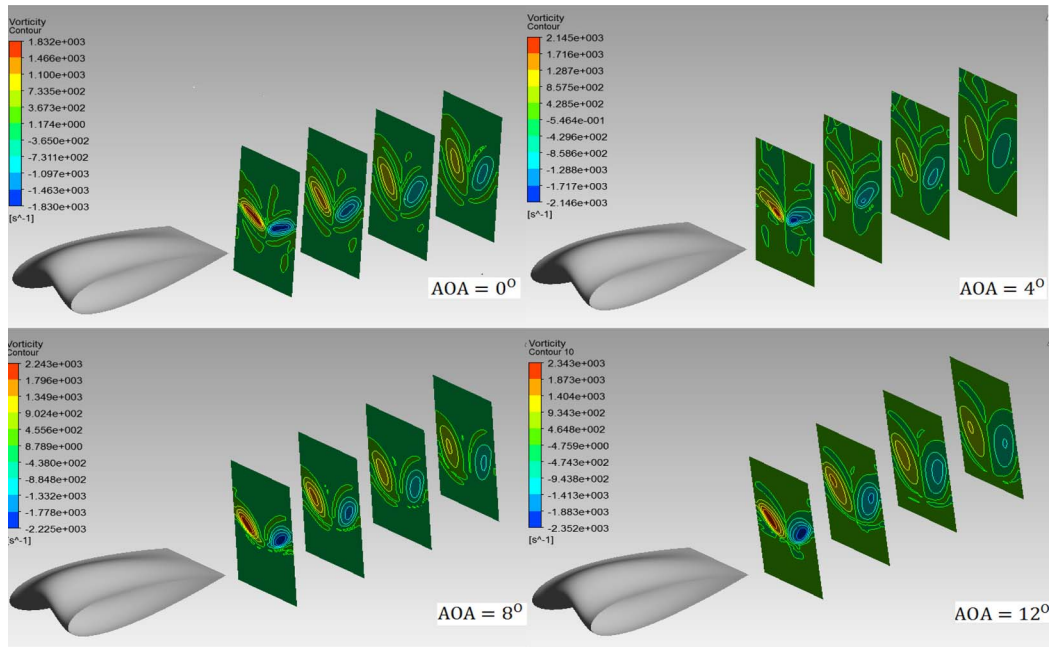


FIG. 18. Contours of streamwise vorticity on planes located at  $x = 30$  (mm),  $60$  (mm),  $90$  (mm), and  $120$  (mm) downstream of the trailing edge at  $0^\circ$ ,  $4^\circ$ ,  $8^\circ$ , and  $12^\circ$  incidence angles ( $\theta 6.5w30$ ,  $Re = 120\,000$ ).

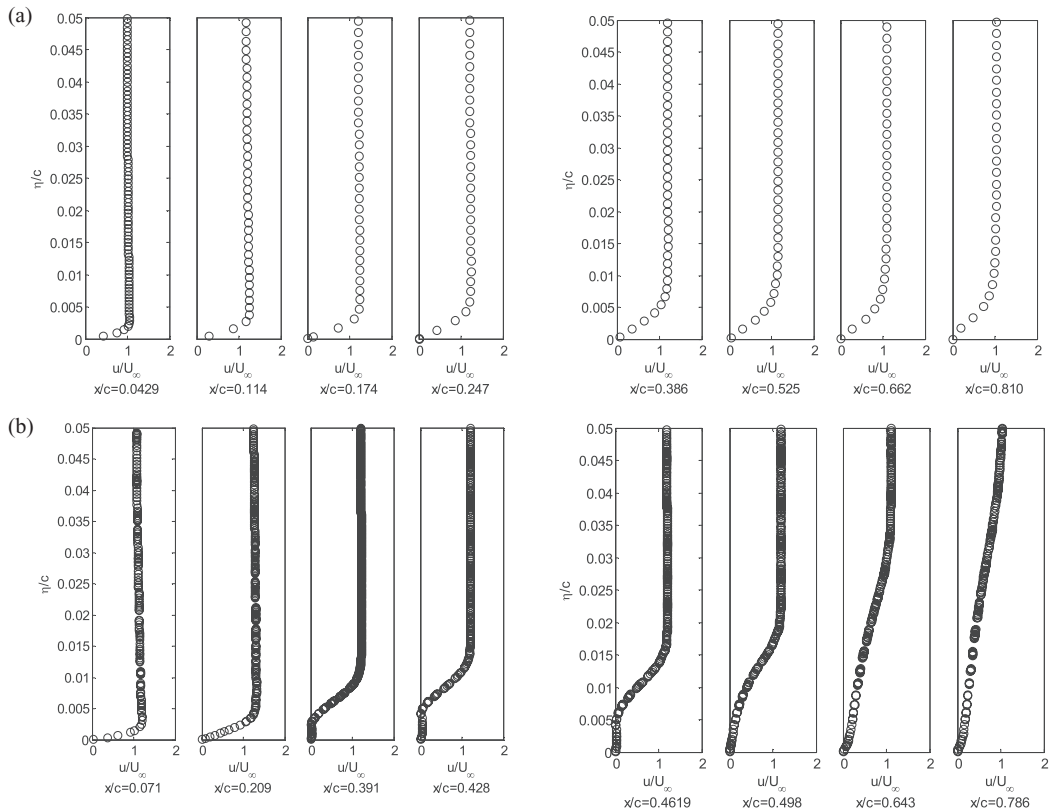


FIG. 19. Normalized magnitude of mean velocity in the normal to wall direction on a peak cross-section at various chordwise locations (a) and normalized magnitude of mean velocity in the normal to wall direction on a trough cross-section at various chordwise locations (b).

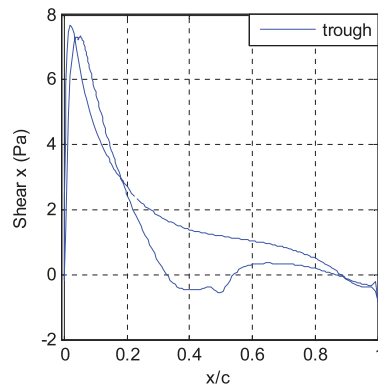


FIG. 20. Wall shear along a trough cross-section at  $\alpha = 0^\circ$ .

downstream. The presence of streamwise vortices confirms the prediction by Prandtl's lifting-line theory.

In order to analyse flow separation characteristics, absolute values of non-dimensionalized mean velocity have been plotted (Figure 19) in the wall-normal direction, ( $\eta$ ), on a peak and a trough of the wavy wing at a zero angle of attack on the suction side. The boundary layer development on the trough, unlike the peak, gives indications of separated flow as evidenced by the inflection point around  $x/c = 0.3$ . The wall shear stress coefficient on the trough cross-section (Figure 20), on the other hand, shows flow re-attachment further downstream as the sign of the shear stress changes. The separation, re-attachment phenomenon signifies the presence of a laminar separation bubble in this cross-section.

The occurrence of flow separation on the suction side of the trough can be explained by considering the contours of adverse pressure gradient as shown in Figure 21(b). It is observed that, compared to that of the peak, the gradient of static pressure is steeper in the trough, making it more susceptible to separation. The contours of limiting streamlines point to a pair of *foci* points (singularities) that leave footprints of the streamwise vortices. A plausible explanation for the more adverse pressure gradient on the trough may be the increase in the local attack angle brought about by the presence of streamwise vortices. Conversely, on the peak, the sense of rotation of the vortices is such that fluid is pushed towards the surface, reducing the local attack angle, thus inhibiting chordwise separation. Furthermore, the contour plot of static pressure (Figure 21(a)) on the wavy foil illustrates the low pressure regions (dark blue) in the trough section in the vicinity of the

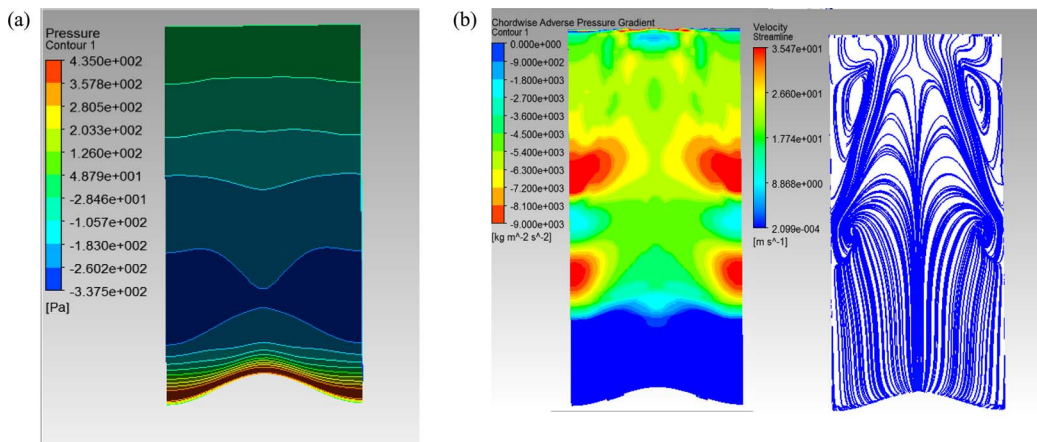


FIG. 21. Contours of static pressure on the upper side of the wavy foil at  $\alpha = 0^\circ$  (a) and contours of adverse pressure gradient and limiting streamlines at  $\alpha = 0^\circ$  on the upper surface of the wavy foil in the perspective view (b).

leading-edge which is consistent with the experimental findings in the current work. The primary flow features reported here were also observed for higher incidence angles in the pre-stall zone and have not been included for brevity.

## V. CONCLUSIONS

In spite of its simplified assumptions, Prandtl's nonlinear lifting-line theory succeeded in demonstrating that both the newly proposed design, referred to as the wavy configuration, and tubercles induce a fluctuating distribution of circulation along the span. This prediction implies that the wavy foils exhibit similar aerodynamic characteristics to those with tubercles. In addition, the pattern of circulation points to the presence of streamwise vortices in flows over wavy lifting surfaces. The results of wind tunnel tests on four wavy foils revealed that three of the wavy foils showed gradual stall, a prominent trait also observed in flows over tubercled wings. Amongst the examined models, the one with the highest peak-to-peak angular amplitude and smallest wavelength yielded the most favourable post-stall behaviour.

The present experimental work on a full-span wavy foil demonstrates that a low pressure region near the leading-edge prevents a sudden loss of lift. This flow feature is analogous to the low pressure zone in the trough of a tubercled foil. In addition, the CFD investigation pre-stall showed the presence of strong counter-rotating streamwise vortices in the wake of the wavy foil, pointing to another notable feature in the flow produced by wings with tubercles. In addition, the more adverse pressure gradient in the trough, compared to the peak, renders the trough prone to flow separation. Nevertheless, with regard to lift generation, the negative effect of separation is offset by the low pressure zone near the leading edge in the trough. In view of these findings, there is sufficient evidence to merit more attention to the proposed novel leading-edge modification, in particular post-stall.

- <sup>1</sup> ANSYS<sup>®</sup> Academic Research, Release 12.1, ANSYS<sup>®</sup> Inc., Pennsylvania, USA.
- <sup>2</sup> J. Anderson, *Fundamentals of Aerodynamics*, 4th ed. (McGraw-Hill International Higher Education, 2005).
- <sup>3</sup> J. B. Barlow, A. Pope, and W. H. Rae, *Low Speed Wind Tunnel Testing*, 3rd ed. (Wiley-Interscience, 1999).
- <sup>4</sup> J. Benyus, *Biomimicry: Innovation Inspired by Nature* (William Morrow and Company Inc., New York, NY, 1997).
- <sup>5</sup> J. N. N. Counsil and K. Goni Boulama, "Validating the URANS shear stress transport  $\gamma - \text{Re}\theta$  model for low-Reynolds-number external aerodynamics," *Int. J. Numer. Methods Fluids* **69**, 1411–1432 (2012).
- <sup>6</sup> D. Custodio, "The effect of humpback whale-like leading edge protuberances on hydrofoil performance," Ph.D. thesis, Worcester Polytechnic Institute, December 2007.
- <sup>7</sup> T. S. Dhanasekaran and M. Govardhanb "Computational analysis of performance and flow investigation on wells turbine for wave energy conversion," *Renewable energy* **30**, 2129–2147 (2005).
- <sup>8</sup> A. V. Dovgal, V. V. Kozlov, and A. Michakle, "Laminar boundary layer separation: Instability and associated phenomena," *Prog. Aerosp. Sci.* **30**, 61–94 (1994).
- <sup>9</sup> F. E. Fish and J. M. Battle, "Hydrodynamic design of the humpback whale flipper," *J. Morphol.* **225**, 51–60 (1995).
- <sup>10</sup> K. L. Hansen, "Effect of leading edge tubercles on airfoil performance," Ph.D. thesis, University of Adelaide, Adelaide, South Australia, Australia, 2012.
- <sup>11</sup> K. L. Hansen, R. M. Kelso, and B. B. Dally, "Performance variations of leading-edge tubercles for distinct airfoil profiles," *AIAA J. Aircr.* **49**, 185–194 (2011).
- <sup>12</sup> H. Johari, C. Henocho, D. Custodio, and A. Levshin, "Effects of leading edge protuberances on airfoil performance," *AIAA J.* **45**, 2634–2642 (2007).
- <sup>13</sup> C. M. Jurasz and V. P. Jurasz, "Feeding modes of the humpback whale, *Megaptera novaeangliae*, in Southeast Alaska," *Sci. Rep. Whales Res. Inst.* **31**, 69–83 (1979).
- <sup>14</sup> R. Langtry and F. Menter, "Correlation-based transition modeling for unstructured parallelized computational fluid dynamics codes," *AIAA J.* **47**, 2894–2906 (2009).
- <sup>15</sup> P. Malan, K. Suluksna, and E. Juntasaro, "Calibrating the  $\gamma - \text{Re}\theta$  transition model for commercial CFD," AIAA paper 2009–1142, 2009.
- <sup>16</sup> D. S. Miklosovic, M. M. Murray, and L. Howle, "Experimental evaluation of sinusoidal leading edges," *J. Aircr.* **44**, 1404–1407 (2007).
- <sup>17</sup> D. S. Miklosovic, M. M. Murray, L. E. Howle, and F. E. Fish, "Leading edge tubercles delay stall on humpback whale flippers," *Phys. Fluids* **16**(5), L39–L42 (2004).
- <sup>18</sup> H. T. C. Pedro and M. H. Kobayashi, "Numerical study of stall delay on humpback whale flippers," 46th AIAA Aerospace Sciences Meeting and Exhibit, AIAA paper 2008–0584, 7–10 January 2008.
- <sup>19</sup> N. Sorensen, "Airfoil computations using the  $\gamma - \text{Re}\theta$  model," Risø-R-1693 (Technical University of Denmark, 2009), Issue 0106–2840, p. 16.

- <sup>20</sup>P. R. Spalart and C. L. Rumsey, “Effective inflow conditions for turbulence models in aerodynamic calculations,” *AIAA J.* **45**, 2544–2553 (2007).
- <sup>21</sup>E. van Nierop, S. Alben, and M. P. Brenner, “How bumps on whale flippers delay stall: an aerodynamic model,” *Phys. Rev. Lett.* **100**, 054502 (2008).
- <sup>22</sup>D. Weihs, “Effects of swimming path curvature on the energetics of fish swimming,” *Fish Bull.* **79**, 171–176 (1981).
- <sup>23</sup>W. P. Wolfe and S. S. Ochs, “*Predicting aerodynamic characteristics of typical wind turbine airfoils using CFD*,” Report No. SAND96-2345, Sandia National Laboratories, Iowa, September 1997.



## Chapter 4

# Flow over Tubercled Foils in the Transitional Regime

As highlighted in Chapter 2, airfoils with tubercled leading edges were shown to achieve higher post-stall lift coefficients and lower maximum lift coefficients compared to the unmodified baseline foils, in the transitional flow regime. Previous studies suggested that streamwise vortices may account for the enhanced aerodynamic characteristics of a tubercled foil at high attack angles. Yet, the formation mechanism of the vortices and the role they play in the lift-generating behaviour of tubercled foils is not completely understood.

In an attempt to seek answers to the aforementioned questions computational methods in the form of numerical simulations were adopted. The current chapter presents the findings in the article, “The formation mechanism and impact of streamwise vortices on NACA 0021 airfoil's performance with undulating leading edge modification”, published in *Physics of Fluids*.

The formation mechanism and the role of vortices in the flow over three tubercled foils in the transitional regime, were explored using the computational fluid dynamics model known as the "transitional Shear Stress Transport model". Validation of the model was performed against the experimental pressure distribution data reported by Hansen [1]. The in-depth examination of the limiting shear stress and the vorticity field, provided sufficient evidence to establish a conclusion on the formation mechanism of the counter-rotating vortices. Two alternate perspectives were thus put forth to elucidate how a tubercled leading-edge gives rise to the development of two types of streamwise vortices.

Probing into the flow field provided an insight into how vortices induce a momentum transfer effect whereby the fluid is transported from the separated flow regions into neighbouring areas where the boundary layer is attached. A number of findings reported here are in agreement with those presented

by Skillen *et al.* [2, 3] as well as the predictions proposed by van Nierop *et al.* [4] in their theoretical analysis.

- [1] K. L. Hansen, "Effect of Leading Edge Tubercles on Airfoil Performance," Doctor of Philosophy Thesis, Mechanical Engineering, University of Adelaide, Adelaide, SA, Australia, 2012.
- [2] A. Skillen, A. Revell, J. Favier, A. Pinelli, and U. Piomelli, "LES Study into the Flow Physics of an Undulating Leading-Edged Wing," presented at the ERCOFTAC international symposium Unsteady separation in fluid-structure interaction, Mykonos, Greece, 2013.
- [3] A. Skillen, A. Revell, A. Pinelli, U. Piomelli, and J. Favier, "Flow over a Wing with Leading-Edge Undulations," *AIAA Journal*, pp. 1-9, 2014.
- [4] E. van Nierop, S. Alben, and M. P. Brenner, "How Bumps on Whale Flippers Delay Stall: an Aerodynamic Model," *Physical review letters*, vol. 100(5): 054502, 7 February 2008.

## Statement of Authorship

Title of Paper	The formation mechanism and impact of streamwise vortices on NACA 0021 airfoil's performance with undulating leading edge modification		
Publication Status	<input checked="" type="checkbox"/> Published	<input type="checkbox"/> Accepted for Publication	
	<input type="checkbox"/> Submitted for Publication	<input type="checkbox"/> Publication Style	
Publication Details	Citation: Physics of Fluids <b>26</b> , 107101 (2014); doi: 10.1063/1.4896748		

Name of Principal Author (Candidate)	Nikan Rostanzadeh		
Contribution to the Paper	Responsible for performing the literature review, numerical simulations, interpretation of the results. Identified the flow mechanism and elucidated how streamwise and transverse vorticity arises due the presence of an undulating leading edge. Provided an explanation for lower pre-stall lift for tubercled foils. Planned and drafted the manuscript. Assumed primary responsibility for responding to the reviewers.		
Signature		Date	28/11/2015

## Co-Author Contributions

By signing the Statement of Authorship, each author certifies that:

- i. the candidate's stated contribution to the publication is accurate (as detailed above);
  - ii. permission is granted for the candidate to include the publication in the thesis; and
- the sum of all co-author contributions is equal to 100% less the candidate's stated contribution

Name of Co-Author	Dr. Kristy Lee Hansen		
Contribution to the Paper	Designed the tubercled airfoil with assistance from Associate Professor Richard M. Kelso. Conducted wind tunnel tests in the form of surface pressure measurements. Analysed the pressure distribution curves. Assisted with editing the manuscript.		
Signature		Date	20/11/2015

Name of Co-Author	Associate Professor Richard M. Kelso		
Contribution to the Paper	Supervised the work. Assisted with the interpretation of the surface flow field by examining the limiting streamlines and the vortex lines. Assisted with the description of the flow mechanism. Helped with the editing process of the manuscript.		
Signature		Date	23/11/2015

Name of Co-Author	Professor Bassam B. Dally		
Contribution to the Paper	Supervised the work. Critically analysed the description of the flow mechanism. Assisted with the editing of the manuscript.		
Signature		Date	23/11/2015



## The formation mechanism and impact of streamwise vortices on NACA 0021 airfoil's performance with undulating leading edge modification

N. Rostamzadeh, K. L. Hansen, R. M. Kelso, and B. B. Dally

Citation: *Physics of Fluids* **26**, 107101 (2014); doi: 10.1063/1.4896748

View online: <http://dx.doi.org/10.1063/1.4896748>

View Table of Contents: <http://scitation.aip.org/content/aip/journal/pof2/26/10?ver=pdfcov>

Published by the [AIP Publishing](#)

---

### Articles you may be interested in

[A direct numerical simulation investigation of the synthetic jet frequency effects on separation control of low-Re flow past an airfoil](#)

*Phys. Fluids* **27**, 055101 (2015); 10.1063/1.4919599

[Turbulent intensity and Reynolds number effects on an airfoil at low Reynolds numbers](#)

*Phys. Fluids* **26**, 115107 (2014); 10.1063/1.4901969

[The effect of undulating leading-edge modifications on NACA 0021 airfoil characteristics](#)

*Phys. Fluids* **25**, 117101 (2013); 10.1063/1.4828703

[Study of mechanisms and factors that influence the formation of vortical wake of a heaving airfoil](#)


*Phys. Fluids* **24**, 103601 (2012); 10.1063/1.4760258

[Flow dynamics past a simplified wing body junction](#)


*Phys. Fluids* **22**, 115111 (2010); 10.1063/1.3500697

---

Did your publisher get  
**18 MILLION DOWNLOADS** in 2014?  
AIP Publishing did.



**THERE'S POWER IN NUMBERS.** Reach the world with AIP Publishing.



## The formation mechanism and impact of streamwise vortices on NACA 0021 airfoil's performance with undulating leading edge modification

N. Rostamzadeh, K. L. Hansen, R. M. Kelso, and B. B. Dally  
*School of Mechanical Engineering, The University of Adelaide, Adelaide,  
 SA 5005, Australia*

(Received 18 March 2014; accepted 15 September 2014; published online 6 October 2014)

Wings with tubercles have been shown to display advantageous loading behavior at high attack angles compared to their unmodified counterparts. In an earlier study by the authors, it was shown that an undulating leading-edge configuration, including but not limited to a tubercled model, induces a cyclic variation in circulation along the span that gives rise to the formation of counter-rotating streamwise vortices. While the aerodynamic benefits of full-span tubercled wings have been associated with the presence of such vortices, their formation mechanism and influence on wing performance are still in question. In the present work, experimental and numerical tests were conducted to further investigate the effect of tubercles on the flow structure over full-span modified wings based on the NACA 0021 profile, in the transitional flow regime. It is found that a skew-induced mechanism accounts for the formation of streamwise vortices whose development is accompanied by flow separation in delta-shaped regions near the trailing edge. The presence of vortices is detrimental to the performance of full-span wings pre-stall, however renders benefits post-stall as demonstrated by wind tunnel pressure measurement tests. Finally, primary and secondary vortices are identified post-stall that produce an enhanced momentum transfer effect that reduces flow separation, thus increasing the generated amount of lift. © 2014 AIP Publishing LLC. [<http://dx.doi.org/10.1063/1.4896748>]

### I. INTRODUCTION

In contrast to active flow control, passive flow control methods to augment the aero/hydrodynamic performance of lifting bodies are of considerable interest due to their ease of manufacture, maintenance, and economic viability, as they primarily rely on stationary components. One intriguing example of a passive flow control model with potential advantages in industrial applications, has been inspired by the undulating protuberances (tubercles) observed on the leading edges of the humpback whale's pectoral flippers.

Fish and Battle<sup>1</sup> were the first to postulate that tubercles contribute to the agility of the humpback in executing rolls and loops<sup>2</sup> by their lift-generating characteristics, in particular at high attack angles. To assess their conjecture, Watts and Fish<sup>3</sup> used an inviscid panel-based numerical flow solver to compare the performance of a tubercled wing at a 10° incidence angle against an unmodified one. The results demonstrated that the tubercled wing yielded a 4.8% increase in lift and a 10.9% reduction in induced drag, pointing to the potential benefits of the modification of wings with tubercles. Subsequently, Miklosovic *et al.*,<sup>4</sup> in a series of wind tunnel tests, showed that a flipper model with tubercles delayed the stall angle by 40% compared to a model flipper with a smooth leading-edge. The increase in the lift coefficient was accompanied by a decrease in drag at mean chord-based Reynolds numbers between 505 000 and 520 000.

In contrast to the previous findings associated with flipper models, Hansen *et al.*<sup>5</sup> found that the pre-stall behavior of modified full-span airfoils was inferior in comparison with that of the baseline NACA 0021 foil. Under conditions of post-stall, however, the modified wings generated more lift

than the unmodified foil. Similar trends were also reported by Johari *et al.*<sup>6</sup> and Miklosovic *et al.*<sup>7</sup> at Reynolds numbers equal to 183 000 and 274 000–277 000, respectively. Furthermore, Hansen *et al.*<sup>5</sup> suggested that reducing the wavelength and amplitude of the tubercles (up to a point), enhances aerodynamic performance by extending the stall angle, in addition to achieving higher values of the lift coefficient post-stall compared to the airfoil with the smooth leading-edge.

To explore the flow mechanism activated by the presence of tubercles, a number of studies have provided valuable insight. Pedro and Kobayashi<sup>8</sup> employed Computational Fluid Dynamics (CFD) to investigate the flow structure around the flipper model adopted in the experimental work by Miklosovic *et al.*<sup>4</sup> They discovered that the flow over the tubercled wing exhibited regions of high streamwise vorticity that energized the boundary layer, and consequently, inhibited flow separation. Thus, it was speculated that the advantageous aero/hydro-dynamic traits of tubercled flippers may be attributed to streamwise vorticity.

In a theoretically based approach, van Nierop *et al.*<sup>9</sup> analyzed the flow around a flipper model using the lifting-line theory developed by Prandtl and Tietjense.<sup>10</sup> The analysis predicted the occurrence of low pressure regions in the troughs (chord minima) of the tubercled wing, and the susceptibility of the trough region to flow separation due to locally large adverse pressure gradients. The numerical scheme, nonetheless, did not capture the higher maximum lift coefficient reported previously for the modified flipper model compared to the unmodified wing by Miklosovic *et al.*<sup>4</sup>

Rostamzadeh *et al.*<sup>11</sup> adopted Prandtl's nonlinear lifting line theory<sup>12</sup> to examine the effect of leading-edge undulations on spanwise circulation. It was concluded that tubercles vary the circulation of the wing's bound vortex, along the span, in an undulating manner, a phenomenon that accounts for the formation of streamwise vortices. Therefore, it was argued that other forms of leading-edge modifications can be devised to exhibit similar loading behaviour to tubercles. The *wavy wing*, wherein the geometric attack angle varies sinusoidally along the span, was introduced as an alternative to tubercles. Wind tunnel tests at a Reynolds number of 120 000, on several full-span wavy wings proved that wavy wings, in a similar manner to tubercled wings, extend the stall angle and yield higher post-stall lift.

While competing theories have attempted to elucidate the flow dynamics associated with tubercle-modified lifting bodies, the formation mechanism of streamwise vortices and their role in the wings' lift generating capabilities remain to be fully explored. In the present work, experimental and numerical tests were conducted to cast light on the formation mechanism of streamwise vortices and their impact on the surface pressure distribution. To this end, wind tunnel pressure measurements were performed on a full-span unmodified and a tubercled airfoil at a Reynolds number equal to 120 000. Furthermore, a Reynolds Averaged Navier Stokes-based CFD model was employed to assist with a detailed investigation into the surface flow topology and vorticity fields that leave clues to the underlying flow dynamics at play. Numerical modelling was performed by the newly proposed transitional model known as the Shear Stress Transport  $\gamma - Re_\theta$ <sup>13</sup> on three full-span modified wings with varying wavelength and amplitude as well as the NACA 0021 baseline airfoil at several attack angles.

## II. AIRFOIL MODELS

The leading edge of the tubercled airfoil used in the pressure measurement tests was designed based on a sinusoidal curve with an amplitude of 8(mm) and a wavelength of 30(mm) (labelled A8W30). Both the unmodified and tubercled airfoils, as illustrated in Figure 1, had the NACA 0021

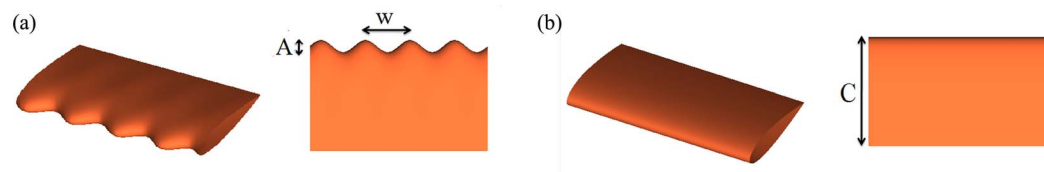


FIG. 1. (a) Tubercled airfoil based on the NACA 0021 profile, denoting wavelength  $W$ (mm) and amplitude  $A$ (mm). (b) Unmodified NACA 0021 airfoil.  $C$ (mm) denotes chord.

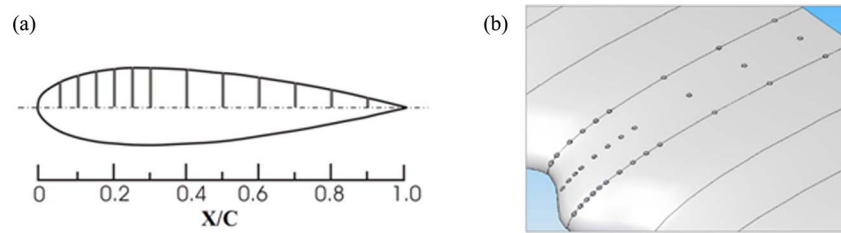


FIG. 2. (a) The locations of the 12 pressure tapings on the unmodified airfoil. (b) Pressure tapping representation for A8W30 on three spanwise rows, namely, the peak, the middle, and the trough cross-sections.

as the cross-sectional profile since it closely matches that of the humpback whale.<sup>4</sup> The span and mean chord of the airfoils were equal to 495 (mm) and 70(mm), respectively.

### III. EXPERIMENTAL SETUP

The low-speed KC Wind Tunnel, at the University of Adelaide, was utilized to carry out the pressure measurement tests on full-span wings. The test section of the wind tunnel has a square cross-section of 0.5(m)  $\times$  0.5(m). A gap size of 0.003(m) was chosen between the free ends of the airfoils and the ceiling of the test section to allow convenient mounting and rotation of the models. This gap size is within the suggested maximum range (0.005  $\times$  span) to minimize three-dimensional effects, according to Barlow *et al.*<sup>14</sup> The test subjects were mounted on a Vertex rotary table to allow for precise and repeatable measurements of the attack angle. A free-stream flow speed of 25(m/s) was maintained in the tunnel's test section where a maximum blockage ratio of 6% occurs with the airfoils oriented at an angle of attack (AOA) equal to 25°. The free-stream flow speed was measured via a Pitot-static tube connected to a 10-Torr MKS Baratron pressure transducer (full scale resolution 0.01%) equipped with a signal conditioner. Ahead of the test subjects, turbulence intensity was evaluated at 0.8% by a hot-wire probe. The flow Reynolds number based on the mean chord was 120 000. It must be noted that direct force measurement tests were previously performed on the same airfoils by Hansen *et al.*<sup>5</sup> at the same Reynolds number.

Pressure tapings were incorporated into the suction surfaces of the unmodified and tubercled foil (Figure 2). To evaluate the pressure distribution on the tubercled airfoil, a total number of 36 pressure tapings were distributed at three spanwise locations, namely, the peak, the trough, and the middle cross-sections. A stepper-motor-driven Scanivalve multiplexer was used to scan the airfoils' surface pressure. The differential pressure between the free stream static pressure and the airfoils' surface pressure was then measured by the transducer. Voltage output data from the transducer was collected via a National Instruments USB 6009 data logger. Data collection sampling time for each pressure port was 30(s) and the sampling rate was maintained at 1(KHz). A time delay of 5(s) between two consecutive sampling periods was incorporated to allow for the surface pressure to stabilize at each location. To evaluate, the pressure distribution on the lower sides, the airfoils were positioned at negative angles of attack.

### IV. SURFACE PRESSURE DISTRIBUTION

Figure 3 displays the time-averaged pressure coefficients plotted versus normalized chordwise positions along three spanwise locations. The tubercled wing is compared to the unmodified NACA 0021 for selected angles of attack prior to and post stall at a Reynolds number equal to 120 000. A comprehensive error analysis on the reported results can be found in Ref. 15.

Observing the pressure coefficient plots in Figure 3, it becomes clear that tubercles remarkably alter the surface pressure distribution in comparison with the baseline foil. Under pre-stall conditions, the trough cross-section assumes the largest suction peak values, compared to the peak and middle cross-sections as the pressure coefficient is most negative, especially near the

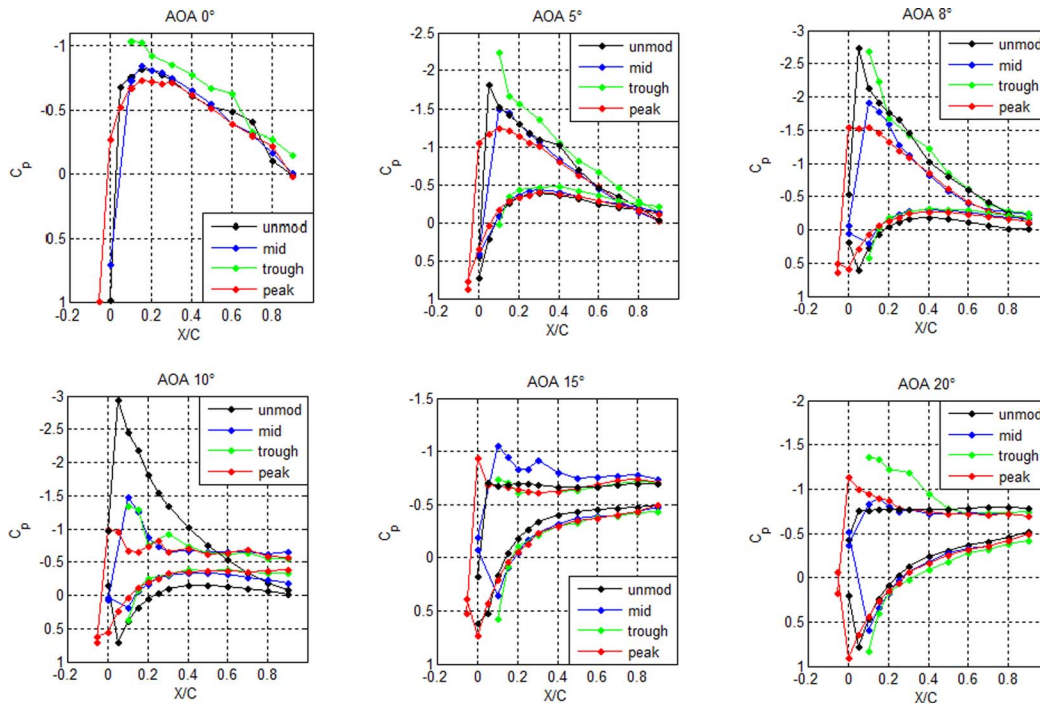


FIG. 3. Measured pressure coefficients versus the normalized chordwise position for the tubercled foil at three spanwise locations, i.e., the middle (mid), trough, and peak and the unmodified foil NACA 0021 (unmod) ( $Re = 120\,000$ ).

leading-edge. The observation that the trough is the lowest pressure region was predicted earlier by van Nierop *et al.*<sup>9</sup> and Weber *et al.*<sup>16</sup> A notable flow feature, as evidenced by the relatively low chordwise pressure gradients (as an example, see Figure 3(a) where  $0.5 \leq X/C \leq 0.6$ ), is the apparent presence of a laminar separation bubble (LSB) on the suction side of the trough. Even though the evidence of the LSB is not substantial, the satisfactory correspondence between the experimental and CFD results, reported in this work, suggest that the presence of the LSB is plausible. Hence, the LSB could have been captured with higher resolution using an increased number of pressure tappings. Similarly, the pressure distribution plots suggest that the flow on the baseline foil undergoes separation and re-attachment, manifesting as the appearance of a laminar separation bubble. Beyond  $AOA = 8^\circ$ , the effect of flow unsteadiness becomes more pronounced. At  $AOA = 10^\circ$ , the unmodified foil produces lower values of pressure on the suction side than any other cross-section of the tubercled foil, suggesting that the lift generated by the baseline foil is higher than the modified wing prior to stall. This observation is in agreement with the study by Hansen *et al.*<sup>5</sup>

At  $AOA = 15^\circ$ , the baseline foil has clearly undergone a significant loss of lift as its pressure coefficient curve is nearly flat along the chord. Even though most thick airfoils experience gradual stall with the increase in the angle of attack,<sup>12</sup> a *bursting* of the observed separation bubble can also occur and lead to an abrupt loss of lift.<sup>17</sup> As the attack angle increases, the bubble is forced to move towards the leading edge. With the rise in the adverse pressure gradient the re-attachment point disappears and stall is initiated near the leading-edge.<sup>18</sup> This phenomenon appears to take place for the baseline NACA 0021 foil at  $Re = 120\,000$ . The foil with tubercles, on the contrary, does not experience a dramatic loss of lift since the three main cross-sections contribute to lift generation at higher angles of attack, low values of the pressure coefficient in the trough, in particular, bear witness to this conclusion. In spite of the observation that, on the pressure side, the peak's contribution to lift seems more favourable than the trough, the effect of tubercles appears to be more pronounced on the trough cross-section as the pressure distribution in this region considerably differs from that of the unmodified foil.



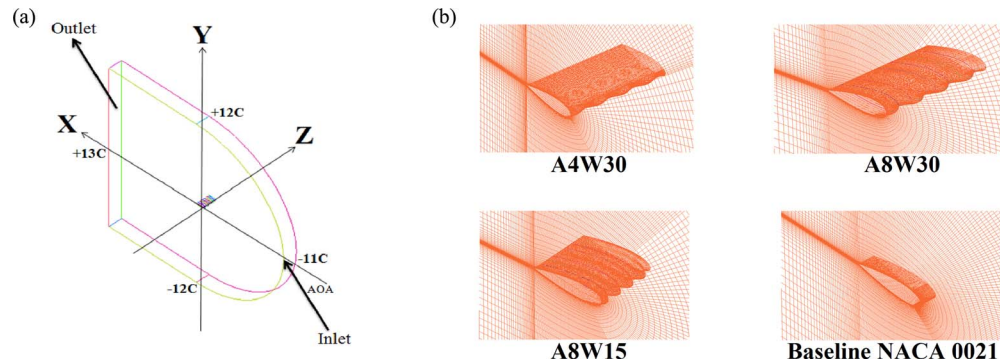


FIG. 4. (a) The computational domain and the coordinate system positioned at the leading-edge. The origin of the Z axis is placed on the middle cross-section. (b) Grid system in the vicinity of the airfoils.

## V. COMPUTATIONAL FLUID DYNAMICS MODEL

The flow over three tubercled wings (A8W30, A4W30, A8W15) and the baseline airfoil (NACA 0021) was modelled in ANSYS CFX 12.1<sup>19</sup> by solving the discretized Reynolds Averaged Navier-Stokes equations. The Shear Stress Transport (SST) transitional model, known as the  $\gamma - Re_{\theta}$ ,<sup>13</sup> was selected for this purpose as transitional flow features such as laminar separation bubbles were expected to develop at  $Re = 120\,000$ , and fully turbulent RANS models are often incapable of resolving them.<sup>20</sup> The computationally efficient SST transitional model is especially suitable for flow scenarios where separation-induced transition is likely to occur. The model operates independently of non-local parameters, and is therefore desirable for transitional flows that are complex.<sup>21</sup>

The computational domain, shown in Figure 4, was constructed based on a C-grid topology with far-field boundaries located at 12 chord lengths from the airfoil's trailing-edge in the streamwise (X) and transverse (Y) directions. Lateral planes, in the Z direction, with Periodic boundary conditions, were positioned at a distance equal to four wavelengths of the tubercled foils. The choice of modelling four wavelengths was based on a sensitivity analysis study that proved smaller spanwise domain sizes were insufficient for post-stall modelling as more complex flow pattern emerge at higher attack angles.

To discretize the transport equations for the SST transitional model,<sup>22</sup> ANSYS CFX adopts a fully conservative Finite Volume-based Finite Element approach. A high resolution scheme was applied for spatial discretization, and an implicit second-order backward Euler scheme was selected for temporal discretization. Additional transport equations for the SST model along with the detailed definitions of all the equation terms can be found in Ref. 22.

## VI. SOLUTION SENSITIVITY ANALYSES

In order to arrive at mesh-independent solutions, three successively refined grid sizes were tested for each wing under the same boundary conditions with the refinement ratio,  $r \simeq \sqrt{2}$ . This refinement ratio was shown by Council and Boulama<sup>21</sup> to be reasonable for mesh sensitivity analysis in the transitional flow regime, using the  $\gamma - Re_{\theta}$  turbulence model. The adequacy of each grid was assessed by their impact on the computed aerodynamic forces, as well as the flow structure. In addition, the Convergence Grid Indices ratio of the tested grids were computed according to the recommendations of Roache.<sup>23</sup> A moderately conservative safety factor of 1.25 was applied to all calculations. Herein, the results of the mesh sensitivity analysis are presented for the cases at  $AOA = 8^\circ$ , where flow separation was expected to occur.

Table I shows the values of the aerodynamic lift and drag coefficient as obtained in the solutions computed using a relatively coarse grid (G1), a fine grid (G2), and a further-refined grid (G3). A comparison of the lift and drag coefficients achieved by grids label G3 and G2 demonstrated that, for the tubercled foils, the further-refined grid (G3) did not yield significant changes in the generated values of lift and drag. Furthermore, no discrepancies in the flow fields computed using these two

TABLE I. Grid sensitivity analysis. All grids yielded  $y^+$  values below one ( $Re = 120\,000$ ,  $AOA = 8^\circ$ ).

Airfoil label	Span (mm)	Chord (mm)	Total elements	Lift coefficient	Drag coefficient	$(\frac{CG1_{32}}{CG1_{21}^{RP}})_{C_L}$	$(\frac{CG1_{32}}{CG1_{21}^{RP}})_{C_D}$
A8W30	120	70	G1:1979316	0.685	0.045	0.97	1.15
			G2:2859012	0.707	0.039		
			G3:4031940	0.704	0.039		
A4W30	120	70	G1:1924335	0.787	0.033	0.99	1.03
			G2:2769165	0.791	0.032		
			G3:3895605	0.792	0.032		
A8W15	60	70	G1:1883294	0.659	0.043	0.97	1.05
			G2:2710106	0.674	0.041		
			G3:3812522	0.674	0.040		
Unmodified NACA 0021	15	70	G1:648150	0.849	0.034	0.99	1.05
			G2:907410	0.850	0.032		
			G3:1296300	0.850	0.032		

grids were noticeable. In light of these observations, G2 was adopted for the rest of this study. Note, however, that the effect of the coarse grid (G1) on flow separation, compared to that of the finer grids (G2 and G3) was not negligible, and is illustrated, as an example, for A8W30 in Figure 5(a). The separation zone as computed by G1 is comparatively larger than that by G2 and G3. This is also reflected in the friction coefficient plot along the trough cross-section of the foil, whereby the friction coefficient values computed by the coarse grid, G1, are larger in magnitude over a longer section of the foil than those predicted by the finer grids, G2 and G3 (Figure 5(b)).

As for the baseline NACA 0021 airfoil, due to the absence of three-dimensional effects, the differences in the respective computed values of the lift and drag coefficients achieved by the three grids were small. While G2 and G3 yielded the same amount of lift and drag, G3 required more computational time and resources. Hence, G2 was selected for the remainder of this work.

A timestep size analysis was carried out based on three timestep sizes:  $T1 = 10^{-5}$  (s),  $T2 = 5 \times 10^{-5}$  (s),  $T3 = 10^{-4}$  (s) at  $AOA = 8^\circ$ . The lift and drag coefficients were monitored over the same time periods for each case. Whereas  $T1$  and  $T2$  would require a considerably longer machine processing time,  $T3$  proved most efficient as the differences between the lift force coefficient achieved by  $T1$ ,  $T2$ , and  $T3$  were on the order of  $10^{-3}$ . Hence,  $T3$  was adopted for the rest of the study.

In Figure 6 the convergence history of the lift coefficient at a  $15^\circ$  angle of attack for all tubercled foils is shown. Periodic values with small amplitudes (standard deviation  $\simeq 0.0033$ ) emerge around  $t = 0.03$ (s). Further computation with arbitrary simulation time periods beyond  $t = 0.03$ (s) did not alter the behavior of the force monitor points significantly. A numerical study with longer modelling time

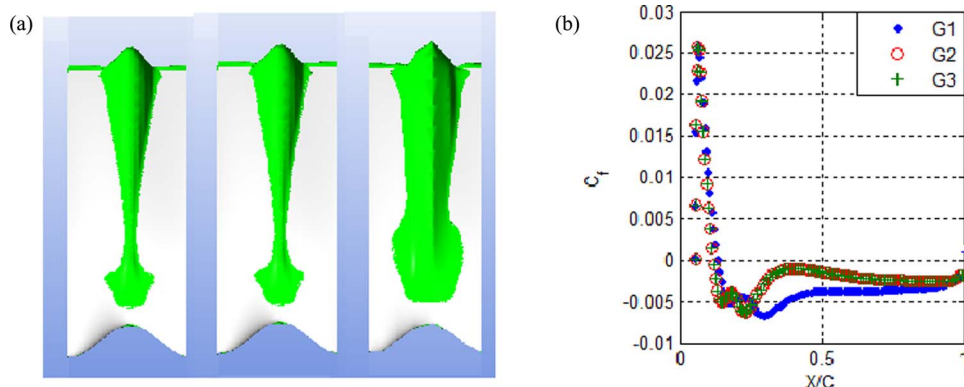


FIG. 5. (a) Separated flow regions (in green) obtained by G1 (left), G2 (middle), and G3 (right). (b) Friction coefficient obtained by G1, G2, and G3 plotted for the trough's suction side (A8W30,  $Re = 120\,000$ ,  $AOA = 8^\circ$ ).

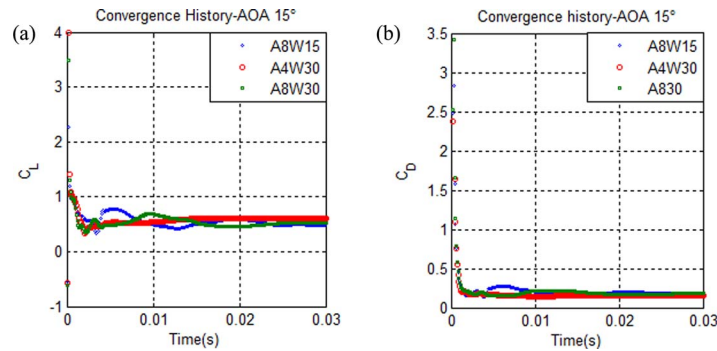


FIG. 6. Convergence history of the lift (a) and drag (b) coefficients for the tubercled wings ( $Re = 120\,000$ ,  $AOA = 15^\circ$ ).

periods would assist with the study of transient parameters such as the vortex shedding frequency and the evolution of the separation bubbles. Nonetheless, it is worth emphasizing that the fundamental flow mechanism explored in the present work, occurred consistently for the tubercled models and was not a time-dependent phenomenon.

The most influential parameter impacting the surface pressure distribution, with the exception of  $y^+$ , was turbulence levels near the leading-edge region. Inappropriate turbulence levels near the airfoil may lead to the dissipation or bursting of the laminar separation bubble<sup>24</sup> that would consequently affect the surface pressure distribution.

Figure 7 compares the pressure distribution on the peak of the tubercled wing A8W30 with three different approximate levels of turbulence intensity around the leading edge (High Tu = 10%, Mid Tu = 5%, Low Tu = 1%). It is evident that the only turbulence level condition that was successful in capturing the pressure gradient around  $X/C = 0.8$  corresponds with the low turbulence intensity case, and hence this turbulence intensity was adopted for the rest of the study. It must be noted that this turbulence level nearly matches the one measured in the wind tunnel's test section.

## VII. VALIDATION RESULTS

Pressure coefficient values obtained in our experimental work for the airfoil A8W30 have been used to validate the results from the transitional SST  $\gamma - Re_\theta$  model at various attack angles. Overall correspondence between experimental and computational data is satisfactory. The pressure distribution is, however, captured with higher accuracy on the peak chord-wise locations compared to the trough. Flow unsteadiness, as pointed out in Sec. IV, influences the distribution of pressure which is most noticeable post-stall. The largest discrepancies were observed to occur at an incidence angle of  $10^\circ$ , and have not been included here. Despite its limitations, the  $\gamma - Re_\theta$  transitional

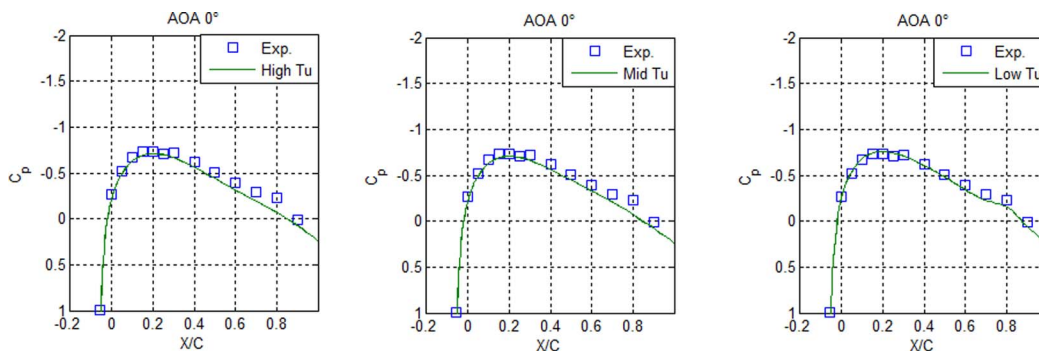


FIG. 7. The effect of turbulence intensity levels on the pressure distribution for a tubercle peak on A8W30 ( $Re = 120\,000$ ,  $AOA = 0^\circ$ ).

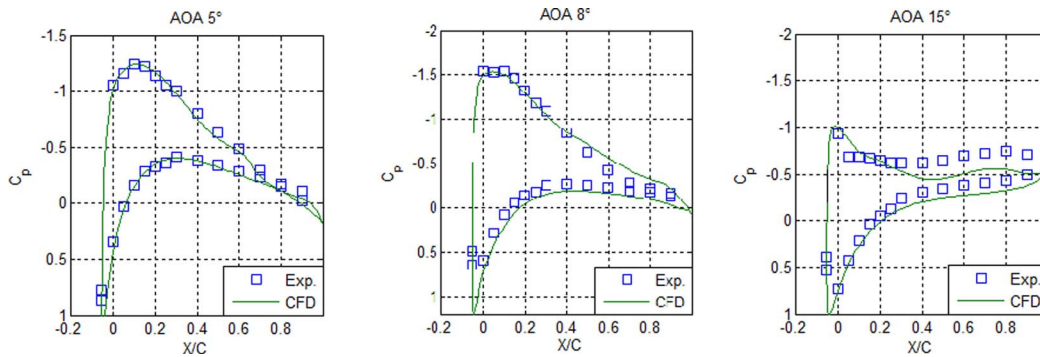


FIG. 8. Pressure coefficient from *SST*  $\gamma - Re_{\theta}$  compared to experimental values for A8W30 on the peak cross-section ( $Re = 120\,000$ ).

model achieved reasonable success in reproducing the wing surface pressure field on the A8W30 airfoil (Figures 8 and 9) and was, therefore, deemed adequate for investigating the underlying flow mechanism.

### VIII. FLOW STRUCTURE: FORMATION OF STREAMWISE VORTICITY

In this section, the tubercled wing with the largest amplitude and wavelength, A8W30, is adopted to elucidate the underlying flow mechanism in the formation of streamwise vortices from two different viewpoints. As established previously,<sup>11</sup> the effect of an undulating leading-edge on spanwise circulation is to generate a cyclic pattern. On the other hand, Stokes' law states that circulation ( $\Gamma$ ) around the wing's cross-section equals the surface integral of vorticity ( $\omega$ ) bound by the curve for which circulation is evaluated. If a closed curve that bounds a surface whose normal vector,  $d\tilde{S}$ , in the spanwise direction is considered, we have

$$\Gamma = \oint \omega \cdot d\tilde{s}, \quad (1)$$

$$\omega = \text{Curl}(u) = (\omega, \eta, \zeta), \quad (2)$$

$$d\tilde{S} = (0, 0, ds). \quad (3)$$

As tubercles induce a cyclic distribution of circulation in the spanwise direction, by virtue of Stokes' law, spanwise vorticity should also vary along the span of the airfoil. Contours of spanwise vorticity on the suction side, plotted on a plane normal to the free stream flow direction attest to the stated

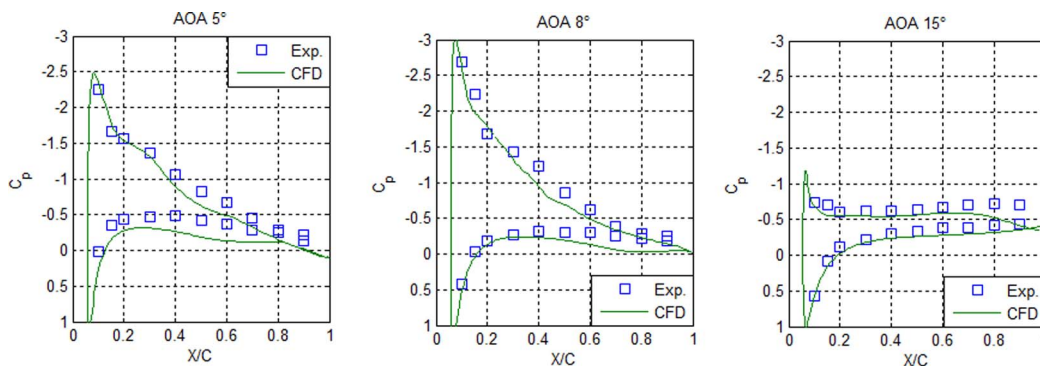


FIG. 9. Pressure coefficient from *SST*  $\gamma - Re_{\theta}$  compared to experimental values for A8W30 on the trough cross-section ( $Re = 120\,000$ ).

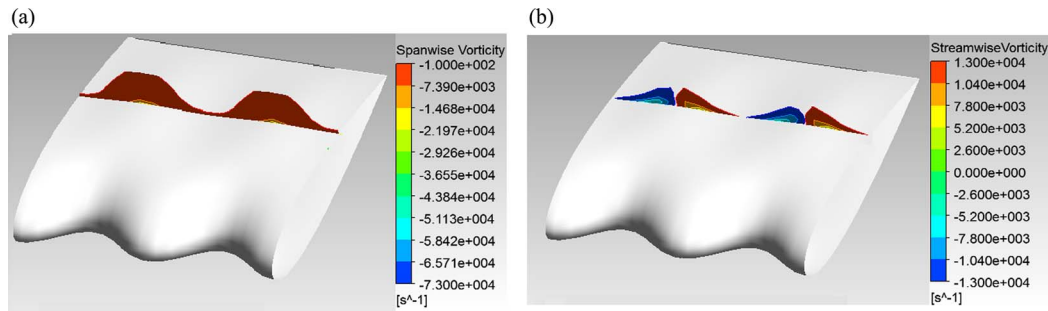


FIG. 10. (a) Contours of spanwise vorticity and (b) streamwise vorticity on a plane located at  $X/C = 0.57$  over the suction side of the foil A8W30. Red indicates a clockwise sense of rotation, while blue corresponds to a counter-clockwise sense of rotation in the perspective view presented. Contours display expanded by a factor of 4 in the vertical ( $y$ ) direction for clarity ( $Re = 120\,000$ ,  $AOA = 2^\circ$ ).

phenomenon (see Figure 10(a)). This implies that one effect of tubercles is to *ripple* the spanwise vortex sheets along the entire span. By the same token, each tubercle wavelength can be regarded analogous to a small finite wing sections. As a finite wing produces counter-rotating tip vortices in the streamwise direction, the cyclic variation of spanwise circulation dictates the development of pairs of counter-rotating streamwise vortices as shown in Figure 10(b).

Viewed from an alternate perspective, there are two principal mechanisms for generating streamwise vorticity which are referred to as “skew-induced” and “stress-induced.”<sup>25</sup> Skew-induced vorticity generation occurs when existing vorticity in the flow, for instance in the boundary layer, turns in the streamwise or transverse direction. This quasi-inviscid phenomenon operates in both laminar and turbulent flows and is also known as *Prandtl’s secondary flow of the first kind*. The second mechanism is referred to as stress-induced generation or *Prandtl’s secondary flow of the second kind* and arises from the anisotropy of turbulence.

In the case of flow over a tubercled airfoil, flow skewness is distinguished by the change in the streamlines’ curvature as they approach the leading-edge (Figure 11). The streamlines in Figure 11 are chosen to identify the structure of the significant vortical features present in the flow adjacent to the airfoil surface. While spanwise vorticity is present in the boundary layer, the abrupt change in the direction of the streamlines points to vorticity being re-organized near the leading-edge in the transverse and streamwise directions. The product of the spanwise component of the vorticity vector and the spanwise component of the streamwise velocity gradient,  $(\zeta \partial U / \partial z)$ , accounts for the turning of the vorticity vector<sup>26</sup> in the streamwise vorticity transport equation expressed in (4).

$$\tilde{u} \cdot \nabla \omega = v \nabla^2 \omega + \omega \frac{\partial U}{\partial x} + \eta \frac{\partial U}{\partial y} + \zeta \frac{\partial U}{\partial z} + \frac{\partial}{\partial x} \left( \frac{\partial \bar{u} v}{\partial z} - \frac{\partial \bar{u} w}{\partial y} \right) + \frac{\partial^2}{\partial y \partial z} (\bar{v}^2 - \bar{w}^2) + \left( \frac{\partial^2}{\partial z^2} - \frac{\partial^2}{\partial y^2} \right) \bar{v} \bar{w}, \quad (4)$$

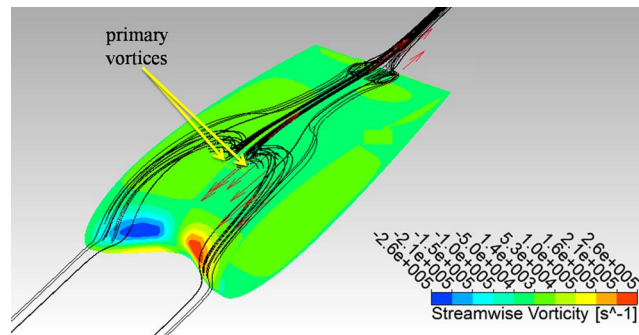


FIG. 11. Normalized streamwise vorticity vectors plotted for one-half of the 3D-streamlines. A8W30 coloured by streamwise vorticity ( $Re = 120\,000$ ,  $AOA = 2^\circ$ ).

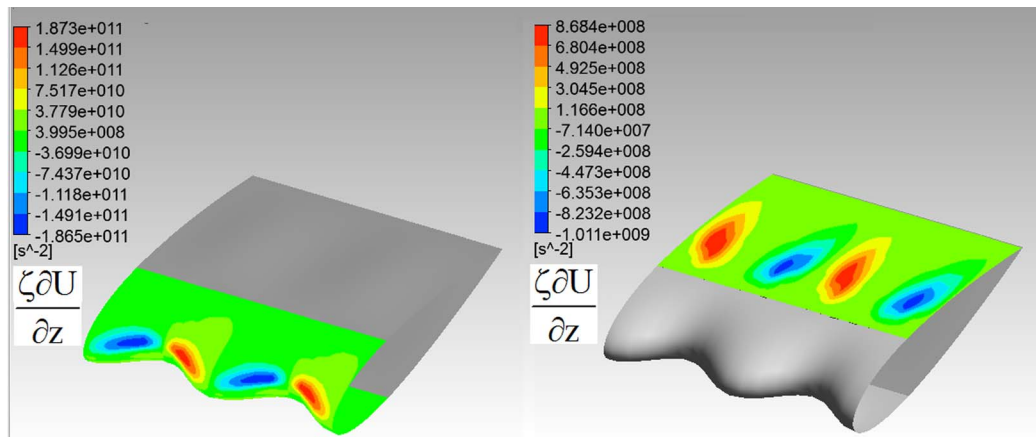


FIG. 12. Contours of the vorticity turning term present in the vorticity transport equation embedded in the boundary layer on the suction side of A8W30 ( $Re = 120\,000$ ,  $AOA = 2^\circ$ ).

where  $\omega$ ,  $\eta$ , and  $\zeta$  represent the components of vorticity in the streamwise, transverse, and spanwise directions. As seen in Figure 12, the magnitude of  $(\zeta \partial U / \partial z)$ , assumes the largest magnitude near the leading-edge of the airfoil, where flow skewness is initially observed. Flow skewness also appears dominant near the trailing-edge as shown in Figure 12.

The flow structure over the tubercled wing can be further investigated by examining the shear stress and vortex lines on the surface of the wing (Figures 13 and 14). The first identified critical point, coincident with the apex of the peak, at the wing's leading edge, is a node of attachment (N1) from which all the streamlines emanate. A bifurcation line (BiL) runs along the leading-edge of the tubercled wing connecting the nodes of attachment at the peaks (Figure 13(a)). Downstream of this region, in absence of any further lateral strain (velocity gradient) the vortex lines re-connect to form spanwise vortex lines downstream of the LSB re-attachment. Where  $X/C = 0.27$ , a node of detachment (N2) is identified in the trough as the second critical point on the suction side. The

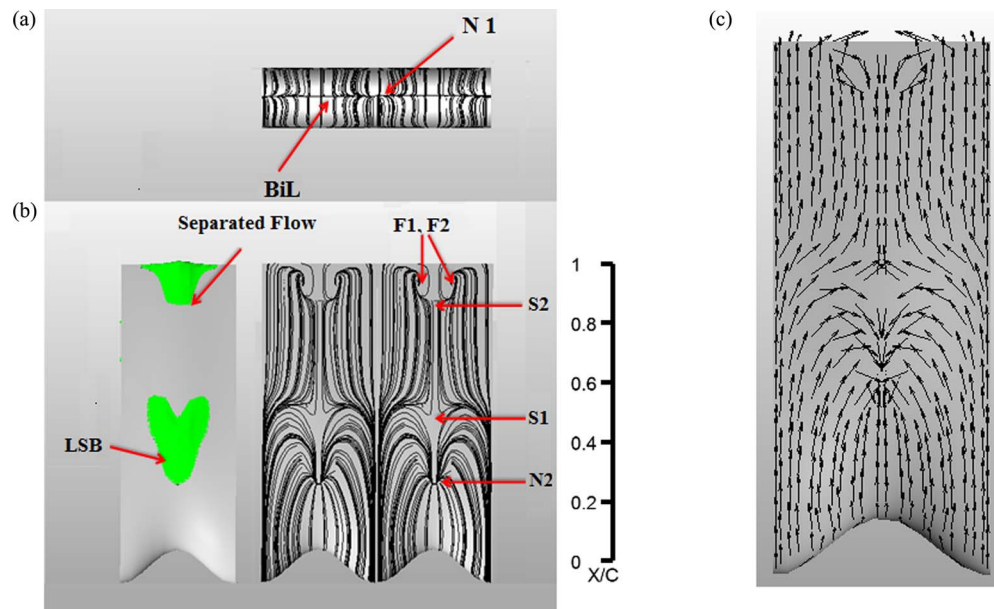


FIG. 13. (a) Front, (b) top orthogonal views of the shear stress lines, and (c) normalized limiting velocity vectors on the suction side of the tubercled foil section A8W30 ( $Re = 120\,000$ ,  $AOA = 2^\circ$ ).

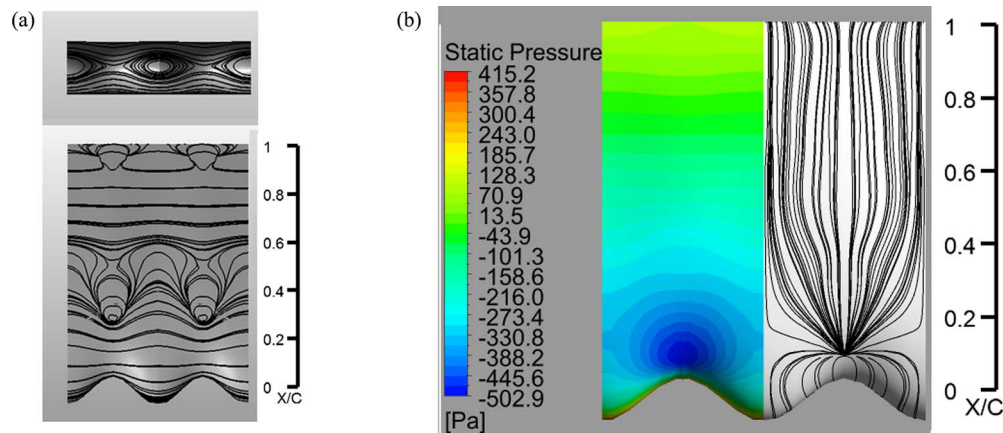


FIG. 14. (a) Front and top orthogonal views of the vortex lines on the suction side of the tubercled foil section A8W30. (b) Static pressure field and the pressure gradient lines on the same foil ( $Re = 120\,000$ ,  $AOA = 2^\circ$ ).

detachment point N2 (Figure 13(b)) marks the location where limiting streamlines converge. The sense of curvature of the shear stress lines near N2 implies that  $(-\nabla p)$  is directed towards the trough region. The pressure gradient lines bear witness to this conclusion (Figure 14(b)). As a result, the lowest pressure region occurs in the trough. This phenomenon was observed on all the modelled tubercled foils.

In the vicinity of N2, spanwise flow leads to the velocity gradient,  $\partial U/\partial z$ , which turns the vortex lines from a spanwise orientation towards the streamwise direction (Figure 13(b)). While a number of streamlines converge at (N2), others move further back and spiral into two foci (F1, 2) near the trailing edge (Figure 13(b)). The two critical points in the forms of a node of detachment (N2) and a saddle point (S1), also mark the respective locations where the flow initially separates and then re-attaches in the trough, designating the boundaries of an *open* laminar separation bubble. The term open LSB, refers to the fact that the bubble is three-dimensional and leads to the formation of streamwise vortices as shown in Figure 11. It is evident that vorticity in the streamwise direction affects the shape of the LSB. The shape of the LSB is consistent with the experimental findings by Karthikeyan *et al.*<sup>27</sup> who examined the flow over a tubercled foil with the NACA 4415 baseline profile at the same Reynolds number. It is noteworthy that the boundary-layer-embedded flow feature near N2 in Figure 13(b) exists within a layer of fluid of 0.4(mm) height/thickness in the wall-normal direction.

Towards the trailing-edge, surface flow spirals into two foci (F1, F2) that, along with the saddle point (S2), hint at the development of tornado-like vortices.<sup>28</sup> As illustrated in Figure 13(b), the formation of stream-wise vortices is accompanied by flow separation in a delta-shaped region near the trailing edge. The attributes of the vorticity field and flow separation pattern, in the pre- and post-stall phases are discussed in more detail in Secs. IX and XII.

## IX. PRE-STALL AERODYNAMIC BEHAVIOR

Iso-surfaces of zero streamwise velocity can be used to interpret how stall is initiated for the modelled wings (Figure 15). At a zero incidence angle, separation occurs in the trough regions of all modified airfoils initially, however, the boundary layer re-attaches further downstream, forming a LSB. Also, further flow separation is observed near the trailing-edge in delta-shaped regions. Conversely, the flow remains more attached over a peak at this incidence angle. As the attack angle increases to  $5^\circ$ , the bubble moves further upstream on all wings while its size is reduced. Similarly, the separated flow region near the trailing edge grows in size, as the initial separation point appears at a location further upstream. At  $AOA = 8^\circ$ , differences in flow separation can be identified more easily. Separated flow from the trailing edge on A8W30 and A8W15 has moved upstream and reached the re-attachment point on the bubble forming larger separated flow regions. In contrast,

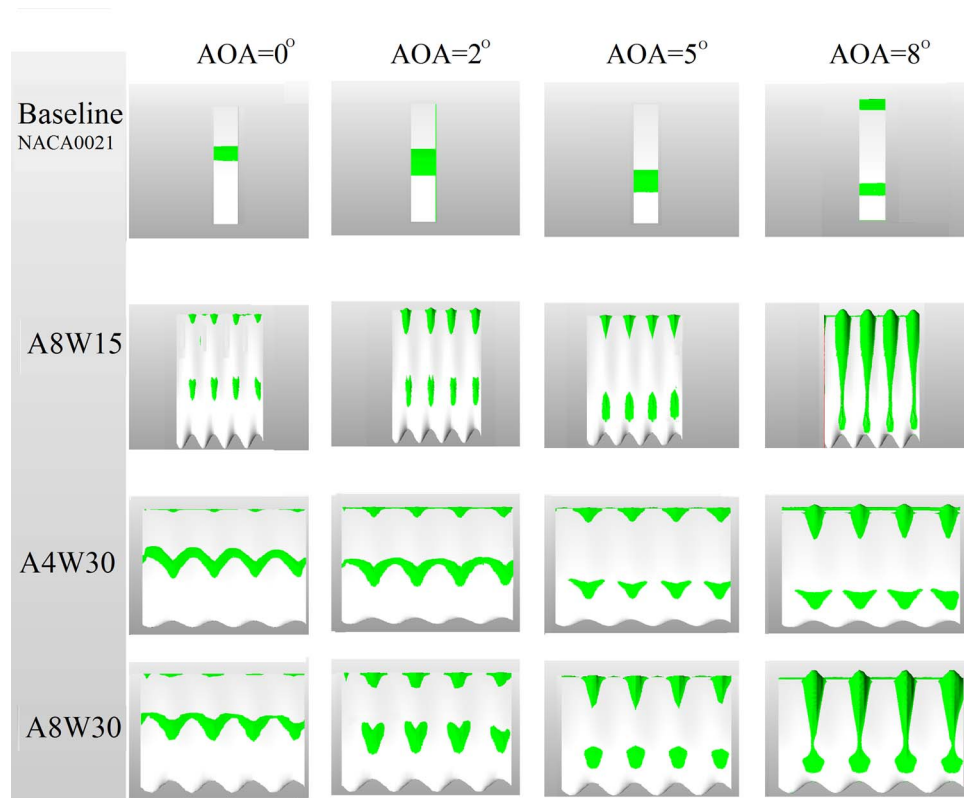


FIG. 15. Separated flow regions (shown in green) over the suction sides of the modified and unmodified wings ( $Re = 120\,000$ ).

the boundary layer remains attached between the re-attachment point of the LSB and the separation point near the trailing edge for A4W30. As is the case for the modified foils, separation is also observed to occur on the unmodified airfoil in the form of a laminar separation bubble that moves towards the leading edge with the increase in the attack angle. Nonetheless, owing to the fact that streamwise vorticity is absent over the unmodified NACA 0021, the shape of the LSB remains essentially two-dimensional. Similar to modified foils, the baseline wing develops trailing edge flow separation that grows in size pre-stall.

In Figure 16, the pressure coefficient plots are presented on the trough, middle, and peak cross-sections of the modified and the unmodified foils at  $AOA = 8^\circ$ . Since experimental data

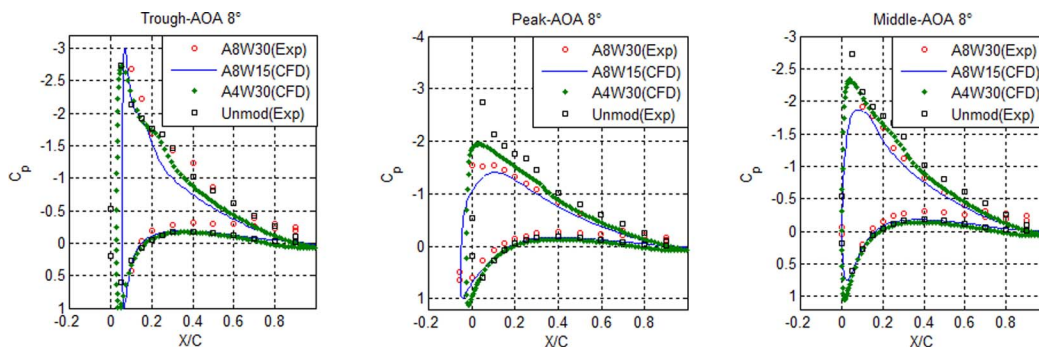


FIG. 16. Comparison of the pressure distribution on three spanwise locations for the modified foils and the unmodified NACA 0021 ( $Re = 120\,000$ ,  $AOA = 8^\circ$ ).



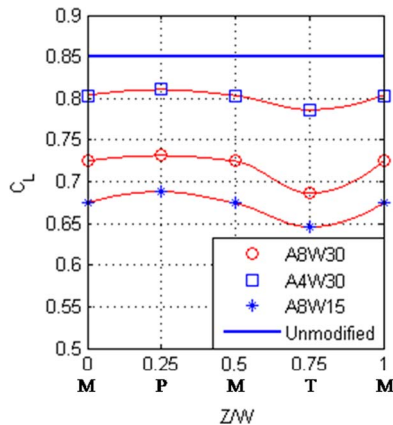
TABLE II. Lift coefficient obtained from the CFD study compared to the values reported in the literature ( $Re = 120\,000$ ,  $AOA = 8^\circ$ ).

Wing label	$C_L$ (Hansen <i>et al.</i> <sup>5</sup> )	$C_L$ (SST $\gamma - Re_\theta$ )
A8W30	0.70	0.707
A4W30	0.84	0.791
A8W15	N/A	0.674
NACA 0021	0.94	0.850

are not available for the modified foils A8W15 and A4W30, the computed pressure coefficient values obtained from numerical modelling have been used instead. A common feature of all the pressure plots for the tubercled airfoils, is the occurrence of the highest suction peaks on the trough cross-section. For all the tubercled foils, the distribution of pressure on the trough appear comparable, nevertheless, the wing A8W15, which has the largest amplitude, achieves the most negative suction peak and the gradient of pressure on this tubercled wing is more adverse than the others. Differences are more noticeable on the tubercle peak and middle cross-sections, as A4W30 has the highest suction peak, followed by A8W30 and A8W15, respectively. The unmodified foil clearly assumes more negative values on the suction side than any modified foil which accounts for its higher lift coefficient than the modified foils in the pre-stall region (Table II). In short, airfoils with larger amplitudes and wavelengths appear to generate lower maximum lift coefficients as the magnitude of the suction peak value on the middle and chord maxima spanwise locations is reduced.

Figure 17 shows the sectional lift coefficient values along one wavelength of the tubercled foils compared to those of the baseline. All modified wings produce the largest values of lift on the peak cross-section, followed by the middle and the trough. Since more flow separation occurs over the trough region (see Figure 15), the lower values of the lift coefficient for the trough are justified. Note the cyclic appearance of the lift coefficient along the span which is indicative of circulation behaving in a similar manner.

The contours of streamwise vorticity have been plotted on three planes normal to the free-stream flow direction in Figure 18 for the tubercled foils at  $AOA = 8^\circ$ . It is seen that the maximum value of vorticity is the highest for A8W15, followed by that of A8W30 and A4W30, respectively. The same trend in the order of peak vorticity was observed for all pre-stall angles. Given the finding that circulation assumes a cyclic spanwise distribution with amplitudes and wavelengths proportional to the amplitude and wavelength of the tubercles,<sup>11</sup> and the fact that the strength of vortices is proportion to the spanwise gradient of circulation ( $d\Gamma/dz$ ), it is plausible that the ratio of amplitude

FIG. 17. Sectional lift coefficients along the span obtained by the transitional SST model. M, P, and T represent, the middle, peak, and trough cross-sections ( $Re = 120\,000$ ,  $AOA = 8^\circ$ ).

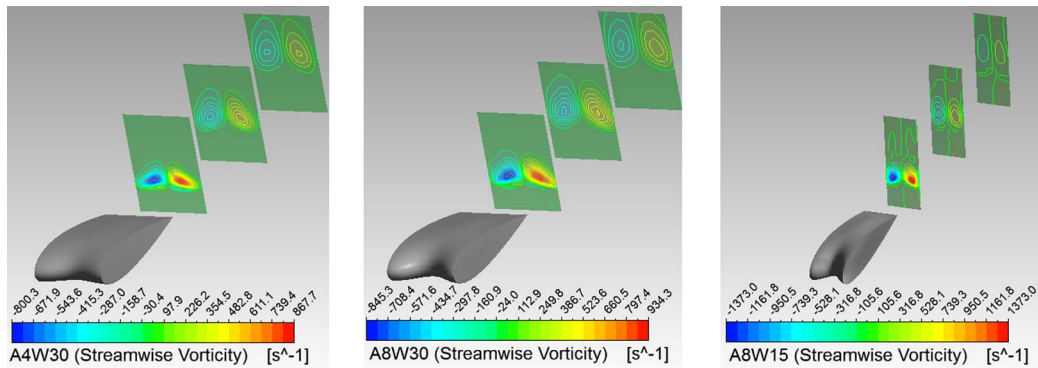


FIG. 18. Contours of streamwise vorticity on three planes oriented normal to the free-stream flow direction, located in the wake ( $Re = 120\,000$ ,  $AOA = 8^\circ$ ).

to wavelength ( $A/W$ ) determines the strength of streamwise vortices,  $d\omega$ , expressed mathematically in Eqs. (5) and (6):

$$\Gamma = kA \sin\left(\frac{2\pi}{W}z\right), \quad (5)$$

$$d\omega = \frac{\partial\Gamma}{\partial z} dz = k2\pi \frac{A}{W} \cos\left(\frac{2\pi}{W}z\right) dz. \quad (6)$$

## X. DETAILED FLOW STRUCTURE ANALYSIS: PRE-STALL

A detailed description of the A8W30 case at an  $8^\circ$  angle of attack is provided collectively by Figures 15–21. Figure 15 shows there to be a long separation bubble in the trough in this case, suggesting that the airfoil is at the onset of stall. Figure 19(a) describes the shear stress pattern on the suction surface of this airfoil. The pattern is topologically similar to that of Figure 13(b), albeit with the separation now initiated closer to the leading edge and extending chordwise to the trailing edge, and the presence of a narrow “alleyway” of reverse flow from the trailing edge to the

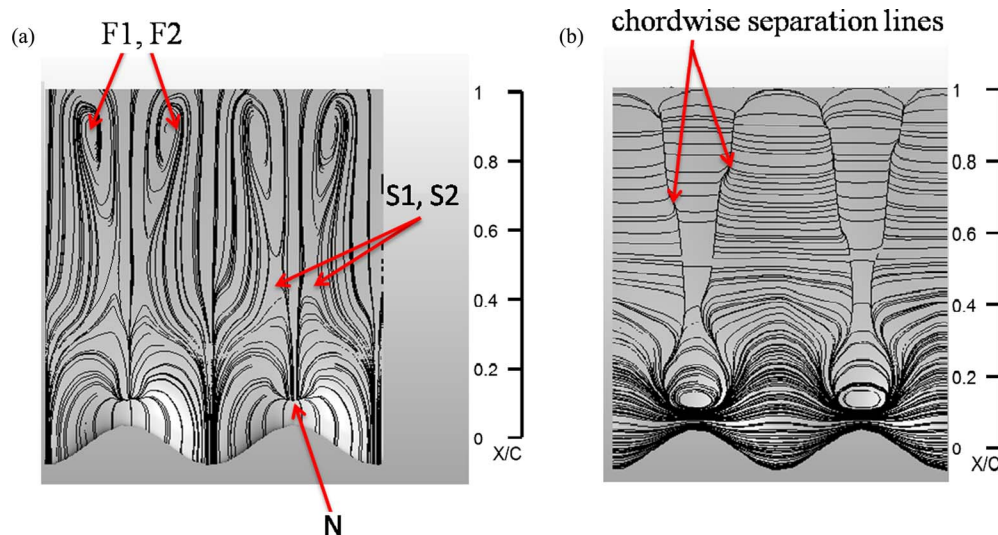


FIG. 19. (a) Top orthogonal views of (a) the shear stress and (b) vortex lines on the suction side of the tubercled foil section A8W30 ( $Re = 120\,000$ ,  $AOA = 8^\circ$ ).

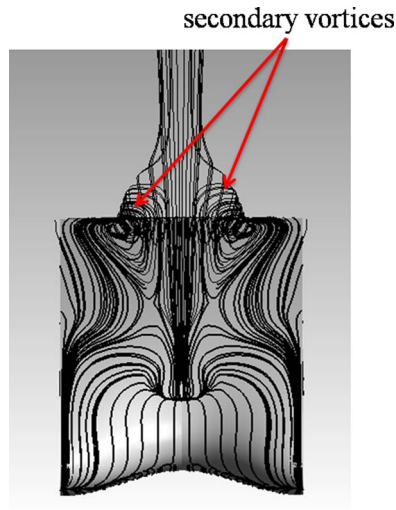


FIG. 20. Three-dimensional and surface streamlines in the vicinity of A8W30 showing a pair of counter-rotating vortices in the oblique view ( $Re = 120\,000$ ,  $AOA = 8^\circ$ ).

initial separation. Foci F1,2 now occupy the rear 40% of the foil's chord. Some signs of asymmetry have now developed in the surface shear stress pattern, particularly mid-chord behind the central peak.

The associated pattern of vortex lines shown in Figure 19(b) also reveals differences from the lower angles of attack cases, consistent with the presence of a long separation bubble in the trough. The pattern shows that as the boundary layer vortex lines convect downstream, they are turned into the streamwise direction due to the lateral velocity gradients, as described in Sec. VIII above. Here the locus of streamwise-turned vortex lines, identified as “chordwise separation lines” in Figure 19(b), define the lines of separation of the boundary layer from the airfoil surface, forming the shear layer over the long separation bubble and leading to the concentrated streamwise vorticity distributions of Figure 21. In addition, vortex lines associated with the reversed flow region beneath the long separation bubble are also present and these are seen to merge into the same flow structure, further contributing to the streamwise vorticity.

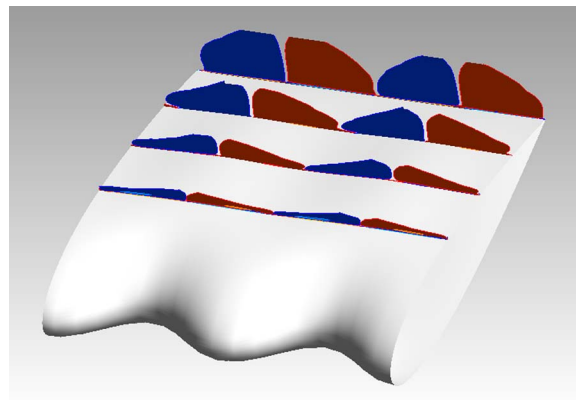


FIG. 21. Evolution of streamwise vorticity over the suction side of A8W30. Blue and red contours show a counter-clockwise and clockwise sense of rotation, respectively. (Maximum vorticity levels limited to  $6 \times 10^4 (\text{s}^{-1})$  on all four cross-sectional planes,  $Re = 120\,000$ ,  $AOA = 8^\circ$ ).

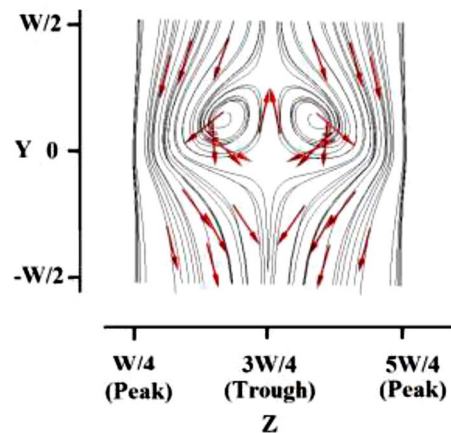


FIG. 22. Pseudo-streamlines plotted on a plane normal to the free-stream flow direction situated 40(mm) downstream of the trailing edge of A8W30. Normalized vectors on the same plane illustrate the direction of fluid motion. Rulers show dimensions with respect to tubercle wavelength ( $W$ ) ( $Re = 120\,000$ ,  $AOA = 8^\circ$ ).

The two large foci, F1 and F2 near the trailing edge in Figure 19(a), and the perspective streamline pattern of Figure 20, are connected to saddle points S1 and S2 on either side of the separation bubble. Note that saddle point S1 identified in Figure 13(b) does not appear here, as the separated flow from the bubble does not re-attach at this incidence angle. It is notable that the sign of rotation of the vortices emanating from F1 and F2 is the same as the primary streamwise vortices that originate upstream, suggesting that these like-sign secondary vortices merge to form larger, stronger streamwise at the trailing edge of the airfoil.

Figure 21 shows the evolution of the streamwise vorticity over the suction side of the foil, in agreement with the vortex line patterns. The pattern is consistent with Figure 8(b) and all investigated pre-stall angles, however in the present ( $AOA = 8^\circ$ ) case of the long separation bubble, the circulation of the primary streamwise vortices appears to grow continuously along the chord of the airfoil before merging with the secondary vortices. Downstream of the trailing edge, the cores of the vortices grow in size while the maximum value of vorticity decreases (Figure 18). Kelvin's circulation theorem may explain this phenomenon. In an inviscid flow situation, as the streamtubes of fluid containing the vortices grow larger in cross-sectional area, due to flow deceleration, vorticity, spreads over a larger area and its peak value is reduced to conserve circulation. With viscous effects present, circulation is not necessarily conserved, however the streamtubes grow larger in size and vorticity is dispersed. Due to their induced velocity fields, the counter-rotating vortices create a downwash on the peak cross-sections, and upwash in the vicinity of the trough region. This conclusion is reached by observing the sign of the streamwise component of the vorticity vector over the suction side of the airfoil (Figure 21). Consequently, it is concluded that this mechanism enhances the momentum transfer in the boundary layer downstream of the peak, and explains why the peak cross-section is less susceptible to flow separation. At pre-stall attack angles, the described phenomenon is more clearly illustrated in the wake by pseudo-streamlines on a plane located at 80(mm) downstream of the trailing edge of the wing A8W30 (Figure 22). It is expected that at lower Reynolds numbers the scales of the vortices over the airfoil's surface would increase due to the increased boundary layer thickness.

## XI. POST-STALL AERODYNAMIC BEHAVIOR

At  $AOA = 15^\circ$ , flow separation occurs over most of the surface area on the suction sides of all airfoils (Figure 23). The patterns of flow separation suggest that the trough regions contribute the most to flow separation, similar to the situation pre-stall. Whereas the unmodified foil is in deep stall, the three modified foils exhibit regions of attached flow, in particular behind the tubercle peaks, which suggests that the modified airfoils produce more lift under post-stall conditions (Table III).

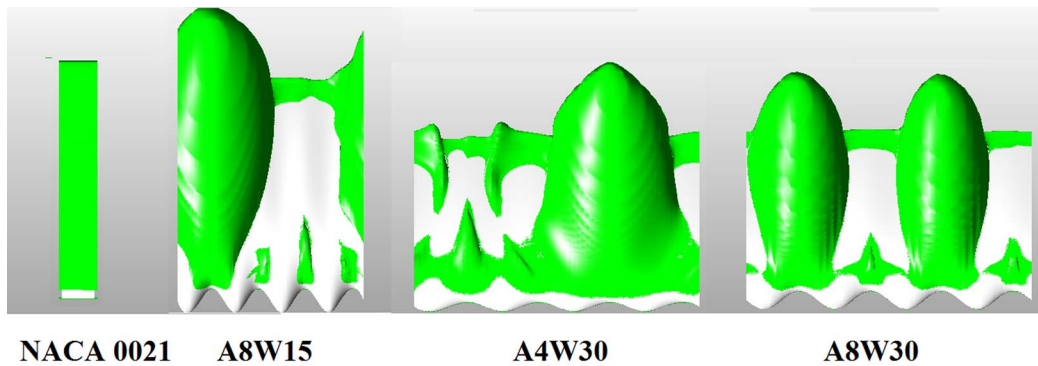


FIG. 23. Separated flow regions (in green) over the suction sides of the modified and unmodified wings ( $Re = 120000$ ,  $AOA = 15^\circ$ ).

TABLE III. Lift coefficients obtained from the CFD study compared to the values reported in the literature. ( $Re = 120000$ ,  $AOA = 15^\circ$ ).

Wing label	Lift coefficient (Hansen <i>et al.</i> <sup>5</sup> )	Lift coefficient (SST $\gamma - Re_\theta$ )
A8W30	0.60	0.53
A4W30	0.59	0.61
A8W15	N/A	0.49
NACA 0021	0.37	0.36

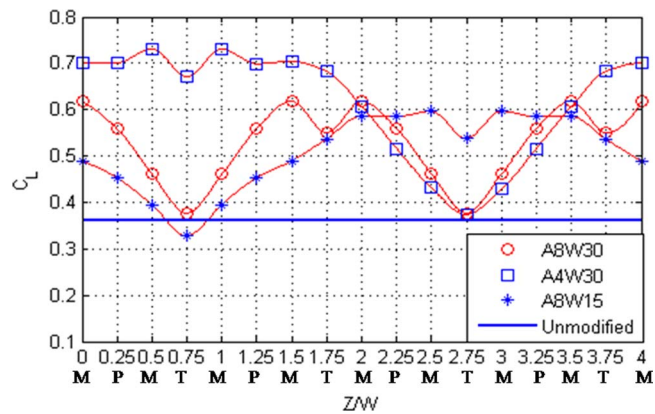


FIG. 24. Sectional lift coefficients along the span obtained by the transitional SST model. M, P, and T represent, the middle, peak, and trough cross-sections ( $Re = 120000$ ,  $AOA = 15^\circ$ ).

The pattern of flow separation appears to be bi-periodic only for A8W30 while more complex flow is realized for the other foils. Johari *et al.*<sup>6</sup> also identified a bi-periodic pattern in their water tunnel flow visualization experiments. It is noted that the reversed shape (compared with the un-stalled cases shown in Figure 23) of the open Laminar Separation Bubble in the A4W30 and A8W30 cases was also observed experimentally by Karthikeyan *et al.*<sup>27</sup>

The distribution of the lift coefficient in the spanwise direction is more complex in the post-stall region, compared to that of pre-stall, as shown in Figure 24. In contrast to the tubercled foils, sectional lift for the unmodified foil is evidently lower over a large portion of the span, pointing to the advantageous behavior of the wings with tubercles in the post-stall zone. Notably, the highest values of the lift coefficient occur for the middle cross-sections. This is followed by the peak and the trough. This trend is consistent with the patterns associated with flow separation.

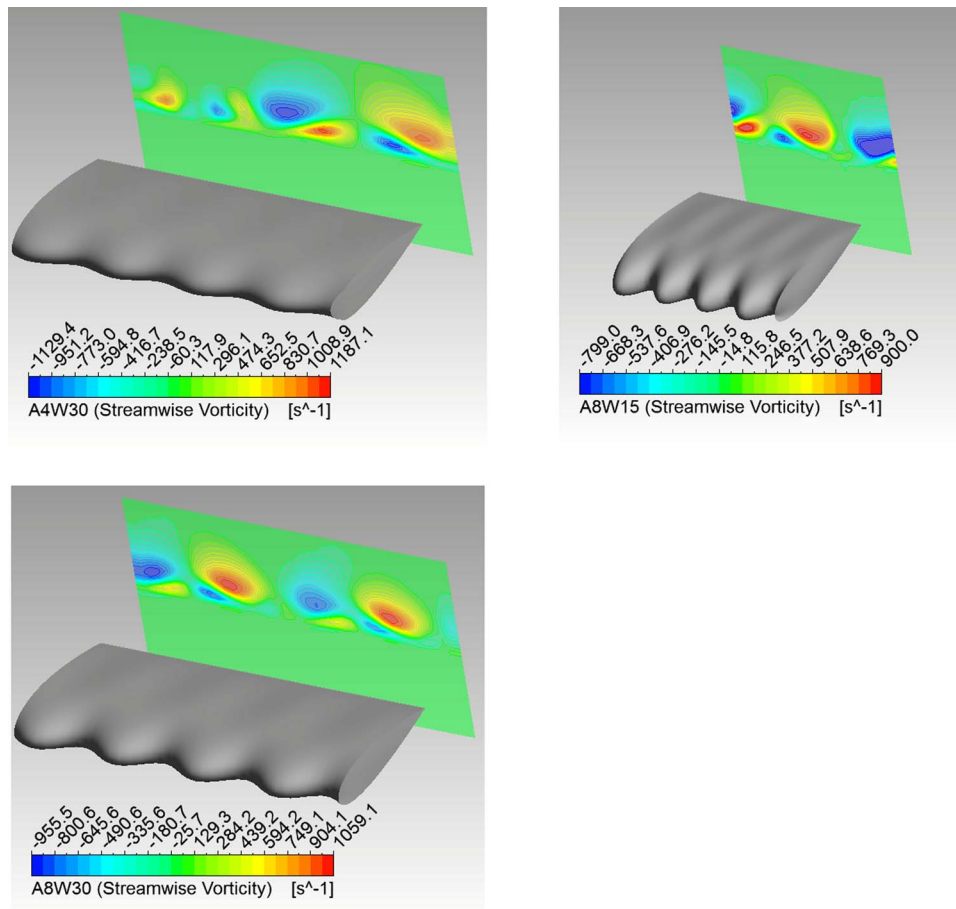


FIG. 25. Contours of streamwise vorticity on three planes oriented normal to the free-stream flow direction, located 30(mm) downstream of the trailing edge ( $Re = 120\,000$ ,  $AOA = 15^\circ$ ).

## XII. DETAILED FLOW STRUCTURE ANALYSIS: POST-STALL

Computed streamwise vorticity contours downstream of the airfoil shown in Figure 25 indicate the presence of a series of vortices with large cores and smaller counter-rotating vortices beneath. To investigate the origins and evolution of these features, the A8W30 (with the largest amplitude and wavelength) case is selected. Collectively, this case is described in Figures 26–28. A distinctive feature of this case is the formation of bi-periodic separation zones (Figure 23), with regions of attached flow behind every second trough, in contrast to the un-stalled cases where the attached flow occurs behind the peaks.

A notable feature of the A8W30 flow pattern is the presence of a small open separation bubble in the central trough (Figure 23), behind which there exists a large attached-flow region. This contrasts with the adjoining troughs which have formed long separation bubbles. Figure 26(a) presents the shear stress pattern on the suction surface of the stalled airfoil, revealing the presence of a number of salient features, including the features noted in the un-stalled flow cases, the reversed flow from the trailing edge of the foil to the open separation bubble, and the reversed directions of foci F1 and F2. The vortex line pattern of Figure 26(b) shows no significant change in the structure of either the open separation bubble or the long separation bubbles compared with those observed at various attack angles in the un-stalled cases. Also note that the separation line (SL) near the leading edge assumes a wavy pattern.

Figure 27 describes the evolution of the streamwise vorticity over the surface of the airfoil at four chordwise locations. At  $X/C = 0.143$ , the vorticity distribution is similar to the patterns present

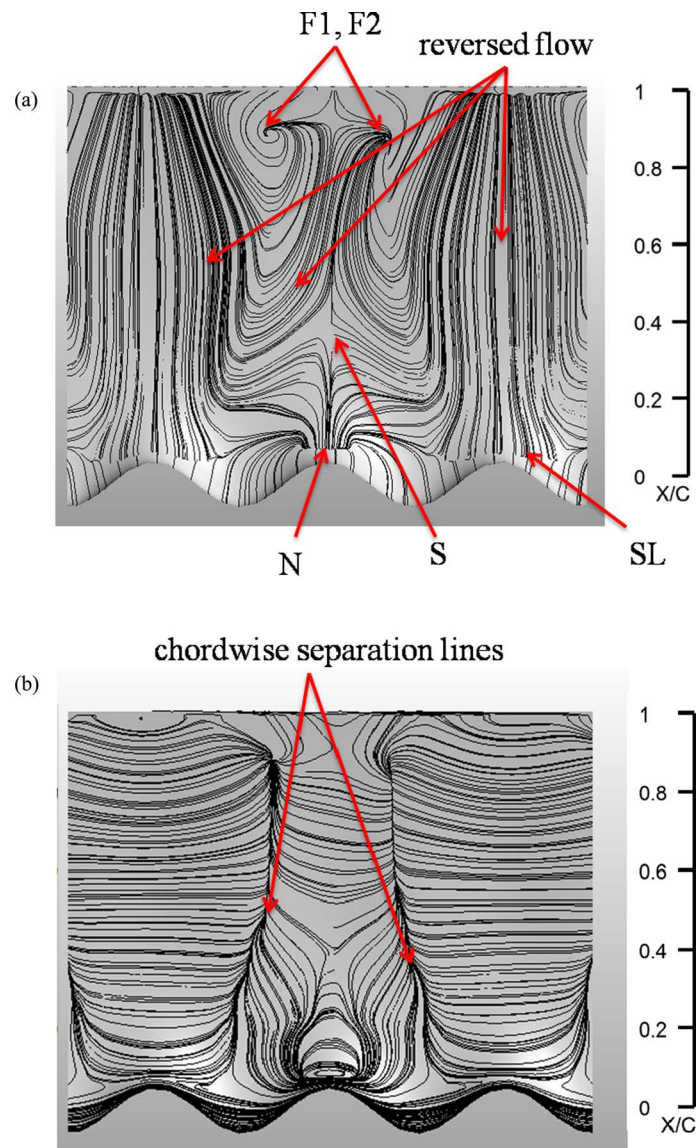


FIG. 26. Top orthogonal view of (a) shear stress and (b) vortex lines. (A8W30,  $Re = 120\,000$ ,  $AOA = 15^\circ$ ).

in the un-stalled flow cases, indicating that the structures of the small and long separation bubbles are consistent with previously described patterns. Further downstream at  $X/C = 0.428$ , the larger primary vortices, which are associated with the long separation bubbles, grow and lift away from the surface while the smaller primary vortices, associated with the small separation bubble in the centre trough, remain closer to the surface. At  $X/C = 0.714$ , the vortex pairs are seen to interact, leading to merging and possibly annihilation of vorticity. Two small unexplained “lumps” of vorticity (red) are also present, which is possibly a sign of inherent asymmetry in this flow. These may be associated with the angled vortex lines mentioned in the previous paragraph.

At the trailing edge, the streamwise vorticity field is seen to have developed substantially, with significant changes in both the size and shape of the dominant primary vortex pairs. This can be attributed to the merging of the secondary vorticity from the vortices emanating from  $F1$  and  $F2$ . It is noted that these foci are of opposite sign to those observed in the un-stalled flows, but so is the sign of the dominant primary vortices in this case. The streamwise vorticity field also reveals the presence of vorticity (of opposite sign) developing beneath the merged primary and secondary

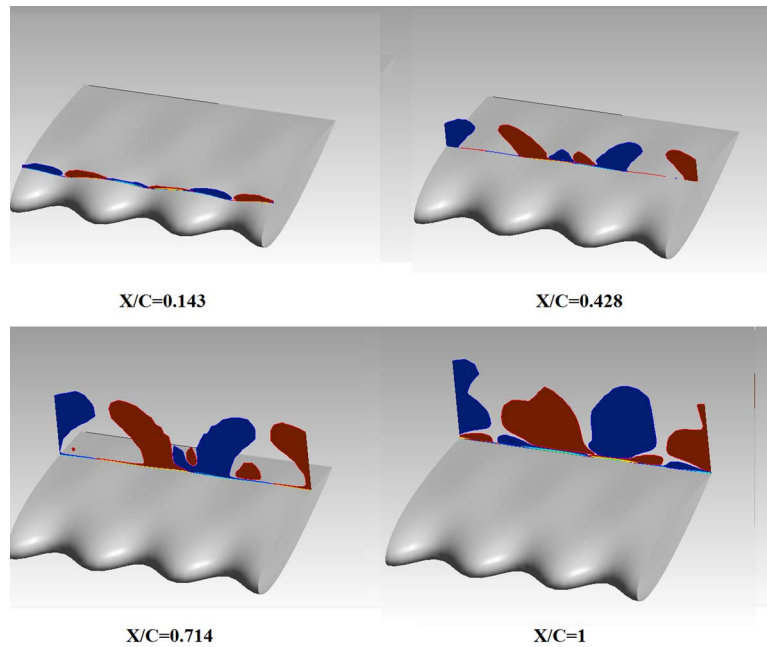


FIG. 27. Evolution of streamwise vorticity over the tubercle foil's suction surface at various chordwise locations. Red and blue contours show a clockwise and a counter-clockwise sense of rotation, respectively (A8W30,  $Re = 120\,000$ ,  $AOA = 15^\circ$ ).

vortices at the trailing edge. This is probably due to the interaction of the longitudinal vortices and the wall boundary layer, generating lateral shear.<sup>29</sup>

The presence of the vortices over the surface of the modified foils at large attack angles dramatically impacts the induced velocity field. The pseudo-streamlines colored by velocity, in Figure 28, demonstrate that the induced velocity of the dominant primary vortices of the long separation bubbles transports high momentum flow towards the central trough region, leading to attached flow. As a result, the two slanted strips behind the peaks that merge in the trough section are marked by attached flow. The described enhanced momentum transfer mechanism, brought about by the presence of streamwise vorticity, was observed to occur all for the modelled flow cases over modified foils, and is believed to account for higher lift coefficients achieved by the tubercled wings

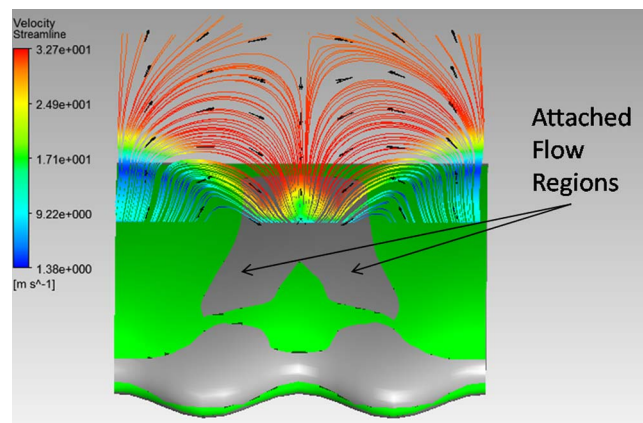


FIG. 28. Enhanced momentum transfer from the separated flow regions to regions where flow is attached shown on the suction side of A8W30 in the oblique view (A8W30,  $Re = 120\,000$ ,  $AOA = 15^\circ$ ).



post-stall, compared to the unmodified NACA 0021 whose significant loss of lift at an angle of attack equal to  $12^\circ$  was reported by Hansen *et al.*<sup>5</sup>

### XIII. CONCLUSIONS

In the present work, the formation mechanism of streamwise vortices in the flow over full-span modified airfoils with tubercles was explored. Computational Fluid Dynamics helped to identify a skew-induced mechanism to account for generating streamwise vorticity, known as Prandtl's secondary flow of the first type. From an alternative standpoint, it was demonstrated that a tubercled leading-edge causes spanwise vortex lines to become *rippled* with the spanwise variation accounting for the formation of streamwise vortices. It was shown that the magnitude of peak vorticity near the leading edge of a tubercled foil is in direct proportion to the amplitude-to-wavelength ratio of the tubercle geometry.

The development of pairs of counter-rotating streamwise vortices is, however, accompanied by flow separation in delta-shaped regions near the trailing edge that move upstream with the increase in attack angle. While wings with larger amplitude-to-wavelength ratios produce stronger vortices, increasing the amplitude or wavelength can lead to more extensive flow separation and inferior performance with regard to the generated lift pre-stall. The suction peak on the middle and chord maxima cross-sections were mostly affected by the increase of these geometric parameters. Post-stall, wind tunnel pressure measurement test results suggest that the "burst" of a laminar separation bubble for the unmodified airfoil NACA 0021 appears to give rise to its abrupt stall, while the tubercle-modified airfoils' loss of lift is more gradual. In addition, the highest suction peak is observed to occur on the trough cross-section which leads to a more adverse streamwise pressure gradient compared to that of the peak and the middle cross-sections. This phenomenon results in more flow separation in the trough region.

The CFD investigation shows that counter-rotating primary and secondary vortices appear over the surface of the modified foils at all angles of attack. The interactions between these vortices are readily described in all three of the presented flow cases. In every case, it is found that the primary and secondary vortices are together responsible for the formation of regions of attached flow. In the unstalled cases, the attached flow regions reside behind the tubercle peaks. However, in the stalled flow, the attached flow may reside behind the peaks or behind alternate troughs in the bi-periodic cases.

- <sup>1</sup> F. E. Fish and J. M. Battle, "Hydrodynamic design of the humpback whale flipper," *J. Morphol.* **225**, 51–60 (1995).
- <sup>2</sup> B. L. Woodward, J. P. Winn, and F. E. Fish, "Morphological specializations of baleen whales associated with hydrodynamic performance and ecological niche," *J. Morphol.* **267**, 1284–1294 (2006).
- <sup>3</sup> P. Watts and P. E. Fish, "The influence of passive leading edge tubercles on wing performance," in *Proceedings of the Twelfth International Symposium on Unmanned Untethered Submersible Technology (UUST)* (Autonomous Undersea Systems Institute, Durham NH, 2001).
- <sup>4</sup> D. S. Miklosovic, M. M. Murray, L. E. Howle, and F. E. Fish, "Leading edge tubercles delay stall on humpback whale flippers," *Phys. Fluids*, **16**(5) L39–L42 (2004).
- <sup>5</sup> K. L. Hansen, R. M. Kelso, and B. B. Dally, "Performance variations of leading-edge tubercles for distinct airfoil profiles," *AIAA J. Aircr.* **49**, 185–194 (2011).
- <sup>6</sup> H. Johari, C. Henocho, D. Custodio, and A. Levshin, "Effects of leading edge protuberances on airfoil performance," *AIAA J.* **45**, 2634–2642 (2007).
- <sup>7</sup> D. S. Miklosovic, M. M. Murray, and L. Howle, "Experimental evaluation of sinusoidal leading edges," *J. Aircr.* **44**, 1404–1407 (2007).
- <sup>8</sup> H. T. C. Pedro and M. H. Kobayashi, "Numerical study of stall delay on humpback whale flippers," AIAA Paper No. 2008-0584, 2008.
- <sup>9</sup> E. van Nierop, S. Alben, and M. P. Brenner, "How bumps on whale flippers delay stall: An aerodynamic model," *Phys. Rev. Lett.* **100**, 054502 (2008).
- <sup>10</sup> *Applied Hydro- and Aeromechanics*, edited by L. Prandtl and O. G. Tietjense (Dover Publications, Inc., New York, 1957).
- <sup>11</sup> N. Rostamzadeh, R. M. Kelso, B. B. Dally, and K. L. Hansen, "The effect of undulating leading-edge modifications on NACA 0021 airfoil characteristics," *Phys. Fluids* **25**, 117101 (2013).
- <sup>12</sup> J. Anderson, *Fundamentals of Aerodynamics*, 4th ed. (McGraw-Hill International Higher Education, 2005).
- <sup>13</sup> R. Langtry and F. Menter, "Correlation-based transition modeling for unstructured parallelized computational fluid dynamics codes," *AIAA J.* **47**, 2894–2906 (2009).
- <sup>14</sup> J. B. Barlow, A. Pope, and W. H. Rae, *Low Speed Wind Tunnel Testing*, 3rd ed. (Wiley-Interscience, 1999).

- <sup>15</sup> K. L. Hansen, "Effect of leading edge tubercles on airfoil performance," in *Doctor of Philosophy, Mechanical Engineering* (University of Adelaide, Adelaide, 2012).
- <sup>16</sup> P. Weber, L. Howle, M. Murray, and D. Miklosovic, "Computational evaluation of the performance of lifting surfaces with leading-edge protuberances," *J. Aircr.* **48**, 591–600 (2011).
- <sup>17</sup> S. F. Hoerner, "Fluid dynamic lift: Practical information on aerodynamic and hydrodynamic lift," NASA STI/Recon Tech. Rep. A 76, 32167 (1975).
- <sup>18</sup> J. G. Leishman, *Principles of Helicopter Aerodynamics* (Cambridge Aerospace Series, England, UK, 2006), Chapter 7.
- <sup>19</sup> ANSYS, "ANSYS-CFX Solver Theory Guide," in *ANSYS CFX 12.1*, edited (ANSYS, Inc., Pennsylvania, 2011).
- <sup>20</sup> X. Zheng, C. Liu, F. Liu, and C.-L. Yang, "Turbulent transition simulation using the  $k-\omega$  model," *Int. J. Numer. Methods Eng.* **42**, 907–926, (1998).
- <sup>21</sup> J. N. N. Counsil and K. G. Boulama, "Validating the URANS shear stress transport  $\gamma - Re\theta$  model for low-Reynolds-number external aerodynamics," *Int. J. Numer. Methods Fluids* **69**, 1411–1432 (2012).
- <sup>22</sup> F. R. Menter, "Two-equation eddy-viscosity turbulence models for engineering applications," *AIAA J.* **32**, 1598–1605 (1994).
- <sup>23</sup> P. J. Roache, *Verification and Validation in Computational Science and Engineering* (Hermosa, New Mexico, 1998).
- <sup>24</sup> J. N. N. Counsil and K. G. Boulama, "Low-Reynolds-number aerodynamic performances of the NACA 0012 and Selig–Donovan 7003 airfoils," *J. Aircr.* **50**, 204–216 (2013).
- <sup>25</sup> P. Bradshaw, "Turbulent secondary flows," *Annu. Rev. Fluid Mech.* **19**, 53–74 (1987).
- <sup>26</sup> H. J. Perkins, "The formation of streamwise vorticity in turbulent flow," *J. Fluid Mech.* **44**, 721–740 (1970).
- <sup>27</sup> N. Karthikeyan, S. Sudhakar, and P. Suriyanarayanan, "Experimental studies on the effect of leading edge tubercles on laminar separation bubble," in *52nd Aerospace Sciences Meeting*, edited (American Institute of Aeronautics and Astronautics, 2014).
- <sup>28</sup> J. Delery, *Three Dimensional Separated Flow Topology* (Wiley, 2013).
- <sup>29</sup> A. D. Cutler and P. Bradshaw, "Strong vortex/boundary layer interactions," *Exp. Fluids* **14**, 393–401 (1993).

## Chapter 5

# Flow over a Tubercled Foils in the Laminar Regime

Previous studies, in particular those by Favier, Pinelli, and Piomelli [1], as well as Stanway [3] pointed out the importance of the Reynolds number effects on the performance of tubercled wings. It is likely that the flow features present in the laminar flow regime, for instance, are different from those observed for the transitional flow cases. In the present chapter, computational fluid dynamics was employed to ascertain the underlying mechanism induced by the presence of a tubercled leading edge in the laminar flow regime. The current chapter, reports the findings presented in the article titled, “Streamwise vortices between tubercles”, accepted for publication in the Journal of Fluid Mechanics.

Numerical simulations were performed on a modified and an unmodified hydrofoil based on the NACA 0021 profile at a Reynolds number equal to 2,230. Validation of the numerical work was done using the vorticity field data obtained by water tunnel Particle Image Velocimetry tests conducted by Hansen [2]. Satisfactory agreement between experimental and numerical data provided assurance of the validity of the flow structure. The mechanism was then determined by examining the surface shear stress and vorticity fields obtained from numerical simulations. This culminated in arriving at a detailed description of the flow behaviour around the tubercled hydrofoil in question.

Finally, the loading characteristics of the tubercled hydrofoil were compared and contrasted to those of the baseline NACA-0021. Pressure distributions obtained for the three main spanwise locations, namely the peak, the trough and middle sections, illustrated their contributions to the total lift force produced by the hydrofoil. Three-dimensional streamline patterns were then utilised to clearly demonstrate the development of the pairs of counter-rotating streamwise vortices between the tubercles. Also, iso-surfaces of vorticity revealed the global effect of the sinusoidal leading edge on the vorticity field.

- [1] J. Favier, A. Pinelli, and U. Piomelli, "Control of the separated flow around an airfoil using a wavy leading edge inspired by humpback whale flippers," *Comptes Rendus Mecanique*, vol. 3401(1):107-114, 2011.
- [2] K. L. Hansen, "Effect of Leading Edge Tubercles on Airfoil Performance," Doctor of Philosophy Thesis, Mechanical Engineering, University of Adelaide, Adelaide, SA, Australia, 2012.
- [3] M. J. Stanway, "Hydrodynamic effects of leading-edge tubercles on control surfaces and in flapping foil propulsion," Master of Science in Ocean Engineering Mechanical Engineering, Massachusetts Institute of Technology, February 2008.

## Statement of Authorship

Title of Paper	Evolution of the streamwise vortices generated between leading edge tubercles
Publication Status	<input type="checkbox"/> Published <input checked="" type="checkbox"/> Accepted for Publication <input type="checkbox"/> Submitted for Publication <input type="checkbox"/> Publication Style
Publication Details	Journal of Fluid Mechanics

Name of Principal Author	Dr. Kristy Lee Hansen
Contribution to the Paper	Reviewed the literature. Independently conducted water tunnel PIV tests. Computed the vorticity fields and the variation of circulation with chordwise location using well-established methods. Analysed the flow mechanism in detail. Investigated unsteady flow effects using sophisticated algorithms. Provided a description for the surface flow behavior. Planned and drafted the manuscript.
Signature	
	Date 20/11/2015

### Co-Author Contributions

By signing the Statement of Authorship, each author certifies that:

- i. the candidate's stated contribution to the publication is accurate (as detailed above);
- ii. permission is granted for the candidate to include the publication in the thesis; and the sum of all co-author contributions is equal to 100% less the candidate's stated contribution

Name of Co-Author (Candidate)	Nikan Rostamzadeh
Contribution to the Paper	Responsible for conducted the numerical simulations using the laminar and transitional flow solvers. Created the CAD models of the hydrofoils. Generated the computational grids. Carried out grid sensitivity analyses. Identified the underlying flow mechanism. Assisted with the description of the flow mechanism. Computed the near-wall vorticity and shear stress fields from CFD data. Assisted with the explanation for peak vorticity attenuation. Helped establish the connection between the spanwise pressure gradient field and vorticity generation mechanism by assembling evidence from the CFD data set. Computed the cross-sectional lift coefficients..
Signature	
	Date 22/11/2015

Name of Co-Author	Associate Professor Richard Malcolm Kelso
Contribution to the Paper	Supervised the work. Critically analysed the flow mechanism. Conceived of the idea of the vortex canopy and the contribution of the reversed flow region to the streamwise vortex development. Also proposed the use of vortex lines to illustrate flow development. Assisted with the editing of the manuscript. Suggested the owl-face flow topology. Provided a description for the owl-face flow topology in regards the flow over the tubercled hydrofoil.
Signature	
	Date 23/11/2015

Name of Co-Author	Professor Bassam B. Dally
Contribution to the Paper	Supervised the work. Assisted with the editing of the manuscript.
Signature	
	Date 23/11/2015

## Evolution of the streamwise vortices generated between leading edge tubercles

Journal:	<i>Journal of Fluid Mechanics</i>
Manuscript ID	JFM-15-S-0209.R3
mss type:	Standard
Date Submitted by the Author:	n/a
Complete List of Authors:	Hansen, Kristy; Flinders University , School of Computer Science, Engineering and Mathematics Rostamzadeh, Nikan; University of Adelaide, Mechanical Engineering Kelso, Richard; The University of Adelaide, Centre for Energy Technology Dally, Bassam; The University of Adelaide, Centre for Energy Technology; University of Adelaide, Mechanical Engineering
Keyword:	Aerodynamics, Flow Control, Mixing enhancement < Flow Control

SCHOLARONE™  
Manuscripts

# Evolution of the streamwise vortices generated between leading edge tubercles

Kristy L. Hansen<sup>1</sup>, Nikan Rostamzadeh<sup>2</sup>, Richard M. Kelso<sup>2</sup> and Bassam B. Dally<sup>2</sup>

<sup>1</sup>School of Computer Science, Engineering and Mathematics, Flinders University.

<sup>2</sup>School of Mechanical Engineering, the University of Adelaide.

Sinusoidal modifications to the leading edge of a foil, or tubercles, have been shown to improve aerodynamic performance under certain flow conditions. One of the mechanisms of performance enhancement is believed to be the generation of streamwise vortices, which improve the momentum exchange in the boundary layer. This experimental and numerical study investigates the formation and evolution of these streamwise vortices at a low Reynolds number of  $Re = 2230$ , providing insight into both the averaged and time-dependent flow patterns. Furthermore, the strength of the vortices is quantified through calculation of the vorticity and circulation and it is found that circulation increases in the downstream direction. There is strong agreement between the experimental and numerical observations and this allows close examination of the flow structure. The results demonstrate that the presence of strong pressure gradients near the leading edge, gives rise to a significant surface flux of vorticity in this region. As soon as this vorticity is created, it is stretched, tilted and diffused in a highly three-dimensional manner. These processes lead to the generation of a pair of streamwise vortices between the tubercle peaks. A horseshoe-shaped separation zone is shown to initiate behind a tubercle trough and this region of separation is bounded by a canopy of boundary layer vorticity. Along the sides of this shear layer canopy, a continued influx of boundary layer vorticity occurs, resulting in an increase in circulation of the primary streamwise vortices in the downstream direction. Flow visualisation and PIV studies support these observations and demonstrate that the flow characteristics vary with time, particularly near the trailing edge and at a higher angle of attack. Numerical evaluation of the lift and drag coefficients reveals that, for this particular flow regime, the performance of a foil with tubercles is slightly better than that of an unmodified foil.

## I. INTRODUCTION

Tubercles are rounded, leading edge protuberances that alter the flow field around a foil. It has been suggested that tubercles on the humpback whale flipper function as lift enhancement

devices, allowing flow to remain attached for a larger range of attack angles, thus delaying stall and increasing the maximum lift coefficient with minimal drag penalties<sup>1</sup>. This improved performance has been demonstrated both experimentally and numerically<sup>1-3</sup>.

A number of explanations for the observed performance enhancement have been proposed which include: increased boundary layer momentum exchange<sup>1, 2, 4-6</sup>; compartmentalisation of the flow and subsequent minimisation of tip stall<sup>2, 5, 7, 8</sup>; non-uniform separation characteristics<sup>2, 6, 9, 10</sup>; alteration of the pressure distribution over the foil surface<sup>10</sup> and vortex lift<sup>4, 7</sup>. The different explanations for performance enhancement may arise from variations in the Reynolds number, aspect ratio, wing tip condition, sweep, taper and tubercle geometry. A more detailed literature review on the effect of these parameters can be found in Hansen *et al.*<sup>11</sup> but here, the discussion will be limited to the effect of the tubercle geometry.

According to a parametric study carried out by Favier *et al.*<sup>12</sup>, variation of the amplitude and wavelength of tubercles affects the wake topology, the size of the recirculation zone and the strength of the wake vortex shedding. These researchers investigated a deep stall condition with an angle of attack,  $\alpha = 20^\circ$  and a low Reynolds number of  $Re = 800$ . It was shown that for amplitude to chord ratios,  $A/c < 0.07$ , the intensity of the vortices is too weak to stabilise the separation region. For  $A/c \geq 0.07$ , the frequency spectrum was observed to flatten, indicating a weakening of the wake vortex shedding. The wavelength between tubercles was found to influence the separation characteristics, where the flow was fully separated for  $A/c = 0.07$ ,  $\lambda/c = 0.5$  but attached behind the peaks for  $A/c = 0.07$ ,  $\lambda/c = 1$ . A parametric study was also performed by Johari *et al.*<sup>6</sup> and it was highlighted that the maximum lift coefficient, highest stall angle and minimum drag was achieved by the tubercle configuration with the smallest amplitude and smallest wavelength of tubercles ( $A/c = 0.025$ ,  $\lambda/c = 0.25$ ). On the other hand, the tubercle configuration with the largest amplitude tubercles ( $A/c = 0.12$ ) exhibited the most gradual stall. These findings were supported by Hansen *et al.*<sup>11</sup> and it was shown that for a given amplitude to wavelength ratio,  $A/\lambda$ , the maximum lift coefficient, highest stall angle and minimum drag were attained for the smallest amplitude and wavelength configuration ( $A/c = 0.029$ ,  $\lambda/c = 0.11$ ). Flow visualisation results indicated that streamwise vortices were present for all tubercle configurations investigated but the size of these structures increased with tubercle amplitude.<sup>11</sup>



Previous studies have shown that streamwise vortices exist as counter-rotating pairs which are located in the troughs between tubercles<sup>4, 13, 14</sup>. The existence of streamwise vortices is of importance since many of the proposed performance enhancement mechanisms can be explained with reference to this flow phenomenon. Various mechanisms have been proposed to be responsible for the generation of streamwise vorticity. Weber *et al.*<sup>15</sup> suggested that each tubercle can be modelled as a small delta wing with a rounded leading edge. For a delta wing, the flow separates from the leading edge as it passes from the pressure surface to the suction surface, leading to formation of a pair of streamwise vortices<sup>16</sup>. On the other hand, Favier *et al.*<sup>12</sup> proposed that the generation of streamwise vortices is attributed to a Kelvin-Helmholtz instability which arises due to differences in flow velocities behind the tubercle peaks and troughs. It was suggested that this instability produces tubes of vorticity, aligned normal to the surface in the leading edge region, which are abruptly rotated into the streamwise direction as the vorticity is advected by the mean flow. The existence of surface normal vorticity was shown experimentally by Stanway<sup>14</sup> using particle image velocimetry. Pairs of vortical structures of opposite sign were identified in the regions downstream from each tubercle<sup>14</sup>. These structures were found to strengthen with increasing angle of attack<sup>14</sup>.

Considering the flow field to contain a series of counter-rotating streamwise vortices as observed by Weber *et al.*<sup>15</sup>, it can be deduced that there is a net downwash at the tubercle peaks and a net upwash at the troughs. This is consistent with the results presented by van Nierop *et al.*<sup>10</sup> which show mathematically that the variation in chord and thickness for a foil with tubercles creates changes in the circulation with spanwise location. Consequently a sheet of streamwise vortices is generated behind the wing, causing a higher relative downwash at the peaks relative to the troughs and a variation in the effective angle of attack with spanwise location<sup>10</sup>. There is also a more severe pressure gradient behind the troughs which leads to earlier separation compared to the peak regions<sup>6, 10, 15</sup>. Moreover, the magnitude of the suction peak within the troughs is higher than that on the peaks for a given angle of attack, which leads to a spanwise variation in pressure<sup>17</sup>.

The strong spanwise pressure gradient near the leading edge is another important aspect of the flow physics specific to tubercles which has been observed in several numerical simulations<sup>15, 17, 18</sup> and also experimentally using pressure taps<sup>13, 18</sup>. According to Skillen *et al.*<sup>17</sup>, this spanwise pressure gradient induces a secondary flow slightly aft of the leading edge whereby low-momentum boundary-layer fluid is transported in the spanwise direction from peak to

trough. The low-inertia fluid which has been transported away from the peak location by this secondary flow is replaced by high-momentum fluid drawn from above. There is a corresponding delay in flow separation behind the tubercle peaks<sup>17</sup>. This mechanism is complemented by a lower effective angle of attack at the peak position which also leads to greater flow attachment<sup>10</sup>. Rostamzadeh *et al.*<sup>19</sup> identified that since spanwise circulation varies along the span of the foil<sup>10, 18</sup>, spanwise vorticity should also vary by virtue of Stokes' law. The cyclic variation in spanwise vorticity was shown to lead to the development of pairs of counter-rotating streamwise vortices. Turning of the vortex lines from a spanwise-dominant orientation towards the streamwise and surface normal directions was attributed to the development of *Prandtl's secondary flow of the first type*. This mechanism is activated by the presence of skewness in the flow, arising from spanwise pressure gradients, and vorticity within the boundary layer<sup>19</sup>. The existence of surface normal vorticity observed in the experiments by Stanway<sup>14</sup> is attributed to this mechanism rather than a Kelvin-Helmholtz instability as suggested by Favier *et al.*<sup>12</sup>.

Therefore, one of the aims of the present work is to investigate the nature, formation and development of streamwise vortices over the suction surface of a foil with tubercles in the laminar flow regime. This is facilitated by the analysis of particle image velocimetry (PIV) results to determine the velocity fields on a series of image planes positioned perpendicular to the mean flow. These image planes are located at different chordwise positions, allowing observation of the downstream development of the velocity field. This information enables vorticity and circulation to be determined thus facilitating identification of the streamwise vortices and quantification of their strength. The PIV investigation is complemented with a computational fluid dynamics (CFD) simulation, where the experimental conditions are matched as closely as possible. The CFD results provide a means of investigating the flow structure in greater depth to reveal the complex nature of the flow pattern and mechanisms of vorticity generation. The evolution of the flow pattern over time is also illustrated using hydrogen bubble visualisation and the results support the observations made in the PIV and CFD investigations.

## II. EXPERIMENTAL WORK

### A. EQUIPMENT

Experiments were undertaken in a free-surface closed-return water channel at the University of Adelaide. The working section of this flow facility is 350mm x 500mm and is made entirely of clear acrylic. The freestream velocity of  $U_\infty = 32$  mm/s was selected for the PIV measurements as the lowest number of outliers (spurious velocity vectors) in the velocity vector field were recorded at this velocity compared to higher freestream velocities. This remained the case even when the timing between laser pulses was varied, since the flow structures moved relatively slowly at this velocity. At a freestream velocity of  $U_\infty = 32$  mm/s, the Reynolds number based on foil chord is  $Re = 2230$  and the measured turbulence intensity was approximately 1.7% based on an ensemble average of 3845 image pairs.

The foil profile chosen for the experiments was the NACA 0021 since it resembles the cross-section of the humpback whale flipper<sup>1</sup>. The mean foil chord length was  $c = 70$  mm and the planform shape rectangular. The foil was machined from aluminium on a numerically-controlled milling machine and in order to reduce laser reflections, it was anodised in matte black. It was mounted such that it extended from the water surface to within 1mm of the channel floor to minimise three-dimensional effects. This is within the range of the suggested maximum gap of  $0.005 \times \text{span}$ <sup>20</sup>.

Based on results from a study by Fish and Battle<sup>5</sup>, the average amplitude,  $A$  and wavelength,  $\lambda$ , for tubercles on a humpback whale flipper is approximately  $A = 4$ mm and  $\lambda = 30$ mm. However, to ensure that the vortex structures would be resolvable with sufficient accuracy, a larger amplitude was chosen compared to the average tubercle amplitude on the humpback whale flipper. Figure 1 (a-b) show the foil with tubercles, where the amplitude was selected to be  $A = 8$  mm and the wavelength,  $\lambda = 30$ mm.

This configuration was chosen based on the results of previous studies, which indicated that a larger amount of post-stall lift is achieved for larger amplitude tubercles<sup>4, 6, 10, 13</sup>. If the streamwise vortices are either directly or indirectly responsible for this increased post-stall lift, it is implied that the strength and perhaps size of vortices for larger amplitude tubercles is greater. An increase in the vortex intensity with tubercle amplitude has, in fact, been demonstrated by Favier *et al.*<sup>12</sup> and flow visualisation results indicate that the size of the

vortices increases with tubercle amplitude<sup>11</sup>. Larger vortex structures with relatively high vorticity are desirable for PIV measurements as there is a corresponding improvement in the spatial resolution and signal-to-noise ratio of the results. Potential applications for larger amplitude tubercles include wind turbines, where increased post-stall lift and more gradual stall characteristics would be beneficial, especially in light and variable conditions.

## B. HYDROGEN BUBBLE VISUALISATION

For the hydrogen bubble visualisation investigation, the foil was mounted vertically at an angle of attack of  $\alpha = 10^\circ$ . Streaklines of hydrogen bubbles were generated by passing a low current through a sinusoidally-kinked platinum wire with diameter of  $40 \mu\text{m}$ . The wire was mounted vertically and connected to electrodes which were wired to a power supply that supplied the current necessary for electrolysis. The mounts were constructed and positioned in such a way as to minimise interference with the flow. The flow was illuminated with a thin light sheet ( $\sim 10\text{mm}$  thick) generated using an overhead projector that was partially covered, leaving a narrow slit. Images were digitally recorded via a SONY DCR-TRV900E Mini-DV video camera which was connected to a laptop computer.

The water channel velocity was selected to give optimum flow conditions for visualisation with the hydrogen bubble method. Thus, a velocity of  $U_\infty = 70\text{mm/s}$  was utilised, corresponding to Reynolds number based on the foil chord length of  $Re = 4370$ . This Reynolds number is still in the laminar range and therefore the corresponding flow patterns would be consistent with the slightly lower Reynolds number of  $Re = 2230$  that was used in the PIV experiments.

## C. PARTICLE IMAGE VELOCIMETRY

A series of image planes at  $x'/c = 0.2, 0.4, 0.6, 0.8$  and  $1$  were used to observe the development of the streamwise vortices as shown in Figure 1 (c). The  $x$ - $y$ - $z$  coordinate system is also shown in the figure and this remains stationary for the remainder of this paper. The  $z$ -axis is perpendicular to both the  $\alpha = 0^\circ$  chordline and the trailing edge. The  $x$ -axis is aligned with the chordline at  $\alpha = 0^\circ$  and the  $x'$ -axis follows the foil chord at all angles of attack and is related to the  $x$ -axis by  $x' = x/\cos \alpha$ , since the foil is rotated about the trailing edge. While the foil is stationary and does not undergo any pitching motion, the angle between the  $z$ -axis and  $x'$ -axis is dependent on the angle of attack. The  $y$ -axis is perpendicular to the chordline and parallel with the trailing edge. The origin is located at the trough location with respect to the span, at the mean chord location with respect to the chord and at the chord line with respect to the thickness. The experimental investigation considered angles of attack of  $\alpha = 5^\circ$  and  $10^\circ$ . The

image plane at  $x'/c = 0.2$  yielded successful results for  $\alpha = 10^\circ$  only, hence this plane is not considered for  $\alpha = 5^\circ$ .

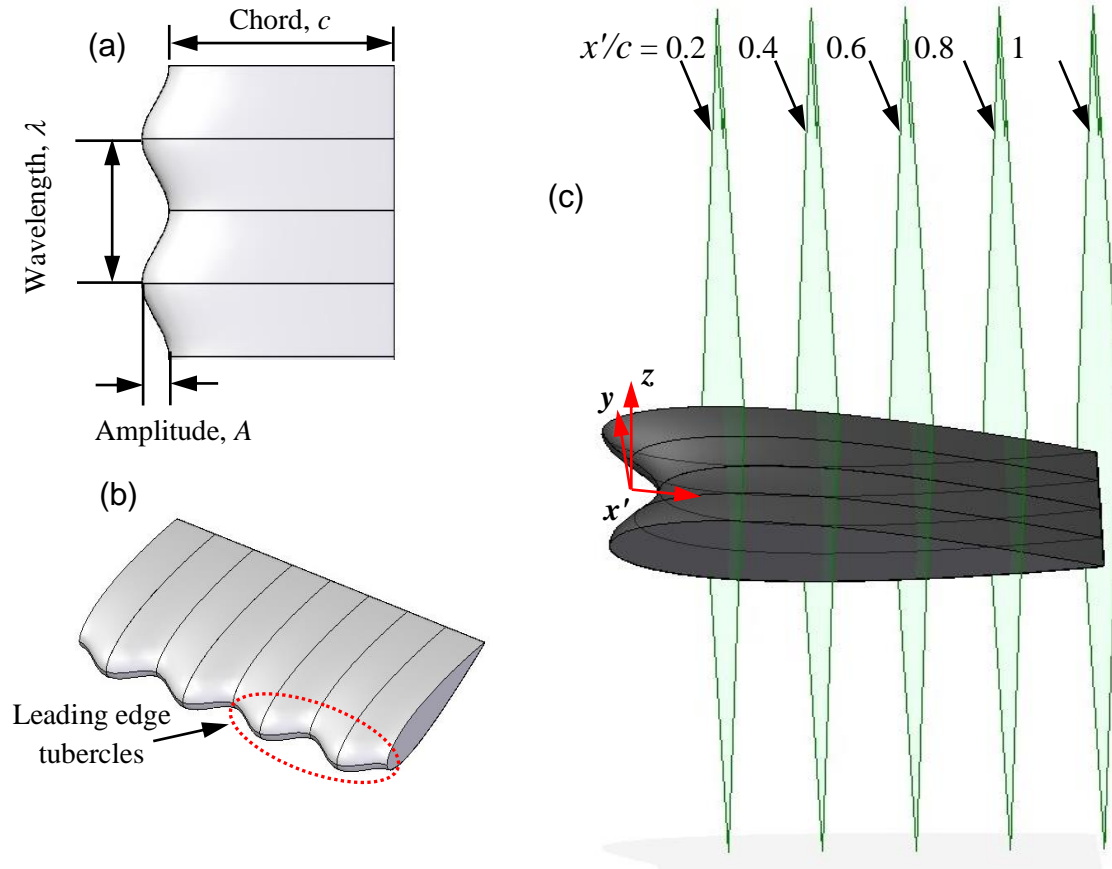


Figure 1. (a) Tubercle dimensions, (b) 3D view of foil section with tubercles, (c) Foil section with tubercles showing particle image velocimetry image planes.

Since the pattern of the sinusoidal tubercles is periodic, it was not necessary to measure the velocity field for the entire foil span. Therefore a compromise was made between resolving the flow patterns and ensuring that the area under investigation was sufficiently large to give an accurate representation of the overall flow behavior. Based on these considerations, the field of view shown in Figure 2 was chosen, giving an area of interest of 40mm x 40mm and including two peaks and one trough. It was expected that the streamwise vortices would exist as counter-rotating pairs in each trough as shown in Figure 2. The measurement plane was located at the mid-span of the foil to minimise end effects.

Velocity components in the plane shown in Figure 2 were measured using two-component PIV. The flow was seeded with polyamid seeding particles (PSP) which had mean diameter of  $d_p = 50\mu\text{m}$  and a density of  $\rho_p = 1030\text{kg/m}^3$ . Illumination was provided by a dual-cavity Quantel

Brilliant B Nd:YAG laser. The wavelength of the laser light was 532nm and the duration of each laser pulse was approximately 5ns. From the laser beam, an optics train generated a 2mm-thick light sheet. The optics set-up and camera positioning are shown in Figure 3.

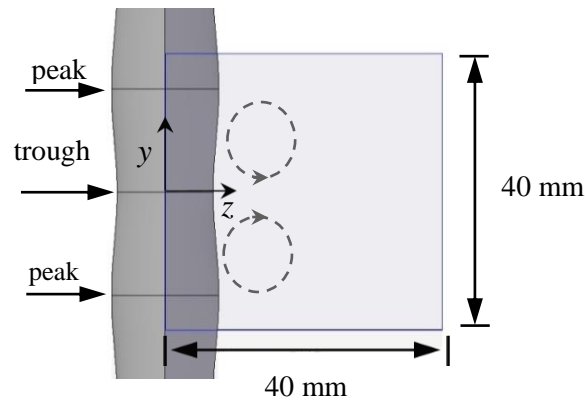


Figure 2. Typical field of view for PIV experiments (as seen by camera), where trailing edge and  $x'$ -axis point out of the page.

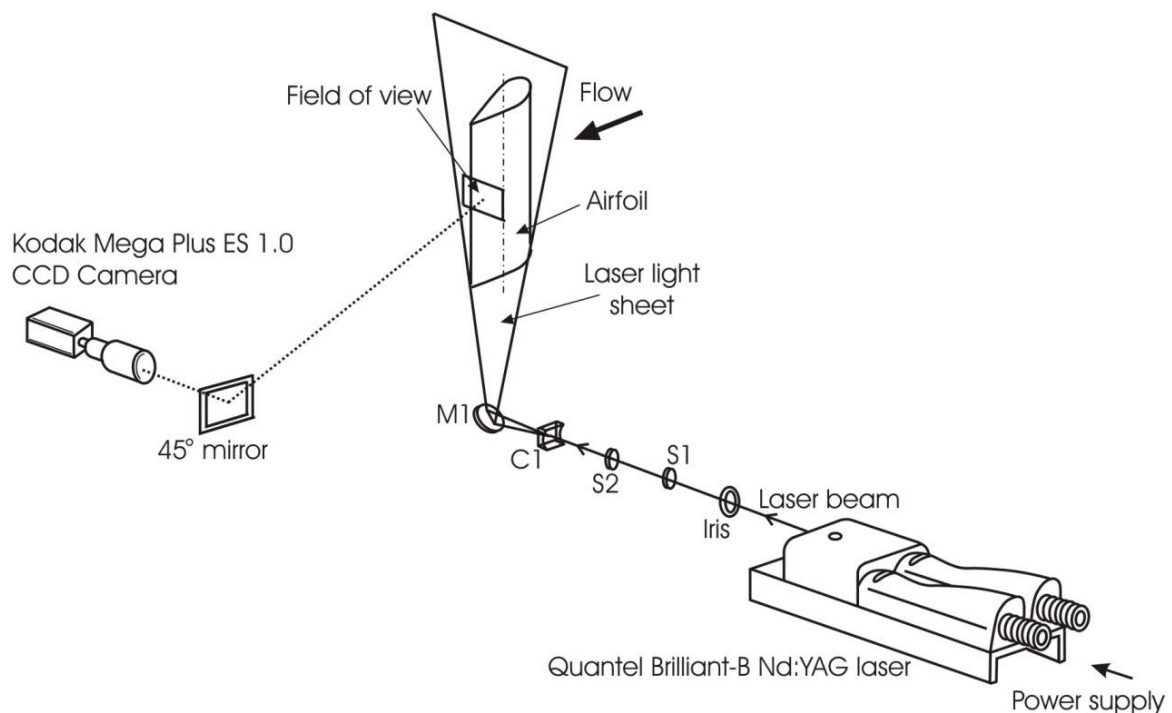


Figure 3. Optics set-up for particle image velocimetry experiments (not to scale).

PIV images were recorded using a Kodak Megaplug ES 1.0 CCD camera with an array of 1008 pixels x 1018 pixels and a Nikon 70-300 mm zoom lens. The image region of 40mm x 40mm gave a spatial resolution of approximately 25pixels/mm. PIV image pairs were collected at a rate of 10Hz, with a time delay between the laser pulses which illuminated the first and second image in each pair ranging from 20 to 32 ms. A Stanford DG535 pulse-delay generator regulated the triggering of the laser pulses from each laser cavity and enabled synchronisation

with the recording system. XCAP-Plus software collected and transferred images to the computer hard disk as uncompressed 16-bit TIFF files. PIV velocity vectors were obtained by cross correlation of the image pairs using the software package PivView v1.75. An interrogation-window size of 32 x 32 pixels was used with 50% overlap. Correlation peaks were detected using a multi-pass double correlation, least squares Gaussian fit. Spurious velocity vectors or outliers were detected using a custom-written Matlab code which implemented the universal median technique described by Westerweel and Scarano<sup>21</sup>.

To minimise uncertainties in the velocity-vector field a total of 2085 image pairs were averaged temporally. Due to the large number of image pairs available, outliers detected using the normalised mean test<sup>21</sup> were not replaced and instead were omitted from the averaging process. For all averaged results presented in this paper, the number of outliers in a given velocity-vector field was less than 1% of the total number of vectors. This confirms the validity of the measurements and verifies that out-of-plane particle motion had negligible effect on the results.

For the instantaneous results which were used to show time-dependent characteristics, detected outliers were replaced with a weighted average of valid surrounding vectors. Subsequently, an adaptive Gaussian window interpolator was implemented to reduce the amount of random noise associated with the velocity-vector field as suggested by Agui and Jiminez<sup>22</sup>.

The average out-of-plane vorticity field,  $\omega_x$ , was calculated from the in-plane velocity components using Equation (1).

$$\omega_x = \frac{\partial w}{\partial y} - \frac{\partial v}{\partial z} \quad (1)$$

The chosen numerical scheme was the central difference scheme, which is adequate for most applications<sup>23</sup>. Other schemes were considered but since the areas of interest were in close proximity to the boundaries of the velocity field, their large computational stencil caused inaccuracies.

The circulation,  $\Gamma$ , of each vortex core was estimated by numerical integration based on the closed curve line integral given in Equation (2).

$$\Gamma_{vel} = \oint_c (v dy + w dz) \quad (2)$$

The region enclosed by the path of integration encompassed the streamwise vortices and remained constant in area for each spanwise plane.

The random and bias uncertainties in particle displacement were calculated with reference to Raffel *et al.*<sup>24</sup>, Willert and Gharib<sup>25</sup>, Fouras and Soria<sup>26</sup>, Lau<sup>27</sup> and Hassan *et al.*<sup>28</sup> The overall uncertainty in vorticity for the averaged data was 1.4% and the uncertainty in circulation is less than 1%. The uncertainty analysis is discussed in further detail in Appendix A.

### III. VORTICITY

A series of vorticity plots are shown in this section for angles of attack of  $\alpha = 5^\circ$  and  $\alpha = 10^\circ$ . In the vorticity plots, a counter-clockwise sense of rotation is defined as positive (red) and a clockwise sense of rotation is defined as negative (blue). Images associated with each spanwise plane have been located adjacent to one another for comparison. Both the y- and z-axes have been made non-dimensional through dividing by the tubercle wavelength. The lower limit of the z-axis values is governed by the foil curvature as well as the angle of attack and hence is nonzero in most cases. For example, at  $x'/c = 0.4$  and  $\alpha = 5^\circ$ , the distance in the z-direction between the origin and the foil surface can be calculated as  $z_{surface} = 10.7$  mm, using the following equation:

$$z_{surface} = (1 - x'/c) \times c \sin \alpha + t(x') \times \cos \alpha \quad (3)$$

Here,  $t(x)$  is the local thickness of the foil, which is evaluated at the point of interest. A schematic diagram is shown in Figure 4 to illustrate the methodology used to derive Equation (3). The corresponding non-dimensional value is  $z/\lambda = 0.36$  which is close to the minimum value of the z-axis in Figure 5 (a). Differences are due to the discretization error associated with the size of the PIV interrogation windows.

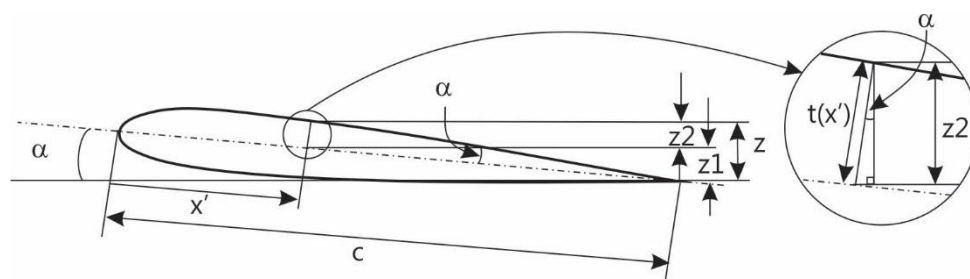


Figure 4. Schematic diagram showing geometric quantities used to derive Equation 4.

Figure 5 (a-d) show that between tubercle peaks, there exist adjacent regions of positive (upper section) and negative (lower section) vorticity for all image planes. These regions of vorticity,



marked “P” in Figure 5 (a-b) will henceforth be described as the primary vorticity. With streamwise distance, vortex spreading leads to a decrease in the peak primary vorticity and an increase in the area over which vorticity is distributed. As shown in Figure 5 (a-b), vortex spreading is greater in the  $y$ -direction than the  $z$ -direction, where it is inhibited due to adjacent vorticity of opposite sign.

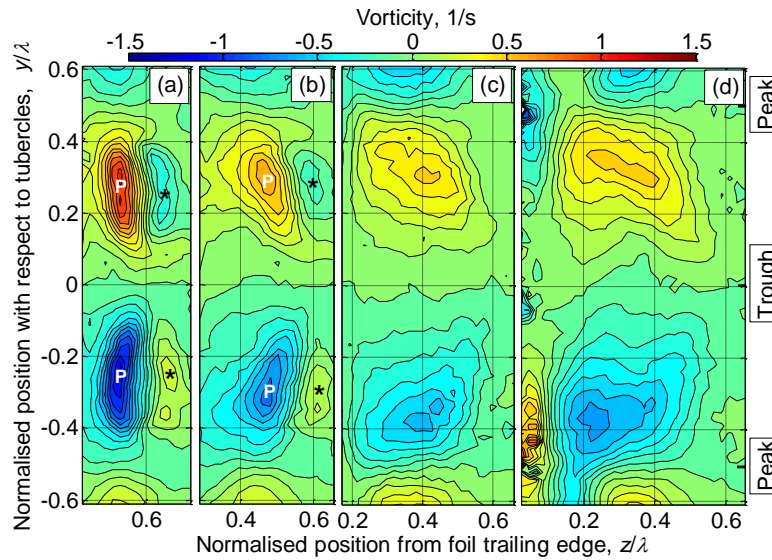


Figure 5. View of vorticity field from behind the foil where counter-clockwise vortex core (red/upper) is positive and clockwise vortex core (blue/lower) is negative. Angle of attack,  $\alpha = 5^\circ$ ,  $Re = 2230$ , image planes are shown for  $x'/c = 0.4, 0.6, 0.8, 1$  (a-d).

This vorticity of opposite sign (or secondary vorticity) has been marked with an asterisk and is evident in the image planes of  $x'/c = 0.4$  and  $x'/c = 0.6$  in Figure 5 (a-b). This vorticity appears to be annihilated by the primary vorticity of opposite sign adjacent to it, as evidenced by its absence for image planes further aft. The process of annihilation is further evidenced by the closely-spaced contours of vorticity between the primary and secondary structures in Figure 5 (a-b).

The asymmetrical appearance of Figure 5 (d) is consistent with the occurrence of unsteady effects at  $x'/c = 1$ , which will be discussed in Section VIII. The asymmetry can also be attributed to possible differences in the flow patterns for adjacent wavelengths of the tubercle pattern. Flow visualisation images have shown that differences in the flow patterns exist for adjacent wavelengths of the tubercle pattern but that alternate wavelengths demonstrate similar characteristics<sup>4</sup>.

Another important feature which is visible in Figure 5 (d) is the existence of wall vorticity which is adjacent to the primary vortices and has an opposite sense of rotation. This wall

vorticity is evident in the streamwise vorticity plots published by Skillen *et al.*<sup>17</sup>, both at similar chordwise locations and at chordwise locations closer to the leading edge. The absence of wall vorticity near the leading edge for the PIV measurements reported here is due to resolution limitations.

Figure 6 shows that increasing the foil angle of attack to  $\alpha = 10^\circ$  gives rise to an increase in the magnitude of the peak vorticity associated with the counter-rotating primary vortices. Consistent with the results at  $\alpha = 5^\circ$ , vortex spreading occurs in the streamwise direction at  $\alpha = 10^\circ$  and the spreading of vorticity is restricted in the  $z$ -direction at  $x'/c = 0.2$  and  $0.4$  due to the proximity of secondary vorticity of opposite sign. Flow asymmetry is evident in the results at  $\alpha = 10^\circ$  for the image planes close to the trailing edge as was observed for  $\alpha = 5^\circ$  and is attributed to the same mechanism.

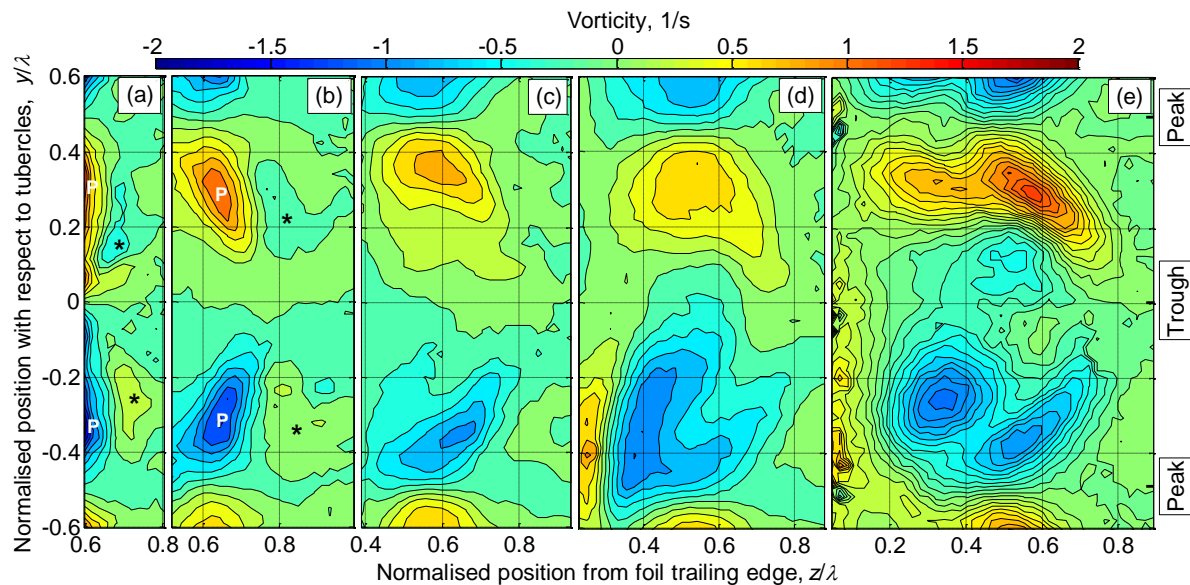


Figure 6. View of vorticity field from behind the foil where counter-clockwise vortex core (red/upper) is positive and clockwise vortex core (blue/lower) is negative. Angle of attack,  $\alpha = 10^\circ$ ,  $Re = 2230$ , image planes are shown for  $x'/c = 0.2, 0.4, 0.6, 0.8, 1$  (a-d).

Figure 7 shows the magnitude of the positive and negative primary vortex peaks corresponding to the contour plots shown in Figure 5 and Figure 6. The magnitude of both vorticity peaks decreases with downstream distance for the image planes nearer to the leading edge ( $x'/c = 0.2 - 0.6$ ) at  $\alpha = 5^\circ$  and  $\alpha = 10^\circ$ . In accordance with Morton<sup>29</sup>, the presence of strong pressure gradients near a foil leading-edge results in the production of vorticity, giving rise to large values of the vorticity field in this region. This vorticity is, then, transported through viscous diffusion as well as the vortex stretching and tilting phenomena into the flow field. With the presence of large velocity gradients, in particular near the leading edge, the mechanism for the

decay of peak vorticity is activated as reflected in Figure 7. Axial compression of streamwise vortices caused by the presence of an adverse pressure gradient on the suction surface of the foil, leads to an increase in the cross-sectional area of the vortices as shown in Figure 5 and Figure 6 and a corresponding reduction in the peak vorticity. The reduction in peak vorticity is also influenced by annihilation of the secondary vorticity, observed in Figure 5 (a-b) and Figure 6 (a-b) as well as diffusion and annihilation between the streamwise vortices themselves. Towards the trailing edge, the magnitude of the peak vorticity increases as a result of the vortex tilting phenomenon as will be discussed in Section VII.

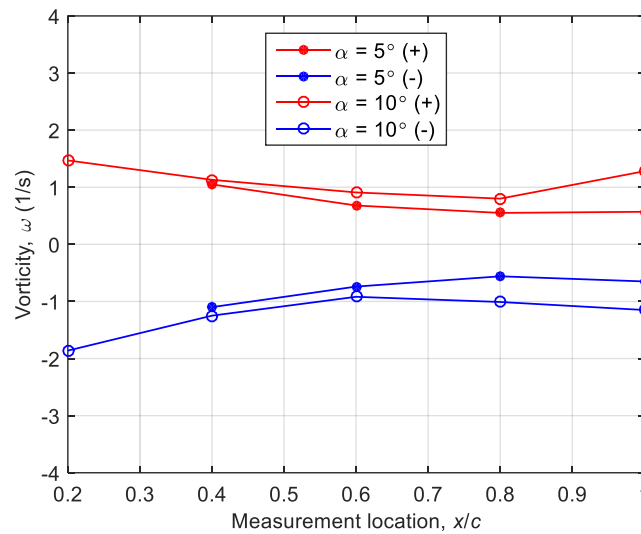


Figure 7. Magnitudes of maximum positive and negative vorticity peaks for  $\alpha = 5^\circ$  and  $\alpha = 10^\circ$ ,  $Re = 2230$ .

#### IV. CIRCULATION OF STREAMWISE VORTICES

The integration paths for calculating the counter-clockwise and clockwise circulation are shown superimposed on the vorticity contour plots for  $\alpha = 5^\circ$  in Figure 8 (a-d). The vorticity plots are shown with the same resolution as in Figure 5 where the increment between contour lines is 0.1 (1/s). The corresponding regions enclosed by the integration paths are of equal size and the left-hand border of each plot aligns with the foil surface. This ensures that all significant vorticity contributions are captured within the integral as  $x'/c$  changes. Extending the right-hand border of these regions has negligible impact on the results. The regions of integration for an angle of attack of  $\alpha = 10^\circ$  are not shown for the sake of brevity.

Results from the integration for  $\alpha = 5^\circ$  and  $\alpha = 10^\circ$  are depicted in Figure 9, where the magnitude of circulation is shown for both the positive and negative primary vortex cores. The circulation of the clockwise and anticlockwise primary vortices increases both with increasing

angle of attack and with streamwise distance from the leading edge. These results were also observed when the region of integration encompassed the primary vorticity only, indicating that the secondary vorticity and wall vorticity have negligible impact on the magnitude of the circulation. To understand the reason behind the increase in circulation, it is first necessary to analyse the flow pattern in detail and this will be done in Section VII. Subsequently, the streamwise increase in circulation will be explained with reference to the identified flow mechanism.

Figure 9 shows that the circulation of the negative vortex is slightly higher than that of the positive vortex for the image planes at  $x'/c = 0.8$  and  $x'/c = 1$  at  $\alpha = 10^\circ$ . This is related to the asymmetry of the primary vortices which is apparent in Figure 6 (d) and Figure 6 (e).

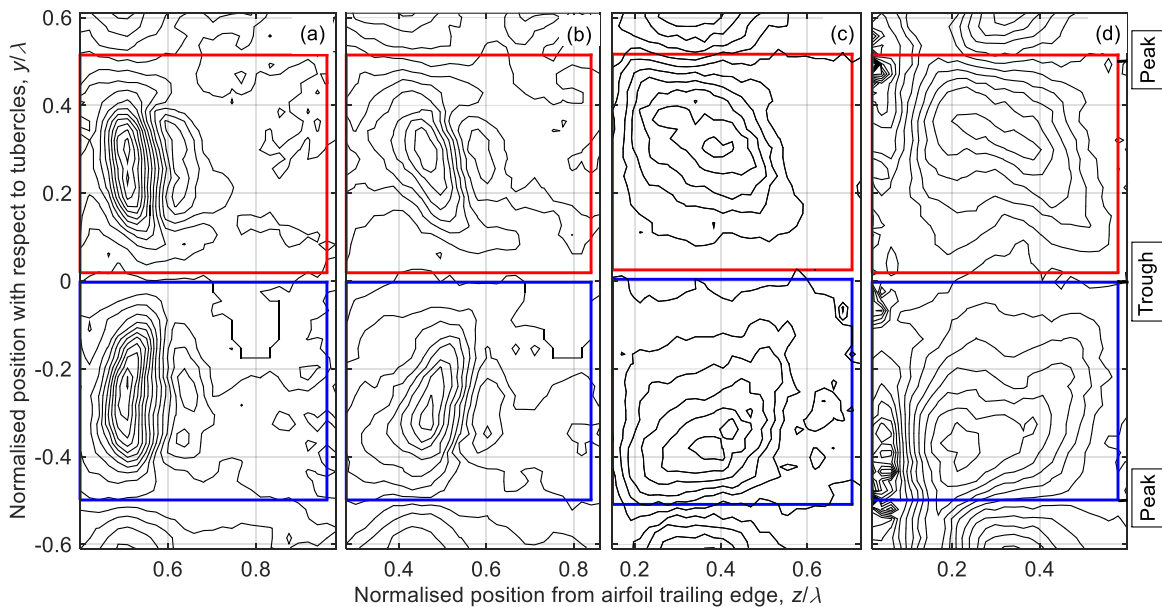


Figure 8. Path of integration and enclosed region for  $\alpha = 5^\circ$ ,  $Re = 2230$ , image planes  $x'/c = 0.4, 0.6, 0.8, 1$  (L to R). Red/upper – integration path for calculating circulation of counter-clockwise vortex, blue/lower - integration path for calculating circulation of clockwise vortex. The vorticity contours are plotted with the same resolution as Figure 5, where the separation between contour lines is 0.1 ( $1/s$ ).

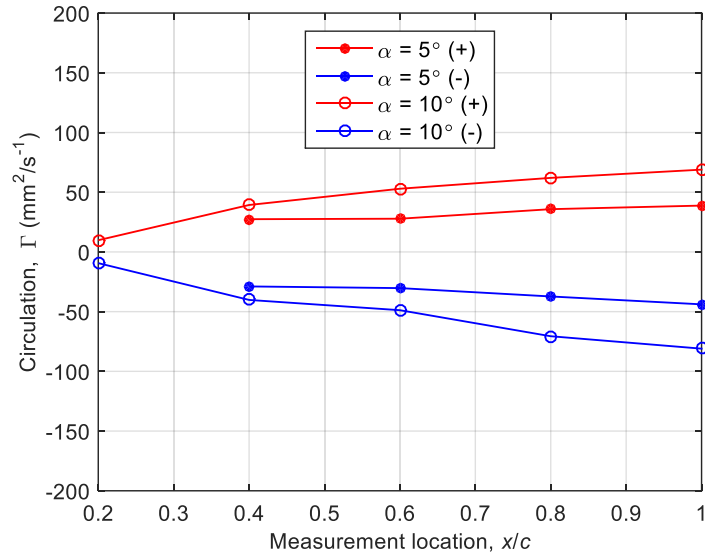


Figure 9. Circulation variation with angle of attack and chordwise position.

A streamwise increase in circulation of the primary vortices has also been observed for delta wings prior to the point at which vortex breakdown occurs<sup>31, 32</sup>. The chord Reynolds numbers investigated were  $Re = 1.9 \times 10^5$  and  $Re = 2.5 \times 10^5$ , and the circulation increase was approximately linear. An approximately linear increase in circulation is also evident in Figure 9.

## V. COMPUTATIONAL FLUID DYNAMICS MODEL

ANSYS CFX 14.5<sup>33</sup> was employed to model the flow over the full-span tubercled and the baseline NACA 0021 foils at  $Re = 2,230$  for the two attack angles described in the experiments ( $\alpha = 5^\circ$  and  $\alpha = 10^\circ$ ). To this end, the transitional SST model  $\gamma - Re_\theta$ ,<sup>34</sup> was used for solving the steady Reynolds Averaged Navier-Stokes equations. The  $\gamma - Re_\theta$  model was successful in capturing the pressure distribution and flow characteristics including the vorticity field around a wavy foil in our previous study<sup>35</sup>.

The boundary layer profile for the CFD results at  $\alpha = 10^\circ$  is shown in Figure 10 for a series of spanwise planes at the peak cross-section. The parabolic flat plate approximation to the laminar boundary layer profile and the turbulent flat plate approximation,  $u/U_\infty = (y/\delta)^{\frac{1}{7}}$ , are also shown for comparison. It can be seen that the boundary layer in the CFD results most closely resembles a laminar profile. This was also found to be the case at the trough and mid cross-sections. This supports the choice of the transitional SST model, since a laminar boundary layer would be expected at the low Reynolds number investigated in this study and a transitional

model allows specification of the freestream turbulence intensity. Initially, a laminar model was implemented but it was found that this model did not resolve the streamwise vortices correctly, leading to discrepancies between the computational and experimental results.

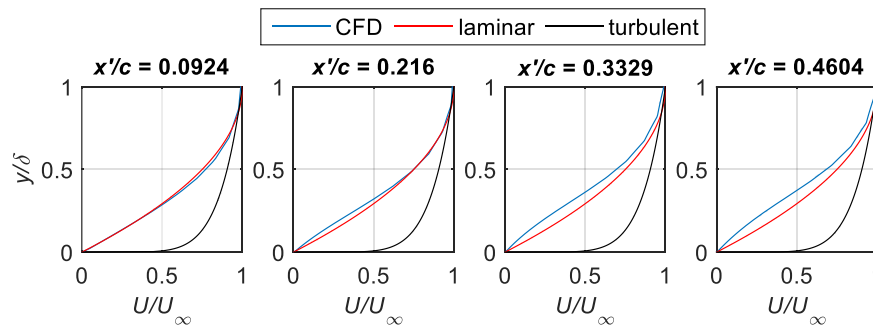


Figure 10. Boundary layer plots for CFD results at an angle of attack of  $\alpha = 10^\circ$  for the foil cross-section corresponding to the tubercle peak.

To discretise the transport equations, ANSYS CFX 14.5 uses an element-based finite volume method<sup>33</sup>. High resolution algorithms were implemented for the advection and turbulence numerical schemes. A C-grid topology with hexahedral elements was adopted as the computational domain with far-field boundaries located at twelve chord lengths from the trailing edges of the foils, as shown in Figure 11. The angle of attack was changed by rotating the model and maintaining constant values for the free-stream velocity components. The foils' surfaces were assigned the no-slip boundary condition, and periodic conditions were applied to the spanwise planes.

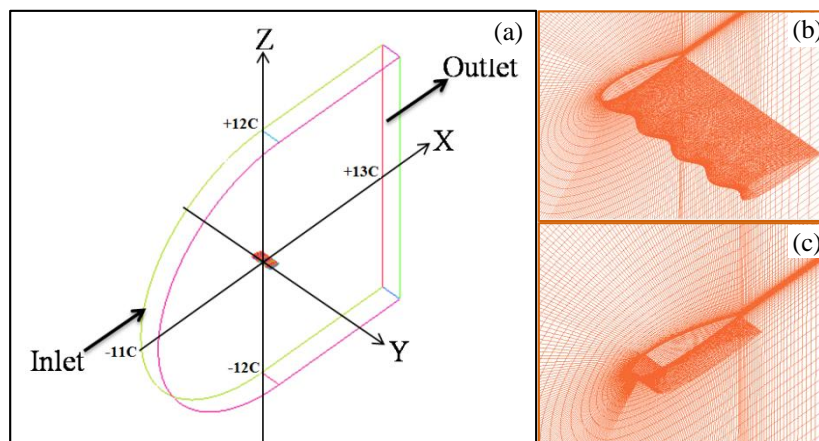


Figure 11. (a) The computational domain and the coordinate system positioned at the leading-edge, (b) grid system in the vicinity of the tubercled foil and (c) unmodified NACA 0021 foil.

As flow separation was expected to occur, the boundary layer had to be resolved with sufficient detail, hence the grid was refined near the wall boundaries such that  $y^+ < 1$ . To assess convergence, the behavior of the force monitor points was considered (see Figure 12) along with a residual target equal to  $10^{-7}$  for the momentum and SST transport equations, and

$1.15 \times 10^{-6}$  for the intermittency transport equation. The force monitor points are the lift coefficient,  $C_L$  and the drag coefficient,  $C_D$ .

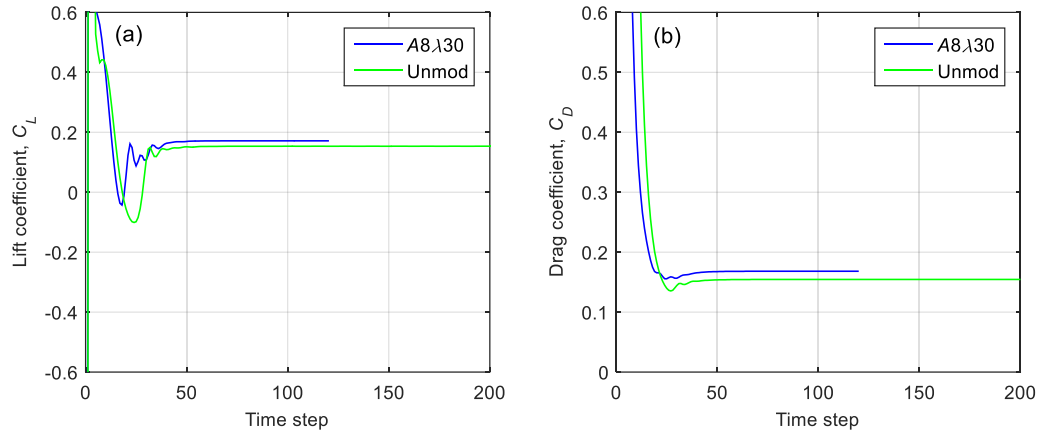


Figure 12. Force monitor plots for (a) lift coefficient and (b) drag coefficient for  $\alpha = 10^\circ$ .

The geometric and the grid characteristics associated with the foils are provided in Table 1. Although the mesh sensitivity analysis showed no difference in the behavior of the forces with a lower density grid test case (total number of hexahedral elements equal to 2,859,012) for the tubercled foil, the adopted grid for simulation was capable of showing finer details of the vorticity field near the foil's surface which was of particular interest in this study. The flow mechanism described in this work was consistently detected across all the test cases, including one with a much higher number of elements (10,748,400).

Table 1. Grid and geometric details of the modelled foils.

Foil Label	Total Number of Hexahedral Elements	Span (mm)	Chord (mm)
A8.130	7,568,400	120 (four wavelengths)	70
Unmodified NACA 0021	907,410	15	70

## A. VALIDATION

The computational model provides information that is not available from the described PIV experiment. However, to ensure that the CFD model accurately captures the flow physics, a series of comparisons were made with the PIV results. The image plane located at  $x'/c = 0.4$  was used for this purpose as it was expected to have a lower associated unsteadiness, in which case, averaging would yield more comparable results. The results for vorticity are shown in Figure 13, where it can be seen that the magnitude and position of the peak vorticity is consistent for the experimental and numerical results for angles of attack of  $\alpha = 5^\circ$  and  $\alpha =$

10°. Differences are apparent in the degree of vorticity spreading, where this is slightly greater for the numerical results shown in Figure 13 (a) and (c). In addition, the CFD technique does not predict the secondary vorticity which was observed in the PIV experiments for image planes close to the leading edge.

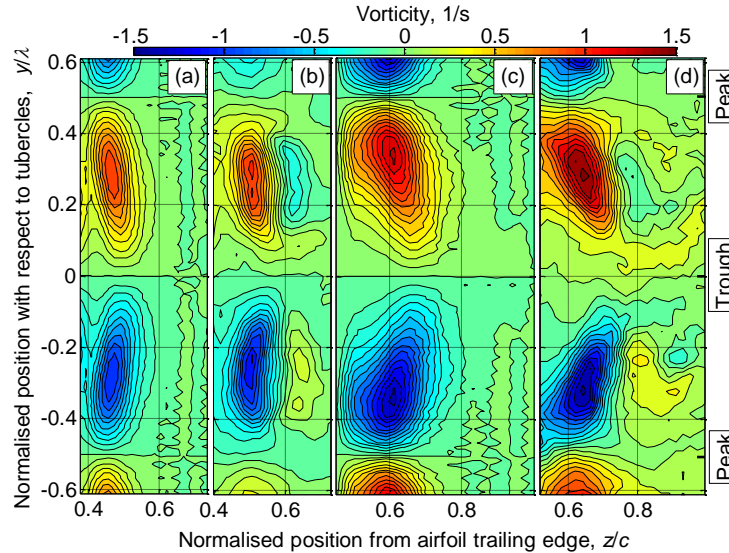


Figure 13. Vorticity at  $Re = 2230$ , image plane  $x'/c = 0.4$ , (a) angle of attack,  $\alpha = 5^\circ$  (CFD), (b) angle of attack,  $\alpha = 5^\circ$  (experiment), (c) angle of attack,  $\alpha = 10^\circ$  (CFD), (d) angle of attack,  $\alpha = 10^\circ$  (experiment).

The CFD results shown in Figure 14 (a) reveal the presence of opposite sign wall vorticity, which was also observed in the PIV experiments as indicated in Figure 14 (b). Figure 14 also indicates that for the image plane at  $x'/c = 0.8$ , CFD predicts a higher peak vorticity and the vortex cores are more symmetrical in comparison to the experimental results.

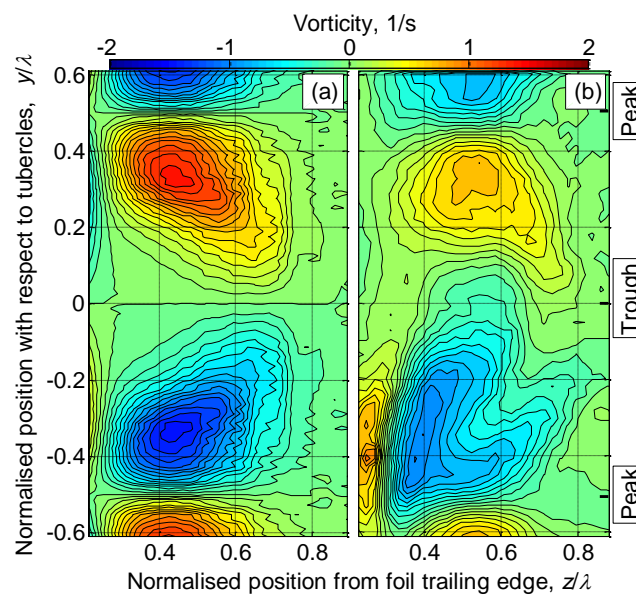


Figure 14. Vorticity at  $Re = 2230$ , image plane  $x'/c = 0.8$ , angle of attack,  $\alpha = 10^\circ$  (a) CFD, (b) experiment.



Comparison between the magnitudes of the peak vorticity determined experimentally and numerically for the other chordwise positions is shown in Figure 15. At an angle of attack of  $\alpha = 5^\circ$ , the magnitude of the peak vorticity is in good agreement for all spanwise planes. There is reasonable agreement between the results at  $\alpha = 10^\circ$ , however the numerical results indicate a higher level of peak vorticity for all image planes. This is attributed to unsteady effects in the PIV experiments that give rise to attenuation of the time-averaged vorticity across the measurement plane as will be discussed in Section VIII. Another notable difference between the experimental and numerical results is the magnitude of the peak vorticity for the image plane at  $x'/c = 0.2$ . Since the vorticity for this particular plane is close to the wall, it may not have been captured in the experiments due to grid resolution limitations and hence, the experimentally determined peak vorticity could be lower than the actual value. This is supported by the fact that the spanwise pressure gradient in the region upstream of  $x'/c = 0.2$  is relatively high, as will be shown in Section VI, and would thus contribute to the generation of streamwise vorticity at the surface in this region<sup>36</sup>.

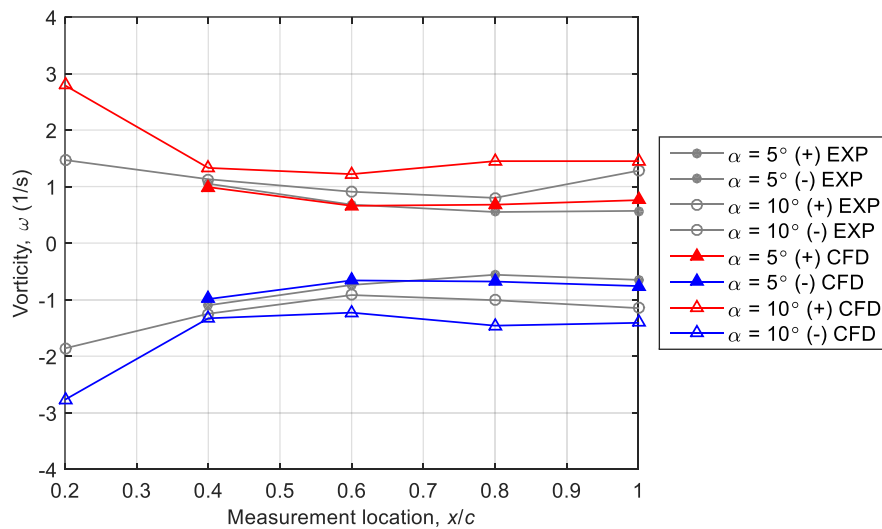


Figure 15. Experimental and numerical magnitude of peak positive and negative vorticity for  $\alpha = 5^\circ$  and  $\alpha = 10^\circ$ ,  $Re = 2230$ .

The circulation was calculated using the method described in Section II.C for both the experimental and numerical cases and is shown in Figure 16. The CFD results confirm that circulation generally increases in the downstream direction for both  $\alpha = 5^\circ$  and  $\alpha = 10^\circ$ . Reasonable agreement was achieved between the circulation results for the various spanwise planes at an angle of attack of  $\alpha = 5^\circ$ . At the higher angle of attack of  $\alpha = 10^\circ$ , the circulation determined from CFD is greater than the value determined experimentally. Also, the CFD results indicate that the circulation decreases between the spanwise planes at  $x'/c = 0.8$  and  $x'/c$

= 1, rather than increasing as determined from the PIV experiments. One explanation for these differences may be that unsteadiness in the experimental flow leads to a variation in the positions and strengths of the vortical features, which manifests as an attenuation of the time-averaged vorticity across the measurement plane as suggested in Section VIII. The result of this phenomenon is a more gradual change in circulation with streamwise location. On the other hand, the differences in the experimental and numerical results may also be an effect of the CFD closure model which influences the location of the separation lines.

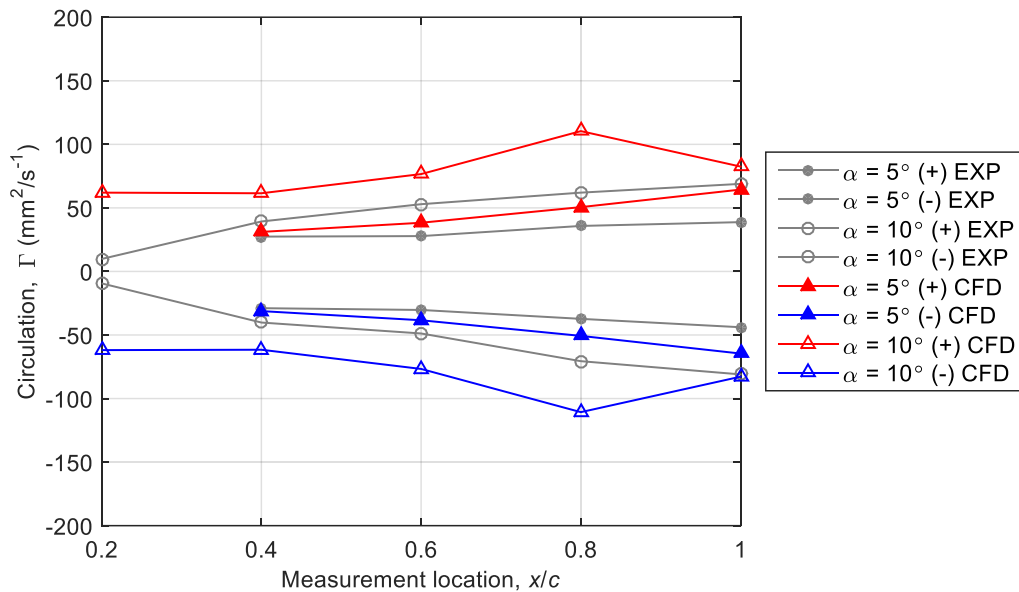


Figure 16. Experimental and numerical results showing variation in circulation with angle of attack and chordwise position.

## VI. PRESSURE FORCES

This section presents the chordwise pressure distributions corresponding to a tubercle peak, trough and midway between. The data were obtained from the CFD simulation described in Section V. Analysis of the surface pressure distributions allows identification of the point at which the adverse pressure gradient initiates for each cross-section, which is relevant to the vortex stretching mechanism. The chordwise pressure distributions show the existence of a spanwise variation in pressure and this is explored further through plotting surface contours of the spanwise pressure gradient. The spanwise pressure gradient is shown to result in generation of streamwise vorticity at the surface. Analysis of the surface pressure data also enables investigation into the spanwise variation in lift.

The chordwise variation in pressure for both the unmodified and tubercled foils at  $\alpha = 10^\circ$  is shown in Figure 17. The most negative values of the peak pressure developed over the suction

surface of the tubercled foil are associated with the trough cross-section. The lowest minimum suction peak occurs at the peak cross-section and the pressure values for the middle cross-section lie somewhere between. This is consistent with results obtained at a higher Reynolds number on a foil with the same profile shape<sup>37</sup>. It must be noted that the slight over-prediction in the pressure coefficient at the stagnation points, is due to numerical error and was not resolved by refining the CFD grids or extending the domain boundaries up to 40 chord lengths. The impact of this error is negligible on the underlying flow mechanism reported in this work.

The location of the suction peak at the trough section is further aft than for the other cross-sections and the unmodified foil. Conversely, the suction peak at the peak cross-section is slightly closer to the leading edge. This variation is attributed to differing positions of maximum thickness as well as changes in chord length with spanwise location. These parameters define the position at which the adverse pressure gradient initiates. At this point, compression of streamwise vortices is initiated, resulting in a larger area over which vorticity is distributed and a reduction in peak vorticity as discussed in Section III.

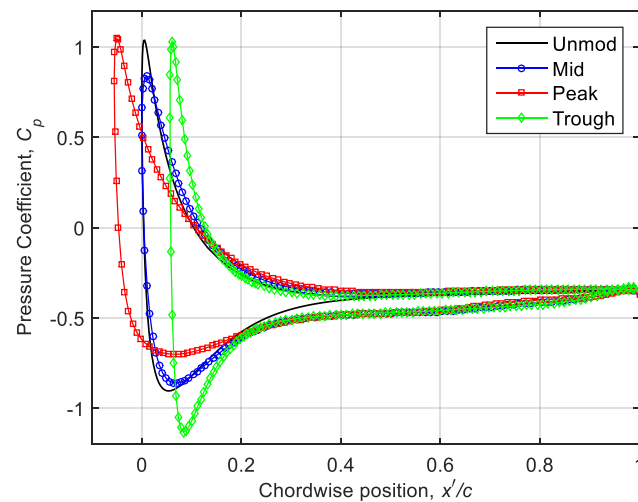


Figure 17. Pressure distribution for the unmodified (unmod) and tubercled foil at  $\alpha = 10^\circ$ , where “Peak”, “Trough” and “Mid” correspond to the cross-sections at the tubercle peak, trough and midway between.

The difference in magnitude and location of the suction peaks for the mid, peak and trough cross-sections gives rise to a spanwise pressure gradient which initiates at the leading edge and persists up to around  $x'/c = 0.2$ . The contour plot shown in Figure 18 indicates the magnitude of the spanwise pressure gradient in the region of the leading edge. It is also evident that a spanwise pressure gradient exists near the trailing edge, however its magnitude is significantly lower.

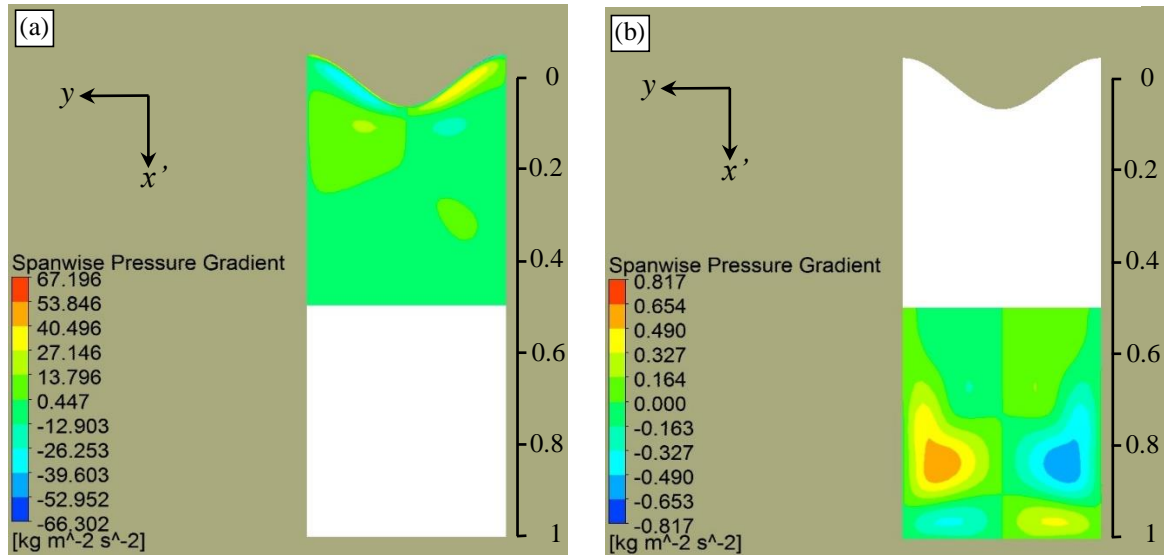


Figure 18. Spanwise pressure gradient on surface of foil at  $\alpha = 10^\circ$ ,  $Re = 2230$ , where highest values occur at foil leading edge.

The presence of a spanwise pressure gradient results in direct production of streamwise vorticity as can be seen by the spanwise momentum equation at the wall expressed in Equation (4)<sup>36</sup>, where coordinate axes are consistent with the diagram in Section I.

$$\rho v_w \left. \frac{\partial v}{\partial z} \right|_{z=0} + \left. \frac{\partial p}{\partial y} \right|_{z=0} - \left. \frac{\partial \mu}{\partial z} \frac{\partial v}{\partial z} \right|_{z=0} = \mu \left. \frac{\partial^2 v}{\partial z^2} \right|_{z=0} \quad (4)$$

The first and third terms on the left-hand side of the equation are equal to zero due to the absence of flow injected from the wall,  $v_w$ , and constant viscosity,  $\mu$ . Therefore, the spanwise pressure gradient,  $\frac{\partial p}{\partial y}$ , can be seen to affect the curvature of the velocity profile shown on the right-hand side of the equation, which is the same as the flux of streamwise vorticity from the wall<sup>36</sup>.

Results from the CFD simulation shown in Table 2 indicate that the lift coefficient achieved by the foil with tubercles is higher than that achieved by the unmodified foil. In addition, the efficiency of the tubercled foil,  $L/D$  is marginally better than the unmodified foil, despite the slight increase in the associated drag. The increased lift for the tubercled foil is attributed to the greater flow attachment which is maintained behind the tubercle peaks. Integration of the pressure at the peak, trough and midway between (mid) cross-sections confirms that the highest proportion of lift is generated at the peak cross-section, as shown in Figure 19. The spanwise variation in the circulation and hence lift coefficient, is also highlighted in Figure 19. The

increased drag for the foil with tubercles is related to the presence of streamwise vortices and the associated increase in surface shear stress.

Table 2. Lift and drag forces at  $\alpha = 10^\circ$  calculated in the CFD simulation.

	$C_L$	$C_D$	$L/D$
Unmodified foil	0.154	0.155	0.994
Tubercled foil	0.172	0.168	1.02

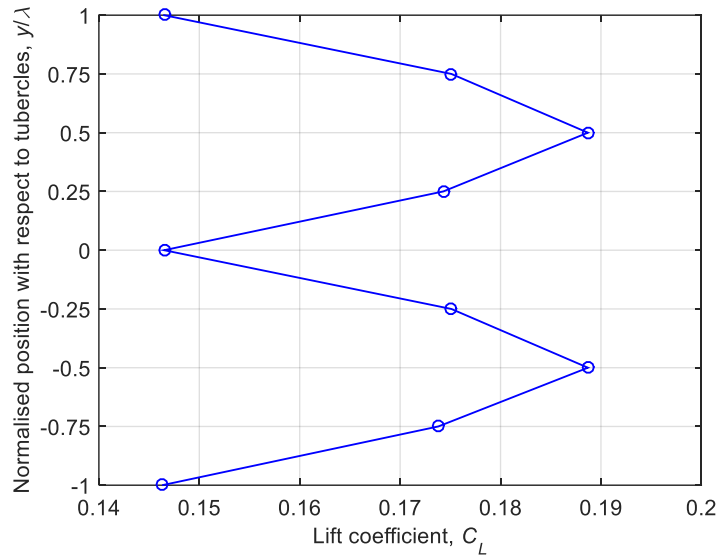


Figure 19. Variation in lift coefficient,  $C_L$ , with spanwise location.

## VII. ANALYSIS OF FLOW CHARACTERISTICS

Regions of separation and attachment of the flow on the foil can be identified from the surface shear stress lines and contours shown in Figure 20 (a-b) and Figure 21 (a-b). These images were obtained from the CFD simulation described in Section V. Behind the tubercle trough, separation occurs much earlier than behind the peak, which is consistent with previous results<sup>6, 10</sup>. The surface shear stress lines show that a large separation zone forms ahead of a pair of foci (F), into which the flow spirals, to be lifted from the surface. The upstream extent of the separation zone is defined by a saddle point (S).

The foci mark the locations at which concentrated vortices separate from the surface of the foil, which occurs at  $x'/c \sim 0.8$  and  $x'/c \sim 0.6$  for  $\alpha = 5^\circ$  and  $\alpha = 10^\circ$ , respectively. Downstream of the foci, aligned with the tubercle peaks, lie a pair of bifurcation lines (BL) which define the spanwise extent of the separation zone. In the following discussion we will describe the downstream evolution of both surface vorticity and vorticity in the separated shear layer. This

analysis provides insight into the mechanisms responsible for the presence of streamwise vorticity in the numerical and experimental results and how these may explain the experimental observations of streamwise vorticity at various spanwise planes above the foil.

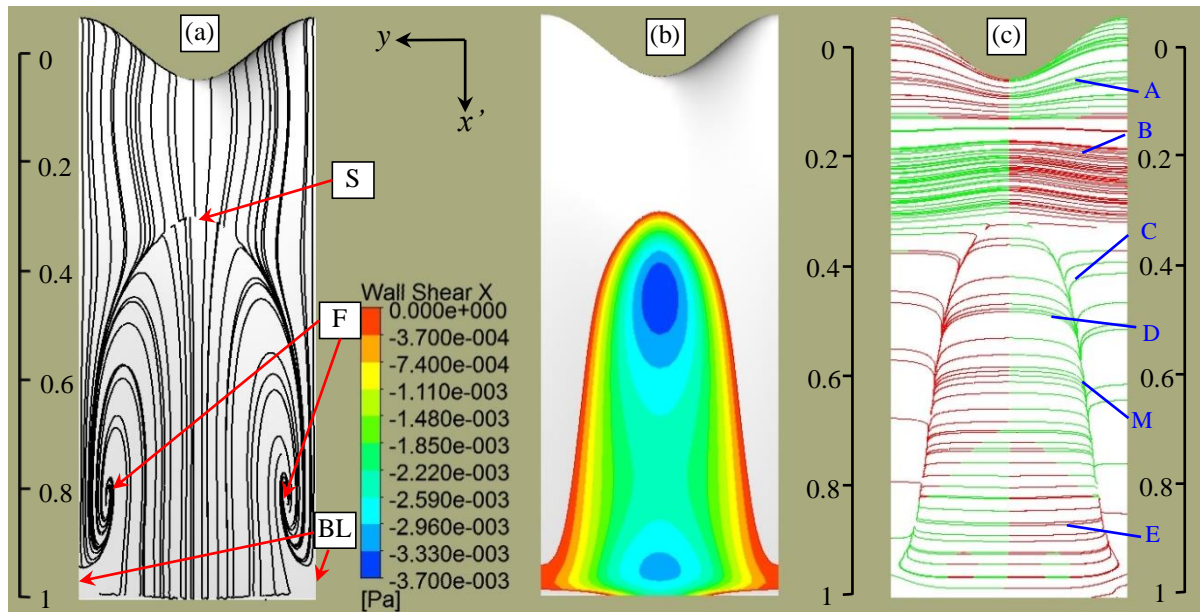


Figure 20.(a) Shear-stress lines, (b) shear-stress contours and (c) vortex lines,  $\alpha = 5^\circ$ ,  $Re = 2230$ .

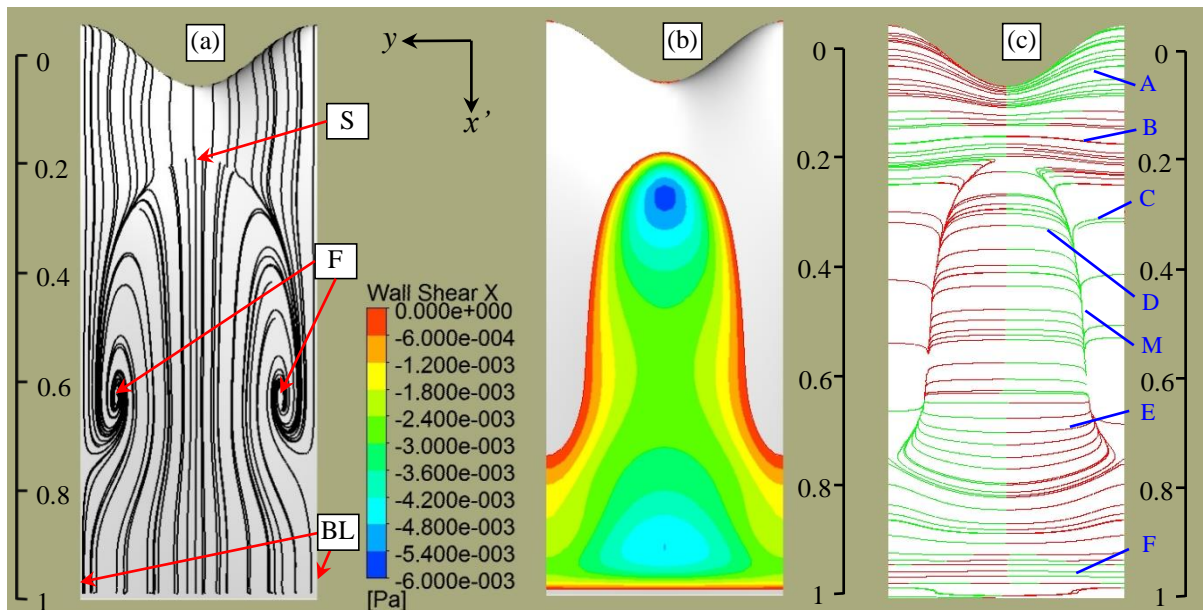


Figure 21.(a) Shear-stress lines, (b) shear-stress contours and (c) vortex lines,  $\alpha = 10^\circ$ ,  $Re = 2230$ .

The evolution of the vorticity vectors over the foil surface is shown by the vortex lines in Figure 20 (c) and Figure 21 (c). In these figures, vortex lines are coloured according to the sign of the streamwise vorticity, where red (darker) and green (lighter) are positive and negative, respectively, in the  $x'$ -direction. For a conventional unswept foil without tubercles, vortex lines are initially aligned in the  $y$ -direction, parallel to the leading edge, with positive vorticity, consistent with the mean shear. However, in the highly three-dimensional flow around the

tubercles, the vortex lines are initially wavy, leading to streamwise vorticity components on the sides (A) of the tubercles themselves. A short distance downstream, the curvature becomes reversed (B) ahead of the separation zone, leading to small streamwise vorticity components of opposite sign to the streamwise vorticity on the tubercles.

Downstream of the saddle the vortex lines can be seen to bend sharply downstream (C), merging into a single line (M), representing the edge of the canopy-like separated vortex sheet that defines the separation zone. The edge of the canopy is also indicated in the associated surface shear stress contours. The downstream orientation of the vortex lines near the foil surface (C) leads to additional streamwise vorticity of the same sign as the primary vortices formed on the sides of the tubercles. In both Figure 20 and Figure 21 the vortex lines are seen to be turned over the entire length of the separation zone, supporting the observations that the circulation of the streamwise vortices formed adjacent to the separation zone increases with downstream distance as shown in Section IV.

In Figure 20 (c) and Figure 21 (c) the vortex lines in the reversed flow region, which are of opposite sign to those of the upstream boundary layer, are also seen to contribute to generation of streamwise vorticity components (D) upstream of the foci. However, downstream of the foci, the vortex line curvature is reversed (E), leading to vorticity of a sign opposite to the primary vortices. The presence of strong streamwise vorticity of opposite sign beneath the primary vortices is confirmed by the experimental and numerical results for the  $\alpha = 10^\circ$  case in Figure 14. Finally, the vortex lines near the trailing edge (F) at  $\alpha = 10^\circ$  in Figure 21 are orientated such that the streamwise vorticity is the same sign as observed at (C).

The turning of the surface vortex lines from a spanwise-dominant orientation towards the streamwise direction is caused by the deflection or skewing of the mean flow, which is described by the term,  $\omega_y \frac{\partial u}{\partial y} + \omega_z \frac{\partial u}{\partial z}$ , in the vorticity transport equation.<sup>30</sup> The magnitude of the vortex turning terms is shown to be largest in the region of the leading edge in Figure 22 (a). Near the trailing edge, after  $x'/c = 0.6$ , the sign of the vortex turning terms changes as shown in Figure 22 (b), which is consistent with the reversal of the vortex line curvature which occurs in this region. Direct generation of streamwise vorticity also occurs in both of these regions as was discussed in Section VI.

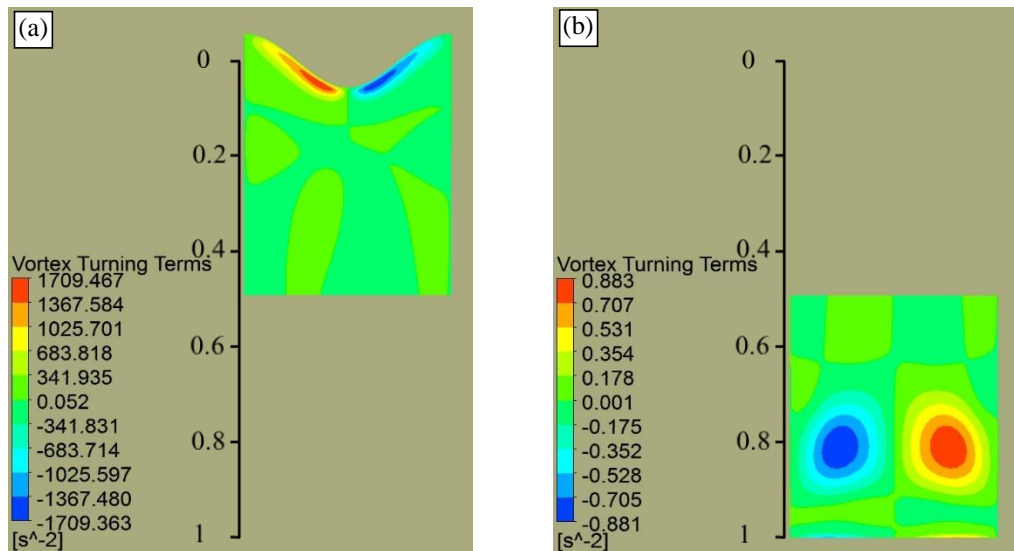


Figure 22. Magnitude of the vortex turning terms for  $\alpha = 10^\circ$ ,  $Re = 2230$ , in the vicinity of the (a) leading edge and (b) trailing edge.

A three-dimensional vortex line interpretation is shown in Figure 23 (a) to provide a more detailed visualisation of the proposed flow mechanism. Along the asymptotic vortex line contour, the vortex lines lift from the foil surface, forming a canopy of vorticity above the separation zone. At the edge of the canopy-shaped vortex sheet, the forward flow and reverse flow vortex lines contribute to streamwise vorticity of the same sign, referred to as “primary vorticity” in this study. This process occurs continuously along the sides of the canopy, consistent with the growth of the circulation of the primary vortices with streamwise distance (see Figure 16).

A pair of foci is revealed by the surface streamlines in Figure 23 (a), and the primary vortices separate from the surface at these points. The vortex lines corresponding to the CFD results are shown in Figure 23 (b) and these results support the vortex line interpretation and show the canopy of vorticity which forms in the separation region aft of the tubercle troughs. The sign of vorticity on the vortex line ring is indicated in Figure 23 (c) and it is emphasised that this is different from the boundary layer vorticity shown in Figure 23 (a).



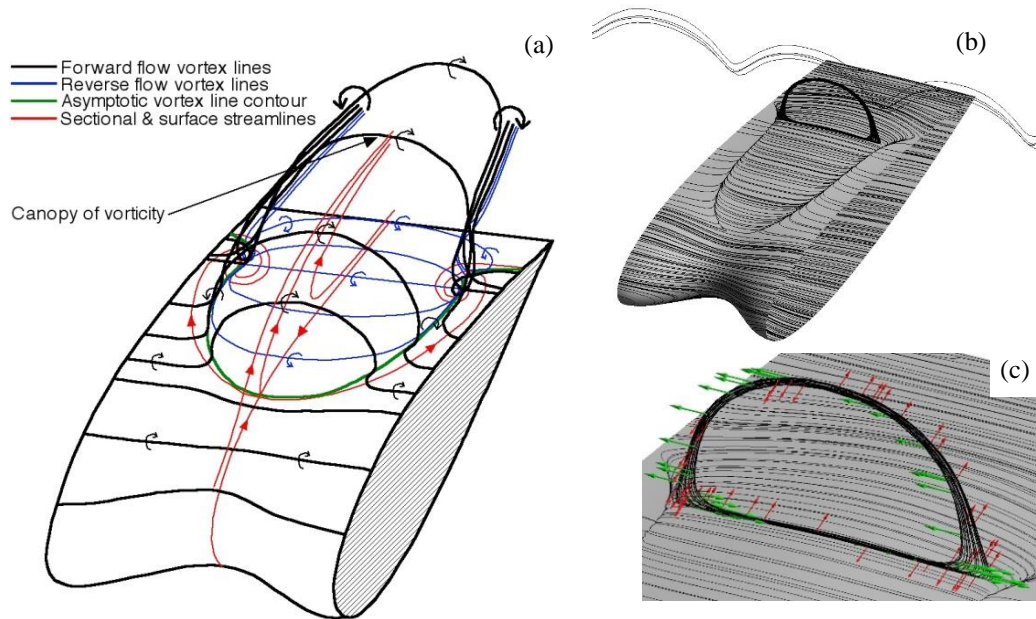


Figure 23. (a) Three-dimensional vortex line interpretation, (b) vortex lines from CFD simulation and (c) vortex lines with normalised green (lighter) and red (darker) arrows indicating spanwise and streamwise orientation of vorticity, respectively.

The orientation of the vortex line ring is shown to vary with streamwise distance in Figure 24, which depicts vortex lines coloured by streamwise vorticity magnitude for  $\alpha = 10^\circ$ . The black line shows a streamline section, corresponding to the same material point moving with the flow from around  $x'/c = 0.6$  to  $x'/c = 0.8$ . The end points of the streamline section are connected to vortex lines that form closed loops. Figure 24 (a-c) indicate that the streamwise vorticity associated with the same material point increases with chordwise distance, which is consistent with the results presented in Figure 15. The side view and top view shown in Figure 24 (b) and (c) respectively indicate that the vortex line rings turn in such a way that they assume stronger streamwise components near the tops in the downstream direction. The turning of the vortex lines can be explained with reference to the streamwise vorticity transport equation expressed in Perkins<sup>30</sup>. Here, the tilting of vorticity into the streamwise direction is accounted for by product of the spanwise vorticity with the spanwise variation in the streamwise velocity,  $\omega_y \frac{\partial u}{\partial y}$  and the product of the normal vorticity with the normal variation in the streamwise velocity,  $\omega_z \frac{\partial u}{\partial z}$ . This is the same mechanism that is responsible for turning of the surface vortex lines from a spanwise-dominant orientation towards the streamwise direction in the surface flow.

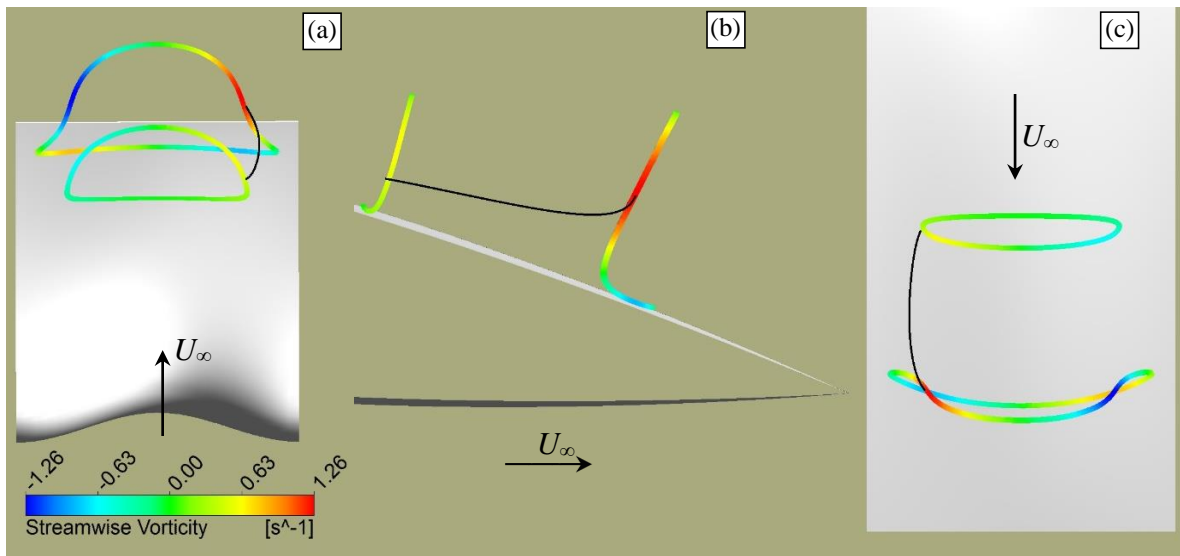


Figure 24. Three-dimensional vortex lines coloured by streamwise vorticity in the vicinity of  $x'/c = 0.6$  and  $x'/c = 0.8$ ,  $\alpha = 10^\circ$ . (a) Three-dimensional view, (b) Side view and (c) Top view.

The deflection or skewing of the mean flow is also evident in Figure 25 (a-b), which depict a streamline section, indicated by a black line, corresponding to the same material point as it travels between vortex lines shown at approximately  $x'/c = 0.07$  to  $0.17$ . It is evident that for this material point, the magnitude of vorticity reduces with chordwise distance, while the orientation of the tangent also changes, as shown in Figure 25 (b). This drop in streamwise vorticity is due to vortex compression as well as tilting. Note that in the side view the transparency of the foil has been adjusted to view the streamline more clearly.

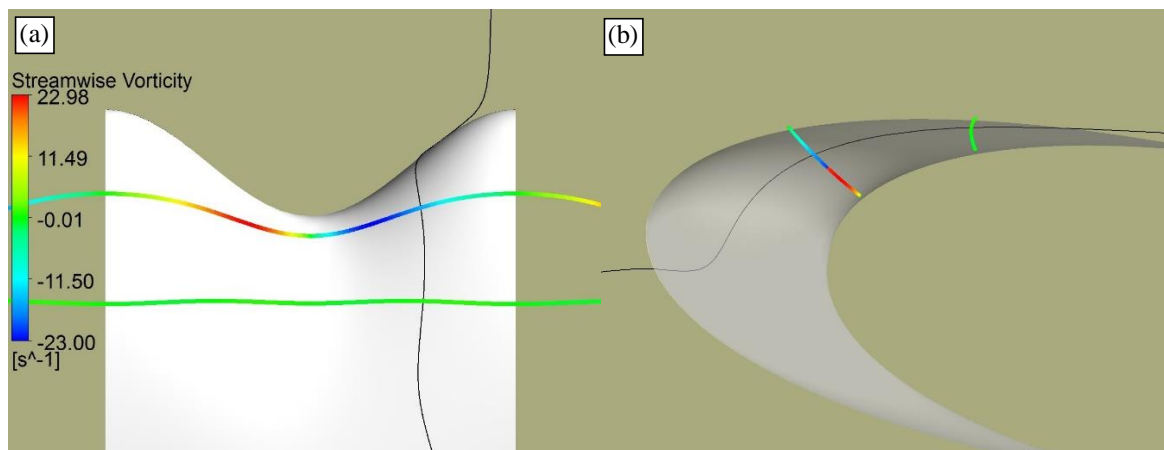


Figure 25. Three-dimensional vortex lines coloured by streamwise vorticity in the vicinity of  $x'/c = 0.07$  and  $x'/c = 0.17$ ,  $\alpha = 10^\circ$ . (a) Top view and (b) Side view.

The deformation and separation of the forward and reversed flow boundary layer vortex sheets are shown in Figure 26 (a-c) for the numerical data. Figure 26 (a) illustrates the canopy-shaped vortex sheet that forms over the separation zone. Figure 26 (b-c) depict the formation of streamwise vorticity on the surface of the tubercled foil at  $\alpha = 5^\circ$ , with the two signs of vorticity shown from different viewing angles. The deformation of the individual vortex lines near the surface agrees with the iso-surface contours shown in this figure.

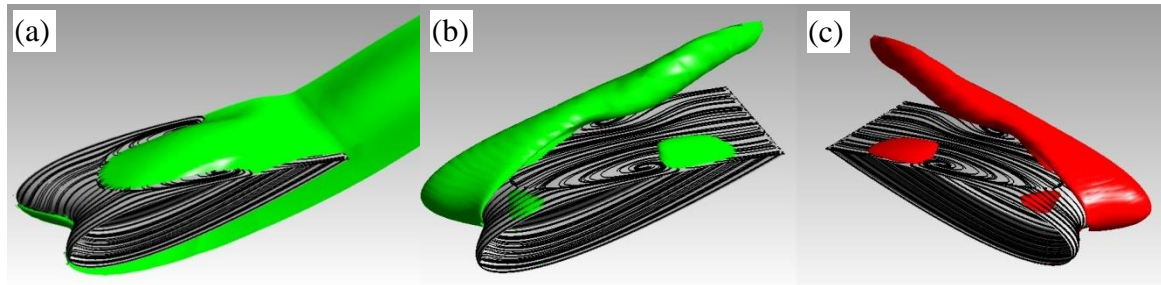


Figure 26. (a) Iso-surfaces of spanwise vorticity in the reverse flow region and below the foil at  $\alpha = 5^\circ$ , (b-c) Iso-surfaces of streamwise vorticity in green (lighter) and red (darker) depicting opposite signs of vorticity values.

A plot of the three-dimensional streamlines is shown in Figure 27 (a). The origins of the streamwise vortices from the separation zone can be seen in this image. The reverse flow in the separation region is clearly evident. Figure 27 (b) shows the end-view of the streamwise vortex formation, emphasising the lift-off of the vortices from the surface of the foil.

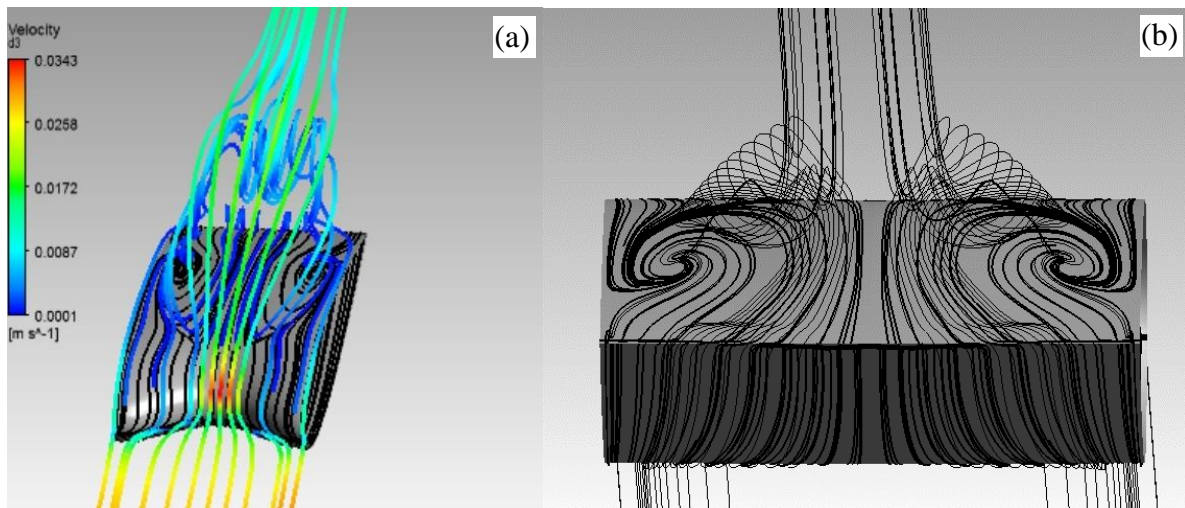


Figure 27. Three-dimensional streamlines at  $\alpha = 5^\circ$ , (a) formation of streamwise vortices and their trajectory downstream, (b) end-view of streamwise vortex formation.

The topology shown in Figure 28 resembles an “owl-face of the first kind”, first defined by Perry and Hornung<sup>38</sup>. The central vertical plane of the owl-face pattern corresponds to the tubercle trough in the present study. It can be seen that the primary vortices create upwash along the vertical plane, which confirms that the sense of rotation of the streamwise vortices is consistent with the current results. The structure is similar to that of stall cells on wings<sup>38, 39</sup>,

which are classified as an owl face of the second kind<sup>38</sup>, although the present structure is somewhat less complex.

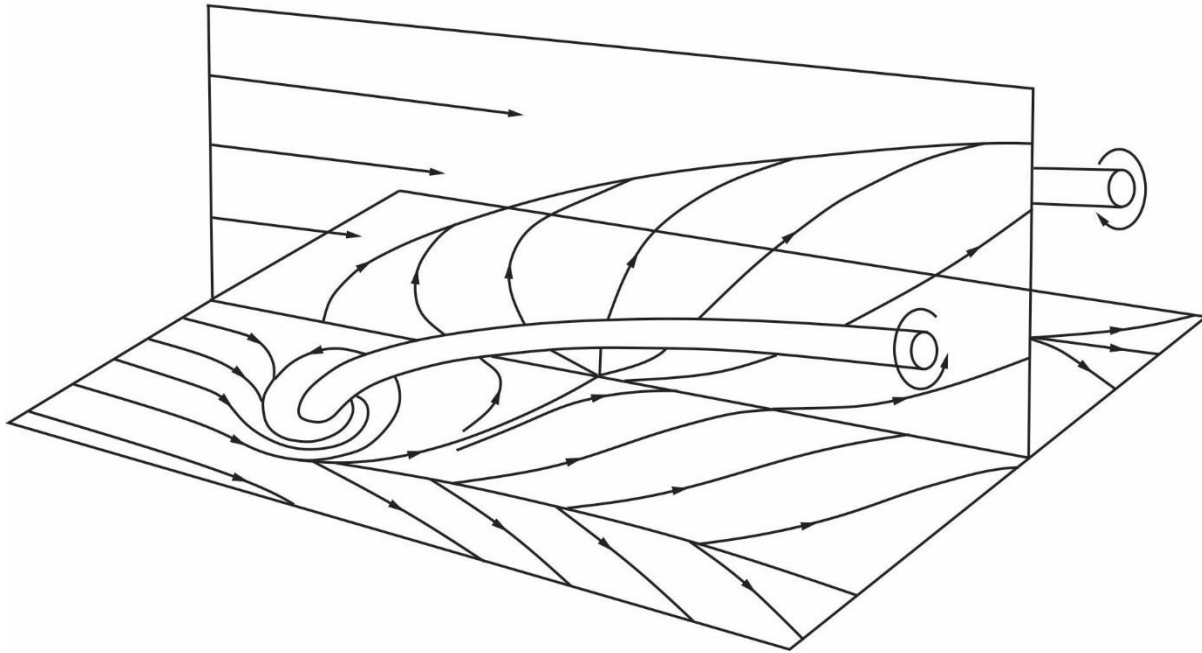


Figure 28. Owl-face of the first kind, after Perry and Hornung<sup>38</sup>.

Figure 29 presents hydrogen bubble visualisation of the flow above the tubercled foil, showing clearly the rollup of vortices in a trough of the  $A8\lambda30$  tubercle case. The appearance of the streaklines and the variations between the images demonstrates that the flow pattern varies with time. Asymmetry in the flow can be seen to increase with time in this image sequence, however in later image frames (not shown here), the vortices appear symmetrical again. Therefore, the mean pattern consists of two counter-rotating vortices between the tubercle peaks, in agreement with the observations and interpretations made elsewhere in this paper. On the other hand, there is a certain degree of time dependency in the flow pattern as has been alluded to previously and this will be discussed further in Section VIII.

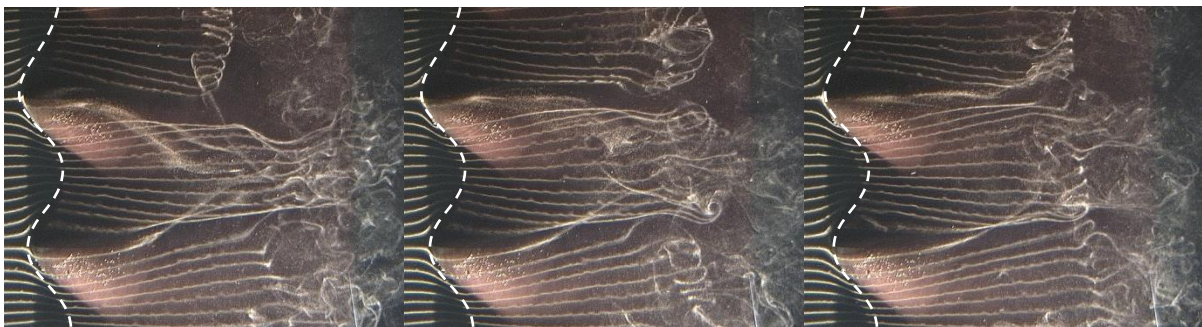






Figure 29. Flow visualisation for  $A8\lambda30$  tubercle configuration at an angle of attack  $\alpha = 10^\circ$  and  $Re = 4370$ . The patterns are frames from a video sequence which are spaced by 3 seconds. The images show the development of streamwise vortices behind the tubercle peaks and it is shown that asymmetry develops over time. Flow is from left to right.

## VIII. TIME DEPENDENCY OF FLOW PATTERNS

The vorticity and circulation results presented in Section III and Section IV were derived from velocity vector fields which represented the average of 2085 image pairs. For a laser pulse rate of 10 Hz, the total acquisition time considered was approximately 209 seconds. The reason for averaging such a large number of samples was to reduce the uncertainty associated with imaging in a cross-flow plane. Based on a comparison between the time-dependent and averaged results, it was found that the averaged flow field data reflects the general flow behavior. Quantification of the degree of unsteadiness was achieved through use of a peak detection algorithm that located the position of peak vorticity for each primary vortex in each instantaneous image. It was found that the mean position of these peaks corresponds well to the position of peak vorticity when the velocity fields are temporally averaged. The standard deviation is within reasonable limits and the movement of the vortices is best described as a fluctuation about the mean as will be shown in Section VIII.A. Results are presented in Table 3 and the units are consistent with other figures in this paper, whereby the y- and z- coordinates have been normalised by the tubercle wavelength.

Table 3. Mean position and standard deviation of peak vorticity. In brackets: position of peak vorticity for temporally averaged experimental data. All values are normalised by tubercle wavelength of 30 mm.

$\alpha$	Location	$x'/c$				
		0.4	0.6	0.8	1	
$5^\circ$		$z/\lambda$	$0.51 \pm 0.03$ (0.51)	$0.51 \pm 0.04$ (0.50)	$0.42 \pm 0.06$ (0.43)	$0.30 \pm 0.08$ (0.39)
		$y/\lambda$	$0.26 \pm 0.07$ (0.30)	$0.27 \pm 0.07$ (0.28)	$0.31 \pm 0.08$ (0.30)	$0.34 \pm 0.10$ (0.30)
		$z/\lambda$	$0.51 \pm 0.03$ (0.51)	$0.51 \pm 0.04$ (0.50)	$0.44 \pm 0.05$ (0.47)	$0.26 \pm 0.08$ (0.22)
		$y/\lambda$	$-0.27 \pm 0.08$ (-0.24)	$-0.29 \pm 0.08$ (-0.33)	$-0.33 \pm 0.08$ (-0.34)	$-0.37 \pm 0.10$ (-0.37)
$10^\circ$		$z/\lambda$	$0.65 \pm 0.04$ (0.64)	$0.63 \pm 0.07$ (0.60)	$0.55 \pm 0.10$ (0.54)	$0.5 \pm 0.11$ (0.58)
		$y/\lambda$	$0.28 \pm 0.07$ (0.28)	$0.31 \pm 0.08$ (0.35)	$0.28 \pm 0.10$ (0.37)	$0.29 \pm 0.09$ (0.28)
		$z/\lambda$	$0.66 \pm 0.04$ (0.64)	$0.63 \pm 0.07$ (0.66)	$0.48 \pm 0.11$ (0.38)	$0.47 \pm 0.12$ (0.34)
		$y/\lambda$	$-0.31 \pm 0.07$ (-0.32)	$-0.34 \pm 0.08$ (-0.35)	$-0.32 \pm 0.13$ (-0.41)	$-0.27 \pm 0.09$ (-0.24)

Despite the general agreement between the mean and instantaneous results, some aspects of the flow patterns are influenced by unsteady effects and these will be explored in this section.

### A. ASYMMETRY

The temporal evolution of vorticity was investigated for the  $\alpha = 10^\circ$ ,  $x'/c = 1$  case to shed light on the unsteady effects that were discussed in Section III. The vorticity results of five sequential ensemble averages carried out over a period of 0.5 seconds each (5 image pairs) are shown in Figure 30 (a) to (e). The sequence shown is representative of a common but intermittent cycle in the  $x'/c = 0.8$  and  $x'/c = 1$  cross-sectional planes at  $\alpha = 10^\circ$ . By comparison, the  $\alpha = 5^\circ$  case is less unsteady and thus shows less variation in the vorticity patterns.

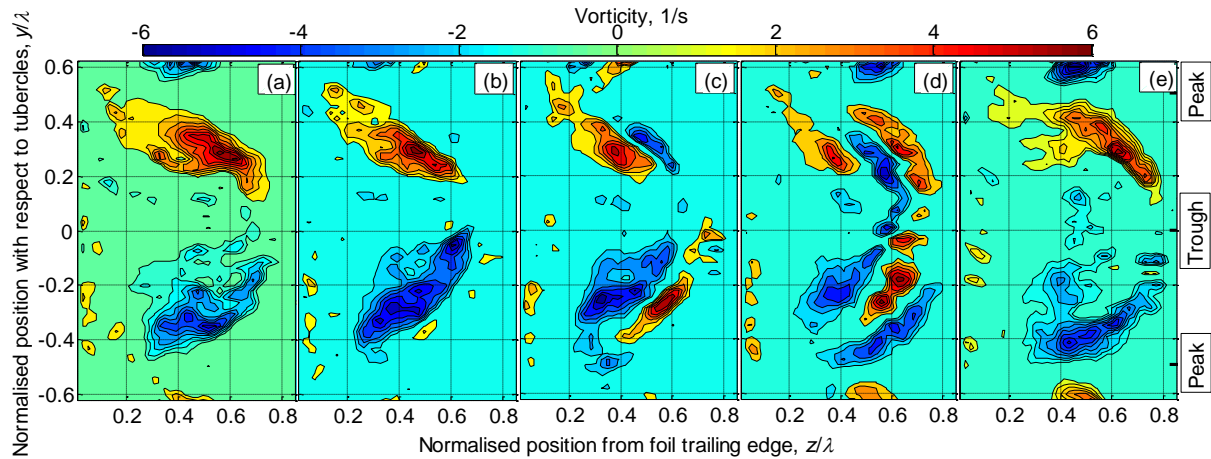


Figure 30. A series of images showing the temporal evolution of vorticity for angle of attack,  $\alpha = 10^\circ$ ,  $Re = 2230$ , image plane  $x'/c = 1$ . Each pattern is averaged over 5 image pairs (0.5 seconds). Note that vorticity with values in the range  $-1 \leq \omega \leq 1$  has not been plotted.

Figure 30 shows that, in this representative cycle, the primary vortices grow and move away from the foil surface, forming a canopy of vorticity behind the tubercle trough where the vortices interact before they collapse back towards the surface. During the interaction phase (images (c-d)) there is an apparent “splitting” of each vortex by layers of vorticity of opposite sign. The splitting is most apparent in Figure 30 (d). The prevalence of this process explains the existence of double lobes in Figure 6 (e) and the increased diffusion and rapid annihilation of vorticity shown in Figure 5 and Figure 6. The opposite-sign vorticity that is present in the primary vortex regions at certain times also manifests as an attenuation of the vorticity across the measurement plane in the 209-second ensemble-average. This attenuation in vorticity gives rise to a corresponding reduction in the magnitude of the experimentally-derived circulation with respect to the numerically-derived circulation at  $\alpha = 10^\circ$  as shown in Figure 16. The attenuation effects could mask the decrease in circulation seen at  $x'/c = 1$ ,  $\alpha = 10^\circ$  in the numerical results. This image sequence highlights the difficulty in interpreting ensemble-average flow patterns of highly unsteady and complex cases such as this.

The unsteady nature of the flow for image planes close to the trailing edge of the foil is further explored through consideration of the mean and fluctuating velocity components in the  $y$  and  $z$  directions ( $v$  and  $w$ , respectively) and these are shown in Figure 31 and Figure 32 for the  $\alpha = 5^\circ$ ,  $x'/c = 0.8$  and  $\alpha = 10^\circ$ ,  $x'/c = 1$  cases, respectively. Comparison between Figure 31 and Figure 32, shows that the magnitudes of both the mean and fluctuating components of velocity in the  $\alpha = 10^\circ$  case are all approximately three times those in the  $\alpha = 5^\circ$  case. In both cases it is also clear that the fluctuating velocity components are of similar magnitude to the

corresponding mean components, confirming that the flow is highly unsteady for these cases. The following discussion assumes that fluctuation velocities are induced by temporal changes in the position of the vortex cores or the strengths of the vortices themselves.

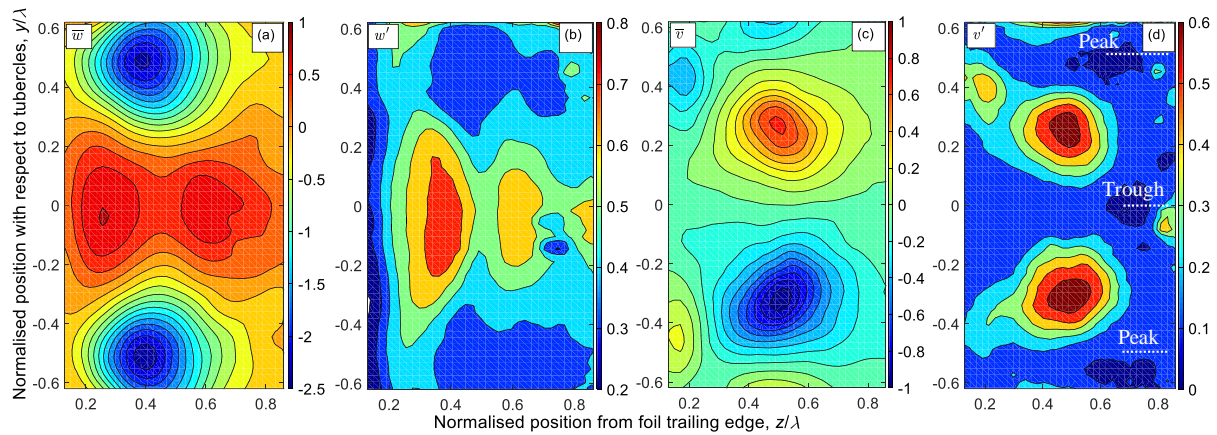


Figure 31. Mean and fluctuating components of velocity for angle of attack,  $\alpha = 5^\circ$ ,  $Re = 2230$ , image plane  $x'/c = 0.8$ . Velocity units are mm/s,  $v$  velocity is in  $y$ -direction and  $w$  velocity is in  $z$ -direction.

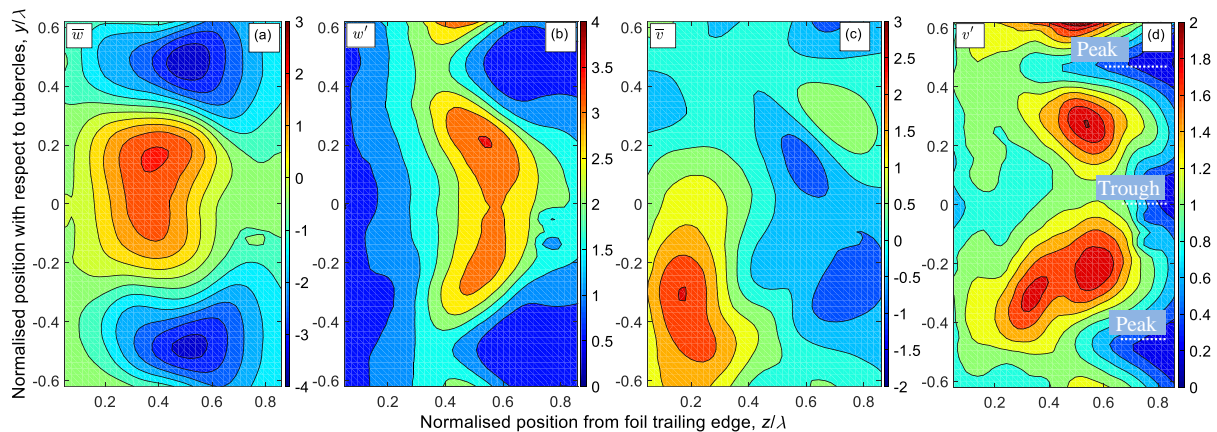


Figure 32. Mean and fluctuating components of velocity for angle of attack,  $\alpha = 10^\circ$ ,  $Re = 2230$ , image plane  $x'/c = 1$ . Velocity units are mm/s,  $v$  velocity is in  $y$ -direction and  $w$  velocity is in  $z$ -direction.

The mean wall-normal component of velocity ( $w$ -direction) is seen in both cases to be largest in the regions between the counter-rotating primary vortices, as expected. The shape and location of the peak  $w$ -fluctuation on the right side of the trough is consistent with both a wall-normal and/or spanwise oscillation in the position of the primary vortex cores.

The mean spanwise component of velocity ( $v$ -direction) is seen in the  $\alpha = 5^\circ$  case to be largest in regions to the right of the counter-rotating primary vortices, with a second peak left and outboard of each core adjacent to the foil surface. The  $v$ -fluctuation peaks are located close to the  $v$ -mean peaks, suggesting that the fluctuations are brought about by a relatively small wall-normal and/or spanwise oscillation in the position of the primary vortex cores. However, in the

$\alpha = 10^\circ$  case, the mean pattern in the  $v$ -direction is highly asymmetric and less clearly defined, with the largest magnitude near the foil surface, to the left of one of the primary vortices. The peak fluctuations in this case are also asymmetric and they occur in regions of generally lower  $v$ -mean values, suggesting that the flow is relatively more unsteady than the  $\alpha = 5^\circ$  case.

Finally, consideration of Figure 32 (b) and (d) together with quasi-instantaneous vorticity fields of Figure 30, shows that the velocity fluctuations support the observations made regarding the growth and collapse of a canopy of vorticity behind the tubercle trough. Specifically, for the  $\alpha = 10^\circ$ ,  $x'/c = 1$  case, the  $w$ -fluctuation is large and the  $v$ -fluctuation is small at  $(y/\lambda, z/\lambda) = (0, 0.6)$ , where the motion of the canopy is seen to be primarily in the wall-normal ( $z$ ) direction. Furthermore, Figure 33 (b) indicates that both the  $v$ - and  $w$ -fluctuations are large at or near  $(y/\lambda, z/\lambda) = (\pm 0.25, 0.5)$  and  $(\pm 0.2, 0.8)$ , consistent with the canopy of vorticity expanding in height and width and then collapsing again. A similar pattern can be observed in Figure 33 (a) at  $\alpha = 5^\circ$ ,  $x'/c = 0.8$ , however the concurrent peaks in the  $v$ - and  $w$ -fluctuations occur closer to the foil surface for this case.

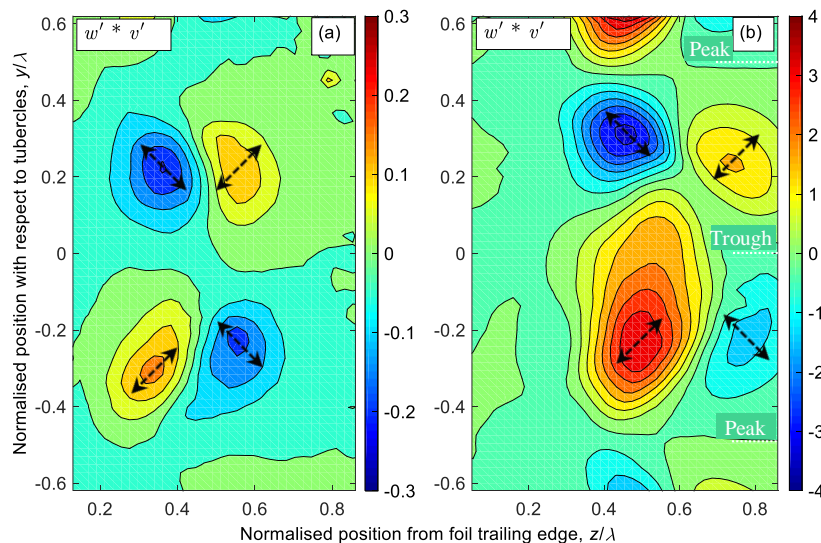


Figure 33. The fluctuating components are multiplied together at each grid position and ensemble averaged for (a) angle of attack,  $\alpha = 5^\circ$ , image plane  $x'/c = 0.8$  and (b) angle of attack,  $\alpha = 10^\circ$ , image plane  $x'/c = 1$ . For both cases,  $Re = 2230$ , velocity units are mm/s,  $v$  velocity is in  $y$ -direction and  $w$  velocity is in  $z$ -direction. Arrows indicate overall fluctuation direction.

## B. UNSTEADY CONTRIBUTION TO THE STREAMWISE INCREASE IN CIRCULATION

The dominant mechanism responsible for the streamwise increase in circulation observed in both the experimental and numerical results presented in Section V.A is steady in nature and was discussed in Section VII. On the other hand, an unsteady mechanism was also observed in



the experimental results. To further examine this mechanism, vorticity was plotted for a series of images for the  $\alpha = 10^\circ$ ,  $x'/c = 0.8$  case. Each image is an average of 15 image pairs and represents 1.5 seconds in time. The three images shown in Figure 34 illustrate that vorticity is transported from the region adjacent to the wall to the streamwise vortices. In Figure 34 (a) the negative wall vorticity is entrained by the clockwise rotating vortex. Figure 34 (b) represents an intermediate state and in Figure 34 (c) the positive wall vorticity is entrained by the anticlockwise rotating vortex.

Therefore, a proposed unsteady mechanism for the increase in circulation with streamwise location is shown in Figure 35, where the primary and wall vortices are indicated in Figure 35 (a). It can be seen in Figure 35 (b) that the negative wall vorticity near the surface is entrained by the negative primary vortex, which describes one extreme pattern of the flow. The opposite extreme pattern is shown in Figure 35 (d) and the pattern shown in Figure 35 (c) represents the intermediate state. This mechanism may also involve vorticity transported to vortices formed behind adjacent tubercles as indicated by the black arrow at the bottom of Figure 34 (b) and in Figure 35 by the dashed arrows which show flow movement from adjacent vortex pairs. The unsteady mechanism is likely to be of secondary importance to the steady mechanism discussed in Section VII since both the experimental and numerical results indicate a streamwise increase in circulation.

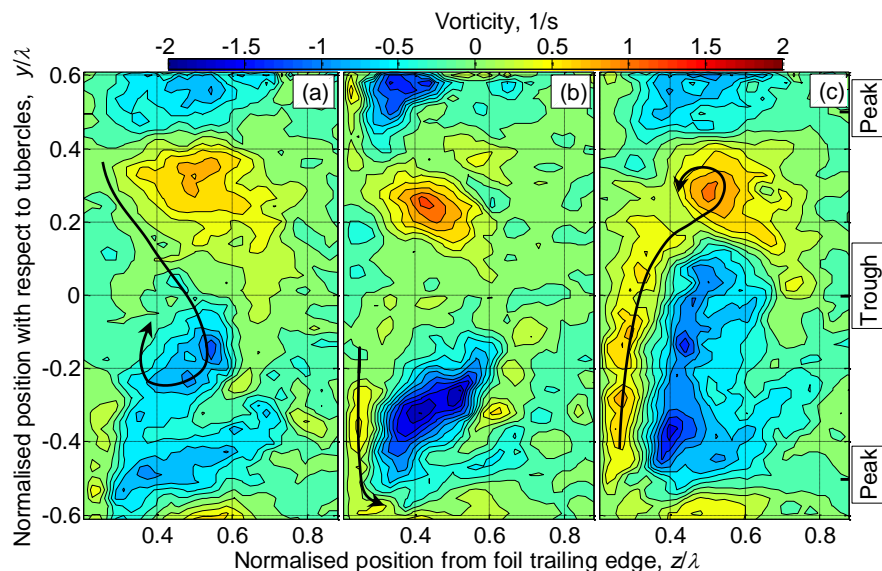


Figure 34. Sequence of vorticity plots on image plane  $x'/c = 0.8$  for  $\alpha = 10^\circ$ ,  $Re = 2230$ , where transport of wall vorticity is shown with the black arrows. (a) Negative wall vorticity entrained by clockwise rotating primary vortex, (b) intermediate state and (c) positive wall vorticity entrained by anticlockwise rotating primary vortex.

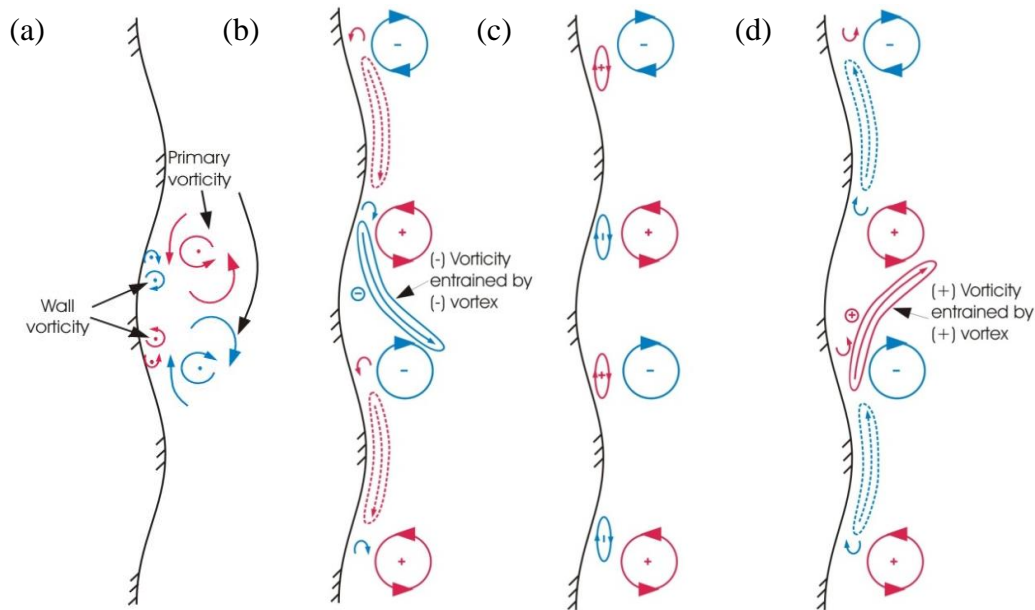


Figure 35. Schematic showing wall vorticity close to the surface being entrained by the primary vortices at adjacent locations. Dashed arrows indicate transport of vorticity to adjacent troughs between tubercles.

## IX. DISCUSSION AND CONCLUSIONS

The combined experimental and numerical studies have identified the salient features of the flow structure produced by a NACA 0021 foil with tubercles at a Reynolds number of 2230. The presence of the tubercles leads to an increased flow velocity along the trough, and a larger adverse pressure gradient. This in turn causes boundary layer separation to occur in the trough at a low angle of attack. These findings are consistent with previous research where the larger adverse pressure gradient in the trough region was attributed to the relatively short chord length at this spanwise location<sup>10</sup>. Hence, the same pressure difference needs to be overcome over a shorter distance behind a tubercle trough relative to a tubercle peak<sup>10</sup>. Previous studies have also identified the presence of a spanwise pressure gradient<sup>17</sup> and the results presented here indicate that this is most significant in the region of the leading edge, where the minimum suction peak occurs. It has been shown that the spanwise pressure gradients, set up by the tubercles, interact with the vorticity distribution, leading to a complex flow pattern. A numerical simulation of the flow is in strong agreement with the experimental observations and allows close examination of the flow structure. The resulting three-dimensional pattern bears a strong similarity to the owl-face of the first kind, first described by Perry & Hornung<sup>38</sup>.

Analysis of the flow field data obtained from both PIV experiments and CFD modeling reveals regions of vorticity of alternate sign in the troughs between tubercles for all spanwise planes investigated. The presence of these streamwise vortices has been shown in previous work<sup>2, 4,</sup>

<sup>12, 17</sup>, however the spanwise location of vorticity was not clear in these results and the vorticity was not quantified as it has been in this study. The current work also shows for the first time that the counter-rotating streamwise vortices lift away from the surface at a certain chordwise location, corresponding to the large foci in the surface streamline (shear-stress) pattern, the locations of which are governed by the angle of attack of the foil. At this point, the flow field becomes highly unsteady and the distribution of vorticity in the region of the primary vortices varies with time, a feature that has not been previously identified.

Considering the averaged experimental results, the magnitude of the peak primary vorticity has been shown to decrease in the streamwise direction, while the region of vorticity expands in area. This effect can be attributed to axial compression of the streamwise vortices caused by the adverse pressure gradient on the suction surface of the foil, vortex tilting and viscous diffusion of vorticity. The results also indicate that the circulation of the primary pair of streamwise vortices increases with streamwise distance, achieving a maximum value at the trailing edge. The increase in circulation occurs due to continued influx of boundary layer vorticity which occurs along the sides of the shear layer canopy. An increasing vortex circulation in the streamwise direction has also been observed for delta wings<sup>31, 32</sup>, but this has not been shown for a tubercled wing prior to this study. This supports the theory that tubercles can be modelled as delta wings with a rounded leading edge<sup>15</sup>.

The numerical study provides novel insights into the flow structure and evolution of vorticity in the flow cases under investigation. The computed sectional velocity and vorticity fields show a strong correspondence to the experimental results. An analysis of the surface vortex lines reveals a number of regions where local turning of the vorticity leads to the formation of streamwise vorticity in the boundary layer, beginning on the sides of the tubercles and occurring at various locations all the way to the trailing edge. The results also demonstrate a source of reverse-sign secondary vorticity beneath the primary vortices downstream of the foci which was shown to occur near the wall in both the experimental and numerical results. These observations are corroborated by the iso-surfaces of streamwise and spanwise vorticity presented in Figure 26. The turning of the boundary layer vorticity from a spanwise-dominant orientation towards the streamwise direction, suggests the development of *Prandtl's secondary flow of the first type*. This is a quasi-inviscid mechanism which is activated by the presence of skewness in the flow, arising from spanwise pressure gradients. This mechanism has been observed to operate for a foil with tubercles in the transitional flow regime<sup>19</sup> and is also

observed to be at play in the laminar flow regime investigated in this study. The local turning of vorticity was also observed by Favier *et al.*<sup>12</sup>, however these researchers referred to vorticity that was initially normal to the surface, rather than being aligned in the spanwise direction. The generation of the vorticity is not attributed to a Kelvin Helmholtz instability which was referred to by Favier *et al.*<sup>12</sup>.

In general, there is strong correspondence between the experimental and numerically-derived magnitudes and trends of the peak vorticity and circulation of the primary vortices. The main differences lie towards the trailing edge of the foil in the  $\alpha = 10^\circ$  case. In the numerical results, the slight decrease in the circulation between  $x'/c = 0.8$  and 1 is attributed to a source of negative vorticity in the reverse flow, as shown in Figure 26 (b-c). In the experimental results, no sudden drop is observed, but the overall magnitude of primary vortex circulation is generally lower than the corresponding CFD results. Whilst some of these differences may be due to inadequacies in the transitional SST closure model used in the numerical study, the effects of unsteadiness are also likely to be a significant cause. In particular, the time-variant nature of the flow pattern demonstrated in Section VIII indicates the high degree of unsteadiness near the trailing edge for both  $\alpha = 5^\circ$  and  $\alpha = 10^\circ$ . Unsteadiness of this magnitude, greater in the  $\alpha = 10^\circ$  case, will result in axial and lateral oscillation of the flow pattern, leading to a higher rate of generation, diffusion and annihilation of the vortices in the flow, consistent with the structure shown in Figure 30. From a measurement perspective, the unsteadiness will lead to attenuation and spreading of the time-averaged vorticity across the measurement plane as well as in the streamwise direction, obscuring the instantaneous flow structure. In fact, due to the strong influence of unsteadiness in this flow, it is likely that small errors in the computed flow structure due to the choice of closure model, such as the axial location of the flow separation, will not affect the validity of the CFD results as an interpretive tool.

The aerodynamic performance of a NACA 0021 foil with  $A8\lambda30$  tubercles has been shown to be slightly better in comparison to an unmodified foil under the conditions of this study. Improved performance has also been observed in previous studies under different flow conditions<sup>1, 3</sup>. Integration of the pressure distributions at various chordwise locations has revealed that the largest amount of lift is generated at a cross-section corresponding to a tubercle peak. This is consistent with the observation that flow separation occurs further aft at

this location. A delayed separation at the peak cross-section has also been observed in previous studies<sup>6, 10, 13</sup>.

In spite of the strong correspondence between the experimentally and numerically-determined flow features and trends, there are still a number of unresolved features, such as the regions of vorticity marked with an asterisk in Figures 5 and 6. Further investigation into the time-dependent characteristics of the flow field surrounding a foil with leading edge tubercles is suggested for future work. In particular, it would be useful to study the three-dimensional evolution of the streamwise vortices in the unsteady flow to gain more insight into the formation and annihilation processes which were touched upon briefly in this paper.

## X. REFERENCES

- [1] D. S. Miklosovic, M. M. Murray, L. E. Howle, and F. E. Fish, "Leading-edge tubercles delay stall on humpback whale (*Megaptera novaeangliae*) flippers," *Physics of Fluids*, vol. 16, p. L39, 2004.
- [2] H. T. C. Pedro and M. H. Kobayashi, "Numerical study of stall delay on Humpback whale flippers," in *46th AIAA Aerospace Sciences Meeting and Exhibit*, Reno, Nevada, 2008.
- [3] P. Watts and F. E. Fish, "The influence of passive, leading edge tubercles on wing performance," in *Proceedings of the Twelfth International Symposium on Unmanned Untethered Submersible Technology UUST*, Lee, NH, 2001.
- [4] D. Custodio, "The effect of Humpback whale-like leading edge protuberances on hydrofoil performance," Masters, Worcester Polytechnic Institute, 2007.
- [5] F. E. Fish and J. M. Battle, "Hydrodynamic design of the Humpback whale flipper," *Journal of Morphology*, vol. 225, pp. 51-60, 1995.
- [6] H. Johari, C. W. Henoeh, D. Custodio, and A. Levshin, "Effects of Leading-Edge Protuberances on Airfoil Performance," *AIAA Journal*, vol. 45, pp. 2634-2642, 2007.
- [7] D. S. Miklosovic and M. M. Murray, "Experimental Evaluation of Sinusoidal Leading edges," *Journal of Aircraft*, vol. 44, pp. 1404-1407, 2007.
- [8] B. Stein and M. M. Murray, "Stall mechanism analysis of Humpback whale flipper models," in *Unmanned Untethered Submersible Technology (UUST)*, Durham, NH, 2005.
- [9] F. E. Fish and G. V. Lauder, "Passive and active flow control by swimming fishes and mammals," *Annual Review of Fluid Mechanics*, vol. 38, pp. 193-224, 2006.
- [10] E. van Nierop, S. Alben, and M. Brenner, "How Bumps on Whale Flippers Delay Stall: An Aerodynamic Model," *Physical Review Letters*, vol. 100, 2008.
- [11] K. L. Hansen, "Effect of Leading Edge Tubercles on Airfoil Performance," PhD, School of Mechanical Engineering, The University of Adelaide, 2012.
- [12] J. Favier, A. Pinelli, and U. Piomelli, "Control of the separated flow around an airfoil using a wavy leading edge inspired by humpback whale flippers," *Comptes Rendus Mécanique*, vol. 340, pp. 107-114, 2012.
- [13] K. L. Hansen, R. M. Kelso, and B. B. Dally, "Performance Variations of Leading-Edge Tubercles for Distinct Airfoil Profiles," *AIAA Journal*, vol. 49, pp. 185-194, 2011.

- [14] M. J. Stanway, "Hydrodynamic effects of leading edge tubercles on control surfaces and in flapping foil propulsion," Masters, Massachusetts Institute of Technology, 2008.
- [15] P. W. Weber, L. E. Howle, M. M. Murray, and D. S. Miklosovic, "Computational Evaluation of the Performance of Lifting Surfaces with Leading-Edge Protuberances," *Journal of Aircraft*, vol. 48, pp. 591-600, 2011.
- [16] J. D. Andersen Jr., *Fundamentals of aerodynamics: Fourth edition*. Singapore: McGraw-Hill, 2007.
- [17] A. Skillen, A. Revell, A. Pinelli, U. Piomelli, and J. Favier, "Flow over a wing with leading-edge undulations," *AIAA Journal*, 2014.
- [18] N. Rostamzadeh, R. M. Kelso, B. B. Dally, and K. L. Hansen, "The effect of undulating leading-edge modifications on NACA 0021 airfoil characteristics," *Physics of Fluids*, vol. 25, p. 117101, 2013.
- [19] N. Rostamzadeh, K. L. Hansen, R. M. Kelso, and B. B. Dally, "The formation mechanism and impact of streamwise vortices on NACA 0021 airfoil's performance with undulating leading edge modification," *Physics of Fluids*, vol. 26, p. 107101, 2014.
- [20] J. B. Barlow, W. H. Rae Jr., and A. Pope, *Low-speed wind tunnel testing*, 3rd edition ed. New York: John Wiley & Sons Inc., 1999.
- [21] J. Westerweel and F. Scarano, "Universal outlier detection for PIV data," *Experiments in Fluids*, vol. 39, pp. 1096-1100, 2005.
- [22] J. C. Agui and J. Jimenez, "On the performance of particle tracking," *J. Fluid Mech.*, vol. 185, pp. 447-468, 1987.
- [23] A. Etebari and P. P. Vlachos, "Improvements on the accuracy of derivative estimation from DPIV velocity measurements," *Experiments in Fluids*, vol. 39, pp. 1040-1050, 2005.
- [24] M. Raffel, C. E. Willert, and J. Kompenhans, *Particle image velocimetry: a practical guide*. Berlin: Springer, 2007.
- [25] C. E. Willert and M. Gharib, "Digital particle image velocimetry," *Experiments in Fluids*, vol. 10, pp. 181-193, 1991.
- [26] A. Fouras and J. Soria, "Accuracy of out-of-plane vorticity measurements derived from in-plane velocity field data," *Experiments in Fluids*, vol. 25, pp. 409-430, 1998.
- [27] T. Lau, "The flow around a fish-inspired heaving and pitching hydrofoil," PhD, The University of Adelaide, 2010.
- [28] E. R. Hassan, T. C. W. Lau, and R. M. Kelso, "Accuracy of circulation estimation schemes applied to discretised velocity field data," in *16th Australasian Fluid Mechanics Conference*, Gold Coast, Australia, 2007.
- [29] B. R. Morton, "The generation and decay of vorticity," *Geophysical & Astrophysical Fluid Dynamics*, vol. 28, pp. 277-308, 1984.
- [30] H. J. Perkins, "The formation of streamwise vorticity in turbulent flow," *Journal of Fluid Mechanics*, vol. 44, pp. 721-740, 1970.
- [31] K. D. Visser and R. C. Nelson, "Measurements of circulation and vorticity in the leading-edge vortex of a delta wing," *AIAA Journal*, vol. 31, pp. 104-111, 1993.
- [32] H. Johari and J. Moreira, "Direct measurement of delta-wing vortex circulation," *AIAA Journal*, vol. 36, pp. 2195-2203, 1998.
- [33] Ansys, "ANSYS-CFX Solver Theory Guide," in *ANSYS CFX 14.0*, ed. Pennsylvania, 2014.
- [34] R. Langtry and F. Menter, "Correlation-based transition modeling for unstructured parallelized computational fluid dynamics codes," *AIAA Journal*, vol. 47, pp. 2894-2906, 2009.

- [35] N. Rostamzadeh, R. M. Kelso, B. B. Dally, and K. L. Hansen, "The effect of undulating leading edge modifications on NACA 0021 airfoil characteristics," presented at the 18th Australian Fluid Mechanics Conference, Launceston, Australia, 2012.
- [36] Gad-el-Hak, *Flow Control: Passive, Active, and Reactive Flow Management*: Cambridge University Press, 2006.
- [37] K. L. Hansen, "The effect of leading edge tubercles on airfoil performance," PhD, Adelaide University, 2012.
- [38] A. E. Perry and H. G. Hornung, "Some aspects of three-dimensional separation, Part II: vortex skeletons," *Z. Flugwiss. Weltraumforsch*, vol. 8, pp. 155-160, 1984.
- [39] M. Manolesos and S. G. Voutsinas, "Study of a stall cell using stereo particle image velocimetry," *Physics of Fluids*, vol. 26, 2014.

## Appendix A – Uncertainty analysis

The most significant bias uncertainty with respect to particle displacement is attributed to the perspective error. This was estimated to be in the range of 0 - 12%, depending on the size and position of the vortices. A greater distance between the particle of interest and the centreline of the image plane would lead to a larger uncertainty in particle displacement.

The sources of random uncertainty which were deemed to have the most significant impact on the results are related to the following parameters: laser jitter,  $\delta_t$ ; particle image diameter,  $\delta_e$ ; uncertainty in particle displacement,  $\delta_{AD}$ ; seeding density,  $\delta_N$ ; magnification,  $\delta_m$  and the displacement gradient,  $\delta_g$ . Where relevant, a seeding density of approximately 20 particles per interrogation window was assumed in the following analysis based on visual inspection of the raw data. A particle displacement of 0.9 px is assumed as this was a typical amount by which a particle within the vortex core was displaced between laser pulses.

The camera jitter was determined from manufacturer's specifications, where  $\delta_t = 250\text{ns}$ . The uncertainty related to the particle image diameter was found from Figure 5.32a in Raffel *et al.*<sup>24</sup>, where  $\delta_e = 0.03$ . The uncertainty in particle displacement was determined from Figure 6b in Willert and Gharib<sup>25</sup>, where  $\delta_{AD} = 0.04$ . The uncertainty related to seeding density is given in Figure 5.40 of Raffel *et al.*<sup>24</sup>, where  $\delta_N = 0.05$ . The uncertainty arising from the magnification scale used was estimated by visual inspection of the target image, giving  $\delta_m = 0.002$ . The displacement gradient was determined in the region of the vortex by plotting the particle displacement along axes which intersect the vortex core. The slope of these plots corresponds to the displacement gradient, where the maximum is around 0.015 for the  $\alpha = 10$ ,

$x'/c = 1$  case. The value of the uncertainty related to the displacement gradient was then determined from Figure 5.42 in Raffel *et al.*<sup>24</sup>, where  $\delta_g = 0.04$ .

The relative uncertainties related to laser jitter and magnification were normalised by the time delay between image pairs,  $\Delta T$  and the grid width,  $w_g$ , respectively. All other relative uncertainties were normalised by the value of a typical displacement in the region of the vortex core of 0.9 px. The overall uncertainty,  $\varepsilon_u$ , for a given image pair was determined by combining the relative uncertainties as given in Equation (2)

$$\varepsilon_u = \sqrt{\left(\frac{\delta_t}{\Delta T}\right)^2 + \left(\frac{\delta_e}{\Delta D}\right)^2 + \left(\frac{\delta_{\Delta D}}{\Delta D}\right)^2 + \left(\frac{\delta_N}{\Delta D}\right)^2 + \left(\frac{\delta_m}{w_g}\right)^2 + \left(\frac{\delta_g}{\Delta D}\right)^2} = 0.08 \quad (2)$$

The error propagation analysis of Fouras and Soria<sup>26</sup> with reference to Lau<sup>27</sup> was applied to determine the maximum random and bias uncertainty in vorticity, which are 6% and 1.4% respectively for an instantaneous velocity vector field. Thus the maximum total uncertainty in vorticity is approximately 6.4%. The random uncertainty in vorticity for the averaged data is determined by finding the overall uncertainty in particle displacement for an average of 2085 image pairs:  $\varepsilon_{u(avg)} = \frac{0.06}{\sqrt{2085}} = 0.0013$ . The overall uncertainty in vorticity for the averaged data is thus dominated by the bias uncertainty of 1.4%.

Details of the method and the associated uncertainty analysis for circulation are given in Figure 2 and 3 in Hassan *et al.*<sup>28</sup>. The maximum random and bias uncertainties are 3% and 15%, respectively. Hence, the total uncertainty in circulation for an instantaneous velocity vector field is 15.3%. Once again, the uncertainty for the average data is substantially lower and should be less than 1%.



## Chapter 6

# Flow over a Tubercled Foil in the Transitional and Near-Turbulent Flow Regimes

In the preceding chapters, the flow mechanism activated by the presence of leading-edge tubercles was analyzed in the transitional and laminar flow regimes. With the availability of high-performance resources at the University of Adelaide (the clusters of supercomputers at eResearch SA) in the years 2014-2015, it became possible to carry out numerical simulations in the near-turbulent regime. Accordingly, to investigate the influence of Reynolds number effects on the flow developed over a tubercled foil, CFD was employed to simulate the flow at two Reynolds numbers: 120,000 and 1,500,000, corresponding to the transitional and near-turbulent regimes. Chapter 6 reports the findings of this investigation presented in the manuscript titled "Exploring Reynolds Number Effects on the Flow Mechanism over a Tubercled Airfoil Based on the NACA 0021 Profile", submitted to the *Journal of Theoretical and Computational Fluid Dynamics*.

The tubercled airfoil adopted in this study (based on the NACA 0021 profile) was the best-performing full-span wing in the experimental study by Hansen *et al.* [2] in the transitional zone. This airfoil had a tubercle amplitude equal to 2mm, a tubercle wavelength of 7.5mm and a mean chord of 70mm. To model the flow in the near-turbulent regime, however, this airfoil had to be re-scaled in three dimensions to avoid compressibility effects. Hence the chord was increased and the free-stream velocity was adjusted to yield a Reynolds number equal to 1,500,000.

To carry out simulations in the near-turbulent regime, highly-refined grids were constructed. This allowed the resolution of small-scale topological features to be achieved. Validation work in this study was performed using the wind tunnel experimental data from Gregorek, Hoffmann, and Berchak [1], in the form of surface pressure distributions over the unmodified foil at  $Re=1,500,000$ .

- [1] M. Gregorek, M. J. Hoffmann, and M. J. Berchak, "Steady State and Oscillatory Aerodynamic Characteristics of a NACA 0021 Airfoil: Data Report," Ohio State University, Columbus, OH 1989.
- [2] K. L. Hansen, R. M. Kelso, and B. B. Dally, "Performance variations of leading-edge tubercles for distinct airfoil profiles," *AIAA Journal Journal of Aircraft*, vol. 49:185-94, 2011.

## Statement of Authorship

Title of Paper	Exploring Reynolds Number Effects on the Flow Mechanism over a Tubercled Airfoil based on the NACA 0021 baseline profile
Publication Status	<input type="checkbox"/> Published <input type="checkbox"/> Accepted for Publication <input checked="" type="checkbox"/> Submitted for Publication <input type="checkbox"/> Publication Style
Publication Details	Journal of Theoretical and Computational Fluid Dynamics

Name of Principal Author (Candidate)	Nikan Rostamzadeh		
Contribution to the Paper	Responsible for performing the literature review, numerical simulations, interpretation of the results. Identified the flow mechanism and elucidated how streamwise and transverse vorticity arises due the presence of an undulating leading edge in both flow cases. Analysed the topological features in both flow regimes. Planned and drafted the manuscript.		
Signature			
		Date	22/11/2015

## Co-Author Contributions

By signing the Statement of Authorship, each author certifies that:

- i. the candidate's stated contribution to the publication is accurate (as detailed above);
  - ii. permission is granted for the candidate to include the publication in the thesis; and
- the sum of all co-author contributions is equal to 100% less the candidate's stated contribution

Name of Co-Author	Associate Professor Richard M. Kelso		
Contribution to the Paper	Supervised the work. Assisted with the interpretation of the surface flow field by examining the limiting streamlines and the vortex lines. Assisted with the description of the flow mechanism. Helped with the editing process of the manuscript.		
Signature		Date	23/11/2015

Name of Co-Author	Professor Bassam B. Dally		
Contribution to the Paper	Supervised the work. Critically analysed the flow mechanism. Assisted with the editing of the manuscript.		
Signature		Date	23/11/2015

## **Exploring Reynolds Number Effects on the Flow Mechanism over a Tubercled Airfoil based on the NACA-0021 baseline profile**

Nikan Rostamzadeh, Associate Professor Richard M. Kelso, Professor Bassam Dally

Mechanical Engineering Department, The University of Adelaide, Australia

### **Abstract**

Leading-edge modifications based on designs inspired by the protrusions on the pectoral flippers of the humpback whale (tubercles), have been the subject of research for the past decade primarily due to their flow control potential in ameliorating stall characteristics. Previous studies have demonstrated that, in the transitional flow regime, full-span wings with tubercled leading-edges outperform unmodified wings at high attack angles. The flow mechanism associated with such enhanced loading traits is, however, still being investigated. Also, the performance of full-span tubercled wings in the turbulent regime is largely unexplored. The present study aims to provide a comprehensive examination of the flow structure around a full-span tubercled wing with the NACA-0021 cross-sectional profile, in the transitional and near-turbulent regimes using Computational Fluid Dynamics. The analysis of the flow field suggests that, with the exception of a few different flow features, the same underlying flow mechanism, involving the presence of transverse and streamwise vorticity, is at play in both cases. With regard to lift generation characteristics, the numerical simulation results indicate that, in contrast to the transitional flow regime where the unmodified NACA-0021 undergoes a sudden loss of lift, in the turbulent regime, the baseline foil experiences gradual stall and produces more lift than the tubercled foil. This observation highlights the importance of considerations regarding the Reynolds number effects and the stall characteristics of the baseline foil, in the industrial applications of tubercled lifting-bodies.

## Introduction

When attempting to catch prey, protuberances on the humpback whales' pectoral flippers (tubercles) enable this baleen species to execute sharp turns without loss of lift [7]. Similarly, leading-edge tubercles, incorporated into the design of lifting bodies, have been shown to yield aerodynamic benefits by ameliorating stall characteristics [8]. Miklosovic *et al.* [17] demonstrated that, compared to a flipper model without tubercles, a tubercled flipper model improved the maximum lift coefficient by 6% at  $Re = 502,000 - 520,000$ . In contrast, the wind tunnel tests by Hansen *et al.* [10-12] at  $Re = 120,000$ , showed that, when tubercles were placed on the leading edges of untapered, full-span and finite-span airfoils, the pre-stall performance was degraded, while aerodynamic efficiency at post-stall angles was enhanced. Similar findings were reported by Miklosovic *et al.* [16] and Johari *et al.* [13]. Thus, the performance enhancement of tubercles appears to be dependent on geometric parameters, as well as the flow regime in which they operate.

Several attempts have been made to explain higher post-stall lift, generated by lifting bodies with tubercles. Analogies of tubercles to delta wings [27], vortex generators and wing fences [18], that improve the lift characteristics have been suggested. Through a series of flow visualization tests, Custodio [3], illustrated that full-span wings with tubercles, generate counter-rotating streamwise vortices, that may account for the enhanced performance of tubercled wings at high attack angles. Stanway [24], who performed force measurements at  $Re = 44,000 - 120,000$  and Favier *et al.* [6] who carried out a numerical investigation at  $Re = 800$ , reported the presence of wall-normal (transverse) vorticity in the flow field. A Large Eddy Simulation-based numerical study by Skillen *et al.* [22] showed that tubercles on a full-span wing give rise to a secondary flow mechanism that enhances momentum transfer and reduces flow separation in the transitional flow regime. In agreement with this study, Rostamzadeh *et al.* [20], suggested that tubercles re-organize spanwise vorticity into streamwise and transverse vorticity through a mechanism known as *Prandtl's secondary flow of the first kind*. Furthermore, numerical modelling pointed to the development of primary and secondary vortices that induce a downwash effect over tubercle peaks and upwash on tubercle troughs, as suggested by van Nierop *et al.* [26] and Weber *et al.* [27]. Hence, the flow is more susceptible to flow separation in the trough regions.

While previous research has illuminated a number of key flow features associated with the mechanism brought about by the presence of tubercles at relatively low Reynolds numbers, the effect of tubercles on the flow structure in the turbulent flow regime is largely unexplored. The present work, aims to investigate Reynolds number effects on the flow mechanism developed over a tubercled foil at  $Re = 120,000$  and  $Re = 1,500,000$ , respectively. To this end, computational fluid dynamics was employed to probe into the flow structure and aerodynamic behaviour.

## Airfoil Models

Two tubercled airfoils and one with a straight leading-edge, whose geometric parameters are defined in Figure 1, were adopted. The baseline foil was the NACA-0021, that has a maximum thickness of 21% at 30% of the chord ( $C$ ) and closely matches the cross-sectional profile of the humpback whale [17]. The other two were tubercled airfoils labelled: A2W7.5 and A14W52.5 with the same cross-sectional profiles as the NACA-0021. A2W7.5 was the best performing airfoil in the wind tunnel tests by Hansen *et al.* [12] at  $Re=120,000$ . Hence, this foil was chosen for flow modelling. Due to dimensional similitude, the scaled-up equivalent of A2W7.5, labelled A14W52.5, was adopted for simulations at  $Re=1,500,000$ . Note that scaling up the geometric parameters for A14W52.5 was implemented to avoid compressibility effects that would arise had A2W7.5 with the same chord line (70mm) been selected at  $Re=1,500,000$ . All the grids are of high quality with ratios of the smallest determinant of the Jacobian matrix to the largest determinant of the Jacobian matrix above 0.7.

Table.1 Geometric properties of the modelled airfoils

Label	Amplitude (mm)	Wavelength (mm)	Mean Chord (mm)	Span (mm)	Associated Flow Reynolds number
NACA-0021	N/A	N/A	490	105	1,500,000
A2W7.5	2	7.5	70	30 (for pre-stall simulation) 120 (for post-stall simulation)	120,000
A14W52.5	14	52.5	490	210 (for pre-stall simulation) 840 (for post-stall simulation)	1,500,000

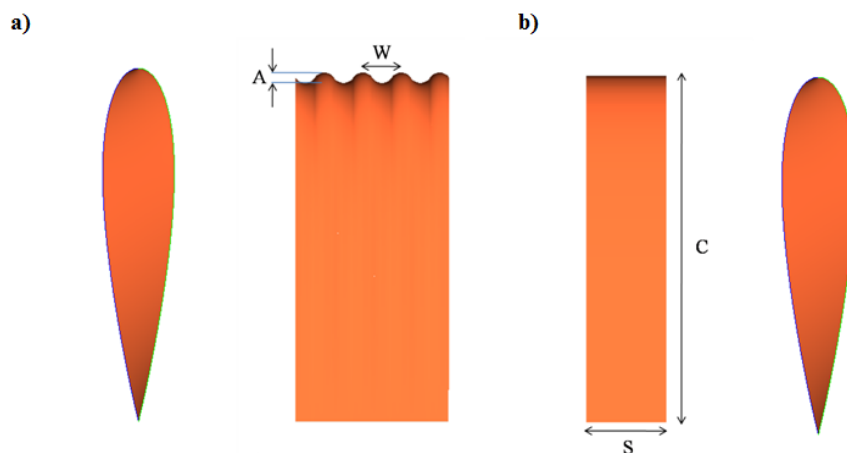


FIG.1 The geometric parameters defined for the tubercled and the unmodified foil.

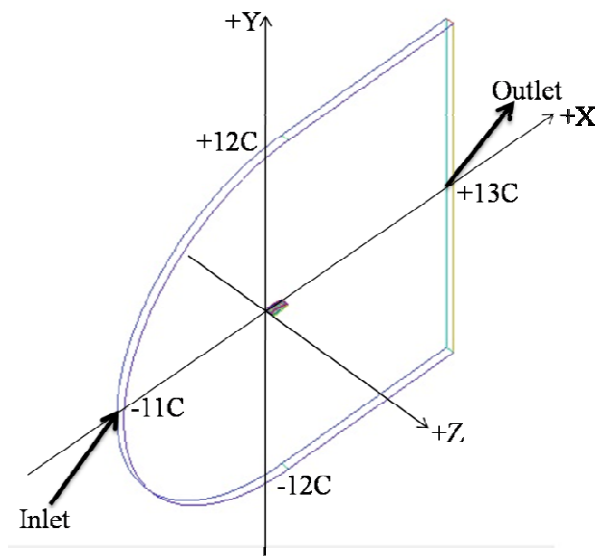
## Computational Setup

The  $\gamma-Re_\theta$  model [14], based on the Unsteady RANS scheme, was utilised for flow modelling in this work. The rationale for using a transitional model was predicated on the fact that, as opposed to fully-turbulent models that often assume the development of a turbulent boundary layer from the leading

edge, the SST transitional model is capable of capturing transition from a laminar boundary layer as was expected to occur in the present cases of chord Reynolds numbers of 120,000 and  $Re=1,500,000$ .

As shown in Figure 2, a C-grid topology with structured hexahedral elements was constructed for the computational domain. The far-field boundaries were placed at 12 chord-lengths from the trailing edge of the airfoils. The lateral planes were assigned periodic and symmetric boundaries for the modified and unmodified foils, respectively, while the airfoils' surfaces were set to the no-slip boundary condition. The boundary layer was resolved with sufficient grid points near the airfoils' surface to yield  $y^+$  values below unity over the airfoils. Simulation test cases performed with the grids spanning four wavelengths in the post-stall zone limited the spanwise development of the central bubble (see Figure 42). Hence, to capture the full development of the flow, grids with sixteen wavelengths of the tubercled airfoils were adopted in the post-stall zone. It was verified that the four and sixteen wavelength-based models produced the same flow characteristics under pre-stall conditions. The angle of attack was adjusted by the velocity components at the Inlet boundary.

a)



b)

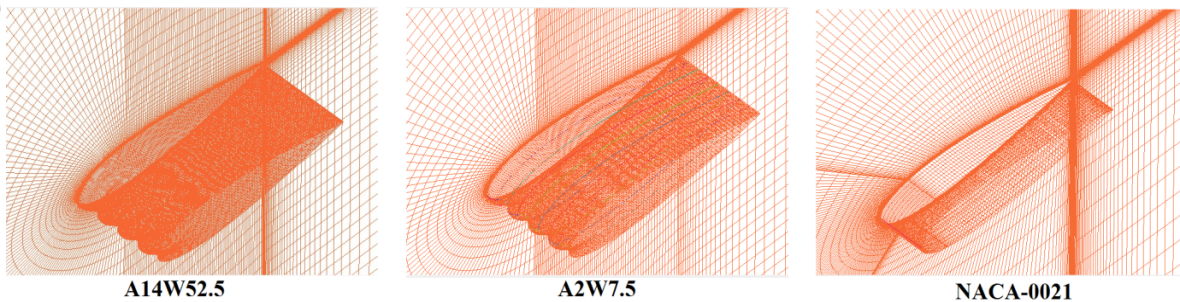


FIG.2 (a) The computational domain and (b) the grid systems around the modelled airfoils.

To solve the governing equations, ANSYS CFX 14.5 [1] was employed. The solver adopts a Finite-Volume, Finite Element scheme to discretize the transport equations. For temporal and spacial discretization, a second-order backward Euler method and a high-resolution scheme were selected respectively.

### Solution Sensitivity Study (Re=120,000)

Three successively-refined grids were tested for A2W7.5 in the transitional regime. All the grids were highly refined and yielded identical force coefficients up to the second decimal place for the force, as detailed in Table 2. In addition to the aerodynamic force, the flow structure was examined to determine the suitability of the grids. The patterns of reversed flow obtained from the solutions by these grids (Figure 2) show that slightly more reversed flow is observed in the results derived from G1, compared to that of G2 and G3 that produced identical patterns. In light of the findings, G2 was adopted for the remainder of the study. The grid density of G2 on the foil, was, thus, incorporated into the construction of the grid for the airfoil with 16 wavelengths.

Lift and drag monitor points were defined and followed throughout the different runs. This is shown for the aerodynamic coefficients associated with the flow over A2W7.5 tubercled foil at an attack angle equal to 2 degrees in Figure 4, whereby the forces plateau once a converged solution is obtained. A conservative time-step size equal to  $7.8 \times 10^{-5}$  (s) was selected for the transient run. This time-step was sufficiently small to ensure the convergence behaviour of the governing equations, and follows the suggestions for time-step size for turbulent flow modelling by Egorov *et al.* [5].

Table.2 Details of the grid sensitivity study. (A2W7.5, Re=120,000, AOA= 2°)

Airfoil label	Total elements	Lift coefficient	Drag coefficient
A2W7.5	G1: 5236486	0.166	0.020
	G2:7899106(for pre-stall simulation)	0.165	0.020
	G2:12588694(for post-stall simulation)		
	G3: 11183004	0.165	0.020

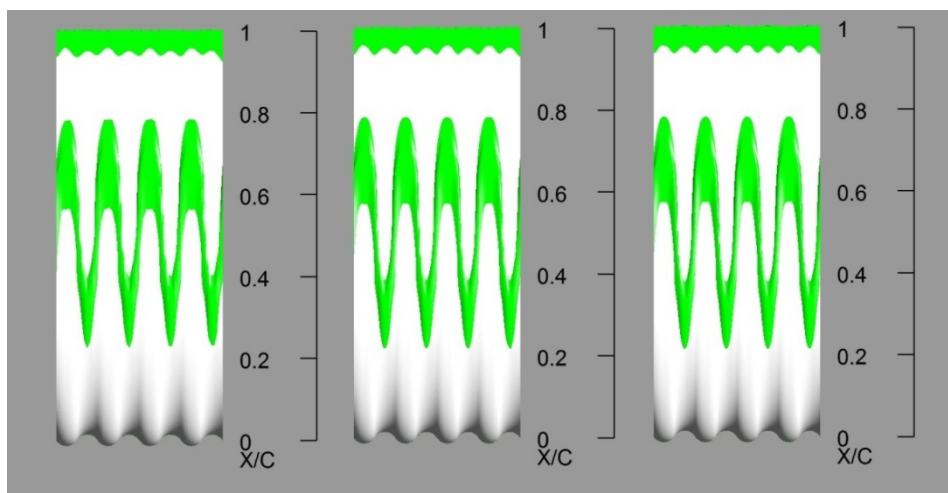


FIG.3 Reversed flow in green achieved by the solutions from different grids: G1 (left) G2 (middle) and G3 (right). (A2W7.5, Re=120, 000, AOA= 2° )



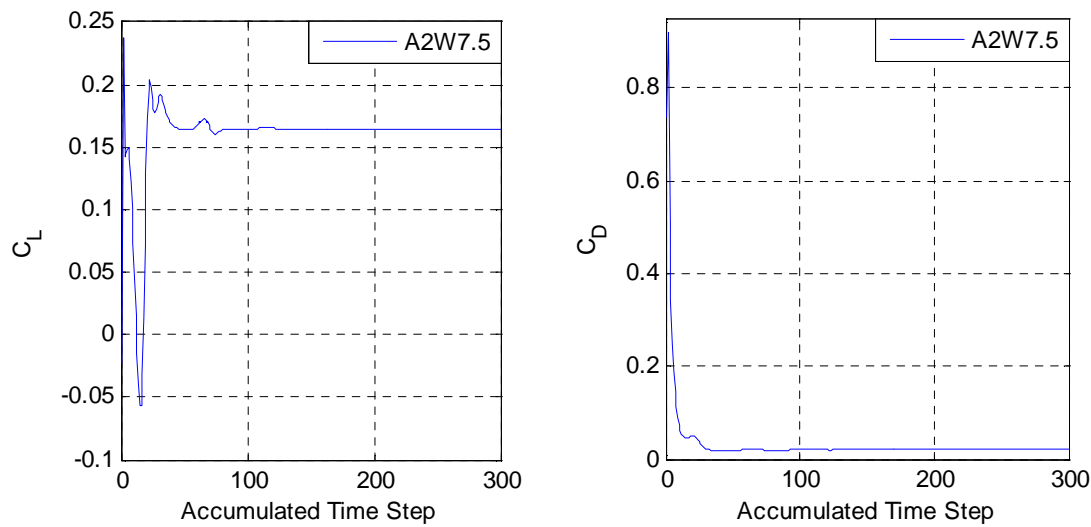


FIG.4 Behaviour of the lift and drag coefficients using grid G2. (A2W7.5,  $Re=120,000$ ,  $AOA=2^\circ$ )

### Solution Sensitivity Study ( $Re=1,500,000$ )

Three successively-refined grids were generated to enable the determination of mesh-independent solutions of the governing equations. The lift and drag coefficients, as well as the flow structure were used to assess the adequacy of the grids. As shown in Table 2, the lift and drag coefficients achieved by the grids were the same for this modified foil. In addition to the forces, the reversed flow patterns arising from the solutions by these grids were examined. In spite of the fact that all three grids yielded similar values of the force coefficients, the effect of refinement was more pronounced on the flow structure. This is illustrated in Figure 5, where flow visualisation demonstrates that grid refinement led to more detailed flow features. In particular, the reversed flow regions near the mid-chord section were captured with the highest resolution by G3. Therefore, G3 was maintained for the rest of the study. The integrated lift and drag monitor points are shown for the 6-degree attack angle in Figure 6.

As for the unmodified foil, three grids (G1, G2 and G3) were tested. G2 and G3 produced identical lift and drag coefficients up to the second decimal point (Table 3). G2 which required fewer computational resources compared to that of G3, yet was more refined than G1 was maintained for the rest of the study. Lift and drag monitor points were defined and followed throughout the different runs (see Figure 7 as an example). The time-step size for the simulation run was maintained at a conservative value of  $t = 3 \times 10^{-4}$  (s), that comply with the recommendations by Egorov *et al.* [5].

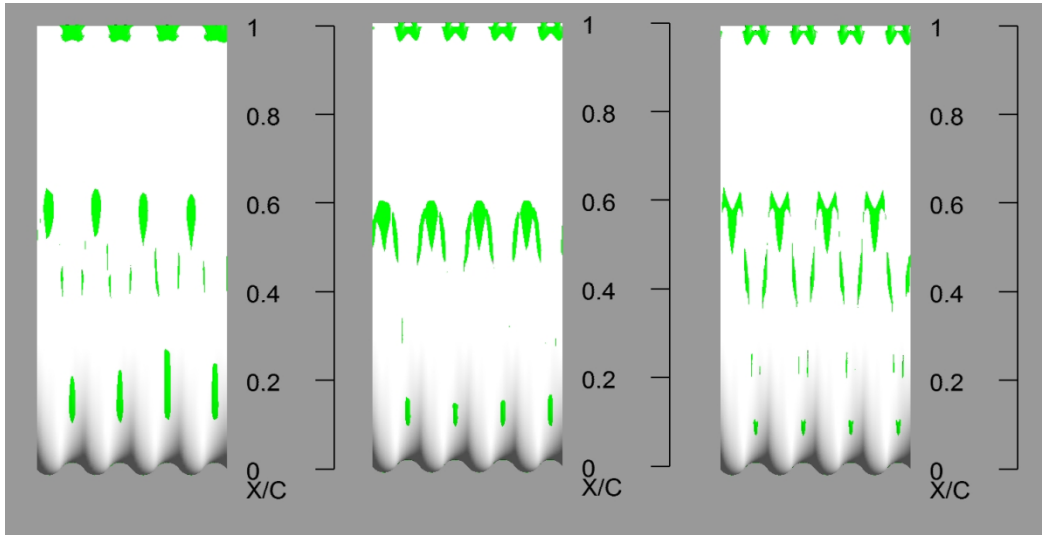


FIG.5 Reversed flow regions, in green, obtained from solutions by G1 (left), G2 (middle) and G3 (right). (A2W7.5,  $Re=1,500,000$ ,  $AOA=6^\circ$ )

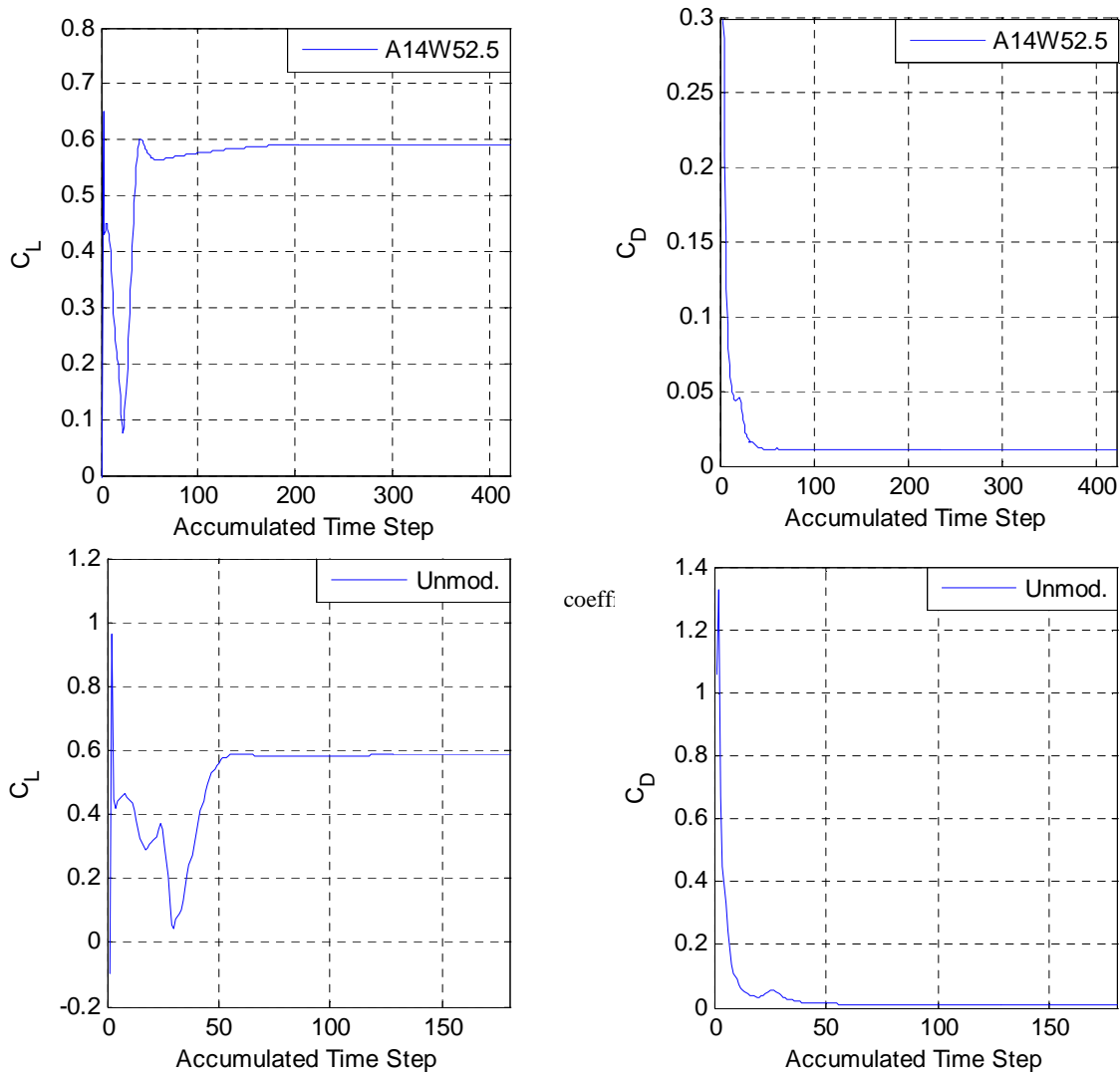


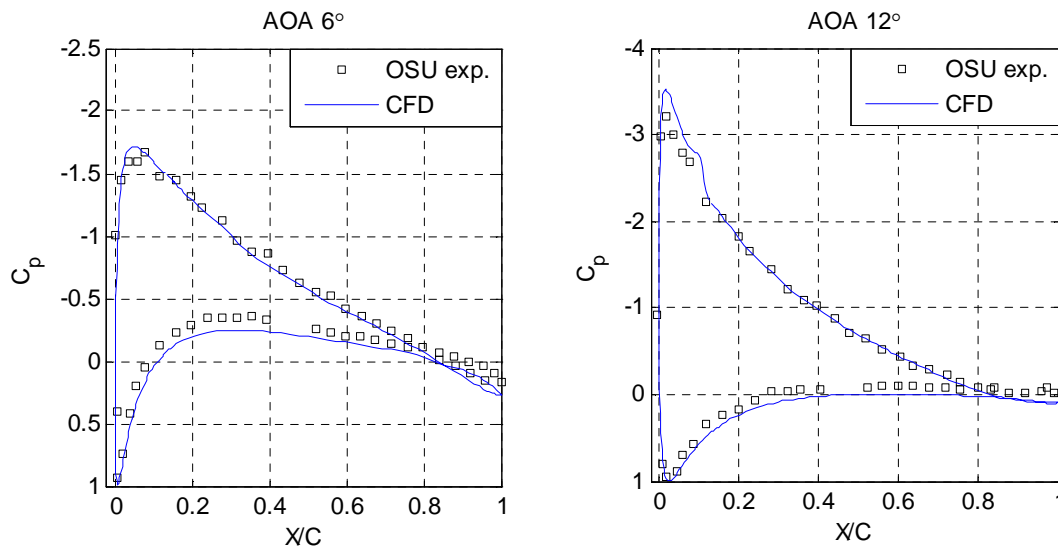
FIG.7 History of the lift and drag coefficient. (NACA-0021,  $Re=1,500,000$ ,  $AOA=6^\circ$ )

Table.3Details of the grid sensitivity study. (Re=1,500,000, AOA= 6°)

Airfoil label	Total elements	Lift coefficient	Drag coefficient
A14W52.5	G1: 5800054	0.588	0.010
	G2:8749234	0.588	0.010
	G3:12386556 (for pre-stall simulation)	0.588	0.010
	G3:13441064 (for post-stall simulation)		
NACA 0021	G1: 782250	0.584	0.010
	G2: 811454	0.588	0.010
	G3: 982506	0.588	0.010

### Validation for Selected Attack Angles (Re=1,500,000)

Gregorek *et al.* [9] conducted wind tunnel pressure measurement tests on the NACA 0021 airfoil at Re=1,500,000. The data, in the form of pressure distribution, were later used for validation by Wolfe *et al.* [29], who used the  $k-\epsilon$  model to predict the aerodynamic behaviour of the same airfoil. Herein, the data reported by Gregorek *et al.* [9] are presented for the validation of the SST transitional model, adopted in this study (Figure 8). Overall, the SST transitional model, predicts the observed trends in the pressure distribution satisfactorily. The largest discrepancies are seen for attack angles at 16 and 20 degrees where lower suction pressure values are obtained by the transitional model. Nonetheless, very good agreement between experimental and numerical data is evident for attack angles up to 12 degrees and reasonable agreement is observed for larger angles of attack.



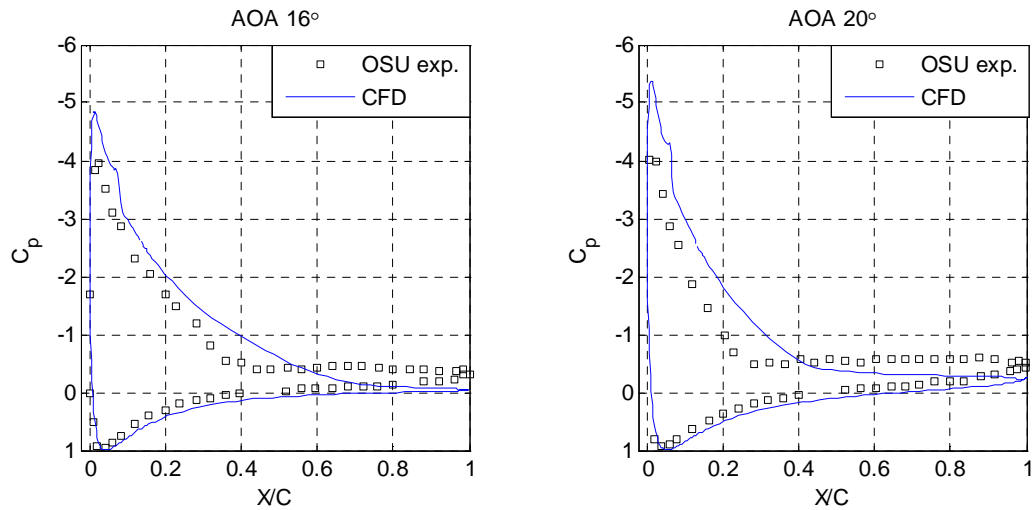


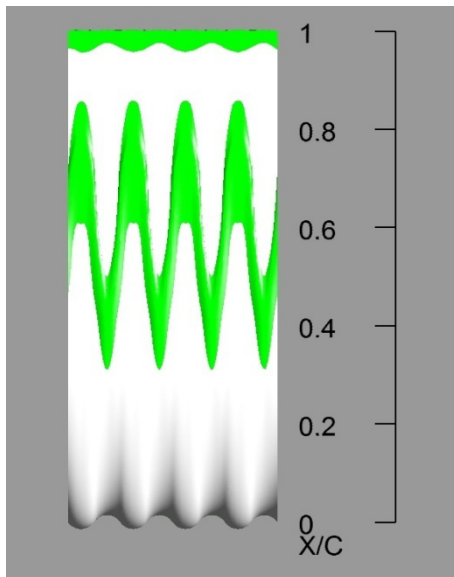
FIG.8 Pressure coefficient achieved by SST transitional model, compared to experimental data of Gregorek *et al.*[9]

### Flow Over the Tubercled Foil A2W7.5 (Re=120,000)

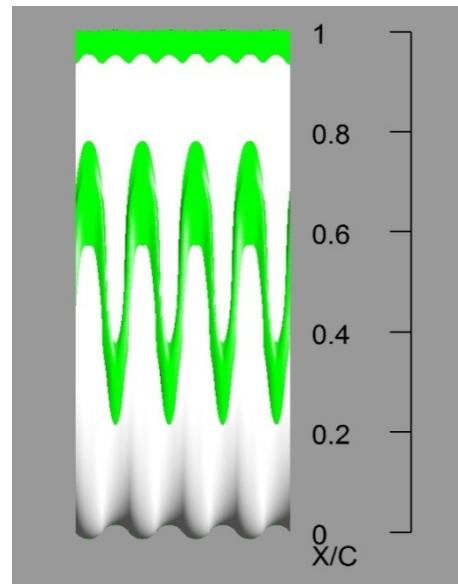
#### Pre-stall Flow Analysis

Figure 9 displays the regions over the suction side of the airfoil where reversed flow occurs for three attack angle cases. Note that the streamwise component of the surface shear force in these regions is oriented against the free-stream flow direction. Thus, the values of the shear stress in the streamwise direction are negative (see Figure 10 as an example).

a)



b)



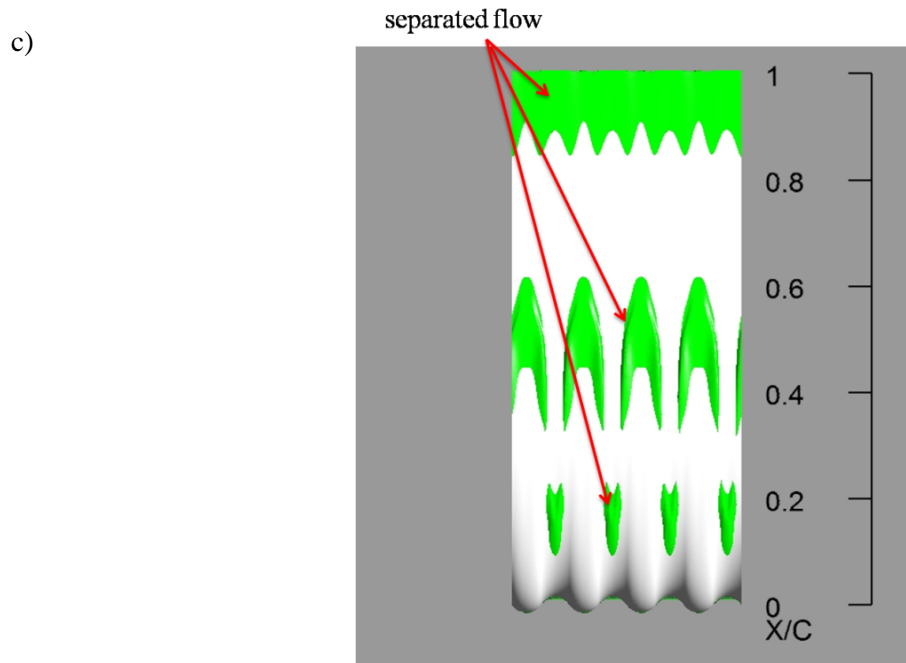


FIG.9 (a-c) Reversed flow displayed in green for (a)AOA = 0° (b)AOA = 2° (c)AOA = 6° (A2W7.5, Re=120,000)

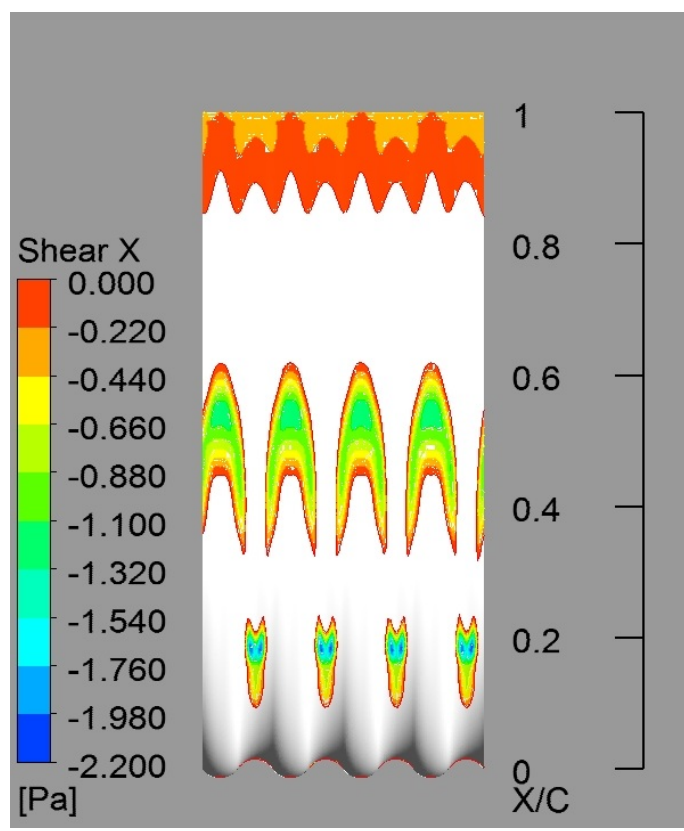


FIG.10 Contours of shear stress in the streamwise direction in the regions where shear stress is negative in the streamwise direction. White shows regions of attached flow. (A2W7.5, Re=120,000, AOA=6°)

At AOA = 0°, two primary regions of separated flow are identified. A wavy and a zigzag pattern are observed near the trailing edge and the mid-chord section, respectively. As the attack angle increases

to 2 degrees, the boundaries of all the separation zones move further upstream. Notably, while the wavy separation region at the trailing edge of the foil moves forward, the number of peaks and troughs on this pattern is doubled. In contrast to the lower attack angle cases, at  $AOA = 6^\circ$ , three primary flow separation zones where flow separation occurs are identified. What follows is a closer examination of the flow structure at this representative pre-stall attack angle.

As illustrated in Figure 11, the flow is driven by the presence of strong spanwise pressure gradient, established by the undulating leading edge. Spanwise pressure gradient assumes a cyclic variation along the span, with blue-coloured areas highlighting regions where the static pressure decreases in the positive Z direction, and red marking areas where the static pressure rises. The static pressure contours in Figure 12 illustrates that the trough is the location where the lowest suction peak occurs, an observation that is consistent with previous studies [10, 23, 26, 27].

One implication of the presence of a low-pressure region in the trough is the tendency of the flow over the peak sections to move towards the trough, driven by the pressure gradient. This fluid motion leads to the development of the first notable flow feature on the suction side: a three-dimensional laminar separation bubble (LSB). The bubble is bound on the trough spanwise location by a saddle of separation, S1, and a saddle of attachment S2. Also within the bubble, two stable foci are found (Figure 13).

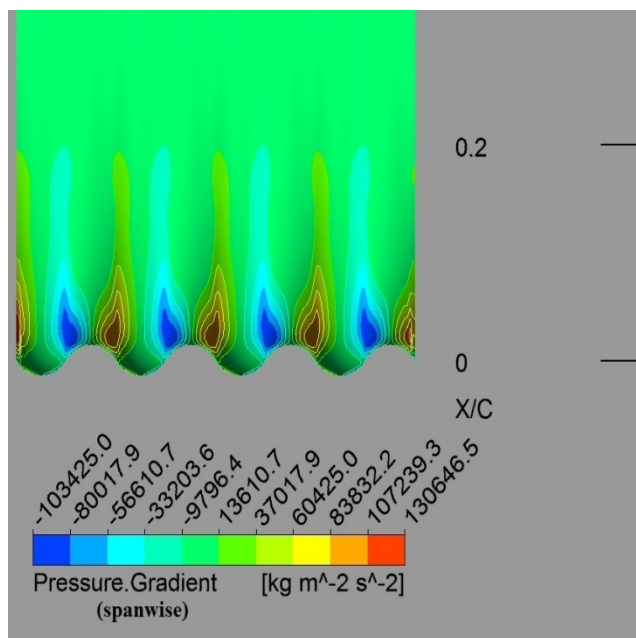


FIG.11 Spanwise pressure gradients near the leading edge (A2W7.5,  $Re=120,000$ ,  $AOA=6^\circ$ )

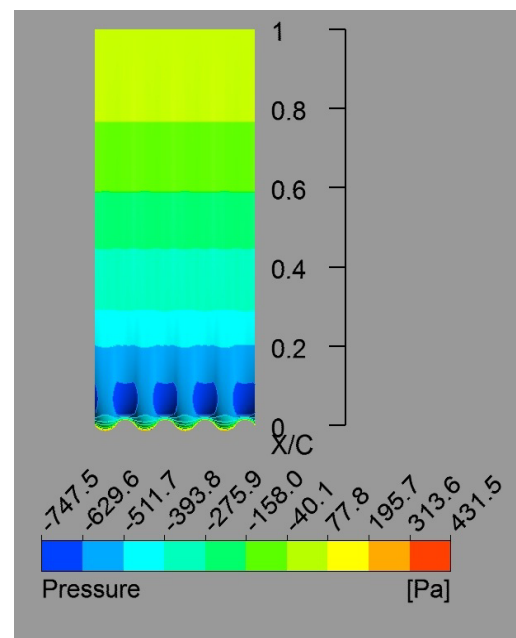


FIG.12 Contours of static pressure on the suction side. (A2W7.5,  $Re=120,000$ ,  $AOA=6^\circ$ )

To probe further into the formation of the laminar separation bubble, the vortex lines, near the leading edge are drawn in Figure 13. It is apparent that the vortex lines assume a spanwise-dominant sense of direction, accounted for by the presence of vorticity within the boundary layer. Further downstream, however, the vortex lines' direction change, such that small streamwise components are developed. This is particularly noticeable around the chordwise edges marked in Figure 13. These are the locus of points where vorticity is lifted away from the surface of the foil, to form the edges of a canopy-like vortex structure.

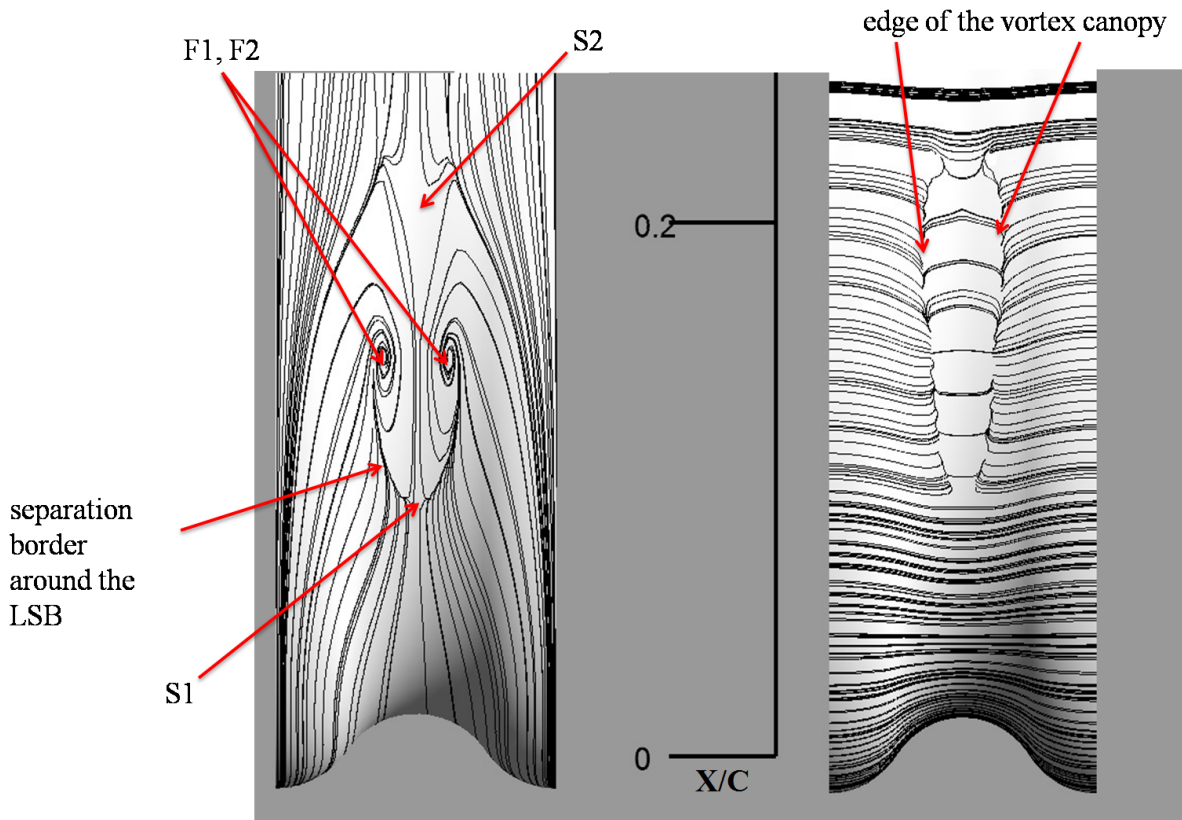


FIG.13 Shear stress lines (left) and vortex lines (right) in the vicinity of the LSB. (A2W7.5,  $Re=120,000$ ,  $AOA=6^\circ$ )

The approaching three-dimensional streamlines, under the influence of the spanwise pressure gradient, turn towards and around the focal points (see Figure 14). The turning of the streamlines gives rise to the re-arrangement of the vortex lines into the streamwise and transverse directions. The secondary flow mechanism was also reported by Skillen *et al.* [23]. As demonstrated by the authors' previous work [20], this mechanism is identified as *Prandtl's secondary flow of the first type*: a quasi-inviscid mechanism which is responsible for generating streamwise and transverse vorticity, due to the presence of skewness and spanwise vorticity within the boundary layer.

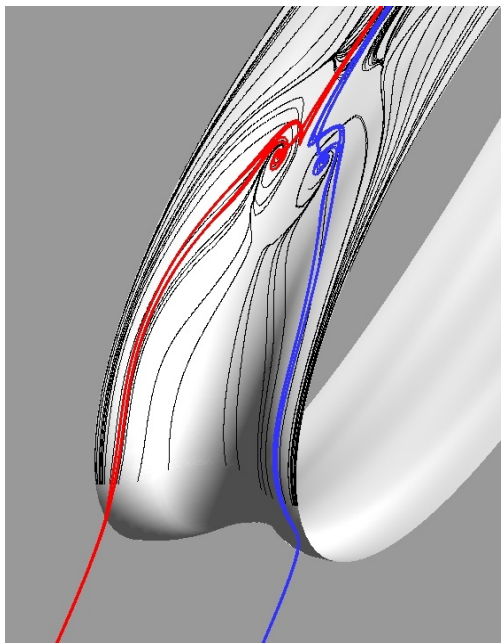


FIG.14 Behaviour of the three-dimensional streamlines around the LSB. Surface shear stress lines are drawn on the suction side of the airfoil. (A2W7.5,  $Re=120,000$ ,  $AOA=6^\circ$ )

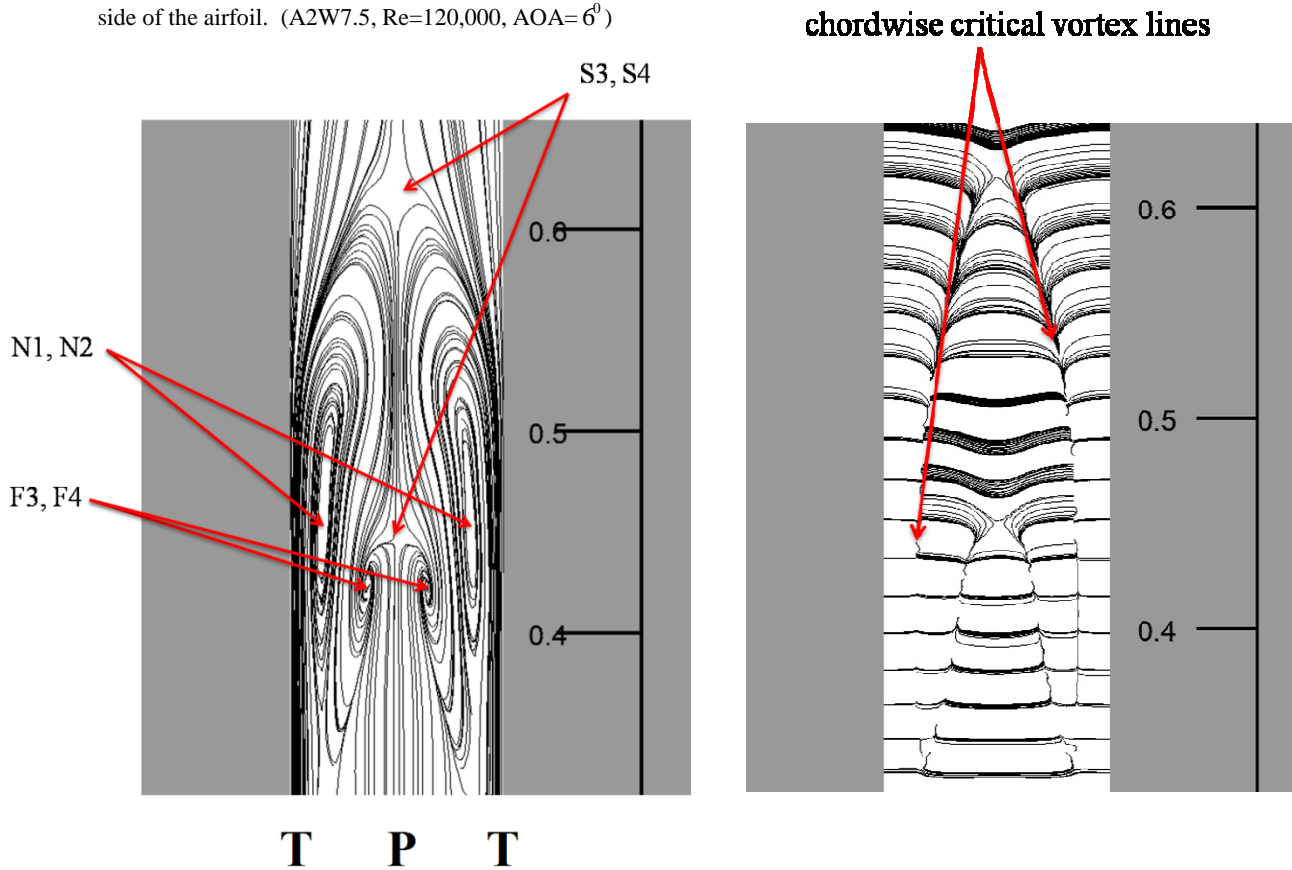
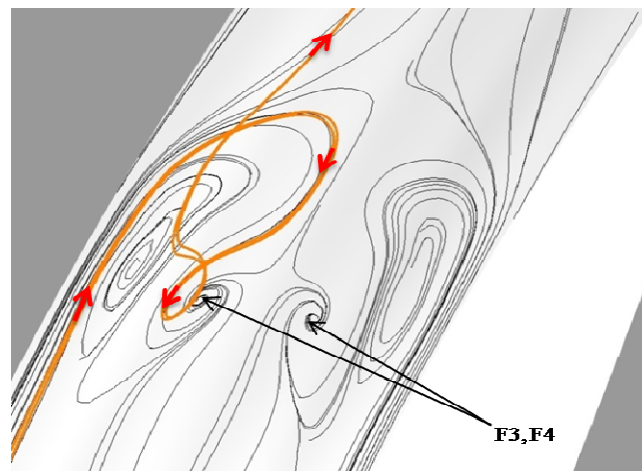


FIG.15 Shear stress lines (left) and vortex lines (right) near the mid-chord line. T and P denote, trough and peak, respectively. (A2W7.5,  $Re=120,000$ ,  $AOA=6^\circ$ )

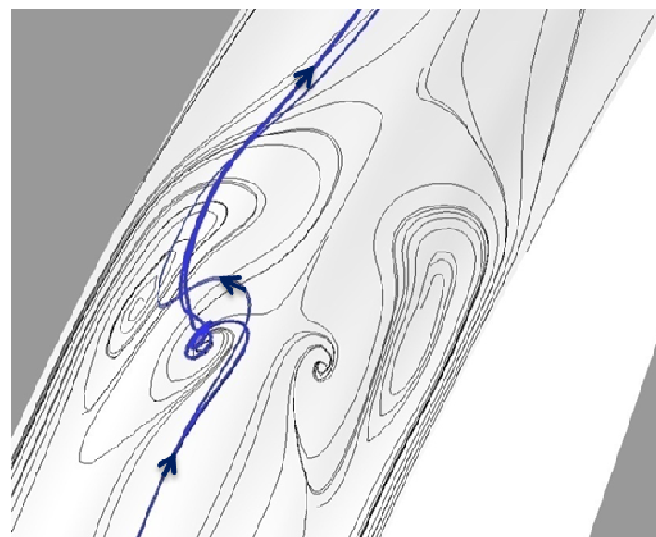


The topological characteristics associated with the separated flow feature near the mid-chord section is more complicated as shown in Figure 15. Two saddles, one of detachment,  $S3$  ( $X/C \approx 0.45$ ) and one of attachment,  $S4$  ( $X/C \approx 0.62$ ) are readily seen on the peak spanwise location (Figure 15). The presence of transverse vorticity is suggested by the two pairs of chordwise critical vortex lines, pointing to the location where transverse vorticity is lifted away from the surface. To cast more light on the flow structure in close proximity to this separated flow region, three-dimensional streamlines have been plotted (Figure 16) in close proximity to the salient topological critical points near the mid-chord section.

a)



b)



c)

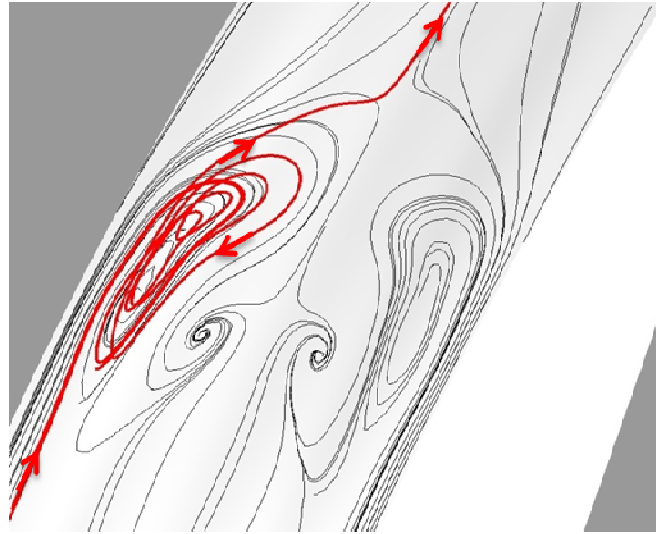


FIG.16 Flow behaviour around the mid-chord flow feature displayed in the perspective views (a-c) ( $Re=120,000$ ,  $AOA=6^\circ$ )

It is observed that the oncoming flow takes three distinct pathways. One path marks the forward-moving flow from the trough taking a sharp turn towards the peak and spiralling into the stable focus, F3. Past the focal critical point, the flow continues to convect downstream as depicted in Figure 16(a). In contrast, the flow approaching from either side of the peak, spirals into the foci (F3 and F4) before moving further downstream (Figure 16(b)). Finally one group of streamlines coming from the trough spanwise location, are strongly twisted near the surface, to the left and right of the focal points, F3 and F4, before continuing on their way downstream (Figure 16(c)).

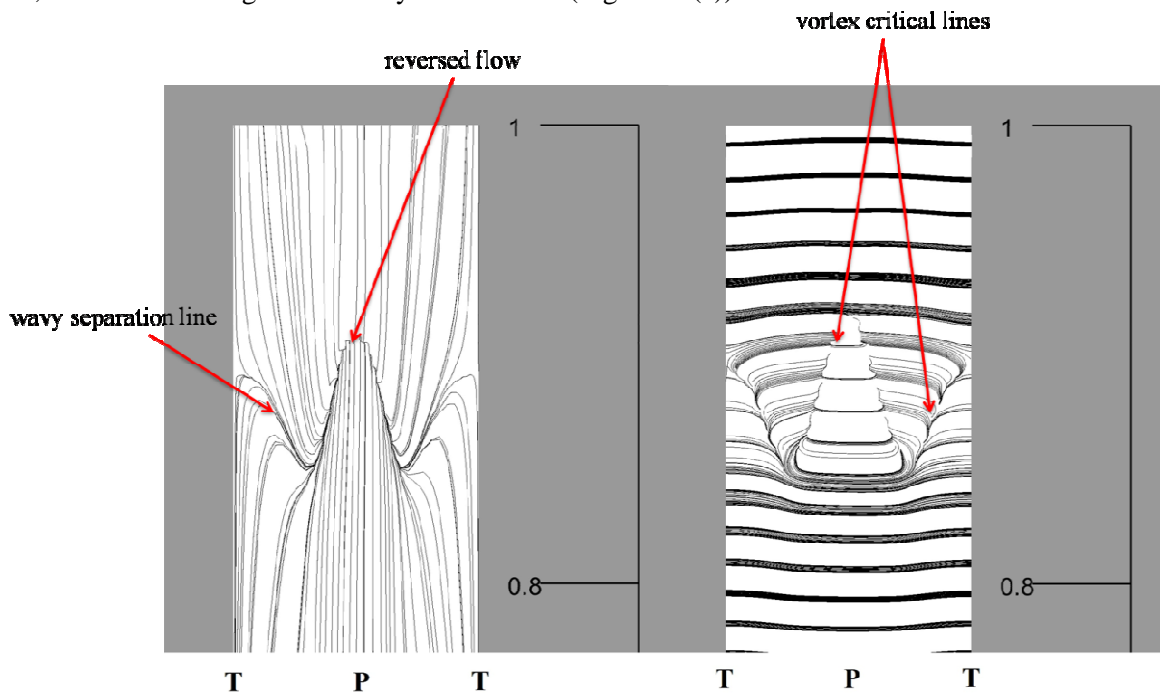


FIG.17 Shear stress lines (left) and vortex lines (right) in the vicinity of the trailing edge. (A2W7.5,  $Re=120,000$ ,  $AOA=6^\circ$ )

As pointed out previously, the flow separation near the trailing edge assumes a wavy pattern (Figure 17). The shape of the separation line suggests that the separation point on the peak occurs further downstream, compared to the trough. The forward-most separation point, however, occurs on the middle spanwise location. Therefore, the middle spanwise location for A2W7.5 sees the largest amount of flow separation in comparison with the peak and the trough. The vortex lines, on the other hand, illustrate that chordwise critical lines align themselves with the wavy separation lines. These points suggest that surface-normal vorticity is present and lifts from the surface of the foil in this region.

To examine the effect of the undulating leading edge on the vorticity field, the three components of vorticity are studied individually. In accordance with the Cartesian coordinates system in Figure 2, these components are defined as streamwise (parallel to the free-stream flow direction), transverse (normal to streamwise) and spanwise vorticity (along the Z axis), whose mathematical formulations are given below:

$$\begin{aligned} \vec{\omega} &= \text{Curl}(\vec{u}) = (\omega, \eta, \zeta); \\ \text{Streamwise Vorticity} &= \omega \cos(\alpha) + \eta \sin(\alpha) \\ \text{Transverse Vorticity} &= -\omega \sin(\alpha) + \eta \cos(\alpha) \\ \text{Spanwise Vorticity} &= \zeta \end{aligned} \quad (1-4)$$

Iso-surfaces of vorticity in the spanwise direction are displayed in Figure 18(a). It is noticed that the sheets of spanwise vorticity appear to be rippled, an effect which was also observed for the other tubercled foils detailed in the previous chapters. The rippling effect is a direct corollary of the cyclic variation in spanwise circulation. Iso-surfaces of streamwise vorticity (see Figure 18(b)), on the other hand, illustrate regions of vorticity of opposite sign, interpreted as pairs of counter-rotating vortices in the streamwise direction.

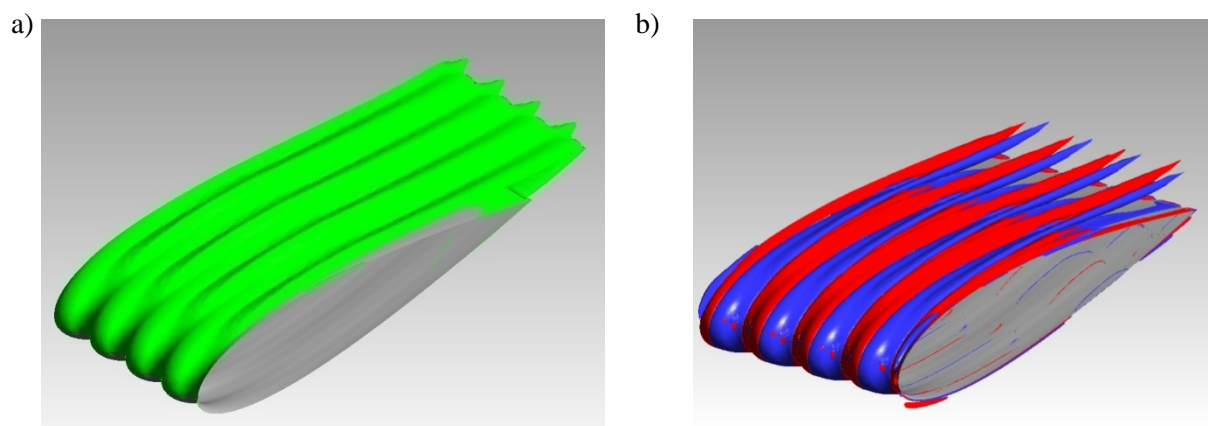


FIG.18 Iso-surfaces of (a) spanwise and (b) streamwise vorticity. Blue shows a counter-clockwise sense of rotation, while red indicates a clockwise sense of rotation. (A2W7.5, Re=120,000, AOA= 6°)

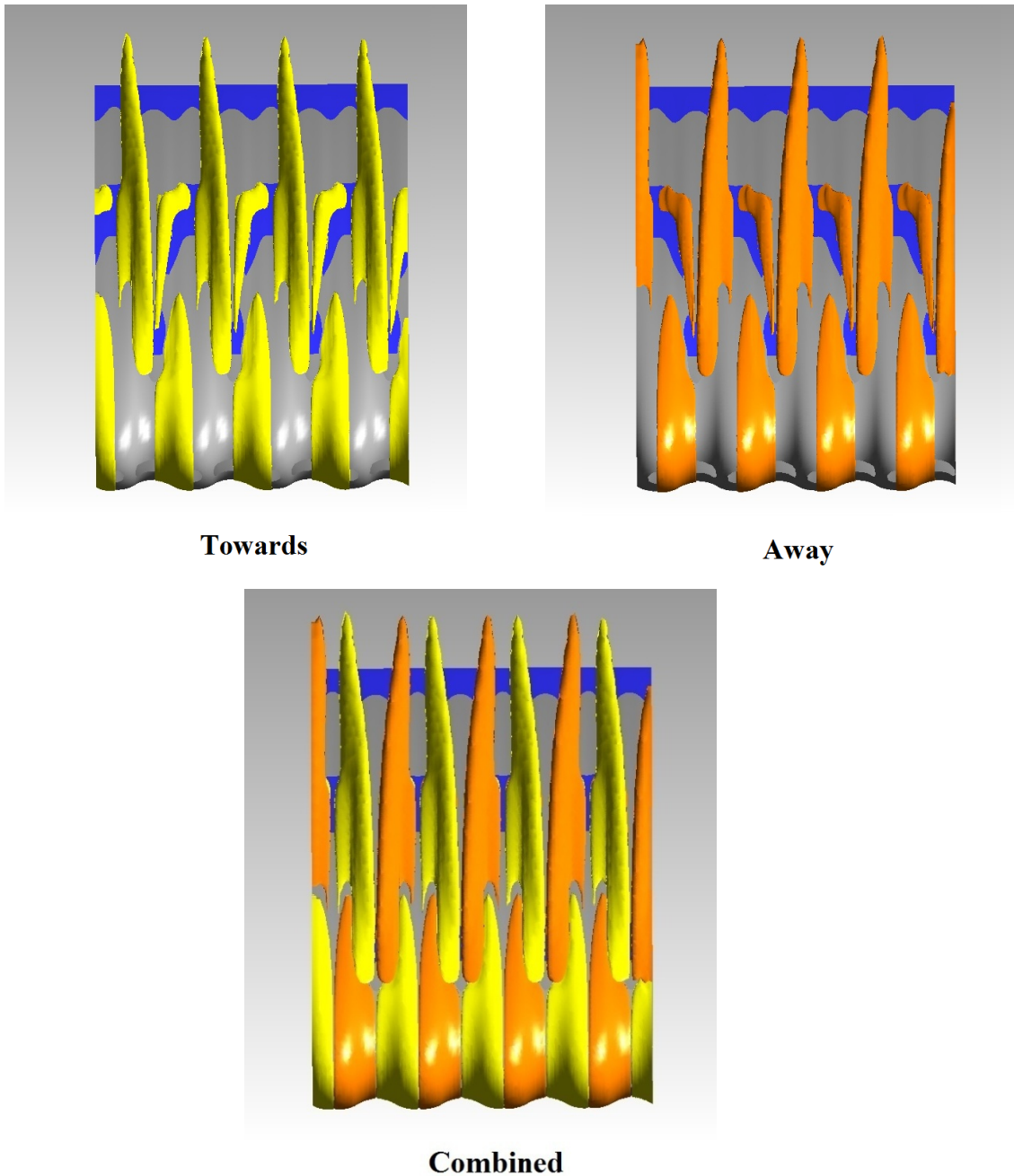


FIG.19 Iso-surfaces of vorticity in the transverse direction in the oblique view. Yellow indicates vorticity pointing towards the wing's surface, while orange shows vorticity oriented away from the surface. (A2W7.5,  $Re=120,000$ ,  $AOA=6^\circ$ )

Figure 19 presents iso-surfaces of transverse vorticity over the tubercled foil in three oblique views. To examine the origins of the vortical features, areas over the foil where reversed flow is present are coloured in blue. It is clearly observed that two vortical surfaces of opposite sign arise from the laminar separation bubble, near the focal critical points. This observation reinforces the notion that strong skewness reorganises vorticity in the streamwise and transverse directions near the leading edge. Further downstream, transverse vortical structures convect towards the separated flow region in the vicinity of the spiralling flow near the mid-chord section of the foil. Note that the orientation

associated with the vortical structures is such that they depart from the LSB and arriving at an angle to the separated flow region downstream.

Streamwise vorticity is also present in the wake region, although, as seen in Figure 20, its magnitude is attenuated, as the flow moves downstream, in accordance with Kelvin's circulation theory. Note how the decrease in the magnitude of streamwise vorticity is accompanied by an enlargement in the vortex cores. This observation is consistent with the flow behaviour over the other tubercled foils investigated in the authors' previous study [20].

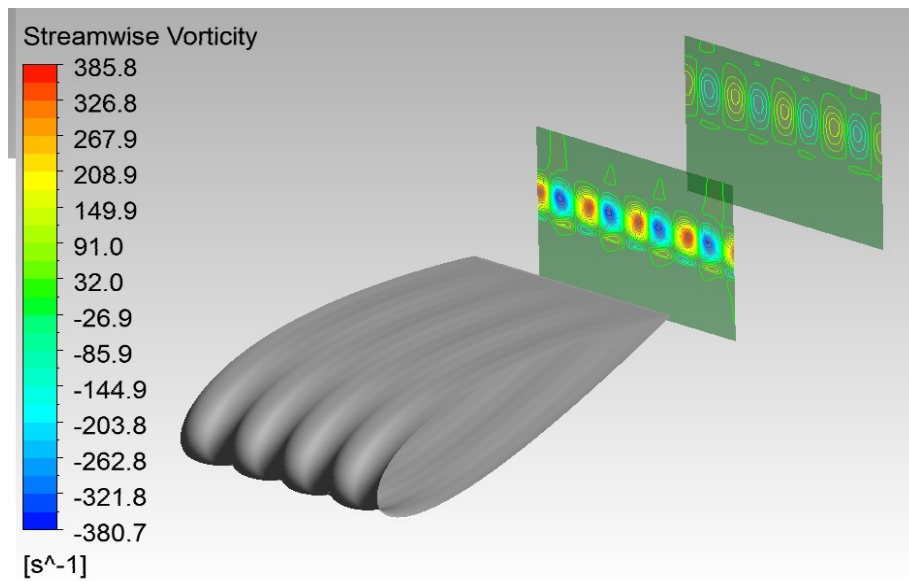


FIG.20 Contours of streamwise vorticity in the wake region. (A2W7.5,  $Re=120,000$ ,  $AOA=6^\circ$ )

## Post-stall Flow Analysis

In this section, the flow over the tubercled foil A2W7.5 is analysed at an attack angle equal to  $20^\circ$ . Figure 21 shows iso-surfaces of zero-velocity over the suction side of the foil. It is noted that separated flow in the form of a stalled cell [19] envelops a large region on the suction side of the airfoil at this attack angle. In contrast to the troughs, the boundary layer behind all tubercle peaks in the vicinity of the leading edge is attached to the foil. Flow attachment extends further downstream behind tubercles located on either side of a large recirculation zone originating from the central trough region. In addition, narrow separation bubbles exist along the chord, in several troughs. It is noteworthy that the extent of the attached flow in the chordwise direction was observed to be time-dependent, however the mechanism described here did not vary with time and was consistently found over the simulation time. The pattern of flow separation near the extremities of the airfoil, in the spanwise direction, suggests that periodicity in the flow field is plausible. Periodicity was also reported by Custodio [3] who conducted flow visualization tests at  $Re=1,500$ .

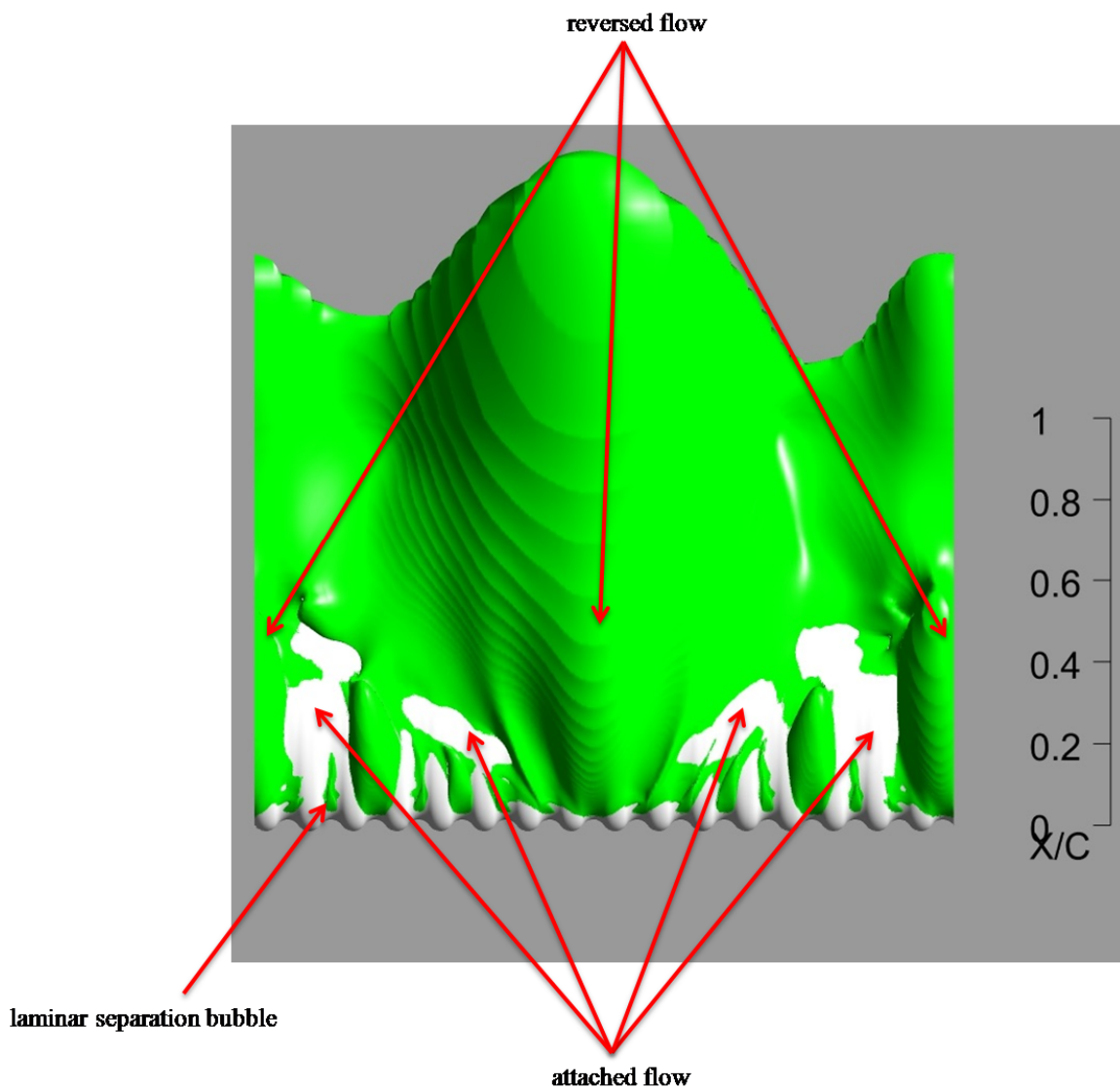


FIG.21 Separated flow, displayed in green, over the suction side. (A2W7.5,  $Re=120,000$ ,  $t=0.055(s)$  AOA =  $20^\circ$  )

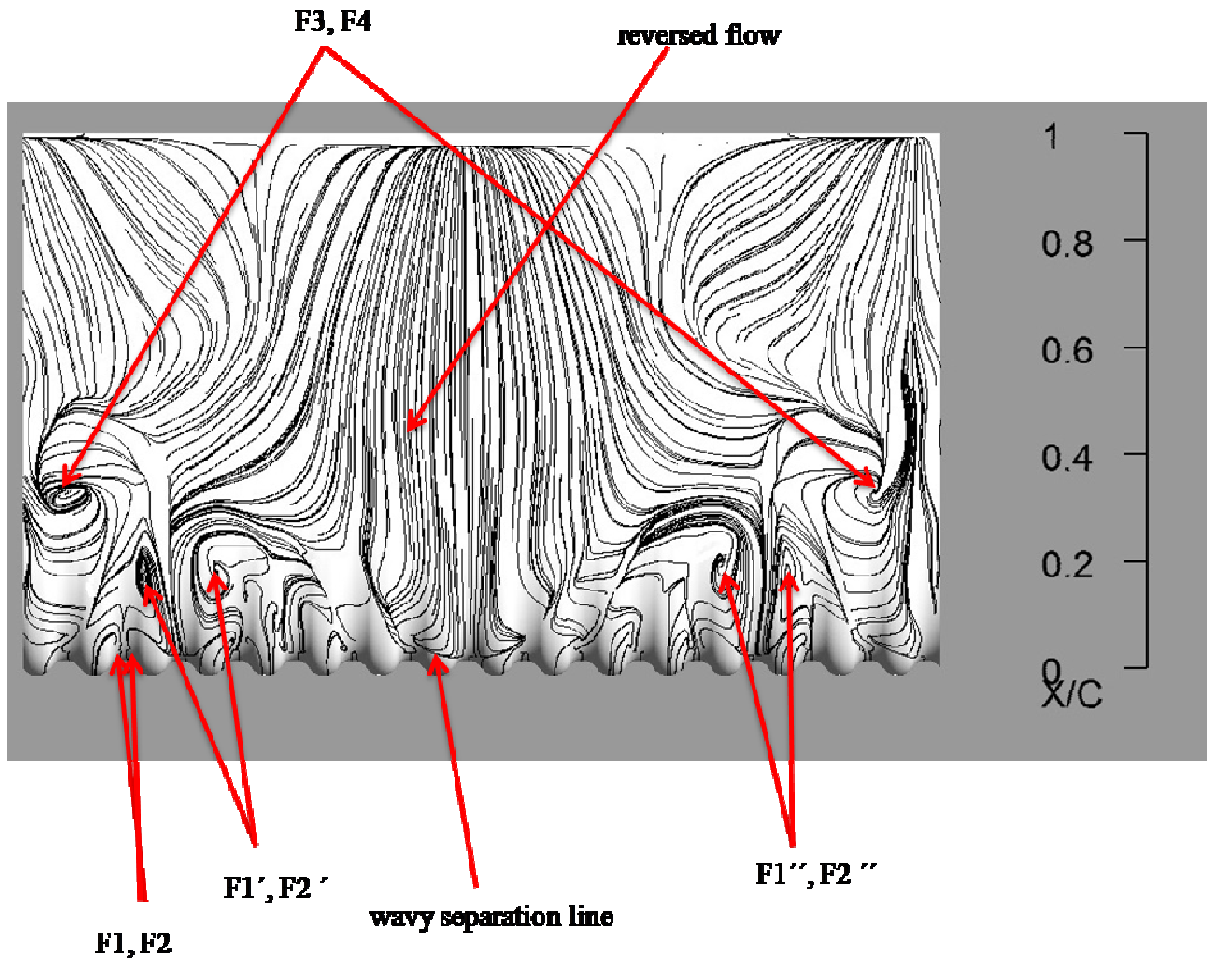


FIG.22 Limiting streamlines (a) over the entire suction side (b) in the close-up view. (A2W7.5,  $Re=120,000$ ,  $AOA = 20^\circ$ )

Several critical points are identified in the limiting streamlines (Figure 22), the most prominent of which are the two foci, F3 and F4 that mark large regions of swirling flow emanating from the reversed flow region. Focal points are also identified near the leading-edge (F1, F2). These are the same focal points, associated with narrow laminar separation bubbles, found for the pre-stall case at  $AOA = 6^\circ$ . The other pairs of focal points (F1', F2' and (F1'', F2'')) are attributed to longer separation bubbles. Figure 21 suggests that the boundary layer downstream of these bubbles do not re-attach and instead merge with the reversed flow. The appearance of focal critical points, suggest the presence of coherent vortical features above the foil.

To visualise regions containing high streamwise vorticity, iso-surfaces of streamwise vorticity are presented in Figure 23(a). The colour red represents positive streamwise vorticity in the free-stream flow direction (clock-wise sense of rotation), while blue indicates the opposite. It is noted that an alternating pattern of vorticity is realised along the span near the leading edge, similar to the pre-stall case. The sense of rotation associated with the vortical features, in this zone, is such that, above all tubercle peaks, a downwash effect is created, in accordance with the original predictions by van Nierop *et al.* [26]. Two pairs of larger zones containing interwoven streamwise vorticity, on either side

of the central bubble, are also identified near the mid-chord section. The position of these coherent structures, suggests that above the surface of the foil, vortices of opposite sign stand on top of one another.

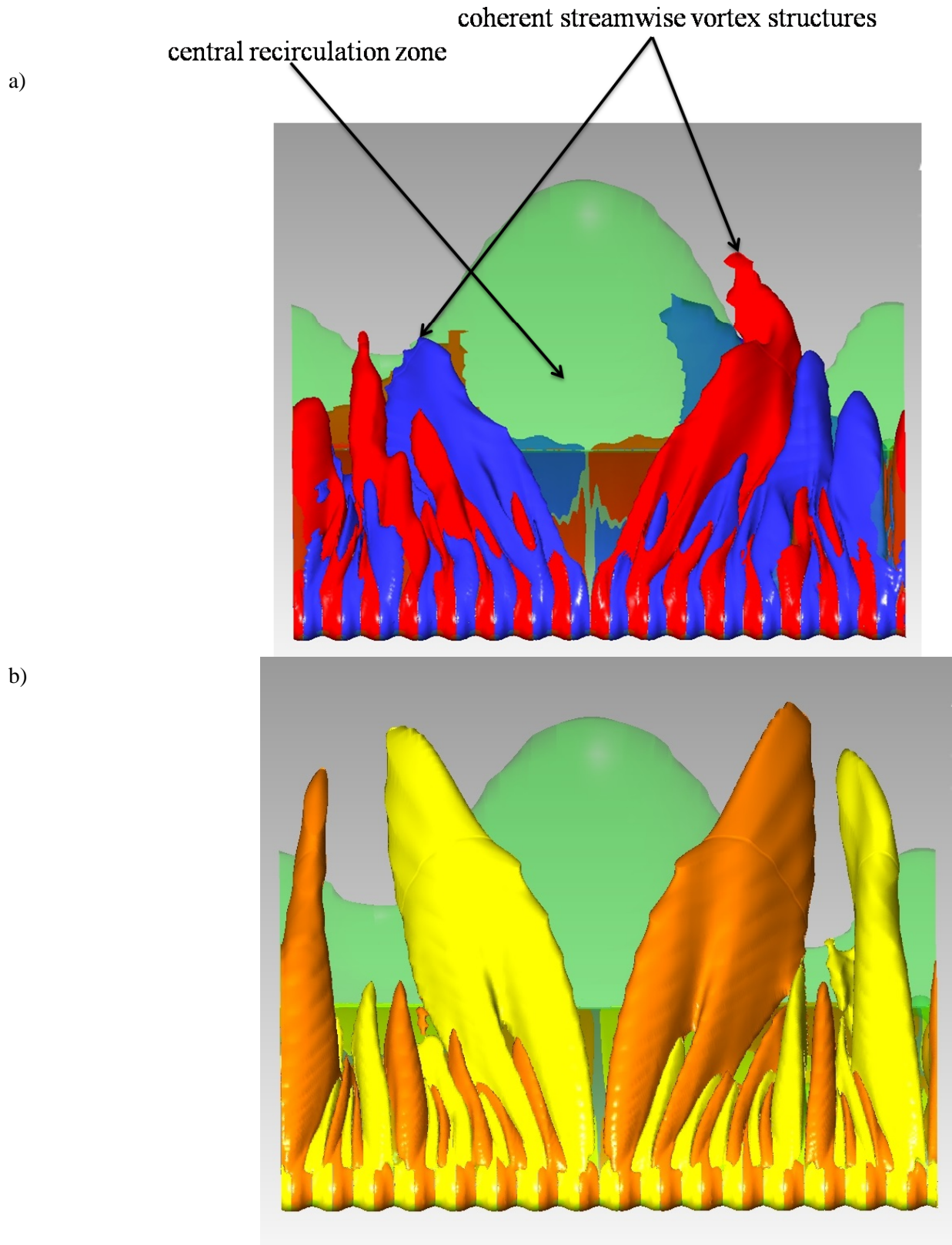


FIG. 23 (a) Iso-surfaces of streamwise vorticity over the suction side in the oblique view. Blue represents counter-clockwise while red stands for a clockwise sense of rotation. Streamwise vorticity level:  $800 \text{ s}^{-1}$ . (b) Transverse vorticity level:  $5000 \text{ s}^{-1}$  (A2W7.5,  $\text{Re}=120,000$ ,  $t=0.055(\text{s})$ ,  $\text{AOA} = 20^\circ$ )



Iso-surfaces of transverse vorticity in Figure 23(b) also demonstrate the presence of a spanwise alternating pattern in the formation of transverse vorticity near the leading edge. Two diagonally-shaped surfaces stand out on either side of the central recirculation zone, while smaller regions filled with transverse vorticity appear in the other troughs. Pairs of iso-surface of transverse vorticity of opposite sign, occupying smaller volumes, are found in the trough regions that likely arise from the focal points near the leading-edge.

The effect of the presence of strong vorticity over the foil on momentum transfer can be elicited from Figure 24 that shows a three-dimensional streamline over a small wing section where both attached and separated flow are identified. Observing the diagram, it is found that, as the oncoming flow climbs over the tubercle in zone (1), it moves sideways (2) and is driven into the recirculation zone. In this region the flow swirls around and upon exist, transfers momentum from zone 3 to 4. Finally, the flow re-enters the recirculation zone (5) and continues downstream via (6). As a result of the motion of the bulk of the flow out of the re-circulating zone and over the neighbouring regions, the boundary layer over the peak is re-energizes, and separation is inhibited. This mechanism is consistent with the observations reported for the other tubercled foils in the findings by Skillen *et al.*[22].

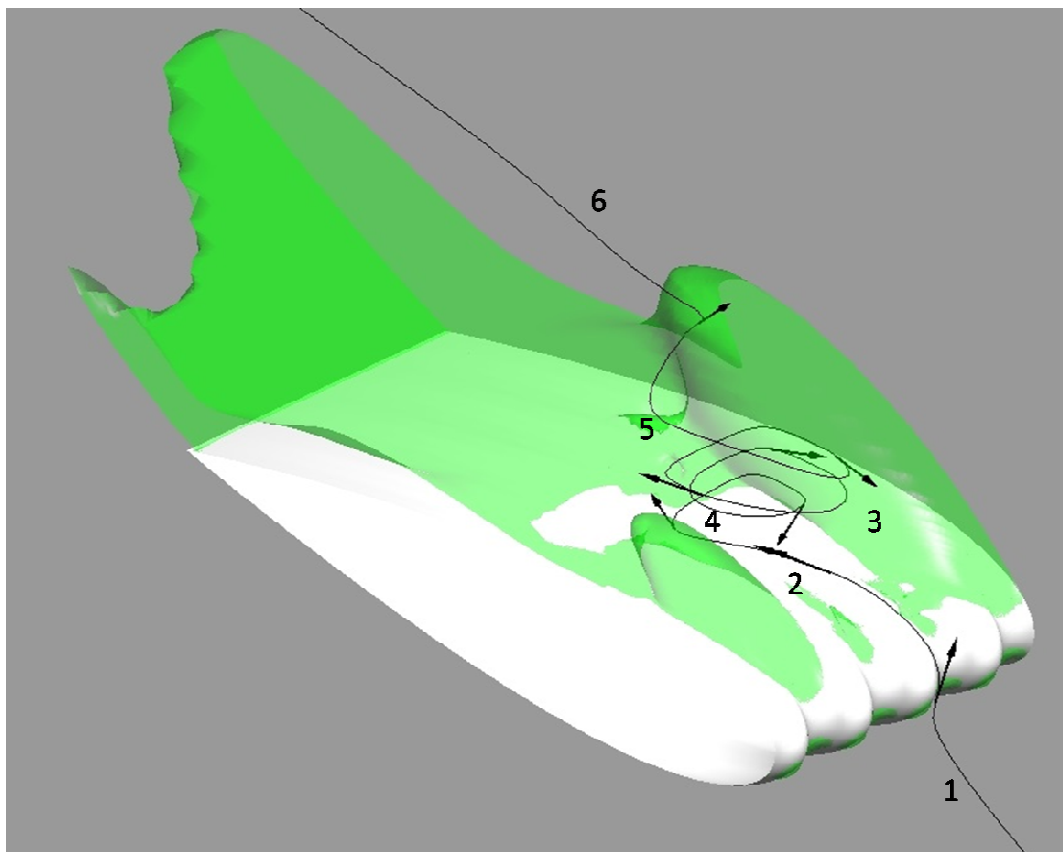
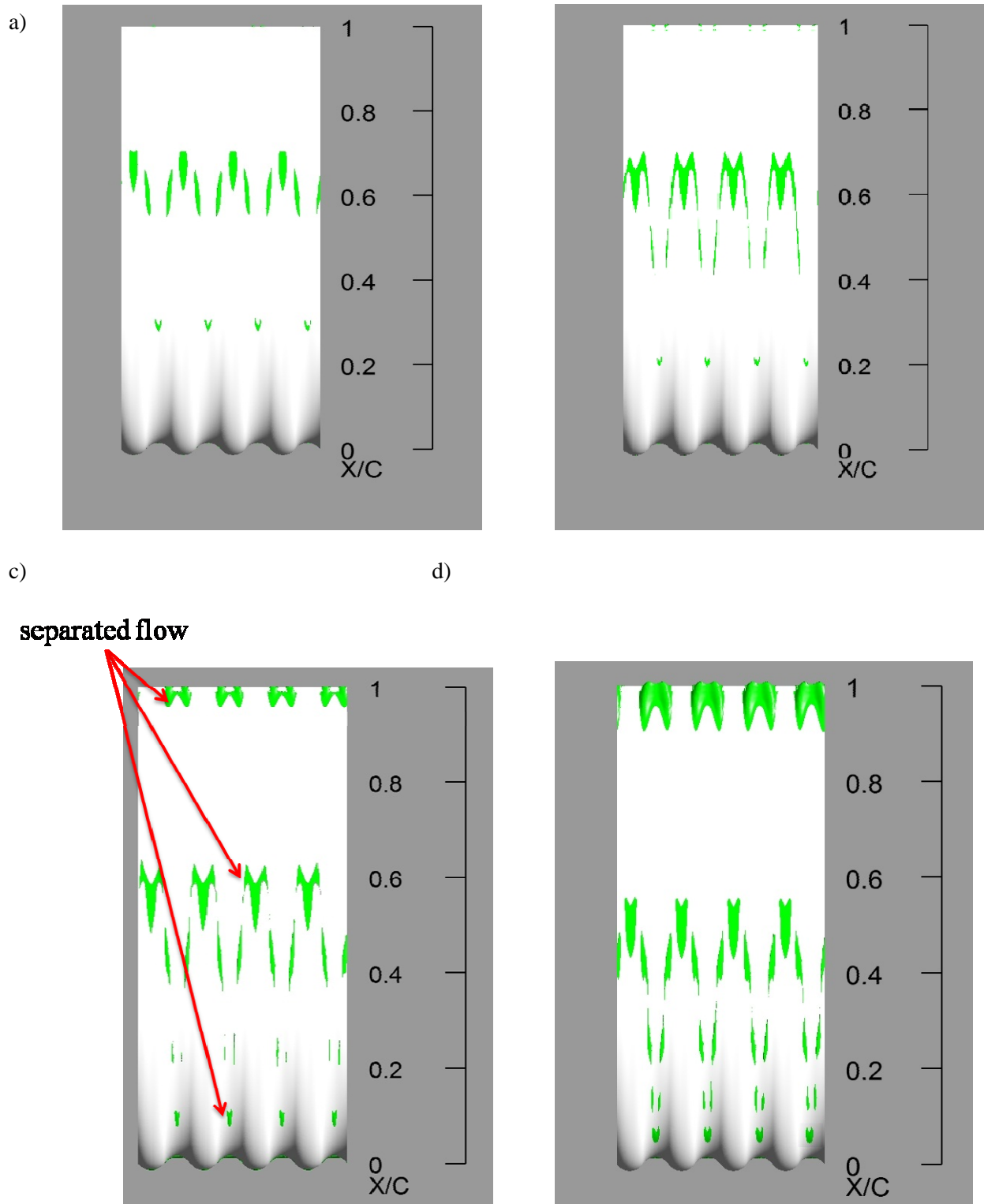


FIG.24 Momentum transfer illustrated by a three-dimensional streamline. Wing section shown for  $Z > 0.09\text{m}$  for clarity. Green sheet shows the separated flow zone. (A2W7.5,  $Re=120,000$ ,  $AOA = 20^\circ$ )

## Turbulent Flow Cases (Re=1,500,000)

### Pre-Stall Flow Structure Analysis

Reversed flow over the suction of the foil A14W52.5 is displayed for four pre-stall attack angles in Figure 25. With the exception of a few common flow features, the pattern of reversed flow appears, for the most part, different than what was observed for the same airfoil at Re=120,000.



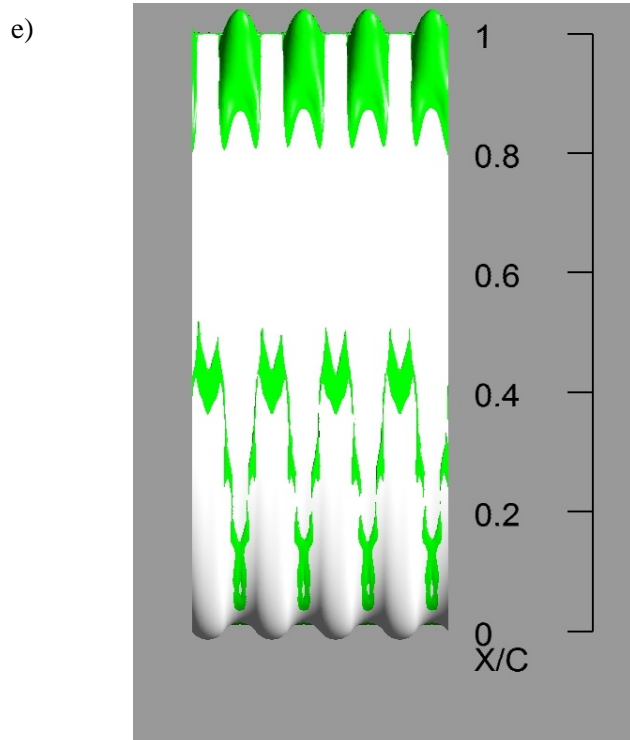


FIG.25(a-e) Regions of reversed flow at AOA = 0°, AOA = 2°, AOA = 6°, AOA = 10° and AOA = 14°. (A14W52.5, Re=1,500,000)

At AOA = 0°, two primary regions of separated flow are identified, one near the mid-chord section and the other in the trough mid-span location. As the attack angle increases to 2°, the boundaries of all the separation zones move further upstream. While flow separation near the trailing edge is minimal, as the attack angle increases to 6 degrees, a distinct wavy pattern develops towards the trailing-edge of the foil. The delay in trailing edge flow separation at Re=1,500,000, compared to that of Re=120,000 is expected, as the turbulent boundary layer in this instance is more resistant to flow separation, owing to the presence of fully-turbulent flow. The separation pattern is more noticeable as the separation zones grow in size and move upstream at AOA = 10° and AOA = 14°.

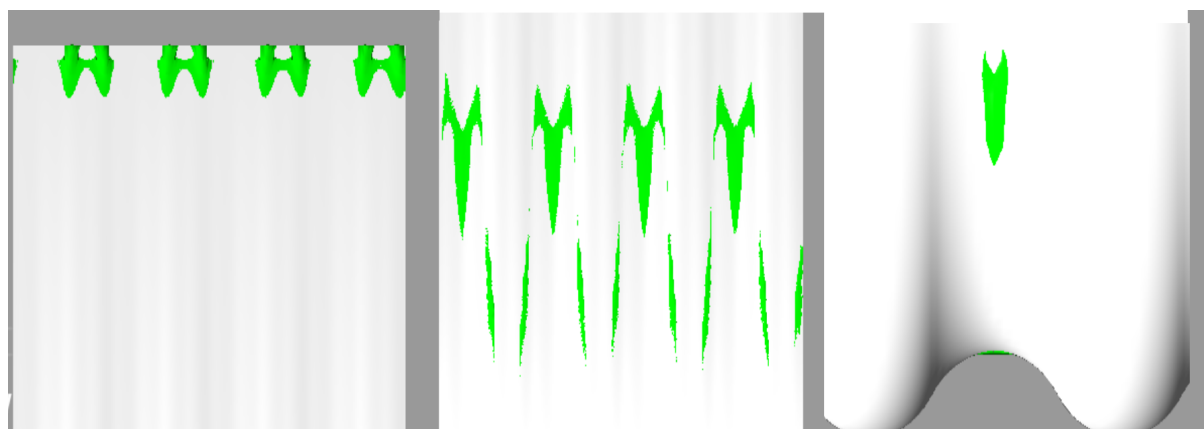


FIG.26 Close-up views of the regions of reversed flow at a 6-degree attack angle (A14W52.5, Re=1,500,000)

In a similar manner to the flow at  $Re=120,000$ , the tubercled leading edge establishes a strong spanwise pressure gradient, that displays a cyclic variation, along the span (Figure 27). As a result, the pressure falls to a minimum (suction peak) in the troughs (Figure 28). The gradient between the peak and the trough drives the flow towards the minimum pressure region, where the three-dimensional laminar separation bubble lies.

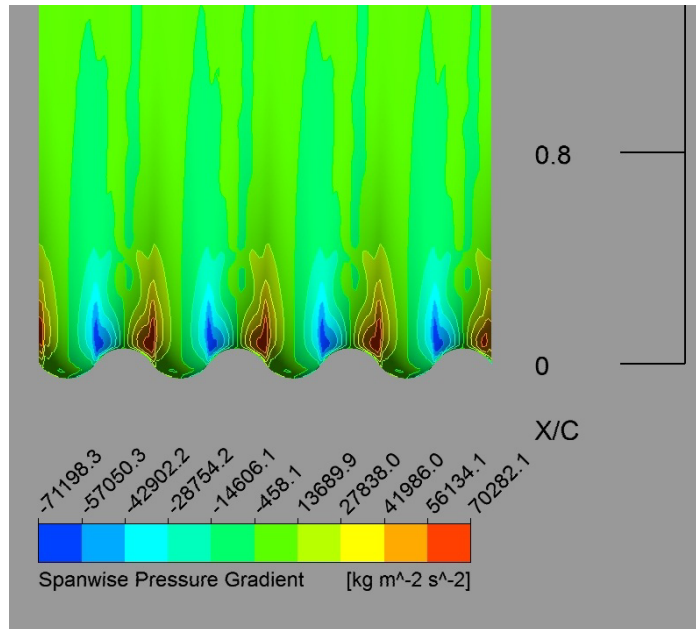


FIG.27 Spanwise pressure gradient near the leading edge. (A14W52.5,  $Re=1,500,000$ ,  $AOA=6^\circ$ )

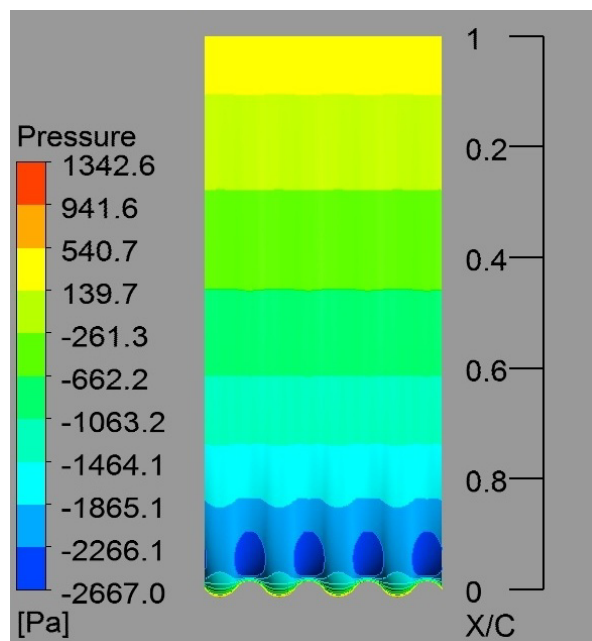


FIG.28 Contours of the static pressure on the suction side. (A14W52.5,  $Re=1,500,000$ ,  $AOA=6^\circ$ )

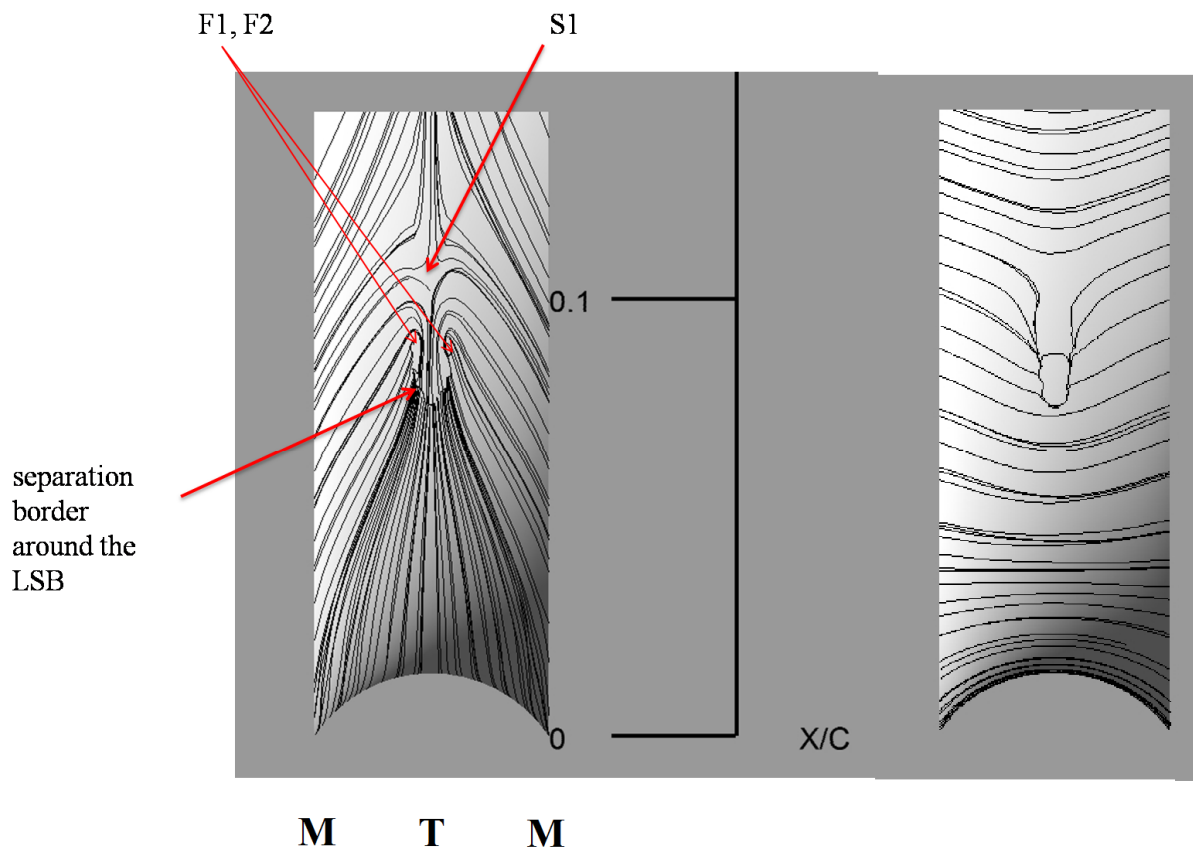


FIG.29 Limiting streamlines (left) and vortex lines (right) near the Laminar Separation Bubble (right). (A15W52.5,  $Re=1,500,000$ ,  $AOA=6^\circ$ )

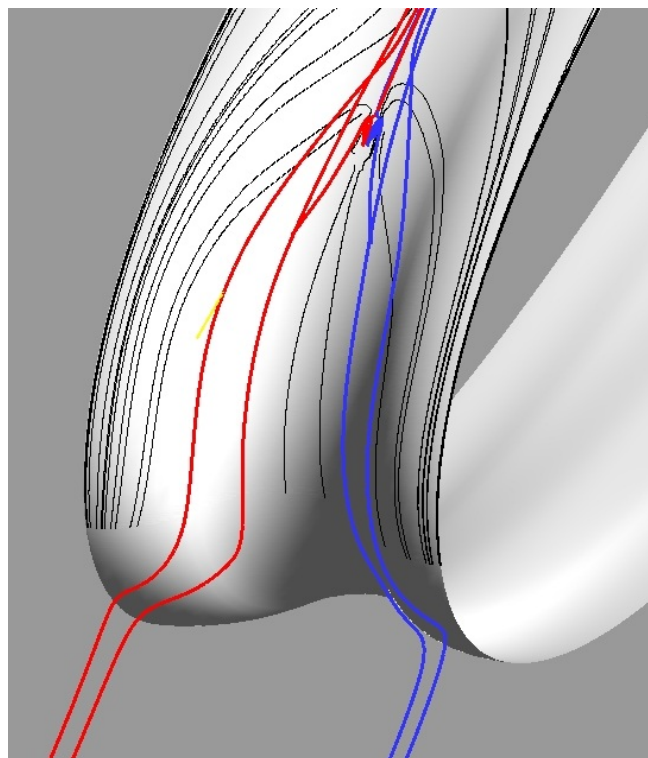


FIG.30 Three-dimensional streamlines in the vicinity of the LSB (A14W52.5,  $Re=1,500,000$ ,  $AOA=6^\circ$ )

In what follows, the flow is analysed in detail at an attack angle equal to  $6^\circ$ . The first notable flow feature is identified as an open laminar separation bubble (Figure 29), which was also identified for the transitional flow case. The only difference here is the smaller scale of the open LSB, compared to the case where  $Re=120,000$ . Two small focal points and a saddle of attachment are the primary critical points associated with the LSB on the trough. In Figure 30, three-dimensional streamlines approaching the airfoil, display the tendency of the flow to converge towards the trough section, due to the presence of a strong spanwise pressure gradient. Upon reaching the zone where suction pressure is minimum, under the influence of vorticity, the streamlines turn abruptly, indicating the formation of vortical features. Examining the skin friction coefficient along the suction side of the trough (Figure 31), confirms the occurrence of a flow separation and a flow attachment process. This is evidenced by the change in the sign of the skin friction coefficient from positive to negative, initially around  $X/C \approx 0.077$ , and subsequently from negative to positive, where  $X/C \approx 0.104$ . The re-attachment confirmed that S1 is a saddle of attachment. The vortex lines around the LSB, show a distinct change in the direction of the tangent vector associated with each vortex line, as the spanwise-dominant vortex lines turn in the streamwise direction, giving rise to the re-organisation of vorticity into the streamwise and transverse directions. Thus, the secondary flow mechanism is activated by the presence of the tubercled leading edge, for the transitional and near-turbulent regimes.

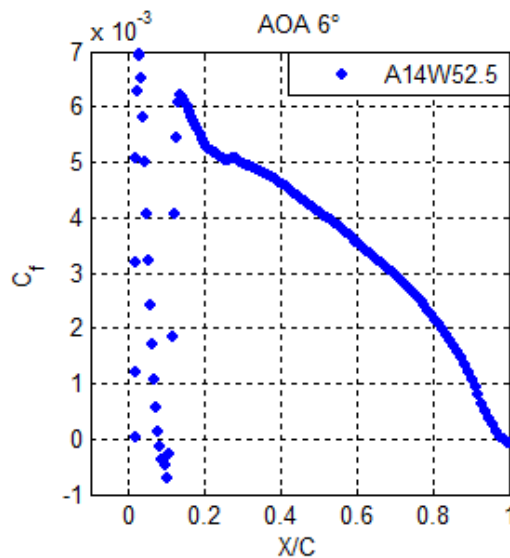


FIG.31 Skin friction along the trough spanwise location.(A14W52.5,  $Re=1,500,000$ ,  $AOA=6^\circ$ )

The flow near the mid-chord region shows more complex behaviour. The key critical points in the mid-chord region, where the shear stress vanishes, are two saddle points (one of detachment and the other of attachment) and two stable foci (Figure 32(a)). The shear stress coefficient plot along the peak spanwise location, illustrates that the flow separates at  $X/C=0.48$ , and then re-attaches further downstream at  $X/C=0.58$ . These locations coincide with the saddle of detachment, S3 and saddle of attachment, S4.

The surface vortex lines, near the mid-chord region, reveal remarkable characteristics. While the strong spanwise component of vorticity is evident at most locations (Figure 32(b)), in the vicinity of  $X/C=0.6$ , a star-like feature is realised whereby the vortex lines assume streamwise orientation. Also note that the canopy of vorticity analogy introduced earlier, is also relevant in this case, as transverse vorticity lifts along two chordwise critical vortex lines.

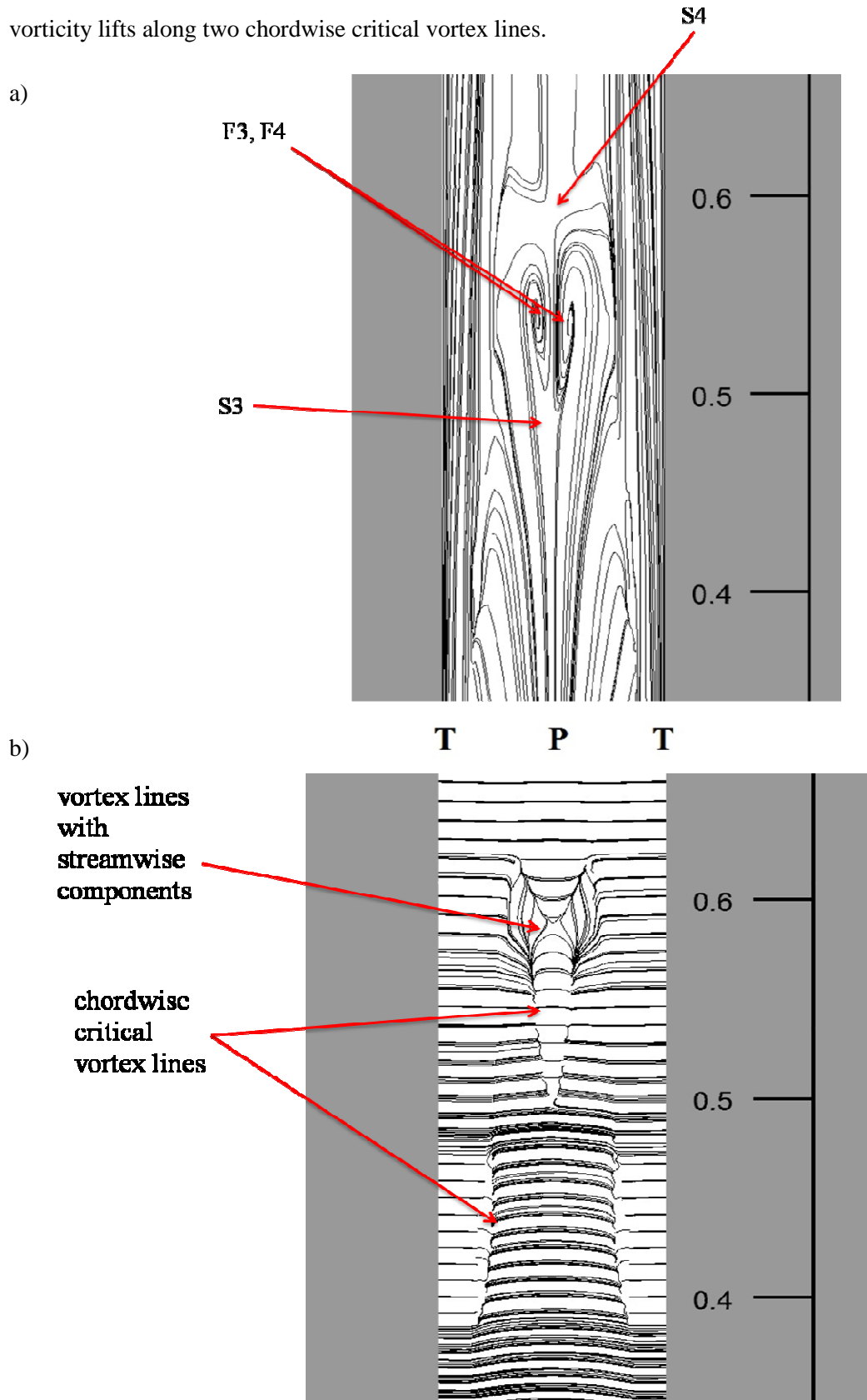


FIG.32 (a) Shear stress and (b) vortex lines near the mid-chord section. Diagram shows one tubercle wavelength. (A14W52.5,  $Re=1,500,000$ ,  $AOA=6^\circ$ )

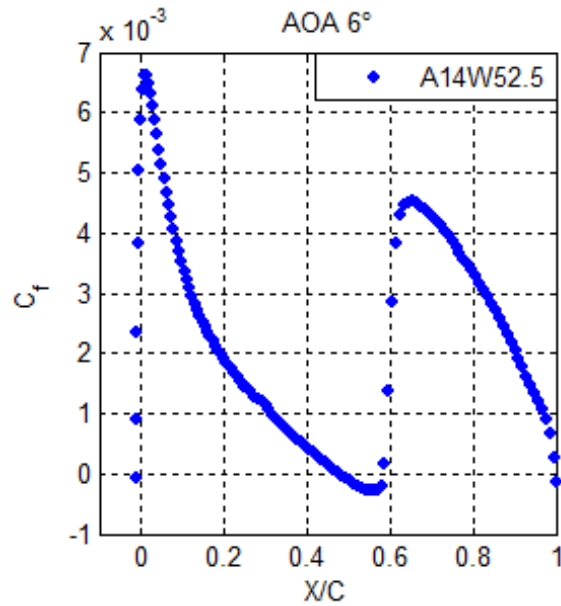


FIG.33 Skin friction, plotted along the peak spanwise location. (A14W52.5,  $Re=1,500,000$ ,  $AOA=6^\circ$ )

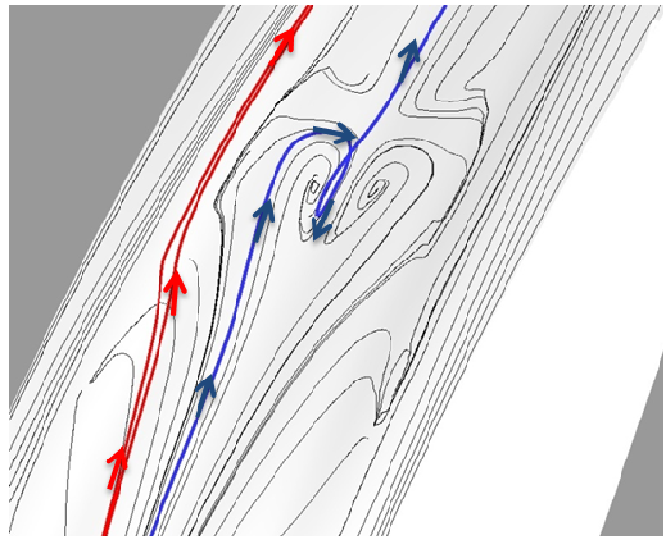


FIG.34 Three-dimensional streamlines as they approach the separated flow region near the mid-chord section. (A14W52.5,  $Re=1,500,000$ ,  $AOA=6^\circ$ )

The flow approaching the mid-chord section, takes two distinct paths, as shown in Figure 34. One group of streamlines flowing over the peak spanwise location undergo a twisting motion near the focal points F3 and F4, as illustrated by the blue in Figure 35. Another group of streamlines move to the side of the separated flow region without becoming engulfed into the spiralling flow zone over the peak. The locus of points where the spiralling flow and the forward-moving flow meet, mark the boundaries of the reversed flow region.



Further downstream, in the vicinity of the trailing edge, the flow is convected into two focal points, F5 and F6 (Figure 35), leading to the formation of three-dimensional counter-rotating vortices, near the trailing edge(see Figure 36). In regions where the surface flow moves upstream, a wavy separation line forms that encompasses the focal points. The critical vortex lines attest to vorticity lifting from the wing's surface in this region.

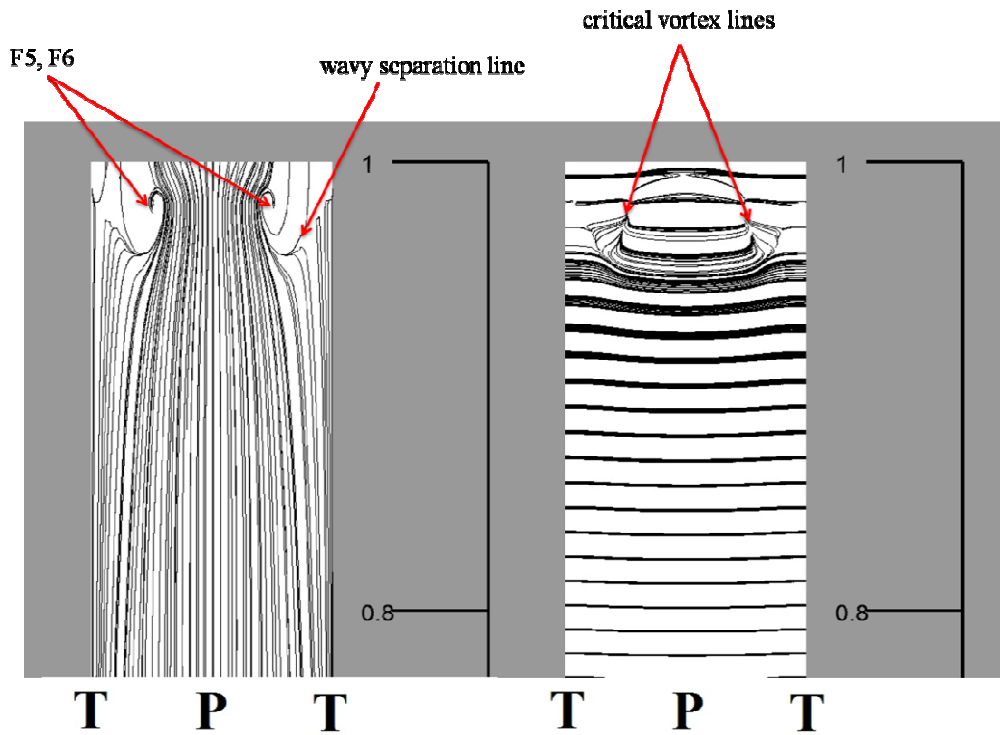


FIG.35 Limiting streamlines(left) and vortex lines (right) near the trailing edge. (A14W52.5,  $Re=1500,000$ ,  $AOA=6^\circ$ )

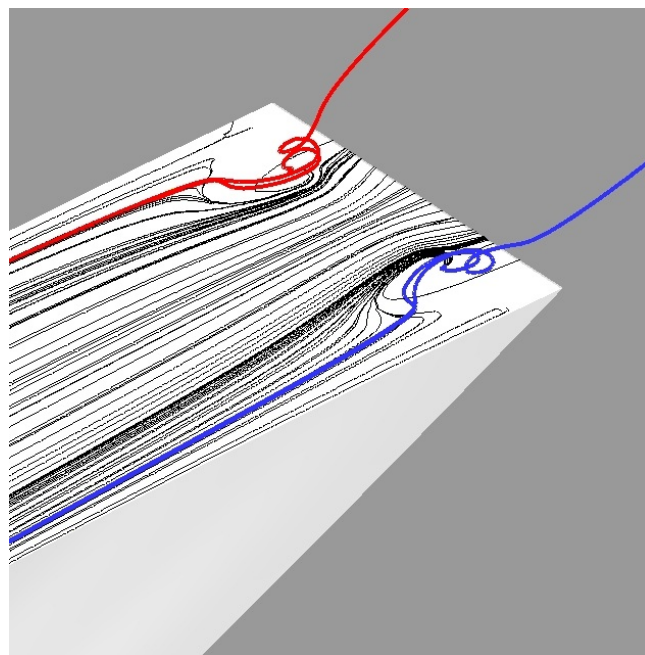


FIG.36 Streamlines near the trailing edge.(A14W52.5.  $Re=1500,000$ .  $AOA=6^\circ$ )

In summary, the approaching streamlines either converge into the trough where the open laminar separation bubble is established, or move past it and develop twisting trajectories near the mid-chord section and the trailing edge of the foil (Figure 37). In all flow patterns, spanwise vorticity is re-organised into streamwise and transverse-oriented vorticity in a complicated fashion which is explored in more detail in what follows.

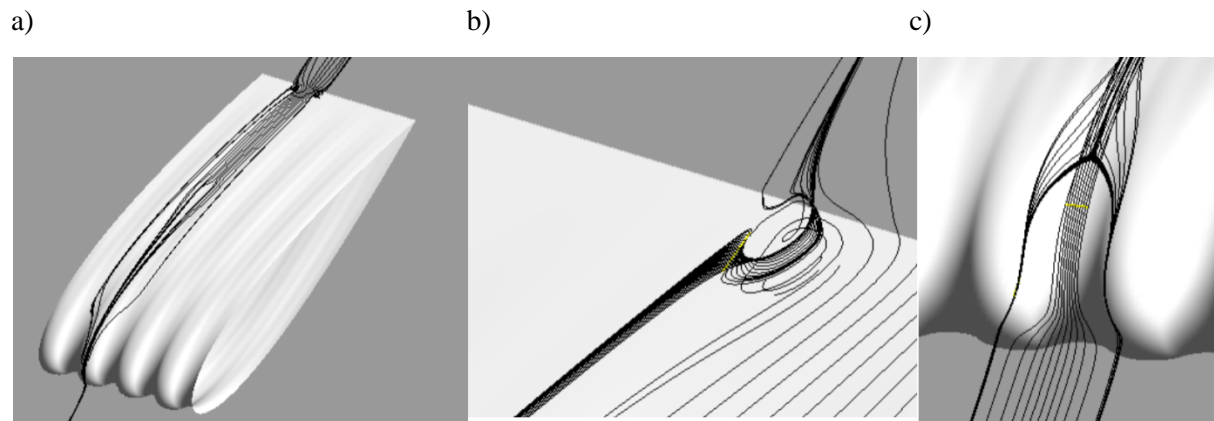


FIG.37 Three dimensional streamlines shown at various locations.(A14W52.5,  $Re=1,500,000$ ,  $AOA=6^\circ$ )

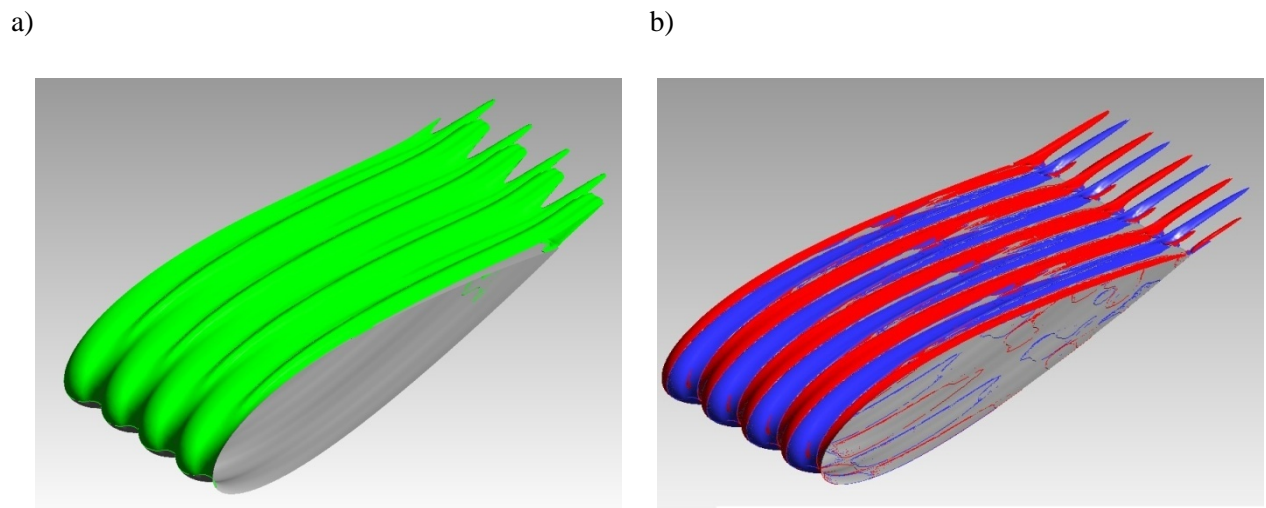


FIG.38 (a) Spanwise and (b) streamwise iso-surfaces. Blue indicates a counter-clockwise sense of rotation, while red shows a clock-wise sense of rotation. (A14W52.5,  $Re=1,500,000$ ,  $AOA=6^\circ$ )

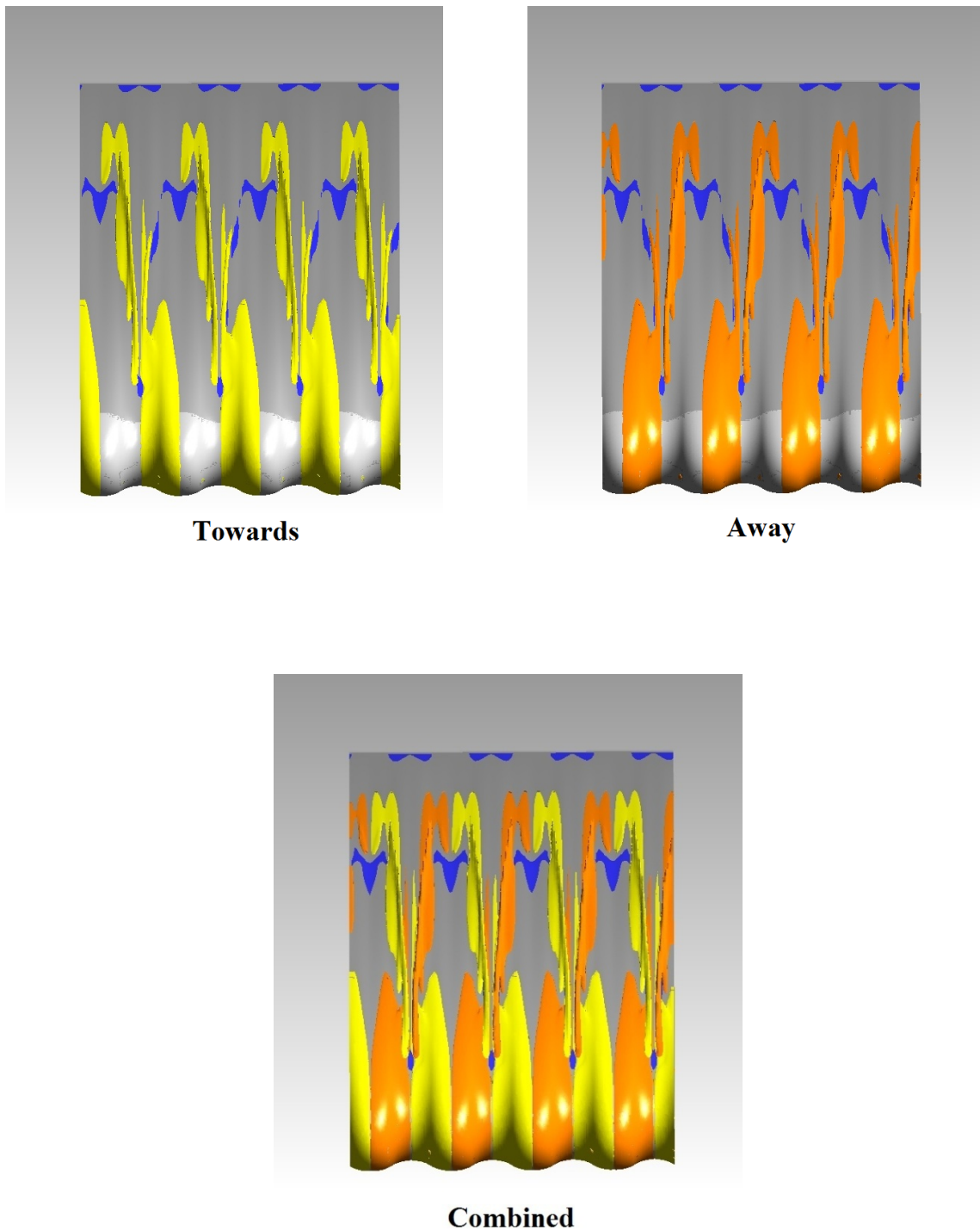


FIG.39 Transverse vorticity in the vicinity of the foil. Yellow and orange show vorticity towards and away from the wing's surface, respectively. (A14W52.5,  $Re=1,500,000$ ,  $AOA=6^\circ$ )

The effect of the undulating leading edge on the vorticity field is now examined in this part. Similar to the flow scenario where  $Re=120,000$ , at  $Re=1,500,000$ , the spanwise vortex sheets appear rippled (Figure 38 (a)). Also, streamwise vorticity of opposite sign is present (Figure 39(b)). Note that the streamtubes of streamwise vorticity appear closer to the surface of the foil compared to the

transitional flow case, as less flow separation is realised for the near-turbulent case and the counter-rotating vortices are embedded further down within the boundary layer.

Transverse vorticity of opposite sign also exists over the suction side of the airfoil, in regions shown in Figures 39. Similar to the transitional flow case, two vortex tubes emerge from the laminar separation bubble, near the leading edge. The vortex tubes, however, undergo abrupt twists in the vicinity of the separated flow region near the mid-chord section. The twisting pattern of the vortex tubes is remarkably similar to the shape of the separated flow region in this region.

In Figure 40, contours of the streamwise component of vorticity have been plotted on two planes which are oriented normal to the free-stream flow direction in the wake region. It is evident that streamwise vorticity of opposite sign is present, a phenomenon that points to the generation of pairs of counter-rotating vortices. The strength of the vortices is weakened as the flow convects downstream, due to a vorticity diffusion process. Note that the values are markedly larger than those at the same attack angle for  $Re=120,000$ .

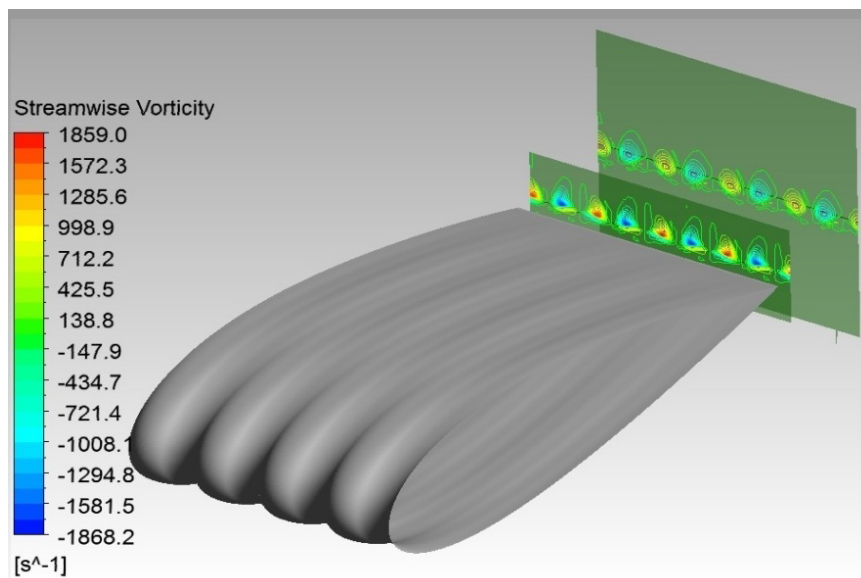


FIG.40 Streamwise vortices on planes orthogonal to the free stream flow direction, in the wake region. (A14W52.5,  $Re=1,500,000$ ,  $AOA=6^\circ$ )

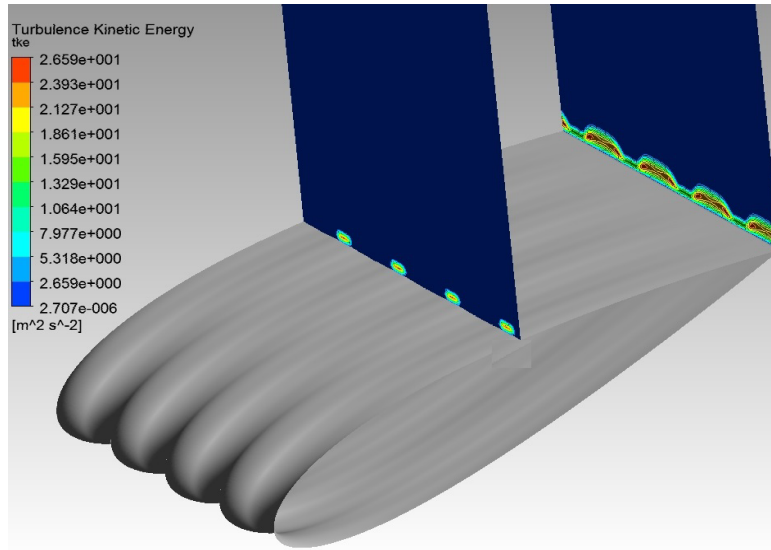


FIG.41 Contours of turbulent kinetic energy over the foil. (A14W52.5,  $Re=1,500,000$ ,  $AOA=6^\circ$ )

Contours of turbulence kinetic energy (TKE) are presented in Figure 41 for two chordwise locations over the suction side of the foil. The diagram shows that, on the mid-chord plane, the values of TKE are larger near the troughs in small concentrated areas, compared to the neighbouring regions. As the flow develops over the foil, turbulence kinetic dissipates over larger areas, as indicated by the pattern of TKE on the plane placed at the trailing edge. This observation is consistent with the finding by Lohry *et al.* [15] whereby a sharp increase in the turbulent kinetic energy near the trough spanwise location was reported over a tubercled foil with a NACA-0020 baseline profile.

## Post-stall Flow Analysis

Separated flow regions over the airfoil at  $AOA = 20^\circ$  are illustrated in Figure 42. It is readily seen that at this attack angle a large area on the suction side is occupied by a stalled cell. Contributing to the separated flow region, is a long separation bubble that originates from a trough, situated in close proximity to the leading edge and extending down to the trailing edge. This is an identical flow feature which was observed for the case where  $Re=120,000$ . A number of laminar separation bubbles appear in the troughs on either side of the large separation bubble. Also a narrow strip of separated flow is observed near the trailing edge.

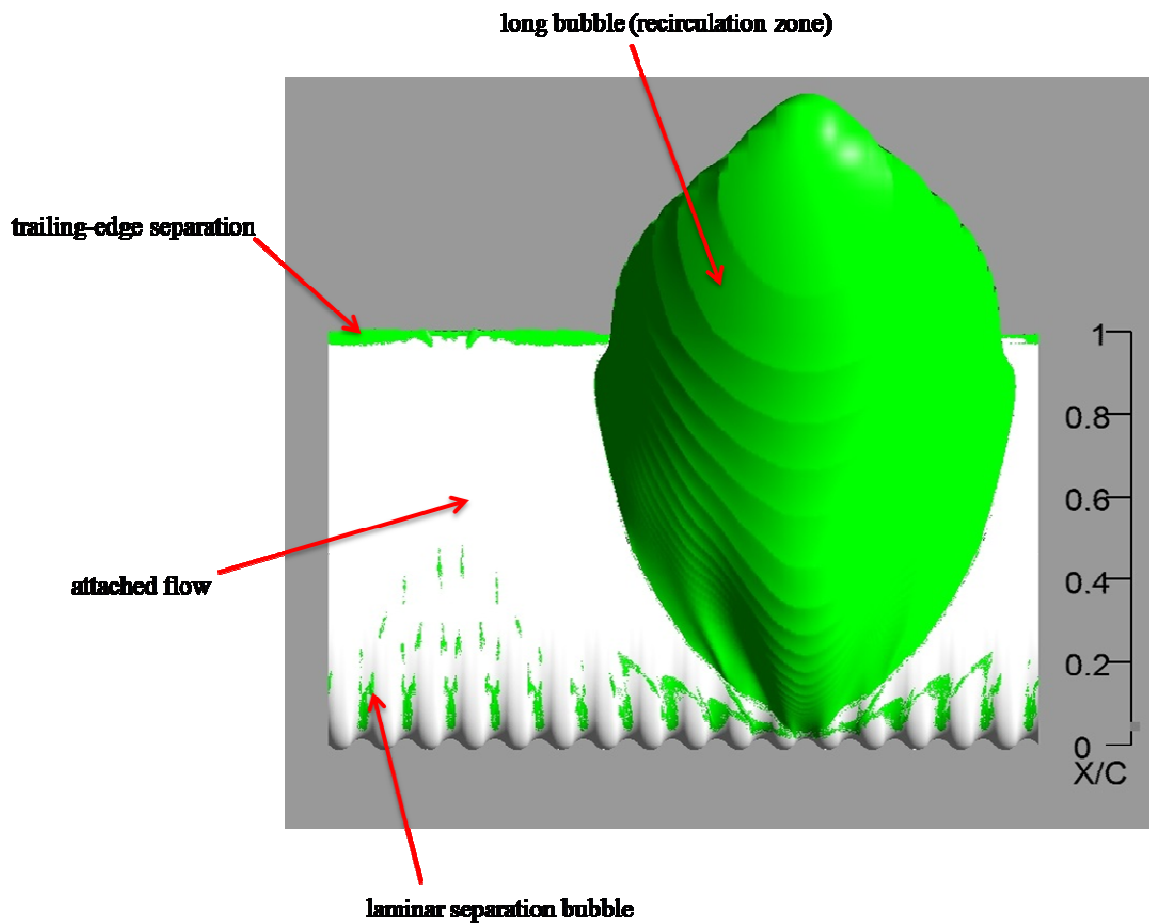


FIG.42 Reversed flow regions on the suction side illustrated by the zero-streamwise velocity iso-surfaces (  $AOA = 20^\circ$  , A14W52.5,  $Re=1,500,000$ )

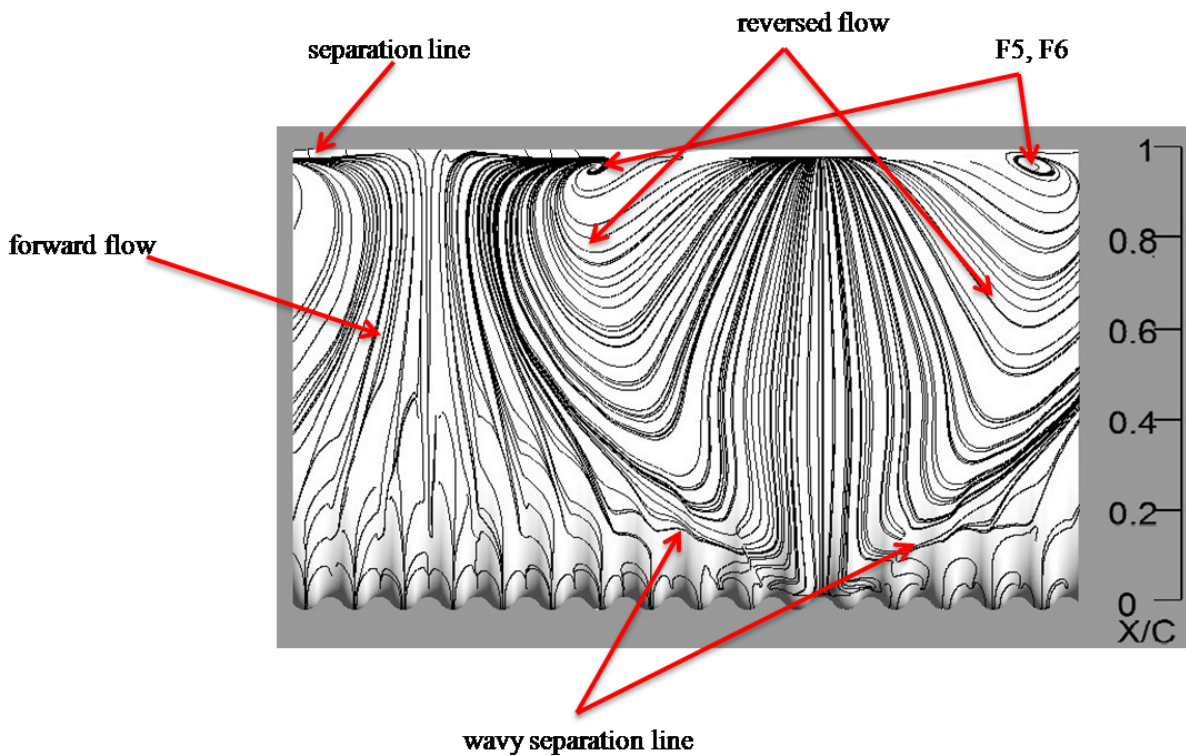
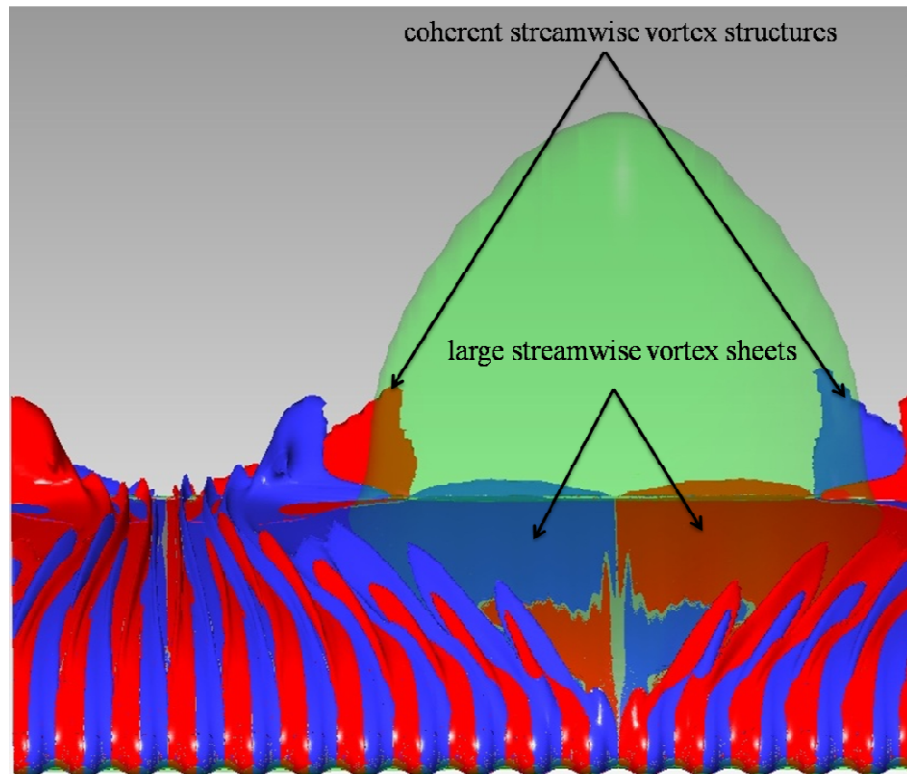


FIG.43 Shear stress lines over the suction side (A14W52.5,  $Re=1,500,000$ ,  $AOA = 20^\circ$ )

Figure 43 shows the limiting streamlines on the surface of A14W52.5. The presence of strong skewness within the boundary near the leading edge is evident. The critical points associated with the LSBs in the troughs are the same as those identified for the pre-stall case and are not shown here. Two noticeable focal points, F5 and F6, mark the locations of spiralling flow, residing within the long bubble. These focal points are the signature of coherent vortical features. Observing the pattern of limiting streamlines near the extremities of the foil in the spanwise direction, suggests the development of spanwise periodicity in this flow regime.

Iso-surfaces of streamwise vorticity in Figure 44 (at the same levels as those shown previously for  $Re=120,000$ ) highlight an alternating pattern of vorticity of opposite sign along the span. This is identical to the situation at  $Re=120,000$ , with the exception that the iso-surfaces of the same level of vorticity are closer to the wall. In the zone where the long bubble lies, two distinct large sheets of streamwise vorticity of opposite sign are found. The sense of vorticity associated with these sheets can be explained by the presence of reversed flow in this region. To clarify, spanwise vorticity in the boundary layer (in the opposite direction as that of forward flow) is turned in the streamwise direction in this region where flow skewness, in the vicinity of the foci F5 and F6, is present. Note that the sense of rotation of the swirling flow associated with each focus is opposite to the other. Hence, the arising streamwise vortex sheets contain values of vorticity of opposite sign. Another notable feature is the formation of coherent streamwise vortex structures near the trailing edge, on either side of the large bubble. These structures play a key role in the transfer of momentum, as will be described later.

a)



b)

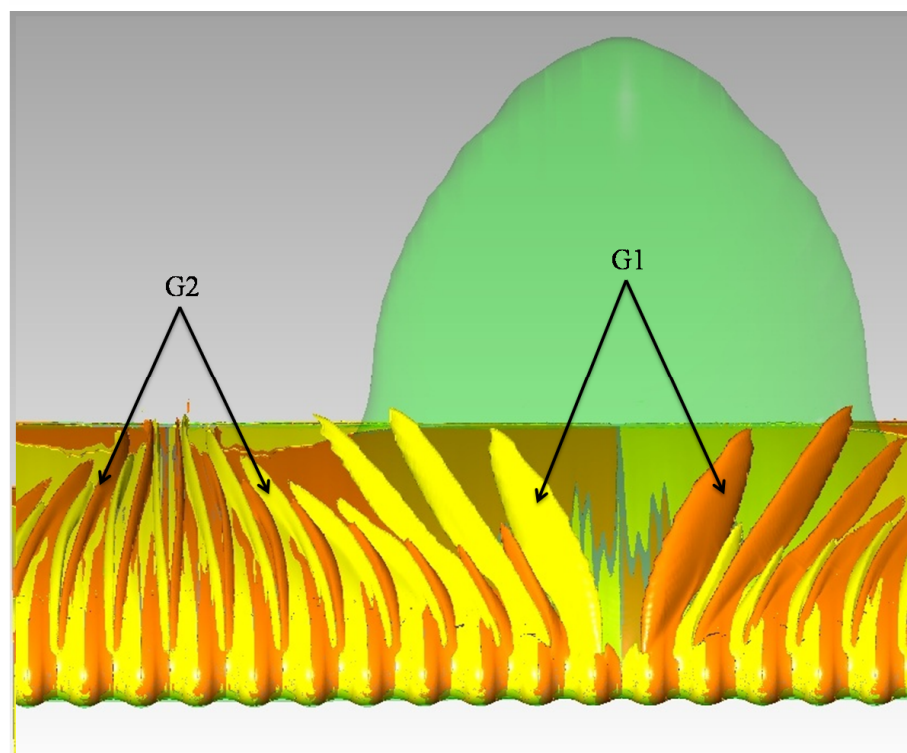


FIG.44 Iso-surfaces of (a) streamwise 800 and (b) transverse vorticity 1238 over the suction side of the foil (A14W52.5,  $Re=1,500,000$ ,  $AOA = 20^\circ$ )

Iso-surfaces of transverse vorticity (Figure 44(b)), illustrate similar patterns to those detected at  $Re=120,000$ . The sign of transverse vorticity alternates along the span at each trough and peak location. Two distinct sets of coherent patterns are detected. The first group of transverse vorticity iso-



surfaces (G1) emanate from the wavy separation line associated with the long separation bubble in the front, and the other (G2) appears outside this zone from the regions where the laminar separation bubbles are located. While both sets of iso-surfaces, depart from the wall, G1 lifts higher from the surface than G2. The orientation of the former group, influenced by large-scale spanwise flow, is highly diagonal, standing in opposite directions on either side of the long separation bubble. This is in contrast to the situation for G2, wherein transverse vorticity iso-surfaces lifting from the LSBs, are channelled along the chord in the forward flow zone shown in Figure 44.

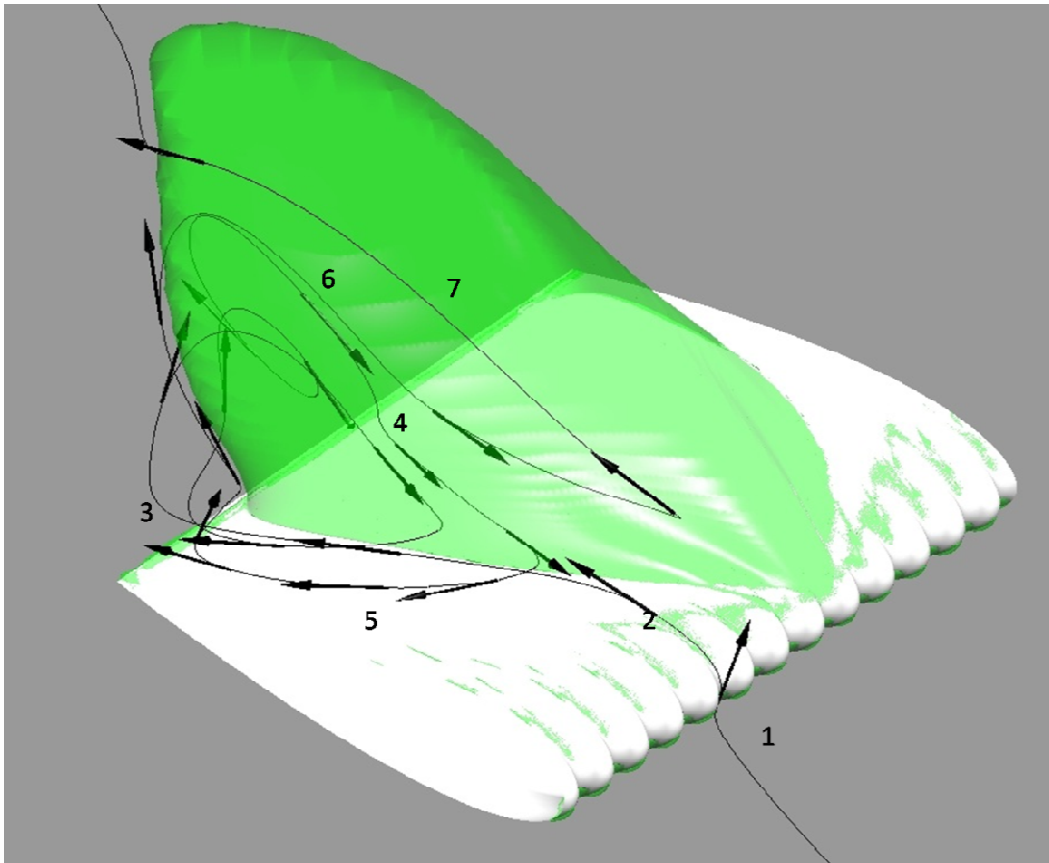


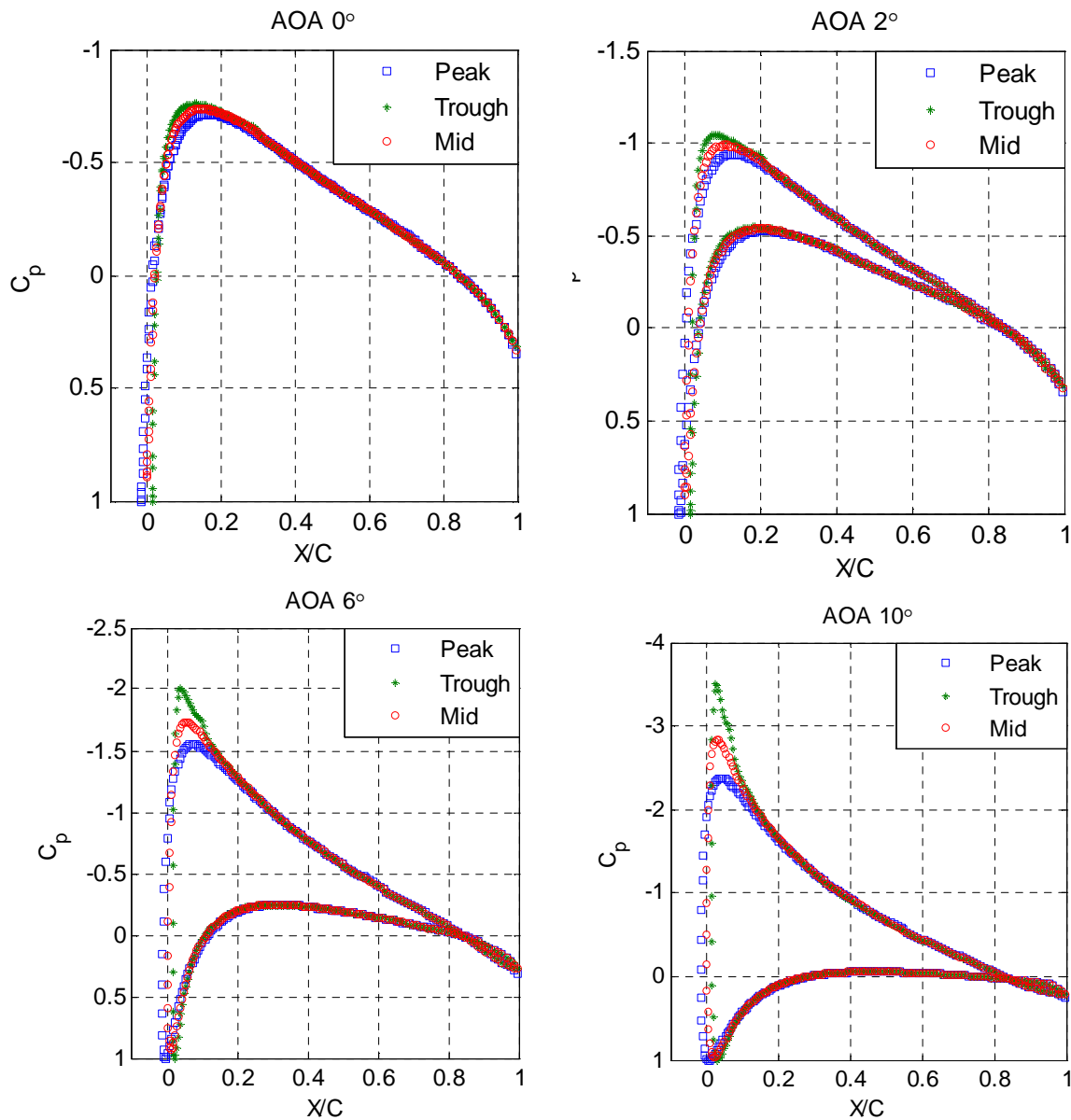
FIG.45 Velocity vectors plotted over the foil, on a plane oriented normal to the free-stream flow direction. Wing section shown for region near the separation bubble  $Z > 0.16m$ . (A14W52.5,  $Re=1,500,000$ ,  $t=0.04(s)$ ,  $AOA = 20^{\circ}$ )

In Figure 45, a three-dimensional streamline shows how the fluid moves over the suction side of the foil in the vicinity of the large bubble. As the flow approaches the foil from zone 1, it climbs around and over the tubercle reaching zone 2, located adjacent to the bubble. Subsequently, the flow spirals within the bubble near the trailing edge under the influence of the streamwise vortex structures and moves forward in zone 4. The transfer of momentum occurs from zone 4 to 5, whereby the momentum from the re-circulation zone within the bubble is injected into the boundary layer of the attached-flow region. Finally the flow re-entering the bubble through zone 6, is lifted and by the action of spanwise vorticity within the bubble is turned backwards as it leaves the separation bubble towards the wake.

## Pressure Coefficient Plots

The pressure coefficient plots, displaced for the peak, trough and middle spanwise locations show that the highest suction peak occurs over the trough at all attack angles, while the pressure distribution over the pressure side of the airfoil for the three main spanwise locations is almost identical (Figure 46). The pressure gradient, also, is more adverse along the trough, in line with observations at  $Re=120,000$ . The occurrence of the LSB on the trough, is reflected subtly in the change of the pressure gradient (for example at  $AOA = 6^\circ$ , where  $X/C=0.1$ ).

As the attack angle increases, the difference in the pressure peak value on the suction side at the trough, compared to that of the peak and the middle spanwise locations, become more pronounced. Consequently, the pressure gradient in the chordwise direction becomes more adverse. Thus, the early onset of separation on the trough spanwise location, in comparison with that of the peak, is explained.



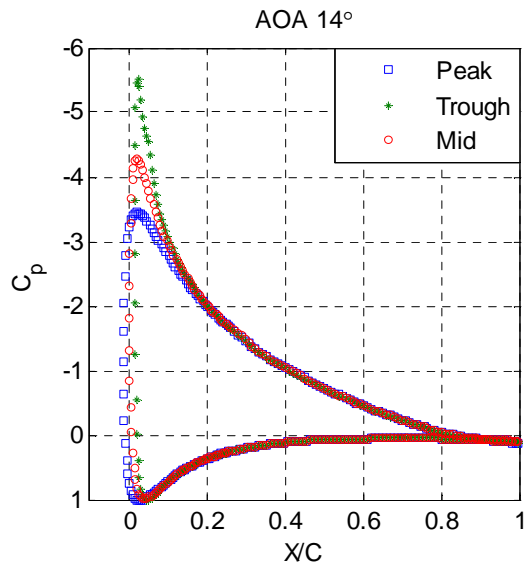
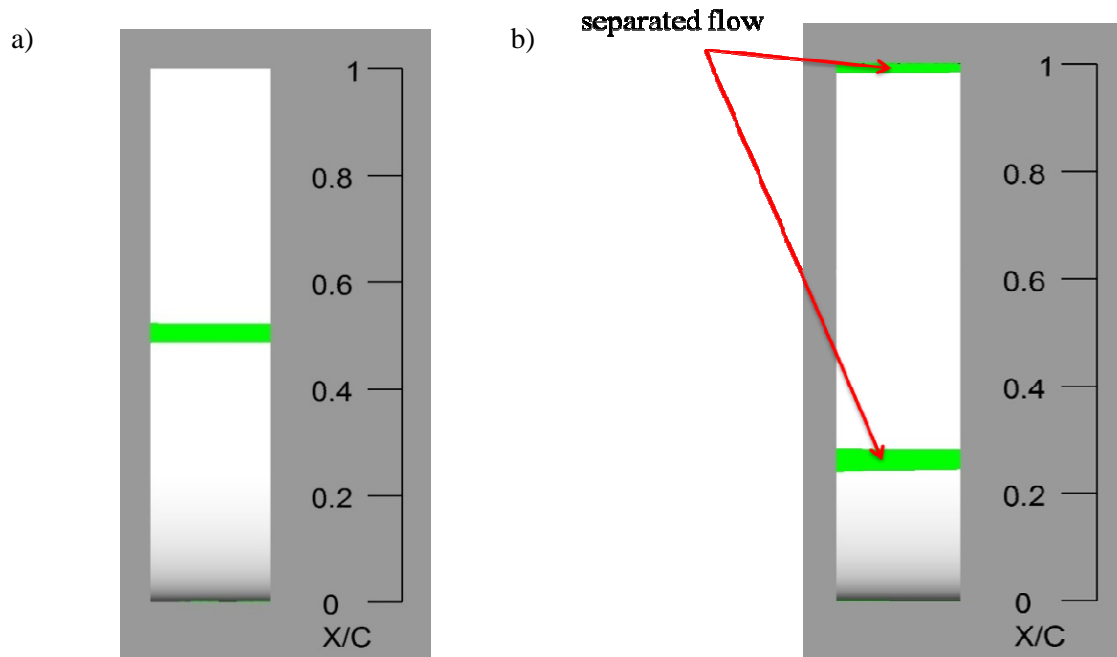


FIG.46 Pressure coefficient plots for the peak, trough and middle spanwise locations at several attack angles. (A14W52.5,  $Re=1,500,000$ )

### Flow Structure Analysis Over the Baseline NACA-0021( $Re=1,500,000$ )

The flow structure over the baseline NACA-0021, is analysed in this section at several attack angles. At  $AOA = 0^\circ$ , a Laminar Separation Bubble appears on the suction side of the airfoil (Figure 47(a)). Since the change of the sign of the skin friction along the chord (Figure 48) from positive to negative indicates the occurrence of flow separation while its change from negative to positive shows a flow attachment process, the length of the bubble at  $AOA=0(\text{deg})$  could be estimated at 18(mm),



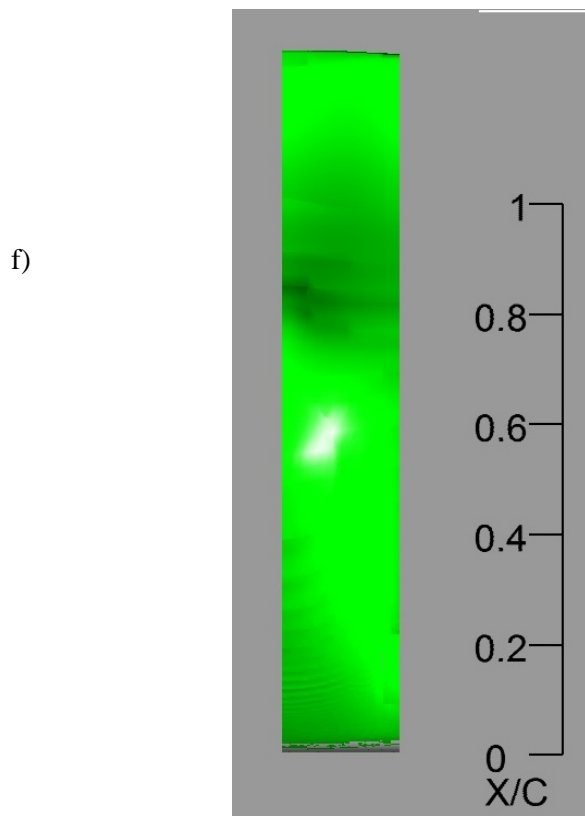
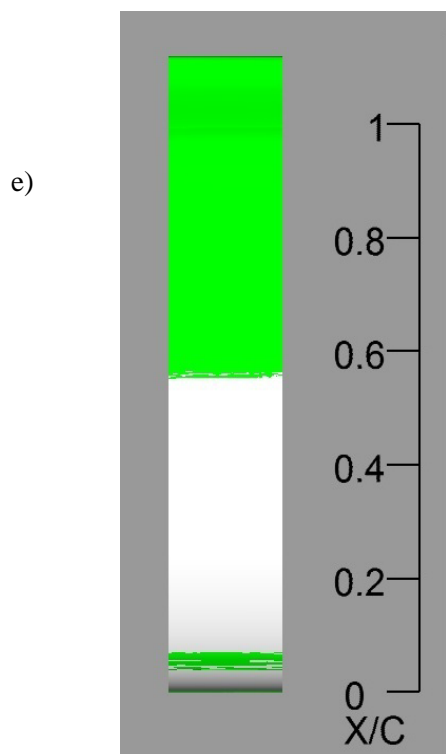
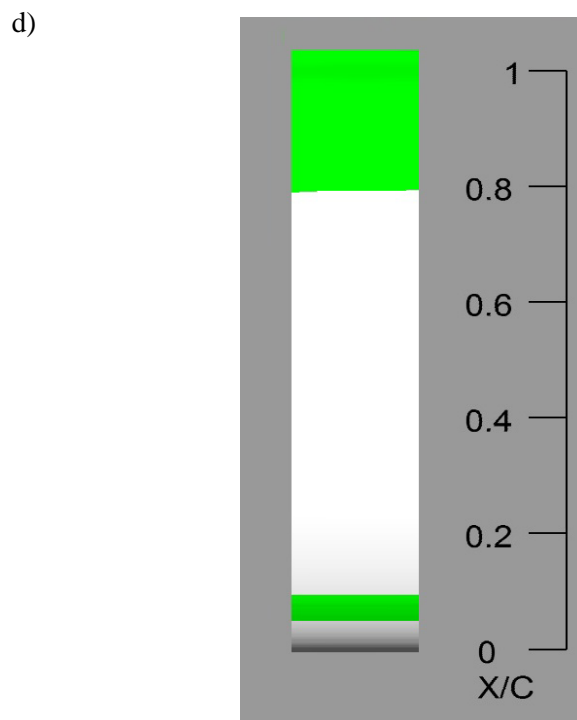
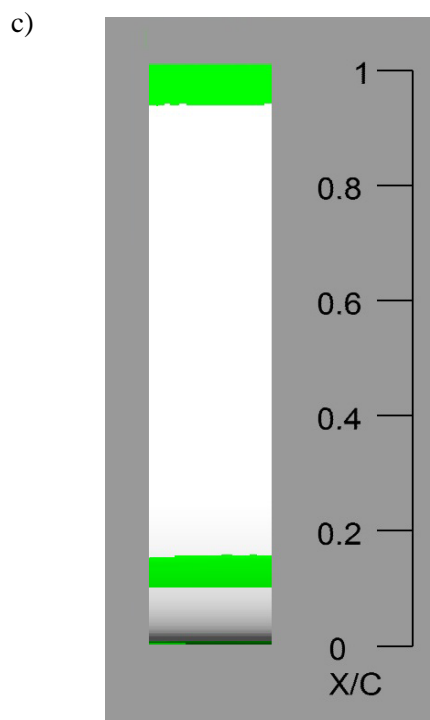


FIG.47(a-f) Separated flow regions, displayed in green, over the suction side of NACA-0021. ( $Re=1,500,000$ ,  $AOA=0^\circ, 6^\circ, 10^\circ, 14^\circ, 18^\circ, 25^\circ$ )

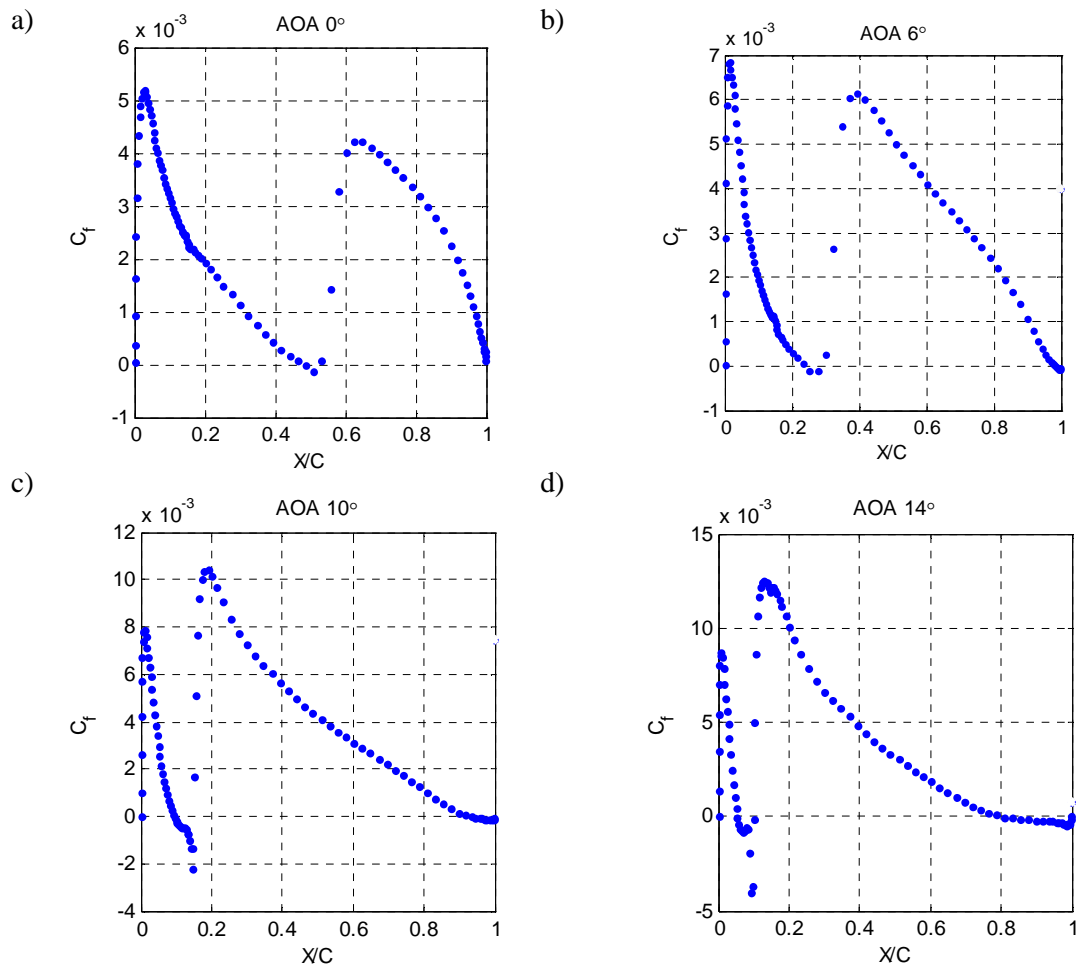


FIG.48(a-d) Friction coefficient on the suction side of NACA-0021 ( $Re=1,500,000$ ,  $AOA = 0^{\circ}, 6^{\circ}, 10^{\circ}, 14^{\circ}$ )

At  $AOA = 6^{\circ}$ , two distinct regions of separated flow are identified. The first region corresponds to the Laminar Separation Bubble that has moved further upstream, whereas the second one is a small zone of trailing edge flow separation. The length of the bubble at this attack angle was estimated using the data in Figure 48 at 19(mm). At  $AOA = 10^{\circ}$ , the LSB, whose length is estimated at 27(mm), is seen to have moved further upstream, towards the leading. Flow separation from the trailing edge is also initiated at a location further upstream. The length of the bubble is, however, slightly decreased to 22 (mm) at  $AOA=14^{\circ}$ . With the increase in the attack angle up to  $20^{\circ}$ , stall is evident as flow separation envelops over half of the suction side. In addition, the flatness of the pressure coefficient curve in Figure 8, confirms the occurrence of stall.

### Aerodynamic Loading Behaviour

The lift and drag coefficients, obtained from the numerical simulations of the present work and those reported in previous experiments, are plotted (Figure 49) for the tubercled and unmodified foils at  $Re=1,500,000$  and  $Re=120,000$  at several attack angles.

Observing the experimental data corresponding to the unmodified foil ( $Re=120,000$ ) reveals that the NACA-0021 airfoil undergoes an abrupt loss of lift in the transitional regime. The flow simulation work by Choudhry *et al.* [2] concluded that abrupt stall, on this thick airfoil, is initiated by the bursting of a laminar separation bubble. The tubercled foil produces more lift and less drag at post-stall angle. It is evident that the loss of lift for this foil is gradual.

In stark contrast, in the turbulent regime, the unmodified airfoil's loss of lift is gradual, possibly due to the presence of higher momentum fluid in the boundary layer and the resistance of the LSB to bursting near the stall angle. This is reflected in both the numerical and experimental data. Considering the CFD results of the present study it is found that, for the turbulent case, up to the stall angle at  $14^\circ$ , the tubercled foil and the NACA-0021 generate almost the same amount of drag. However, post-stall, the tubercled foil's drag is considerably larger than that of the unmodified. The lift curve, on the other hand, illustrates that the amount of lift produced by both foils is almost the same for angles of attack below  $10^\circ$ . The tubercled foil, however, produces slightly more lift than the unmodified at  $AOA = 14^\circ$ . At  $AOA = 20^\circ$ , the lift force generated by A14W52.5 is markedly lower than the foil with the straight leading edge. The lower post-stall lift associated with the tubercled foil, is in contrast to the findings by previous studies performed at low Reynolds numbers. Nonetheless, the loss of lift for the tubercled foil for attack angles between 18 to 25 degrees is still less abrupt, compared to that of the unmodified foil.

Herein, the findings are in agreement with the numerical simulation results by Dropkin *et al.* [4] who previously showed that at  $Re=3,000,000$ , the unmodified foil NACA-634-021 produced more lift for a large range of post-stall attack angles than the tubercled foil. Also, Weber *et al.* [28] who studied the effects of cavitation by conducting water tunnel experiments at  $Re=200,000-800,000$  reported the inferior performance of rudders modified with leading-edge tubercles at  $AOA=15^\circ - 20^\circ$ . This points out the significance of Reynolds number effects on the stall mechanism of the lifting bodies with leading edge tubercles. Furthermore, it demonstrates that the aerodynamic behaviour of the tubercled foil is dependent on the cross-sectional profile of the baseline foil, operating in a particular flow regime.

It must be noted that while discrepancies are apparent between the coefficients reported from the experimental work by Gregorek *et al.* [9] and those obtained through numerical simulations, the SST transitional model is in better agreement with the simulation results conducted by Wolfe *et al.* [29]. One possible explanation for the differences in the lift coefficients can be attributed to turbulence levels in the wind tunnel tests that could not be determined from the report by Wolfe *et al.* [29]. The effect of turbulence intensity on the maximum lift coefficient achieved by NACA-0021 was

previously investigated by Swalwell *et al.* [25]. In the present study the turbulence levels were maintained around 0.4% in the upstream vicinity of the two airfoils.

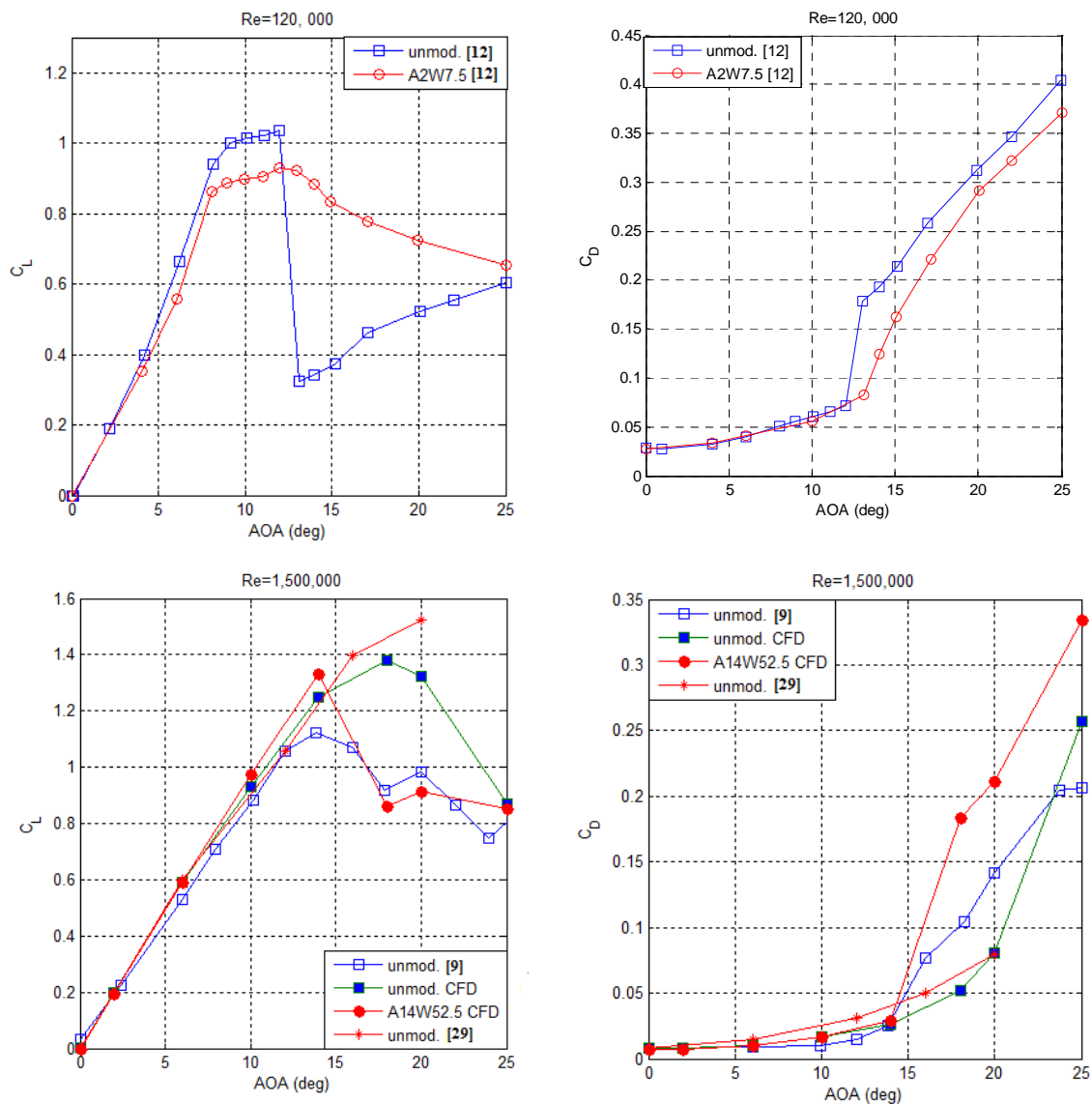


FIG.49 The lift and drag coefficient curves for the tubercled and unmodified foil at several attack angles.

## Conclusions

Numerical modelling of the flow over the full-span tubercled foil, A2W7.5 and its scaled-up equivalent A14W52.5 was conducted at  $Re=120,000$  and  $Re=1,500,000$ . These Reynolds numbers correspond to the transitional and near-turbulent flow regimes, respectively. While wind tunnel force measurement tests were carried out on A2W7.5 at  $Re=120,000$  by Hansen *et al.* [12], no experimental aerodynamic loading data are yet available for the tubercled airfoils in the turbulent flow regime.

To capture details of the flow structure using the SST transitional model, high-resolution grids were generated and grid-independent studies were performed accordingly. All the grids had structured,

hexahedral elements with sufficient number of nodes within the boundary layer to resolve regions of separated flow with reasonable accuracy. This is the first computational study, to the authors' knowledge, where the flow over tubercled airfoils with spans larger than four wavelengths was simulated. Validation of the model was done using the experimental data in the form of surface pressure distribution along the chord for the NACA-0021 baseline foil. The SST transitional model was capable of capturing the trends associated with the pressure distribution with reasonable accuracy and was thus, deemed suitable for the analysis of the flow structure.

The results of flow topology analyses revealed a number of common, as well as different flow features in the studied flow regimes. One primary feature observed in both cases, was the presence of spanwise pressure gradients in the vicinity of the leading edge. The cyclic variation in pressure gradient is induced by the leading edge tubercles and results in the highest suction peak to occur in the trough spanwise location. The pressure difference between the trough and the peak drives the flow to move towards the trough. On the other hand, the abrupt change in the flow direction in this region, leads to strong velocity gradients that account for the turning of the already-present spanwise vorticity within the boundary layer towards the streamwise and transverse directions. This mechanism operates in both flow regimes and is identified as Prandtl's secondary flow of the first type.

Chordwise pressure gradient in the trough region was also observed to be the most adverse. Hence, the flow is more susceptible to separation along the trough. However, due to transition effects, the boundary layer re-attaches further downstream. This leads to the formation of a laminar separation bubble, whose shape is highly influenced by the presence of vorticity. It was shown that a pair of vortex tubes of opposite sign leave the focal critical points from the laminar separation bubble. Spanwise vortex sheets, in contrast, appear rippled, a result which is consistent with the predictions from Prandtl's lifting line theory and Stokes' law as proposed in our previous studies [20, 21]. In addition, the cyclic variation in spanwise vorticity explains the generation of pairs of counter-rotating streamwise vortices. In case of the near-turbulent flow, these vortices are much stronger and are closer to the surface, as flow separation, in particular near the trailing edge occurs at larger attack angles compared to the case where  $Re=120,000$ .

Another notable flow feature, in the form of a separated zone, was detected near the mid-chord section. For the flow in both regimes, this flow feature was the location where transverse vortex tubes, emanating from the laminar separation bubbles further upstream end on the surface. The shape of the separated flow region, as well as the critical points associated with the mid-chord flow feature were different for the studied flow regimes at pre-stall angles.

Differences were also noticed in the pattern of flow separation, near the trailing edge. Whereas the separated flow occupied distinctly isolated areas in the shape of round re-circulation zones at  $Re=1,500,000$ , the separated flow region for  $Re=120,000$  maintained a continuous wavy pattern along



the span, with the exception of the flow at zero incidence. Also, flow separation near the trailing edge appeared to occupy smaller volumes for the turbulent flow case, due to the resistance of the turbulent boundary layer to flow separation.

In the post-stall zone, remarkably similar flow features were detected in both flow regimes. In the central trough, a long separation bubble was observed that originated from the leading edge and extended down to the trailing edge. Within the bubble, the velocity field showed the strong tendency of the flow to move towards the two neighbouring areas, located on either side of the bubble. This flow motion, introduced higher momentum fluid into the boundary layer in those areas and, as a result, separation was inhibited. In addition, in both flow cases, reversed flow, appearing from the trailing edge was engulfed into two large zones marked with strong swirl, forming streamwise vorticity of opposite sign above the foil. The separated flow region associated with the tubercled foil at the examined attack angle ( $AOA = 20^\circ$ ) caused the airfoil to lose a considerable amount of lift, in comparison with the unmodified foil. Hence, signifying the effects of the Reynolds number on the performance of full-span tubercled foils.

As for the unmodified foil at  $Re=1,500,000$ , two primary zones of flow separation were identified. The first one was formed by the separation and re-attachment of the boundary layer in the shape of a laminar separation bubble. And the second separated flow region, corresponded to flow separation near the trailing edge. With the increase in the attack angle, the laminar separation bubble moves forwards and the separation zone from the back grows larger in size. This trend continues into post-stall where the airfoil's lift coefficient drops. Nevertheless, the loss of lift for the unmodified foil appears to be less severe than that of the tubercled foil.

The numerical simulation results suggest that, in the turbulent flow regime, unlike the transitional flow cases (for instance at  $Re=120,000$  in the study by Hansen *et al.* [12]), the laminar separation bubble over the unmodified foil does not burst and a sudden loss of lift is not observed. Hence, in comparison with a tubercled model, the unmodified foil yields higher lift co-efficient at post-stall angles. Accordingly, future studies will focus on the experimental investigation of the influence of the cross-sectional profile, as well as the flow regime on the performance of lifting bodies modified with leading-edge tubercles.

## References

- [1] ANSYS, "ANSYS-CFX Solver Theory Guide," in *ANSYS CFX 14.5.7*, ed. Pennsylvania, 2013.
- [2] A. Choudhry, M. Arjmonadi, and R. M. Kelso, "A study of long separation bubble on thick airfoils and its consequent effects," *International Journal of Heat and Fluid Flow*, vol. 52, 2015.
- [3] D. Custodio, "The Effect of Humpback Whale-Like Leading Edge Protuberances on Hydrofoil Performance," Thesis submitted to Worcester Polytechnic Institute, December 2007.
- [4] A. Dropkin, D. Custodio, C. W. Henoeh, and H. Johari, "Computation of Flowfield Around an Airfoil with Leading Edge Protuberances" *Journal of Aircraft*, vol. 49, September-October 2012
- [5] Y. Egorov, F. R. Menter, R. Lechner, and D. Cokljat, "The Scale-Adaptive Simulation Method for Unsteady Turbulent Flow Predictions, Part 2: Application to Complex Flows," *Flow Turbulence Combust* pp. 139-165, 2010.
- [6] J. Favier, A. Pinelli, and U. Piomelli, "Control of the separated flow around an airfoil using a wavy leading edge inspired by humpback whale flippers," *Comptes Rendus Mecanique*, vol. 3401(1):107-114, 2011.
- [7] E. F. Fish, L. Howel, and M. Murray, "Hydrodynamic flow control in marine mammals," *Integrative and Comparative Biology*, vol. 48, pp. 788-800, 2008.
- [8] E. F. Fish, P. Weber, M. Murray, and L. Howel, "The Tubercles on Humpback Whales' Flippers: Application of Bio-Inspired Technology," *Integrative and Comparative Biology*, vol. 51, pp. 203-213, 2011.
- [9] M. Gregorek, M. J. Hoffmann, and M. J. Berchak, "Steady State and Oscillatory Aerodynamic Characteristics of a NACA 0021 Airfoil: Data Report," Ohio State University, Columbus, OH 1989.
- [10] K. L. Hansen, "Effect of Leading Edge Tubercles on Airfoil Performance," Doctor of Philosophy, Mechanical Engineering, University of Adelaide, Adelaide, SA, Australia, 2012.
- [11] K. L. Hansen, R. M. Kelso, and B. Dally, "An Investigation of Three Dimensional Effects on the Performance of Tubercles at Low Reynolds Numbers," presented at the 17th Australian Fluid Mechanics Conference, Auckland, New Zealand, 2010.
- [12] K. L. Hansen, R. M. Kelso, and B. B. Dally, "Performance variations of leading-edge tubercles for distinct airfoil profiles," *AIAA Journal Journal of Aircraft*, vol. 49:185-94, 2011.
- [13] H. Johari, C. Henoeh, D. Custodio, and A. Levshin, "Effects of Leading Edge Protuberances on Airfoil Performance," *AIAA Journal*, vol. 45:11, November 2007.
- [14] R. Langtry and F. Menter, "Correlation-based transition modeling for unstructured parallelized computational fluid dynamics codes," *AIAA Journal*, vol. 47: 2894–2906, 2009.
- [15] M. Lohry, D. Clifton, and L. Martinelli, "Characterization and Design of Tubercle Leading-Edge Wings," presented at the Computational Fluid Dynamics (ICCFD7), Big Island, Hawaii, 2012.
- [16] D. S. Miklosovic, M. M. Murray, and L. Howle, "Experimental Evaluation of Sinusoidal Leading Edges," *Journal of Aircraft*, vol. 44:1404–1407, 2007.
- [17] D. S. Miklosovic, M. M. Murray, L. E. Howle, and F. E. Fish, "Leading Edge Tubercles Delay Stall on Humpback Whale Flippers," *Physics of Fluids*, vol. 16(5) pp. L39-L42, 2004.
- [18] H. T. C. Pedro and M. H. Kobayashi, "Numerical Study of Stall Delay on Humpback Whale Flippers," *AIAA Paper 2008-0584*, 7-10 January 2008.
- [19] D. Rodriguez and V. Theofilis, "On the birth of stall cells on airfoils," *Theoretical and Computational Fluid Dynamics*, vol. 25, pp. 105-117, 2011.
- [20] N. Rostamzadeh, K. L. Hansen, R. M. Kelso, and B. B. Dally, "The formation mechanism and impact of streamwise vortices on NACA 0021 airfoil's performance with undulating leading edge modification," *Physics of Fluids*, vol. 26, 2014.

- [21] N. Rostamzadeh, R. M. Kelso, B. B. Dally, and K. L. Hansen, "The effect of undulating leading-edge modifications on NACA 0021 airfoil characteristics," *Physics of Fluids*, vol. 25, 117101 2013.
- [22] A. Skillen, A. Revell, A. Pinelli, U. Piomelli, and J. Favier, "Flow over a Wing with Leading-Edge Undulations," *AIAA Journal*, pp. 1-9, 2014.
- [23] A. Skillen, A. Revell, A. Pinelli, U. Piomelli, and J. Favier, "Flow over a Wing with Leading-Edge Undulations," *AIAA Journal*, 2014.
- [24] M. J. Stanway, "Hydrodynamic effects of leading-edge tubercles on control surfaces and in flapping foil propulsion," Master of Science in Ocean Engineering Mechanical Engineering, Massachusetts Institute of Technology, February 2008.
- [25] K. E. Swalwell, J. Sheridan, and W. H. Melbourne, "The Effect of Turbulence Intensity on Stall of the NACA 0021 Aerofoil," presented at the 14th Australasian Fluid Mechanics Conference, Adelaide University, Adelaide, Australia, December 2001.
- [26] E. van Nierop, S. Alben, and M. P. Brenner, "How Bumps on Whale Flippers Delay Stall: an Aerodynamic Model," *Physical review letters*, vol. 100(5): 054502, 7 February 2008.
- [27] P. Weber, L. Howle, M. Murray, and D. Miklosovic, "Computational Evaluation of the Performance of Lifting Surfaces with Leading-Edge Protuberances," *Journal of Aircraft* vol. 48, March-April 2011.
- [28] P. W. Weber, L. Howel, and M. Murray, "Lift, drag and cavitation onset on rudders with leading edge tubercles," *Marine Technology* pp. 27-36, 2010.
- [29] W. P. Wolfe and S. S. Ochs, "Predicting Aerodynamic Characteristics of Typical Wind Turbine Airfoils using CFD," Sandia National Laboratories, Iowa September 1997.

# Chapter 7

## Summary, Conclusions and Recommendations for Future Work

The present study set out to explore the underlying flow mechanism, induced by the presence of full-span wings with undulating leading edges in the laminar, transitional and near-turbulent regimes. All the modified airfoils designed and fabricated for this study were based on the NACA-0021 profile which closely matches the cross-sectional profile of the humpback whale. To carry out the investigation, theoretical, experimental and numerical approaches were adopted. The current chapter provides a summary of the work conducted as well as the conclusions and recommendations for future research.

### 7.1 Summary

#### 7.1.1 Similarities in the Characteristics Associated with the Flow over Wavy and Tubercled Wings

In chapter 3, a theoretical analysis, based on Prandtl's non-linear lifting-line theory, revealed that both a wavy and a tubercled leading edge induce a cyclic variation in spanwise circulation. This variation gives rise to the formation of counter-rotating streamwise vortices for the tubercled, as well the wavy wing (see Figures 3.18 and 4.18). A full-span wing with an undulating leading edge can be conceived of as a series of finite-wing sections, each wavelength of which producing counter-rotating vortices, due to the spanwise variation in circulation. It was argued that the amplitude-to-wavelength ratio of the sinusoidal leading-edge configuration was directly proportional to the strength of the streamwise vortices (see Equation 4.6).

Similarity of the loading behaviour of tubercled and wavy wings had been previously reported by Hansen [5] in the transitional flow regime ( $Re=120,000$ ). In the present work, wind tunnel force measurement tests were repeated on the three full-span wavy wings previously adopted by Hansen [5]. In addition, force measurement tests were conducted on a newly-designed and fabricated wavy

airfoil to further assess the effect of geometric parameters on the loading characteristics of wavy wings, defined as one of the aims of the project. The results demonstrated that all the wings with wavy leading edges produced more lift in the post-stall regime than that of the unmodified wing. Of the wings with the same angular amplitude, the one with the smallest wavelength exhibited the most superior aerodynamic behaviour. Among the wings of the same wavelength, however, the one with the largest angular amplitude produced the most favourable performance (see Figures 3.8-3.10).

Surface pressure measurement tests on the newly-designed wavy wing at  $Re=120,000$  showed that, similar to the case with a tubercled wing, the lowest suction pressure occurred in the trough (chord minimum location). In addition, the chordwise pressure gradient along the trough of a wavy wing was observed to be more adverse than that of the peak (chord maximum location), pointing to another common trait with the flow over tubercled foils (see Figure 3.12). This observation suggested the early onset of flow separation along the trough, compared to the peak spanwise location.

To probe into the flow structure around a full-span wavy wing, numerical simulation was carried out on the wavy wing in the transitional flow regime, at  $Re=120,000$ . The Shear Stress Transport transitional model,  $SST \gamma - Re_\theta$ , was successful in reproducing the pressure distribution at several attack angles with reasonable accuracy. The flow structure analysis, confirmed that the wavy foil produced counter-rotating streamwise vortices. Under the influence of vortex stretching and viscous dissipation, the maximum value of streamwise vorticity, in the wake, was observed to decrease with distance from the trailing edge, as the rotational-flow cores associated with the counter-rotating vortices grew in size. This observation was in agreement with Kelvin's circulation theorem. Also, the boundary layer profile along the trough, compared to the peak, showed the onset of flow separation at a chordwise location situated further upstream, compared to that of the peak (see Figure 3.19), a characteristic that was reported for the flow over tubercled foils [5, 9, 10].

### **7.1.2 Flow Mechanism for Tubercled Wings in the Transitional Regime**

As detailed in Chapter 4, the formation mechanism of streamwise vortices was investigated from an alternate perspective by means of numerical simulation in the transitional regime ( $Re=120,000$ ). The

flow over three tubercled airfoils of varying wavelength and amplitude, was simulated using the SST transitional model and compared to that of the unmodified NACA-0021. Contours plots of surface pressure indicated that tubercles establish a cyclic spanwise variation in static pressure, near the leading edge, with the lowest "suction pressure" zone occurring in the trough. Accordingly, the spanwise pressure gradient drives the oncoming flow towards the trough (see Figure 4.14). By analyzing the topological features of the surface flow and the vorticity field, it was found that a skew-induced mechanism identified as *Prandtl's secondary flow of the first type* gives rise to the formation of two types of counter-rotating vortices in the transitional flow regime. The primary pair of vortices originate near the trough region, where the minimum suction peak lies, while the secondary pair of vortices appear in the vicinity of the trailing edge (see Figures 4.11 and 4.20). The formation mechanism of both vortex pairs is associated with the turning of the boundary layer vortex lines from the spanwise into the streamwise and transverse directions. The primary pair of vortices create a secondary flow feature in the trough region which was also reported by Skillen *et al.* [8].

In addition, it was noted that Laminar Separation Bubbles form on both the unmodified and tubercled foils at  $Re=120,000$ . Whereas the shape of the bubble remains essentially two-dimensional for the baseline foil, the presence of streamwise vorticity affects the shape of the bubble for the tubercled foil, rendering it a three-dimensional (*open*) appearance (see Figure 4.13). The flow visualization work by Karthikeyan *et al.* [7] confirmed the presence of the *open laminar separation bubble* in the trough region.

CFD simulations showed that, in the pre-stall zone, the development of the vortices is accompanied by flow separation. The primary vortices induce separation in the form of *open laminar separation bubbles*. The development of the secondary vortices, in the vicinity of the trailing edge, is accompanied by flow separation, a phenomenon which could explain the lower maximum lift coefficient achieved by modified foils compared to the baseline NACA 0021. Airfoils with larger tubercle amplitudes generated vorticity fields of higher vorticity magnitudes, however, achieved lower lift coefficients as larger separation zones produced by the formation of the pairs of vortices. The numerical study also suggested that the amplitude-to-wavelength ratio is directly proportional to the

strength of the streamwise vortices. Furthermore, contour plots of spanwise vorticity showed that the tubercled leading edge imparts a rippled appearance to the vortex sheets along the span, a phenomenon that was explained by the cyclic variation in circulation and Stokes' law (see equation 4.1 and Figure 4.10).

The numerical simulations indicated that, in the post-stall regime, the flow from the separated flow regions, under the influence of the strong vorticity field, moves towards the neighbouring sections. This motion renders a momentum enhancement effect as high momentum fluid is transported into the boundary layer, increasing its momentum, thus inhibiting flow separation. As a result, higher lift coefficients are achieved at high attack angles. The momentum enhancement effect of the vortices was also reported by Skillen *et al.* [8].

The limiting streamlines on one tubercled airfoil (A8W30), showed a bi-periodic pattern. Bi-periodicity in the flow structure was previously reported in the flow visualisation study by Custodio [1]. As illustrated by pseudo-streamlines and contour plots of vorticity, the sense of rotation of the streamwise vortices accounted for the upwash effect in the trough and the downwash effect, originally predicted by van Nierop *et al.* [9] and Weber *et al.* [10] (see Figure 4.22). As explained by these researchers, the local attack angle remains higher over the trough than the peak, creating a steeper chordwise pressure gradient that leads to the early onset of flow separation near the trough region.

The vorticity field on spanwise planes, oriented orthogonal to the free-stream flow direction, revealed the presence of vorticity (of opposite sign) developing beneath the merged primary and secondary vortices at the trailing edge. This was attributed to the interaction of the longitudinal vortices and the wall boundary layer, generating lateral shear, similar to the findings by Cutler and Bradshaw [2] in their study of swept wings.

### **7.1.3 Flow Mechanism for a Tubercled Wing in the Laminar Regime**

In Chapter 5, numerical methods were employed to model the flow past a full-span tubercled and a baseline foil in the laminar flow regime ( $Re=2,230$ ). Previously Hansen [5] had performed water tunnel experiments in the form of Particle Image Velocimetry (PIV) measurements to study the

formation of streamwise vortices between tubercles. Strong correspondence between the vorticity fields computed from the velocity fields resolved by the simulations and those obtained by PIV measurements provided assurance that numerical simulations could be trusted with the examination of the flow structure.

In conjunction with the analyses from the experimental investigation, flow modelling demonstrated that a skew-induced mechanism led to the development of counter-rotating streamwise vortices (Figure 5.24). A vortex sheet indicated by a vorticity iso-surface was shown to lift from the airfoil's surface (Figure 5.23), tilt and stretch in the streamwise direction, in agreement with the observations by Favier *et al.* [3]. Moreover, the vorticity field suggested the apparent development of a vortex-canopy structure whereby, spanwise vortex lines turn initially towards the streamwise direction and eventually lift from the surface as they convect in the streamwise direction (see Figure 5.22). Also, spanwise vortex sheets assumed a rippled appearance above the tubercled foil.

Furthermore, the presence of counter-rotating vortices was accompanied by large regions of flow separation. In the reversed flow region, due to the reversal in the direction of the spanwise vortex lines within the boundary layer (immediately above the foil's surface), regions of vorticity with opposite sign to those away from the wall were identified. As opposed to the situation outside the separation bubble, where the vortex lines assumed a rippled appearance, within the separation region the vortex lines resembled a series of closed-looped rings. The streamwise vorticity field obtained from the PIV measurements near the trailing edge have shown a local increase in the magnitude of peak streamwise vorticity. To explain this phenomenon, CFD was used to further investigate the evolution of the vorticity field. Accordingly, it was found that the turning and tilting of the vortex rings near the trailing edge occurred in such a manner that the streamwise component of the vorticity field grew in magnitude with chordwise distance near the trailing-edge (see Figure 5.23). Therefore, the local increase in the magnitude of peak streamwise vorticity was accounted for.

At high attack angles, the transfer of momentum, from the separated flow regions to neighbouring zones, where attached flow occurred, generated more lift over the tubercled foil than the unmodified



NACA 0021. Integration of the pressure distributions at various chordwise locations implied that the largest amount of lift is generated at a cross section corresponding to a tubercle peak, which is consistent with the observation that flow separation occurs further aft at this location.

#### **7.1.4 Flow Mechanism for a Tubercled Wing in the Near-Turbulent Regime**

As detailed in Chapter 6, numerical simulations were conducted using the SST  $\gamma - Re_\theta$ , to examine the flow structure around a tubercled foil and the unmodified NACA 0021 foil at  $Re=1,500,000$ , in the near-turbulent flow regime. Validation of the model was carried out using the wind tunnel tests data for the baseline foil by Gregorek *et al.* [4]. Flow modelling was also carried out on the same tubercled foil (re-scaled) at  $Re=120,000$  to explore Reynolds number effects on the mechanism triggered by the presence of leading-edge tubercles.

The presence of the open laminar separation bubble in the trough region of the tubercled foil was one flow feature that was found in the near-turbulent and transitional regimes (see Figures 6.9(c)-6.25(a)). Even though the scale of the LSB was markedly smaller than that observed in transitional flow ( $Re=120,000$ ), the fundamental formation mechanism of the LSB was identical in both cases. Investigating the limiting vortex lines on the foil's surface revealed that the turning of spanwise vorticity into the streamwise and transverse direction underpinned the formation of streamwise vortices. Also, the generated streamwise vortices had the same sense of rotation as those corresponding to the transitional flow regime, such that they induced an upwash effect in the trough and downwash over the peak (see Figures 18(b)-38(b)).

Further analysis of the vorticity field indicated that a pair of vortex tubes, of opposite sign leave the focal critical points from the laminar separation bubble. Spanwise vortex sheets, in contrast, appear rippled. In the near-turbulent flow case, these vortices are much stronger and closer to the surface, as flow separation, in particular near the trailing edge, occurs at larger attack angles compared to the case where  $Re=120,000$  (see Figures 6.18-6.19 and 6.38-6.39).

Another notable flow feature, in the form of a separated zone, was detected near the mid-chord section. For the flow in both regimes, this flow feature was the location where transverse vortex tubes, emanating from the laminar separation bubbles further upstream, end on the surface. The shape of the separated flow region, as well as the critical points associated with the mid-chord flow feature, were different for the studied flow regimes (see Figures 6.15 and Figure 6.32).

Differences were also noticed in the pattern of flow separation near the trailing edge. Whereas the separated flow occupied distinctly isolated areas in the shape of round re-circulation zones at  $Re=1,500,000$ , the separation line for  $Re=120,000$  maintained a continuous wavy pattern along the span, with the exception of the flow at zero incidence (see Figure 6.17 and 6.35). Also, flow separation near the trailing edge appeared to occupy smaller volumes for the near-turbulent flow case, due to the resistance of the turbulent boundary layer to flow separation.

In the post-stall zone, remarkably similar flow features were detected in both flow regimes. In the central trough, a long separation bubble was observed that originated from the leading edge and extended down to the trailing edge. In the vicinity of the bubble, three-dimensional streamlines showed the strong tendency of the flow to move from within the re-circulation zone towards the neighbouring areas located outside the bubble (see Figures 6.24 and 6.45). This flow motion introduced higher momentum fluid into the boundary layer in those areas and, as a result, separation was inhibited. In addition, in both flow cases, reversed flow appearing from the trailing edge was engulfed into two large zones marked with strong swirl, forming coherent vortical structures containing vorticity of opposite sign above the foil. In the near-turbulent regime, the separated flow region associated with the tubercled foil at the examined attack angle ( $AOA = 20^\circ$ ), caused the airfoil to lose a considerable amount of lift in comparison with the unmodified foil.

As for the unmodified foil at  $Re=1,500,000$ , two primary zones of flow separation were identified. The first one was formed by the separation and re-attachment of the boundary layer in the shape of a laminar separation bubble. The second separated flow region, corresponded to flow separation near the trailing edge. With the increase in the attack angle, the laminar separation bubble moved forwards

and the separation zone from the back grows larger in size. This trend continues into post-stall where the airfoil's lift coefficient drops. This phenomenon occurs typically for thick airfoils at moderate Reynolds numbers where gradual loss of lift is observed in *trailing-edge stall*. The separation bubble influences the stalling characteristics through its impact on the turbulent boundary layer [6]. Nevertheless, lift coefficients achieved by the unmodified foil at the investigated high attack angles (18 and 20 degrees) were greater than those of the tubercled foil.

## **7.2 Conclusions**

As detailed in Chapter 2, three primary aims were defined for the present project. Firstly, the impact of full-span wing modification with undulating leading edges on the induced underlying flow mechanism was investigated across a broad range of Reynolds numbers. Secondly, the formation mechanism and effect of streamwise vortices on the flow over wings with undulating leading edges were determined. Finally, the influence of the geometric parameters associated with full-span wavy wings on their aerodynamic performance was investigated. The findings related to the first two aims are categorized according to the similar and different characteristics that were observed over the range of the studied Reynolds numbers in sections 7.2.1 and 7.2.2. Section 7.2.3 provides the findings addressing the third aim of the project.

### **7.2.1 Similarities**

1. An undulating leading edge, in both a tubercled and wavy configuration, produces a cyclic variation of spanwise circulation of the bound vortex. Each wavelength of the undulating leading edge can be thought of as a finite-wing section. The cyclic variation of spanwise circulation accounts for the formation of pairs of counter-rotating streamwise vortices.
2. The strength of the streamwise vortices, associated with each tubercle or wave, appears to be proportional to the amplitude-to-wavelength ratio of the sinusoidal leading-edge curve. As the pair of vortices convect downstream, over the airfoil and into the wake, the values of peak vorticity decrease and the rotational flow regions grow larger in size. The attenuation of the peak value of vorticity is

primarily due to vortex compression due to the adverse pressure gradient and is consistent with Kelvin's circulation theorem.

3. The undulating leading edge imparts a rippled appearance to the spanwise vortex sheets.
4. The formation mechanism of the streamwise vortices can be explained by *Prandtl's Secondary Flow of the First Type*. According to this quasi-inviscid mechanism, in the presence of flow skewness the spanwise vorticity in the boundary layer is turned into the streamwise and transverse directions. Flow skewness occurs due to the strong spanwise pressure gradient established by the presence of the undulating leading edge.
5. The spanwise pressure gradient near the leading edge drives the flow towards the trough region on the suction side, where the static pressure reaches a minimum. In other words, the suction peak is most negative at the trough, compared to the peak and the middle spanwise locations. This creates a steep chordwise adverse pressure gradient along the trough that leads to the early onset of flow separation along the trough.
6. Flow separation lines on the tubercled foil move upstream with the increase in the attack angle in all flow regimes.
7. The momentum transfer mechanism at high attack angles operates under the influence of the vorticity field. Accordingly, the fluid from the separated flow regions (re-circulation zones) is transferred to neighbouring zones where the boundary layer remains attached and also downstream.
8. The sense of rotation of the streamwise vortices is such that they induce an upwash effect over the trough and a downwash effect over the peak spanwise locations.

### **7.2.2 Differences**

1. In the transitional and near-turbulent flow regimes, the turning of the vortex lines towards the streamwise and transverse directions leads to the formation of a pair of primary vortices near the trough region. The boundary layer undergoes a detachment and a re-attachment process along the trough whereby a laminar separation bubble is developed. It is observed that the shape of the laminar

separation bubble is influenced by the presence of the primary vortex pair. The size of the LSB is considerably smaller in the near-turbulent regime than that of the transitional. In contrast, in laminar flow the separated flow does not re-attach, and the LSB is not formed.

2. The pattern of flow separation, as well as the critical points, in the vicinity of the mid-chord section, is different for the transitional and the near-turbulent flow cases studied, although in both cases this is the region where the transverse vortex tubes that emanate from laminar separation bubbles end on the surface (see Figures 6.16 and 6.34).

3. In the transitional and near-turbulent flow regimes, patterns of surface limiting-streamlines suggest the presence of spanwise periodicity equal to or greater than two tubercle wavelengths. In the laminar flow regime, the observed pattern assumed periodicity of one tubercle wavelength. It is possible that periodicity is influenced by leading-edge configuration as well as the flow regime in question.

4. In the transitional and laminar flows, post-stall lift generated by the full-span modified foil was greater than that of the baseline foil. This, however, was not the case for the turbulent regime. One plausible explanation of this is the behavior of the laminar separation bubble on the unmodified foil in the transitional and near-turbulent flow regimes. In the transitional flow regime, the bursting of the LSB leads to the sudden loss of lift. Hence, in comparison the tubercled foil produces more lift. In the turbulent flow regime, on the contrary, the LSB on the unmodified foil is maintained on the foil at larger attack angles. Consequently more lift is produced at higher incidence angles for the unmodified foil in the turbulent regime compared to the transitional flow scenario.

### **7.2.3 Influence of Geometric Parameters on the Performance of Wavy Foils**

Wind tunnel tests were conducted at  $Re=120,000$  on four full-span wavy wings with varying amplitudes and wavelengths of the leading edge curve. The results from direct force measurements demonstrated that all the wings with wavy foils generated more lift in the post-stall regime than did the baseline NACA 0021 foil. Of the wings with the same angular amplitude, the one with the smallest wavelength exhibited the superior aerodynamic behaviour, whereas among the wings of the

same wavelength, the one with the largest angular amplitude produced the most favourable performance (see Figures 3.8-3.10). Based on these findings, it may be concluded that full-span wings with wavy leading edges can benefit from large amplitude-to-wavelength ratios to produce more post-stall lift. This conclusion is in agreement with the findings reported by Hansen [5].

### **7.3 Recommendations for Future Work**

In light of the findings of the present project, future studies may focus on the following aspects:

1. Experimental work in the fully-turbulent regime should be conducted to further elucidate the loading behaviour of wavy and tubercled wings. This can be achieved by increasing the flow speed, the chord length or turbulence intensity. Both force and pressure measurement tests can broaden our understanding regarding the modified foils' stall characteristics.
2. Pressure measurements experiments could be carried out by incorporating pressure taps on several troughs, peaks and middle spanwise locations to determine the characteristics associated with the spatially periodic patterns of the surface flow.
3. Flow simulations using more advanced i.e. higher-order CFD models, can provide useful information regarding the evolution of the vortices and their time-dependent behaviour. The study of the interaction of the streamwise vortices, developed over the modified foils, is an area that has not been explored in depth.
4. Optimization analyses can be performed to determine what combination of leading-edge amplitude and wavelength would yield higher aero-hydrodynamic performance in different flow regimes. Also the influence of the parameters such as the tubercle/wave amplitude-to-boundary layer thickness ( $A / \delta$ ) could be further investigated.
5. Experimental work in the form of PIV measurements can be conducted to examine the flow over a wavy foil. Further investigation of the flow structure can shed light on the underlying flow mechanism triggered by a wavy leading edge.

6. Due to the development of streamwise vortices, the potential application of tubercles in heat transfer is plausible. This unexplored area can lead to the design of fluid machinery components that outperform conventional models.

7. Future work could also focus on the behaviour of the modified foils in compressible flow scenarios. The interaction of streamwise vortices and shock waves can be of high interest. Attenuation of shockwaves from a wavy surface may be more rapid than from an unmodified surface. This may lead to the design of quieter supersonic aircraft.

## References

- [1] D. Custodio, "The Effect of Humpback Whale-Like Leading Edge Protuberances on Hydrofoil Performance," Master of Science Thesis submitted to Worcester Polytechnic Institute, December 2007.
- [2] A. D. Cutler and P. Bradshaw, "Strong vortex/boundary layer interactions," *Experiments in Fluids*, vol. 14, 1993.
- [3] J. Favier, A. Pinelli, and U. Piomelli, "Control of the separated flow around an airfoil using a wavy leading edge inspired by humpback whale flippers," *Comptes Rendus Mecanique*, vol. 3401(1):107-114, 2011.
- [4] M. Gregorek, M. J. Hoffmann, and M. J. Berchak, "Steady State and Oscillatory Aerodynamic Characteristics of a NACA 0021 Airfoil: Data Report," Ohio State University, Columbus, OH 1989.
- [5] K. L. Hansen, "Effect of Leading Edge Tubercles on Airfoil Performance," Doctor of Philosophy Thesis, Mechanical Engineering, University of Adelaide, Adelaide, SA, Australia, 2012.
- [6] J. Jacobs, "Iced Airfoil Separation Bubble Measurements by Particle Image Velocimetry," Doctor of Philosophy Thesis, University of Illinois USA, 2007.
- [7] N. Karthikeyan, S. Sudhakar, and P. Suriyanarayanan, "Experimental Studies On The Effect Of Leading Edge Tubercles On Laminar Separation Bubble," in *52nd Aerospace Sciences Meeting*, ed: American Institute of Aeronautics and Astronautics, doi:10.2514/6.2014-1279, 2014.
- [8] A. Skillen, A. Revell, A. Pinelli, U. Piomelli, and J. Favier, "Flow over a Wing with Leading-Edge Undulations," *AIAA Journal*, pp. 1-9, 2014.
- [9] E. van Nierop, S. Alben, and M. P. Brenner, "How Bumps on Whale Flippers Delay Stall: an Aerodynamic Model," *Physical review letters*, vol. 100(5): 054502, 7 February 2008.
- [10] P. Weber, L. Howle, M. Murray, and D. Miklosovic, "Computational Evaluation of the Performance of Lifting Surfaces with Leading-Edge Protuberances," *Journal of Aircraft* vol. 48, March-April 2011.

## The Effect of Wavy Leading Edge Modifications on NACA 0021 Airfoil Characteristics

N. Rostamzadeh, R.M. Kelso, B.B. Dally and K.L. Hansen

School of Mechanical Engineering

University of Adelaide, Adelaide, South Australia 5005, Australia

### Abstract

In spite of its mammoth physical size, the Humpback whale's manoeuvrability in hunting has captured the attention of biologists as well as fluid mechanists. It has now been established that the protrusions on the leading edges of the Humpback's pectoral flippers, known as tubercles, account for this baleen species' agility. In the present work, Prandtl's non-linear lifting-line theory was employed to propose a hypothesis that the favourable traits observed in the performance of tubercled lifting bodies are not exclusive to this form of leading edge configuration. Accordingly, a novel alternative to tubercles was introduced and incorporated into the design of four airfoils that underwent wind tunnel force measurement tests in the transitional flow regime. The experimental results demonstrate similar loading characteristics of the newly designed foils in comparison with those with tubercles, suggesting the presence of an analogous flow mechanism.

### Introduction

The Humpback whale's dynamic agility in executing tight turns when catching prey is remarkable [10]. When rolling in a banking turn, hydrodynamic lift forces are developed on the Humpback's flippers whose horizontal components act as the centripetal force [17]. Fish and Battle [6] postulated that the protuberances on the leading edges of the whale's pectoral flippers, known as tubercles, may account for the Humpback's extraordinary manoeuvrability through maintaining lift at high attack angles.

To assess the hypothesis, Miklosovic *et al.* [12] conducted a series of wind tunnel experiments that unveiled the desirable characteristics of idealised flipper models. It was learned that, compared to the finite-span wing without tubercles, the modified model delayed the stall angle by nearly 40%, achieved a 6% increase in the maximum lift coefficient and incurred lower drag at high incidence angles.

Inspired by the initial promising results, Stein *et al.* [15], Miklosovic *et al.* [11], Johari *et al.* [9] and Hansen *et al.* [7] carried out low Reynolds number force measurement tests on nominally two-dimensional foils, as opposed to finite wings. It was found that, compared to the unmodified models, most foils with tubercles displayed gradual stall characteristics with higher post-stall lift, yet their pre-stall performance was degraded.

Amongst other studies, Custodio [4], van Nierop *et al.* [16], Stanway [14], Pedro and Kobayashi [13], and Hiroshi *et al.* [8] utilised experimental and numerical methods to examine the flow field around foils and wings with tubercles. An important outcome of these investigations indicated the presence of pairs of counter-rotating streamwise vortices in the vicinity of the lifting surfaces. Hence, it was proposed that the beneficial aspects of lifting surfaces with tubercles are associated with streamwise vorticity present in the flow field.

Although the desirable features of tubercles have been identified for full-span and semi-span wings, the underlying mechanisms and the role played by streamwise vortices through which these traits become manifest are not fully understood. In addition, leading edge modifications as alternatives to tubercles that trigger similar flow mechanisms have not been introduced.

In an attempt to gain further insight into the underlying flow dynamics induced by tubercles, Prandtl's non-linear lifting-line theory (PNLLT) was used in the present work. The analysis of span-wise circulation led to the design of a novel leading-edge configuration referred to as the wavy model. The hypothesis adopted was that the alternative modification would exhibit similar aerodynamic traits as predicted by PNLLT. Accordingly, four modified NACA 0021-based airfoils were fabricated to undergo wind tunnel force measurement tests in the transitional flow regime.

### Overview of Prandtl's Non-linear Lifting-line Theory

Ludwig Prandtl (1875-1953) in his classical lifting-line theory presented an innovative approach that enabled the study of significant aerodynamic parameters such as circulation and its distribution along the span of a finite wing [2, 5]. The non-linear lifting-line method as detailed by Anderson [1] is an extension of Prandtl's lifting-line theory with an advantage over a linear approach, as it incorporates experimental data associated with a baseline foil to capture the near and post-stall behaviour of a finite wing. Despite being an approximate method, in the context of wings with passive undulating leading edges, the iterative PNLLT scheme can shed light on the development of circulation.

### Details of Analysis

Herein, two forms of wings with undulating leading edges were considered: tubercles, where the chord varies in a sinusoidal manner along the span of a finite wing [2, 5]. The non-linear lifting-line method as detailed by Anderson [1] is an extension of Prandtl's lifting-line theory with an advantage over a linear approach, as it incorporates experimental data associated with a baseline foil to capture the near and post-stall behaviour of a finite wing. Despite being an approximate method, in the context of wings with passive undulating leading edges, the iterative PNLLT scheme can shed light on the development of circulation.

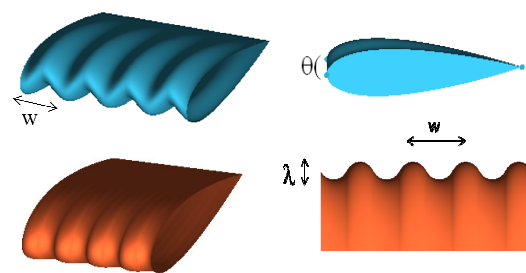


Figure 1. Top row: Wavy wing section showing peak-to-peak angular amplitude and wavelength. Bottom row: Tubercled wing section showing the amplitude and wavelength

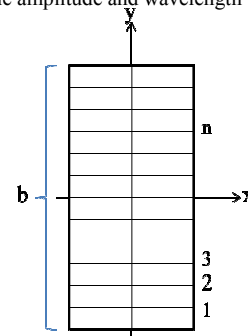


Figure 2. The coordinates system with a number of stations marking various locations along the span (top view)



Each wavelength of the wing was allocated a number of stations to represent various locations along the span (Figure 2). As an initial estimate, an elliptic lift distribution was assigned to the stations according to:

$$\Gamma(y_n)_{\text{initial}} = \Gamma_0 \sqrt{1 - \left(\frac{2y_n}{b}\right)^2} \quad (1)$$

$\Gamma_0$ , an arbitrary initial guess, was set to  $0.4 \text{ (m}^2\text{s}^{-1}\text{)}$ .

The induced angle of attack was found by:

$$\alpha_i(y_n) = \frac{1}{4\pi V_\infty} \int_{-b/2}^{b/2} \frac{d\Gamma/dy}{y_n - y} dy \quad (2)$$

where  $V_\infty = 25 \text{ (ms}^{-1}\text{)}$  is the free-stream speed and  $b=0.495 \text{ (m)}$  is the span. These values were chosen to match the parameters in the present work's experimental setup.

Next, Simpson's rule was applied to compute the integral in (2):

$$\frac{\alpha_i(y_n)}{\zeta} = \sum_{j=2,4,6,8\dots}^k \frac{(d\Gamma/dy)_{j-1}}{(y_n - y_{j-1})} + 4 \frac{(d\Gamma/dy)_j}{(y_n - y_j)} + \frac{(d\Gamma/dy)_{j+1}}{(y_n - y_{j+1})} \quad (3)$$

$$\zeta = \frac{\Delta y}{12\pi V_\infty} \quad (4)$$

Singularities occur at  $(y_n = y_{j-1}, y_n = y_j, y_n = y_{j+1})$ . Therefore, these terms had to be estimated using the average of the neighbouring terms [1]. For instance, at  $(y_n = y_{j-1})$ :

$$2 \frac{(d\Gamma/dy)_{j-1}}{(y_n - y_{j-1})} = \frac{(d\Gamma/dy)_{j-2}}{(y_n - y_{j-2})} + \frac{(d\Gamma/dy)_j}{(y_n - y_j)} \quad (5)$$

For a wavy wing, the geometric angle of attack is given by:

$$\alpha_n = \frac{\theta}{2} \sin\left(\frac{2\pi}{w} y_n\right) \quad (6)$$

By contrast, for tubercles, the chord varies according to:

$$c_n = \frac{\lambda}{2} \sin\left(\frac{2\pi}{w} y_n\right) + c_{\text{mean}} \quad (7)$$

$c_{\text{mean}} = 0.07 \text{ (m)}$  is the mean chord. Given the geometric attack angle and the calculated induced angle in equation (2) at each station, the effective angle of attack was obtained by Prandtl's *Fundamental equation of lifting-line theory*:

$$\alpha_E = \alpha - \alpha_i \quad (8)$$

At each station, the value of the effective attack angle was used to extract the baseline NACA0021 lift coefficient, obtained from experimental data by Hansen *et al.*[7].

Using the Kutta-Joukowski's theorem, a new circulation distribution was found from the lift coefficient distribution:

$$\Gamma_n = \frac{1}{2} V_\infty c_n (C_L)_n \quad (9)$$

The circulation distribution was then compared to the initial guess and updated in (9) where a typical value of 0.04 was selected for the damping coefficient,  $\varepsilon$ .

$$\Gamma_{\text{new}} = \Gamma_{\text{initial}} + \varepsilon(\Gamma_{\text{initial}} - \Gamma_n) \quad (10)$$

Subsequently, a loop was established by replacing  $\Gamma_{\text{initial}}$  with  $\Gamma_{\text{new}}$  in equation (1). Convergence was determined once the difference between two consecutive estimates of circulation at each station diminished to 0.001.

## Results of Theoretical Analysis

Figure 3 (a-d) illustrates how circulation varies along half of the span for a tubercled and a wavy wing pre- and post-stall. The values for wavelength and amplitude are expressed in millimetres, and the peak-to-peak amplitude in degrees.

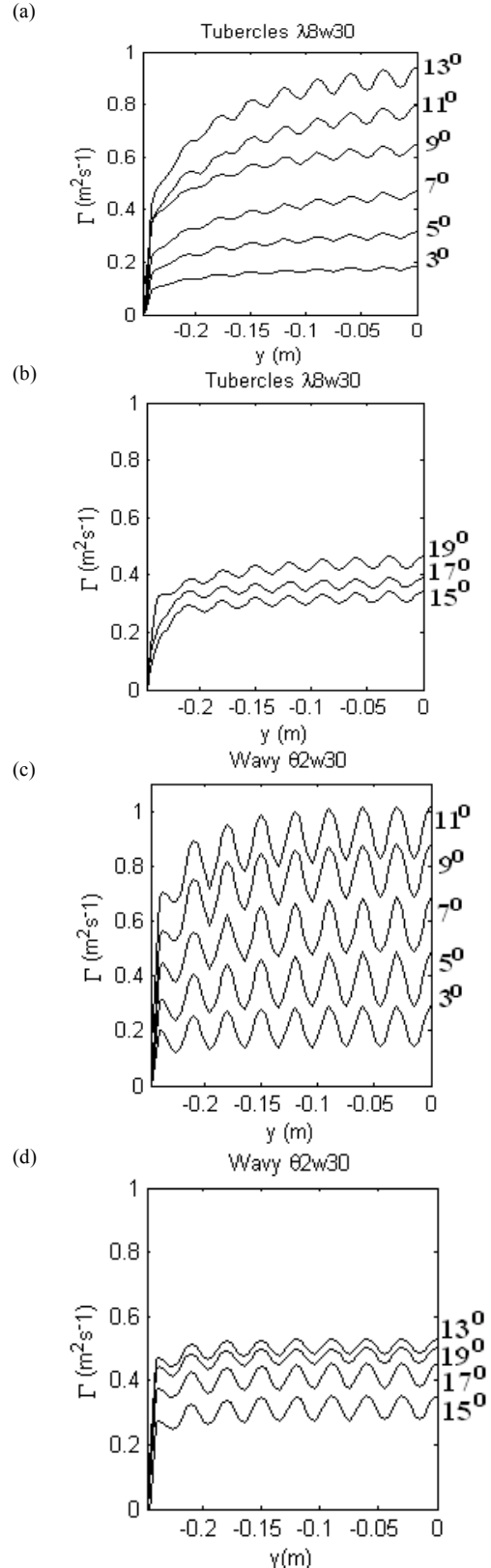


Figure 3 (a-d). Spanwise circulation for a tubercled and wavy foil at various incidence angles along half of the span

To predict the effect of the peak-to-peak angular amplitude and wavelength on the overall performance of wavy wings, circulation was integrated along the span for three finite wings:

$$C_L = \frac{2}{V_\infty b} \int_{-b/2}^{b/2} \Gamma(y) dy \quad (11)$$

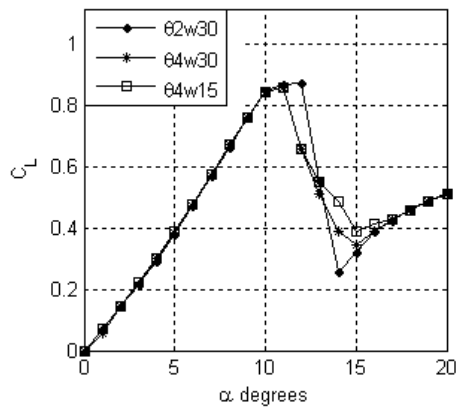


Figure 4. Lift coefficient for three finite wavy wings obtained by Prandtl's non-linear lifting-line theory

Prandtl's non-linear lifting-line theory demonstrates that, for the wavy wing, the distribution of circulation along the span assumes an oscillatory pattern similar to that of tubercles, pointing to the presence of streamwise vortices in both cases. It is also noticed that with the increase in attack angle, the amplitude of oscillations grows for the tubercled wing. Since the strength of the streamwise vortices is proportional to the slope of the circulation curve, it is predicted that stronger vortices are generated at higher attack angles. On the other hand, for the wavy wing, the amplitude of oscillations is noticeably larger even at low angles, signifying the presence of stronger vortices.

As illustrated in Figure 4, the wavy wing with  $\theta = 2(\text{deg})$  undergoes sudden stall while the ones with  $\theta = 4(\text{deg})$  experience a more gradual loss of lift. It is also predicted that ( $\theta 4w15$ ) would stall less abruptly compared to wings with wavelengths equal to 30 (mm). From these observations, it can be deduced that wavy wings with shorter wavelengths and larger peak-to-peak amplitudes are likely to display more desirable attributes such as extended and gradual stall.

Although the results presented here are derived for finite-wings, it is conceivable that the global behaviour of spanwise circulation for full-span lifting surfaces is oscillatory.

#### Details of Experimental Work

To assess the aerodynamic loading characteristics of full-span wavy foils against an unmodified model, a series of force measurement tests were performed at  $Re=120,000$  in the closed-loop KC wind tunnel at the University of Adelaide. The test section of the tunnel has a  $500(\text{mm}) \times 500(\text{mm})$  cross-section with a maximum blockage ratio of 6% at a 25-degree attack angle. The turbulent intensity of the tunnel is approximately 0.8% ahead of the test subject.

Of the four NACA0021-based wavy foils with varying wavelength and peak-to-peak angular amplitude, three were machined from aluminium and one was cast from epoxy resin (Figure 5). All the airfoils have mean chord and span lengths equal to 70 (mm) and 495 (mm) respectively.

A six-component load cell from JR3, with an uncertainty estimate of  $\pm 1\%$ , was used to measure normal and chord-wise forces (with respect to the airfoil) which were then converted into lift and drag. A Vertex rotary table was attached to the base

of the load cell to allow accurate and repeatable changes in the attack angle.

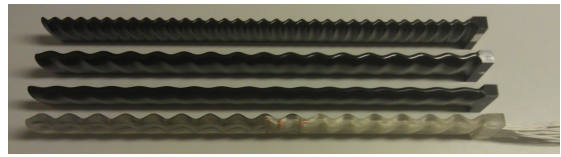


Figure 5. Wavy foils :  $\theta 4w15$  ,  $\theta 4w30$  ,  $\theta 2w30$  ,  $\theta 6.5w30$  (top to bottom)

With the sampling period of the analogue-to-digital converter set to 16 (ms), 3,000 data points, corresponding to normal and tangential force components, were collected at each angle of attack. The tests were repeated five times for every foil and average values of the lift and drag coefficients were calculated accordingly. The average standard errors in estimating the population means for lift and drag coefficients were 0.003 and 0.009. Wind tunnel corrections for solid, wake blockage and streamline curvature were also applied to the results in accordance with recommendations by Barlow[3].

#### Experimental Results

##### Performance Effect of Variation in Wavy Foil Wavelength

It is noticed from Figure 6, that the unmodified and wavy foils produce nearly the same lift-curve slope up to 4 degrees. At this point, the curves deviate from the linear trend which hints at extra lift produced by the presence of laminar separation bubbles (LSB). With regard to the maximum lift coefficient, the unmodified foil achieves the highest value, followed by a dramatic loss of lift past 12 degrees, and a consequent rise in drag.

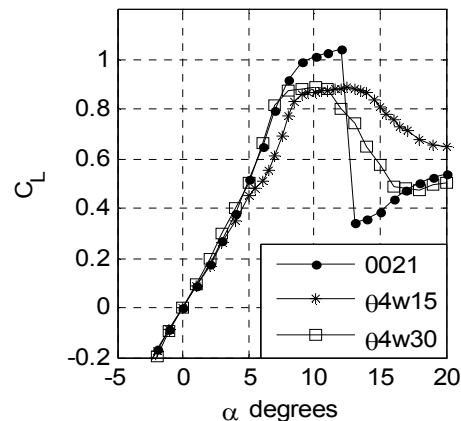


Figure 6. Lift coefficient versus attack angle for two wavy foils of varying wavelength, and the unmodified NACA 0021

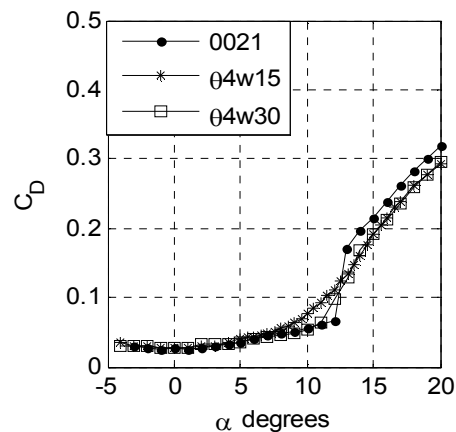


Figure 7. Drag coefficient versus angle of attack for two wavy foils of varying wavelength, and the unmodified NACA0021

Between the wavy foils of the same wavelength,  $\theta 4w15$  outperforms  $\theta 4w30$  post-stall as it undergoes a more gradual stall with a higher amount of lift, indicating that smaller wavelengths may be more beneficial for wavy foils.

#### Performance Effect of Variation in Wavy Foil Peak-to-Peak Angular Amplitude

Comparison of the lift coefficient for the wavy foils of the same wavelength against the unmodified NACA 0021 foil (Figures 8 and 9) reveals that both wavy foils produce lower lift pre-stall. The unmodified and  $\theta 2w30$  foils exhibit a sudden loss of lift and identical post-stall behaviour, however  $\theta 6.5w30$  shows superior performance past 12 degrees with lower drag coefficients. The observations indicate that wavy foils with higher peak-to-peak amplitudes may render more aerodynamic benefits in the post-stall region.

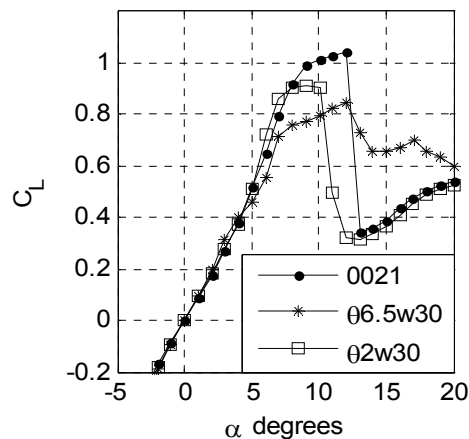


Figure 8. Lift coefficient versus the attack angle for two wavy foils of varying peak-to-peak angular amplitude, and the unmodified NACA 0021

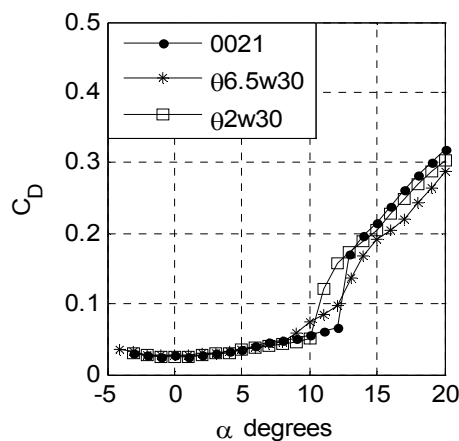


Figure 9. Drag coefficient versus the attack angle for two wavy foils of varying peak-to-peak angular amplitude, and the unmodified NACA 0021

#### Conclusions

The present investigation attempted to broaden our understanding of the flow mechanism triggered by incorporating passive wavy leading edges. In spite of its simplified assumptions, Prandtl's non-linear lifting-line theory succeeded in demonstrating that both the newly-proposed design, referred to as the wavy configuration, and tubercles, induce an oscillatory distribution of circulation along the span. This prediction implies that the wavy foils exhibit similar aerodynamic characteristics to those with tubercles. In addition,

the pattern of circulation points to the presence of streamwise vortices in flows over wavy lifting surfaces.

The results of wind tunnel tests on four wavy foils revealed that three of the wavy foils showed delayed stall, a prominent trait also observed in flows over tubercled wings. Amongst the examined models, the one with the highest peak-to-peak angular amplitude and smallest wavelength yielded the most favourable post-stall behaviour. In view of the findings, there is sufficient evidence to merit more attention to the proposed novel leading edge modification.

#### Acknowledgements

Thanks to Mechanical Engineering workshop staff, in particular Mr. Bill Finch and Mr. Richard Pateman, for their valuable cooperation in the process of manufacturing the wing models.

#### References

1. Anderson, J., *Fundamentals of Aerodynamics*. Fourth ed. 2005: McGraw-Hill International Higher Education.
2. Anderson, J.D., Corda, S., and Van Wie, D.M., *Numerical Lifting Line Theory Applied to Drooped Leading-Edge Wings Below and Above Stall*. Journal of Aircraft, 1981. **17**(12).
3. Barlow, J.B., Pope, A., and Rae, W.H., *Low Speed Wind Tunnel Testing*. 3rd edition (September 1999): Wiley-Interscience.
4. Custodio, D., *The Effect of Humpback Whale-Like Leading Edge Protuberances on Hydrofoil Performance*, in Thesis submitted to Worcester Polytechnic Institute. December 2007.
5. Durrand, W.F., *Aerodynamic Theory*. Vol. 1 and 2. 1935, Berlin: Julius Springer.
6. Fish, F.E. and Battle, J.M., *Hydrodynamic Design of the Humpback Whale Flipper*. Journal of Morphology, 1995. **225**: p. 51-60.
7. Hansen, K.L., Kelso, R.M., and Dally, B.B., *Performance variations of leading-edge tubercles for distinct airfoil profiles*. AIAA Journal Journal of Aircraft, 2011. **49**:185-94.
8. Hiroshi, A., et al., *A Study on Stall Delay by Various Wavy Leading Edges*. Journal of Aero Aqua Bio-mechanisms, 2010. **1**(Special Issue on Fourth International Symposium on Aero Aqua Bio-Mechanisms): p. 18-23.
9. Johari, H., et al., *Effects of Leading Edge Protuberances on Airfoil Performance*. AIAA Journal, November 2007. **45**:11.
10. Jurasz, C.M. and Jurasz, V.P., *Feeding Modes of the Humpback Whale, Megaptera novaeangliae, in Southeast Alaska*. Scientific Reports of the Whales Research Institute, 1979. **31**: p. 69-83.
11. Miklosovic, D.S., Murray, M.M., and Howle, L., *Experimental Evaluation of Sinusoidal Leading Edges*. Journal of Aircraft, 2007. **44**:1404-1407.
12. Miklosovic, D.S., et al., *Leading Edge Tubercles Delay Stall on Humpback Whale Flippers*. Physics of Fluids, 2004. **16**(5) : p. L39-L42.
13. Pedro, H.T.C. and Kobayashi, M.H. *Numerical Study of Stall Delay on Humpback Whale Flippers*. in Proceedings of 46th AIAA Aerospace Sciences Meeting and Exhibit. 7-10 January 2008. Reno, Nevada.
14. Stanway, M.J., *Hydrodynamic effects of leading-edge tubercles on control surfaces and in flapping foil propulsion*, in Mechanical Engineering. February 2008, Massachusetts Institute of Technology.
15. Stein, B. and Murray, M.M. *Stall Mechanism Analysis of Humpback Whale Flipper Models*. in Proc. of Unmanned Untethered Submersible Technology (UUST). August 2005. Durham, NH.
16. van Nierop, E., Alben, S., and Brenner, M.P., *How Bumps on Whale Flippers Delay Stall: an Aerodynamic Model*. Physical review letters, 7 February 2008. **PRL 100**: 054502.
17. Weihs, D., *Effects of Swimming Path Curvature on the Energetics of Fish Swimming*. Fish Bull, 1981. **79**: p. 171-176.

## An Experimental and Computational Study of Flow over a NACA 0021 Airfoil with Wavy Leading Edge Modification

N. Rostamzadeh, R.M. Kelso, B.B. Dally, Z.F. Tian

School of Mechanical Engineering

University of Adelaide, Adelaide, South Australia 5005, Australia

### Abstract

Flow control by means of tubercles, which are spanwise-periodic protrusions observed on the Humpback whale's flippers, has been previously shown to exhibit beneficial aerodynamic traits. Understanding the mechanism that yields the desirable results among nominally two-dimensional airfoils has led to the design of an alternative leading edge configuration. In the present work, this novel variation on tubercles was employed to modify a NACA 0021 airfoil for wind tunnel pressure measurement tests in the transitional flow regime. In addition, a Computation Fluid Dynamics study was performed using the SST transitional model in the context of unsteady RANS at several attack angles. The results from the numerical investigation are in reasonable agreement with those of the experiments, and suggest the presence of features that are also observed in flows over tubercled foils, most notably a distinct pair of streamwise vortices for each wavelength of the tubercle-like feature.

### Introduction

Nature with its elegance and mystique has always served as a generous source of inspiration and creativity. One peculiar instance that has intrigued fluid mechanists and zoologists for the past decade is the Humpback whale's ability to turn around tight angles in its bubble-net feeding strategy [7].

To determine whether the scalloped leading edge of the Humpback's flippers plays a role in the Humpback's swift mobility, Fish and Watts [14] carried out a computational fluid dynamics study. For this purpose, an inviscid flow solver was developed to compare the performance of a scalloped finite-span wing based on the NACA 634-021 profile against its unmodified equivalent at a 10 degree angle of attack. The results showed the overall superior performance of the scalloped wing with a 4.8 % increase in lift, and a 10.9 % reduction in induced drag.

A second numerical study as reported by Fish *et al.* [6] was carried out by Paterson *et al.* [10] in which an unsteady RANS simulation was performed on a tubercled and an unmodified NACA 63-021 baseline foil. The Reynolds number, based on the chord length, was 1,000,000. At an incidence angle equal to 10 degrees, the results demonstrated a dramatic change in the pressure contours on the tubercled model along with large vortices posterior to the troughs. Flow separation was observed to have been delayed behind the peaks to almost the trailing edge, preventing the onset of stall.

Miklosovic *et al.* [9] carried out wind tunnel force measurement tests on half-span scale models of an idealized Humpback whale flipper (1/4 scale) with and without tubercles on a NACA 0020 baseline foil. The Reynolds numbers for the tests were between 505,000 and 520,000, which fall in the operating range of Humpback whales. The experiments yielded a 40% delay in the stall angle for the wing with tubercles accompanied by a 6% increase in the maximum lift coefficient and lower drag coefficients in the post-stall regime. The authors concluded that

a vortex-generating mechanism similar to that employed by vortex generators on an aircraft wing may explain the higher lift characteristics. It was hypothesized that through energizing the scalloped flipper's boundary layer, tubercles inhibit chord-wise separation that accounts for earlier stall on an otherwise smooth wing.

In order to evaluate the influence of tubercles in flow separation and the vorticity field, a numerical simulation was carried out by Pedro and Kobayashi [11] on the scalloped and unmodified flipper models set up for the experiments by Miklosovic *et al.* [9]. In this CFD study, a Detached Eddy Simulation scheme was employed to analyse the flow at a Reynolds number of 500,000. The simulation was run at angles of attack between 12 and 18 degrees since the main differences had been reported to occur in this range. The contours of vorticity showed a chaotic outboard region towards the tip for both wings due to flow separation, however in the midsection of the flippers the differences became evident. The scalloped wing displayed higher values of the magnitude of vorticity compared to the unmodified model in that region, suggesting the presence of streamwise vortices that aligned themselves with the tubercles. Similar findings were reported by Weber *et al.* [15].

Rostamzadeh *et al.* [12] used Prandtl's non-linear lifting-line method to demonstrate that the aero/hydrodynamic benefits of tubercles can be obtained via a novel wavy leading edge modification employing an analogous flow mechanism. Wind tunnel force measurement results confirmed that full-span wavy wings exhibit gradual stall compared to a wing with a smooth leading edge.

The present work is aimed at investigating how pressure and vorticity fields are affected by the incorporation of the wavy leading edge on a NACA 0021 baseline foil. To this end, wind tunnel pressure measurement experiments were conducted in the transitional flow regime, and used to validate the results from a CFD study.

### Experimental Work

Pressure measurement tests were performed at a chord-based Reynolds number equal to 120,000 in the 500(mm)×500(mm) test section of the KC wind tunnel at the University of Adelaide. The test subject was a full-span wavy foil with a 6.5 (deg) peak-to-peak angular amplitude and a wavelength equal to 30(mm) shown in Figures 1 and 2. To ensure 2D flow near the free-end wing tip, a wall clearance of 3 (mm) was maintained [2]. The turbulence intensity of the flow stream ahead of the wing was measured at 0.8%.

Pressure taps were drilled onto the top surface of the foil in three rows along the 70-milimeter-chord lines corresponding to a trough, a peak and a middle cross-section. Of the thirty bored taps, two were blocked including one at the stagnation point on a peak and therefore not used in the experiments.

A series of PVC tubes, embedded in the foil, connected the surface pressure taps to the head-ports of a controller-modulated ScaniValve. To achieve high-precision pressure measurements, a 10-Torr MKS Baratron (model 220BD) with a resolution of 0.01% of the full scale range was utilised.

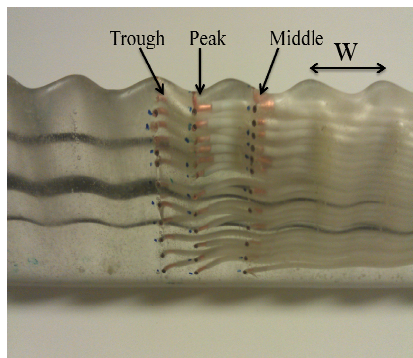


Figure 1. Wavy wing section with three pressure tapping rows, showing the wavelength,  $W$ (mm)



Figure 2. Side view of the wavy wing section, showing the peak-to-peak angular amplitude,  $\theta$  (deg)

The free-stream speed and static pressure were measured at 25 (m/s) and 0.8 (Torr) below the ambient pressure. For a given incidence angle, 2,000 data points (per pressure port) were collected at a sampling rate of 200HZ. It was observed that 200HZ was sufficient to establish a typical small standard error of  $2.5 \times 10^{-5}$  (Torr) in estimating the population mean.

### Experimental Results

As the taps were placed on one side (upper surface) of the wing, the data from the negative attack angles were used to determine the pressure values for the lower surface. Care was taken to ensure that the peak and trough pressure distributions were correctly matched.

At  $AOA = 2^\circ$  (Figure 3a), the wavy foil's trough experiences lower pressure on the suction side than the peak. The abrupt change in pressure gradient at  $x/c=0.4$  on the suction side of the trough, and  $x/c=0.6$  on the lower side of the peak, indicates the presence of Laminar Separation Bubbles (LSB). This flow feature is often observed at low Reynolds numbers where separation due to strong adverse pressure gradients gives rise to Helmholtz-instabilities whose breakdown result in separation-induced transition, and the formation of LSBs [5].

Increasing the angle of attack, forces the LSB to move towards the trough's leading edge, as a drop in pressure occurs on the suction surface. Meanwhile, the pressure on the lower surface of the peak rises, and the LBS on this side moves towards the trailing edge, indicating that the separation point has translated further downstream (Figure 3b).

At  $\alpha = 12^\circ$  (Figure 3c), the overall shape of pressure distribution begins to alter, especially for the suction surface of the middle cross-section. The flatness of the pressure curve past  $x/c=0.3$  on the middle cross-section signifies that flow separation begins to affect a larger area on the airfoil as stall is initiated gradually.

At higher angles, flow separation seems to have dominated the suction side, however the leading edge of the trough cross-section, maintains low values of pressure that account for lift being generated in the post-stall zone.

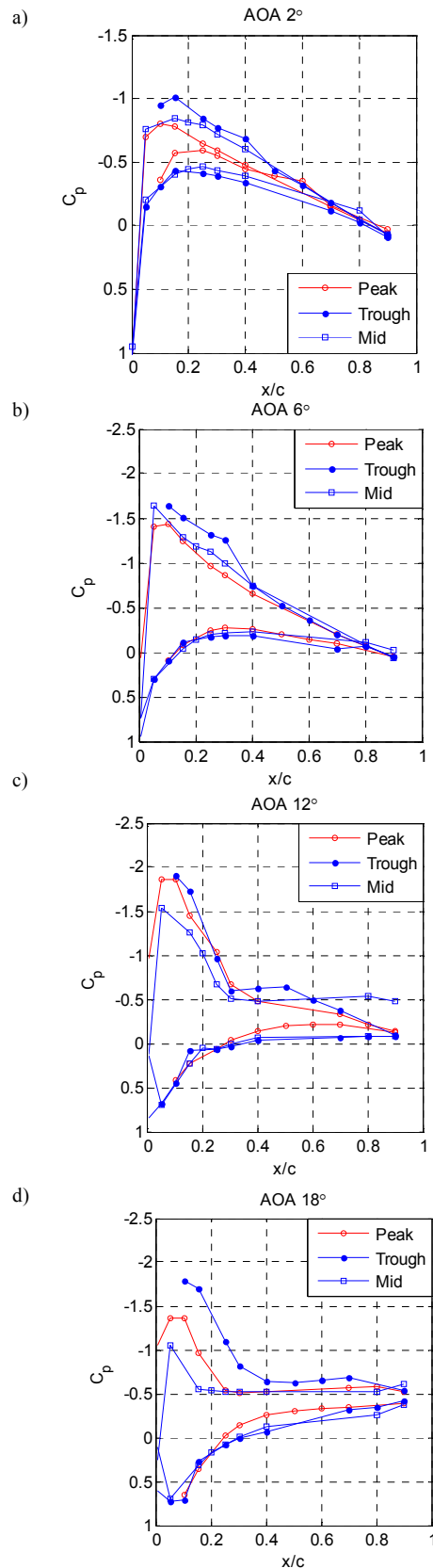


Figure 3(a-d). Chord-wise pressure distribution on a peak, trough and mid cross-section at different attack angles

Using the trapezoidal rule for integration, the amount of lift generated at each cross section was estimated. Since there were no data available for the stagnation point on the trough, a shape-preserving interpolant curve-fit was applied to account for the error incurred. Also, the contribution of shear forces to lift, which in most cases is negligible, is not included.

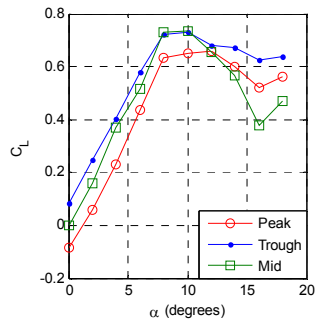


Figure 4. Calculated sectional lift coefficient as a function of attack angle

Figure 4 shows that both prior to and post stall, the trough produces more lift than the two other sections. Pre-stall the mid cross-section contributes to lift generation more than the peak however loss of lift is more prominent in this cross-section post-stall. It must be noted that the total amount of lift on the wing section can not be regarded as the average lift of the three sections as the flow structure is complex, and direct force measurement tests as reported by Rostamzadeh *et al.* [12] is the most reliable method.

#### Computational Fluid Dynamics Study

This section presents a complementary CFD investigation performed using the commercial package ANSYS-CFX 12.1 suite [1] to model the unsteady flow over one wavelength of the wavy foil 06.5w30 at several incidence angles. To capture the transitional nature of the flow, the newly-formulated SST  $\gamma - Re_{\theta}$  [8] model that has been successful [3] in external aerodynamics was employed. The eight transport equations for this model can be found in [8], and have not been included here for brevity.

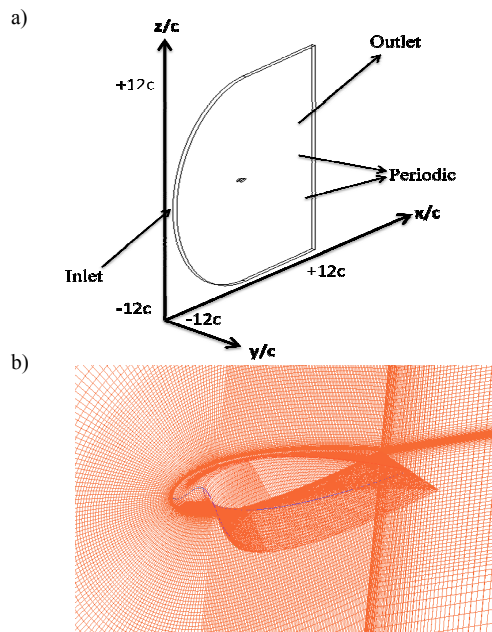


Figure 5(a-b). The computational domain and grid system near the foil

A C-Grid topology (Figure 5) with hexahedral elements was constructed to designate the computational domain. The angle of attack was changed at the *Inlet* via the velocity components and *Periodic boundaries* were assigned to the side planes since one wavelength of the wing was modelled.

A grid resolution study was performed to establish a mesh-independent solution. Of the three generated grids, the one with a total number of nodes equal to  $3.5 \times 10^6$  proved to be sufficient for grid independence whose  $y^+$  values near the foil were maintained below 1.

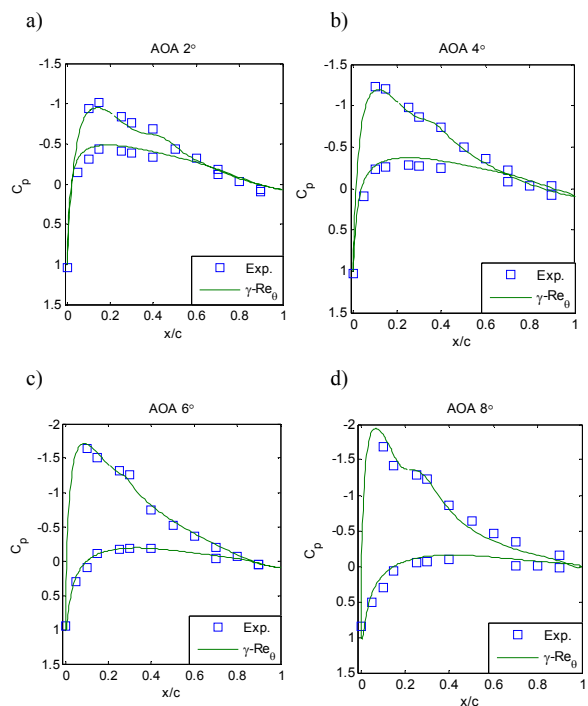
#### Solution Strategy

ANSYS 12.1 implements a finite control volume-oriented finite element method to discretise the partial differential transport equations. A second-order backward Euler scheme was selected for temporal discretisation, while an alternating first and second-order accurate scheme was implemented for spatial discretisation. Solution convergence of the eight transport equations was determined by achieving a maximum residual target of  $10^{-5}$  per time step. In addition, the lift and drag coefficients were used as monitor points during the solution process.

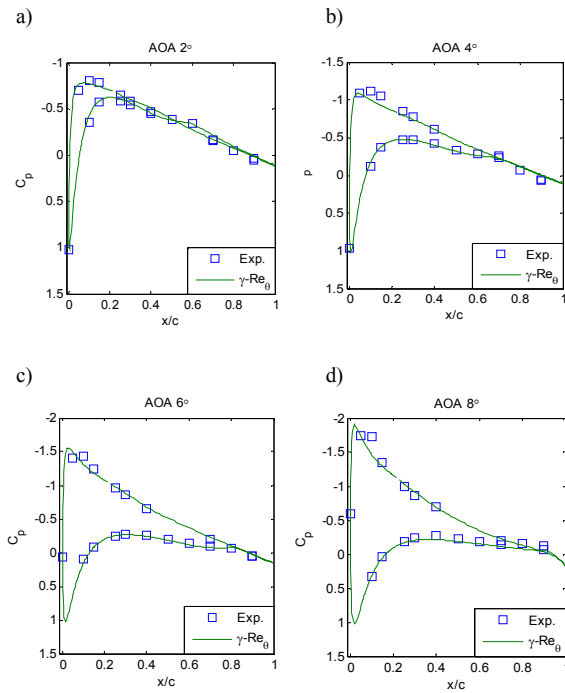
The solution strategy comprised two different stages. Initially, a steady-state run was performed and the behaviour of the residuals was monitored. It was observed that the residuals diminished steadily down to  $10^{-4}$  in the proximity of the seventieth iteration at which point an oscillating pattern emerged. Subsequently, the steady-state solution was used as the initial guess for the transient solver. A time-step equal to  $5 \times 10^{-5}$  (s) with three inner loops was selected for the transient run. The results are presented at  $t=0.01$  (s) where the lift and drag forces have stabilised.

#### Validation Results

Figures 6-7 show that correspondence between the numerical solutions with the data obtained from experiments is very satisfactory.



Figures 6(a-d). Comparison of the experimental and numerical pressure coefficient on a trough.



Figures 7(a-d). Comparison of the experimental and numerical pressure coefficient on a peak cross-section

Contours of surface streamlines colored by streamwise vorticity have been plotted on planes oriented normal to the free-stream flow direction at a zero attack angle (Figure 8). It is observed that a distinct pair of counter-rotating vortices is realised in the wake. Each vortex consists of smaller vortices, one originating from the upper and the other from the lower wing surface, imparting a slanted appearance to the pair. The magnitude of vorticity at the cores of the vortices decreases with distance from the trailing edge, suggesting a diffusion process as vorticity spreads outward from the cores. The pair appears to rotate towards each other, coming to a near-parallel orientation as it convects downstream. The presence of streamwise vortices, confirms the prediction by Prandtl's lifting-line theory as reported by the authors [12].

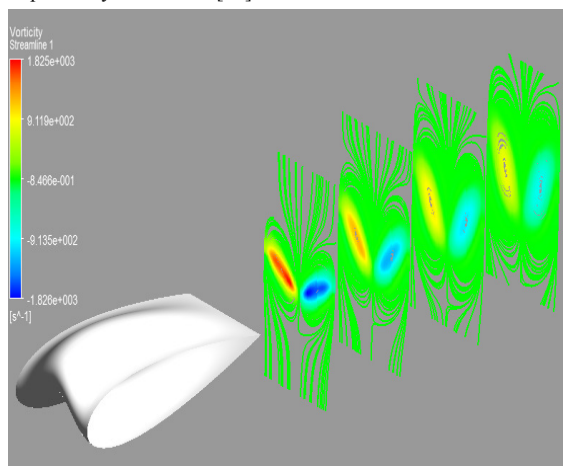


Figure 8. Surface streamlines colored by vorticity on planes located at  $x=30$  (mm),  $60$  (mm),  $90$  (mm) and  $120$  (mm) downstream of the trailing edge at zero incidence angle

## Conclusions

The present experimental work on a full-span wavy foil demonstrates that the low pressure region near the leading edge on the trough cross-section produces the most lift post-stall,

preventing a sudden loss of lift. This flow feature is analogous to the low pressure zone in the trough of a tubercled foil [4, 13]. In addition, the CFD investigation showed the presence of strong counter-rotating streamwise vortices in the wake of the wavy foil, pointing to another notable feature in the flow produced by wings with tubercles. Further work is required to examine the flow field in more detail to assess the role played by vortices in the gradual stall phenomenon.

## References

1. ANSYS® Academic Research, Release 12.1
2. Barlow, J.B., Pope, A., and Rae, W.H., *Low Speed Wind Tunnel Testing*. 3rd edition September, 1999: Wiley-Interscience.
3. Council, J.N.N. and Goni Boulama, K., *Validating the URANS SST  $\gamma$ - $Re_{\theta}$  model for low Reynolds number external aerodynamics*. International Journal for Numerical Methods in Fluids June 20, 2011. **69**(8): p. 1411-1432.
4. Custodio, D., *The Effect of Humpback Whale-Like Leading Edge Protuberances on Hydrofoil Performance*, in Thesis submitted to Worcester Polytechnic Institute. December 2007.
5. Dovgal, A.V., Kozlov, V.V., and Michakle, A., *Laminar boundary layer separation: instability and associated phenomena*. Prog. Aerospace Science 1994. **30**, 61-94.
6. Fish, F.E. and Lauder, G.V., *Passive and active flow control by swimming fishes and mammals*. Annu. Rev. Fluid Mech, 2006. **38**: p. 193-224.
7. Jurasz, C.M. and Jurasz, V.P., *Feeding Modes of the Humpback Whale, Megaptera novaeangliae, in Southeast Alaska*. Scientific Reports of the Whales Research Institute, 1979. **31**: p. 69-83.
8. Langtry, R. and Menter, F., *Correlation-based transition modeling for unstructured parallelized computational fluid dynamics codes*. AIAA Journal, 2009. **47**: 2894-2906.
9. Miklosovic, D.S., Murray, M.M., Howle, L.E., and Fish, F.E., *Leading Edge Tubercles Delay Stall on Humpback Whale Flippers*. Physics of Fluids, 2004. **16**(5) : p. L39-L42.
10. Paterson, E.G., Wilson, R.V., and Stern, F., *General-purpose parallel unsteady RANS CFD code for ship hydrodynamics*. IIHR Hydrosci. Eng. Rep., 2003. **531**.
11. Pedro, H.T.C. and Kobayashi, M.H. *Numerical Study of Stall Delay on Humpback Whale Flippers*. in Proceedings of 46th AIAA Aerospace Sciences Meeting and Exhibit. 7-10 January 2008. Reno, Nevada.
12. Rostamzadeh, N., Kelso, R.M., Dally, B.B., and Hansen, K.L., *The effect of wavy leading edge modifications on NACA 0021 airfoil characteristics*, in 18th Australian Fluid Mechanics Conference. 2012: Launceston, Australia.
13. van Nierop, E., Alben, S., and Brenner, M.P., *How Bumps on Whale Flippers Delay Stall: an Aerodynamic Model*. Physical review letters, 7 February 2008. **PRL 100**: 054502.
14. Watts, P. and Fish, P.E. *The Influence of Passive Leading Edge Tubercles on Wing Performance*. in Proc. of 12th Internat Symp Unmanned Untethered Submersible Technology (UUST). 2001. Durham NH: Autonomous Undersea Systems Institute.
15. Weber, P., Howle, L., Murray, M., and Miklosovic, D., *Computational Evaluation of the Performance of Lifting Surfaces with Leading-Edge Protuberances*. Journal of Aircraft March-April 2011. **48**(2).